A liquid crystal device for speckle reduction in coherent light

David Jonathan Hansford

Brasenose College

Trinity Term 2018

A thesis submitted for the degree of Doctor of Philosophy

Department of Engineering Science

University of Oxford

Abstract

High coherence in laser light causes spatially distributed interference called speckle. In applications such as holographic projection, this undesirable side effect degrades image clarity. The current methods of speckle reduction, such as a rotating ground-glass diffuser, require additional bulky moving parts. In this thesis an alternative technology is presented based upon a compact chiral nematic liquid crystal device. A spatially-random, time-varying phase modulation of the incident light is achieved through the electrohydrodynamic instabilities that are induced by an alternating electric field.

Presented within is a study of material and device properties as a function of speckle reduction and transmission, as well as the electric field conditions required for peak performance. These properties are investigated experimentally and through optical simulation. It is shown that a chiral nematic with short pitch ($p \approx 250\,nm$), moderate birefringence ($1.5 \leq \Delta n \leq 2.0$) and minimal rotational viscosity provide maximum speckle reduction while optimising transmission of light through the device. A glass cell thickness of 20 μm is preferred for maximum speckle reduction and cell lifetime, with minimal hysteresis. Increased cell temperature is found to improve speckle reduction and transmission, while slightly reducing the electric field amplitude required for peak performance. This is expected to be largely due to a significant reduction in viscosity with increased temperature. Additional scattering particulates are shown to only improve speckle reduction in materials with low birefringence ($\Delta n \ll 0.2$). The ionic dopant CTAB is shown to reduce the threshold for EHDI but has no consistent influence on speckle reduction or field amplitude for peak performance. Furthermore, it is shown that CTAB molecules undergo an irreversible electrochemical reaction at the electrodes, limiting or completely preventing a cell from exhibiting further EHDI.

In this thesis, through material and device optimisation, a LC diffuser is fabricated that is capable of reducing speckle contrast to $C = 0.07$ with transmission of just over 50%.

Acknowledgements

I would like to thank my supervisor Steve Morris for giving me a position in his research group and for his constant support throughout the path that led to this thesis. It was a little longer and more winding than intended but I am proud of what has been achieved and it would have been impossible without him. It has been invaluable to have a supervisor who is willing to be constantly interrupted with questions and ideas.

I would also like to thank Steve Elston, a 'kind-of' supervisor to me for most of the DPhil that I was so happy to add as an official supervisor this year. His ability to explain and teach in a clear, friendly and unassuming manner is unrivalled.

I am very fortunate to have spent my time surrounded by a research group that is a great source of friendship, support and adventure, from Jazz club evenings in London to international conferences in Brazil. I'd specifically like to thank Chloe Tartan for the constant source of entertainment and support since day one, Ellis 'I'm-in-my-lab' Parry for the close friendship and his sense of humour, Serena Bolis for all her explanations and genuine liquid-crystal based excitement, Konrad Jakubowski for the arm wrestles and constant positivity, John Sandford O'Neill for the genuine care and interest he has in all those around him and Julian Fells for his experience and support throughout patent applications and funding pitches.

Outside the research group, my time in Oxford during this DPhil was made complete with the four best friends I have been so fortunate to make: Matt Williamson, Alon Witztum, Max Howell and Tom Godleman. You boys are the best, even if Alon did abandon us to move to California. Buffalo! Also, Alex Valeanu, you have been such a good friend and invaluable genius to bounce ideas off.

Finally, none of this would have been remotely possible without the unwavering love and support of my amazing family, to whom I dedicate this thesis. I love you all so much and I hope this makes you proud.

Journal publications

D. J. Hansford, J. A. J. Fells, S. J. Elston and S. M. Morris, "Speckle contrast reduction of laser light using a chiral nematic liquid crystal diffuser", *Applied Physics Letters*, vol. 109, pp. 261104-1-5, 2016.

D. J. Hansford, S. J. Elston and S. M. Morris, "Influence of pitch on speckle contrast reduction in a chiral nematic liquid crystal diffuser", *in submission*

D. J. Hansford, S. J. Elston and S. M. Morris, "Simulating speckle reduction in a chiral nematic liquid crystal diffuser", *in submission*

D. J. Hansford, S. J. Elston and S. M. Morris, "The role of ionic dopants in speckle reduction using a chiral nematic liquid crystal diffuser", *in preparation*

D. J. Hansford, S. J. Elston and S. M. Morris, "Optimising speckle reduction in a chiral nematic liquid crystal diffuser", *in preparation*

Conference presentations

Oxford Photonics Day (OPD) April 2015, May 2016, April 2017 in Oxford (England) – Poster presentations

International conference of Ferroelectric Liquid Crystals (FLC) June 2015 in Prague (Czechia) – Poster presentation

European conference on Liquid Crystals (ECLC) September 2015 in Manchester (England) – Poster presentation

International conference on Optics of Liquid Crystals (OLC) October 2017 in Guarujá (Brazil) – Oral presentation

Awards

Displaying Futures Awards (Merck) September 2016 in Darmstadt (Germany) - Finalist

Patents

D. J. Hansford, J. A. J. Fells, S. J. Elston and S. M. Morris, "Speckle reduction", GB patent application 1614571 .6 *filed* 28.08.2016

D. J. Hansford, J. A. J. Fells, S. J. Elston and S. M. Morris, "Speckle reduction", International patent application WO 2018/037212 Al *published* 01.03.2018

Table of Contents

1 Introduction

This thesis describes the development of a liquid crystal-based speckle reducing device. The opening chapter serves as an overview of the work that is presented in the following chapters.

To begin, an overview of the origin of speckle in coherent light is presented in Chapter 2. The theory of speckle reduction through the superposition of statistically independent speckle patterns is presented, followed by an overview of speckle reduction techniques that have been developed. It is noted that most of these methods require the addition of components that are bulky, vibrating, expensive, fragile and/or power hungry.

In this work, an alternative method is presented that uses the unique electro-optical properties of liquid crystal (LC) materials. Thus, an overview of these mesophases is provided that details the range of LC classifications and their associated physical properties. With this background in place, an overview of existing speckle reduction methods using LCs is provided. It is shown that these methods exhibit limited speckle reduction or require expensive, bulky components. The problem with these methods is that they are either limited by the very small number of independent speckle patterns that they can create or by the complicated nature of the device construction. The method utilised in this work does not suffer from either of these setbacks, utilising a simple cell construction and a physical

phenomenon present in certain LC mixtures called electrohydrodynamic instability. An overview of this process is provided to complete the background information for the experimental and simulation results presented in subsequent chapters.

Chapter 3 provides an overview of the experimental techniques that were developed and used throughout this work to construct and analyse the LC speckle reducing device. Some methods are well known in this field of research, such as the mixing and optical analysis of liquid crystalline materials. However, there is no standardised method for measuring speckle contrast so a detailed review of the factors that affect subjective speckle measurements is provided and the process adopted to design and build a measurement technique that matches human perception as closely as possible is described. The experimental apparatus has been automated using MATLAB to enable the collection of large amounts of experimental data.

Chapter 4 begins with a proof-of-concept experiment using a chiral nematic LC mixture consisting of the nematic LC, E7, and the chiral dopant, BDH1281. The cell was tested over a large range of electric field conditions. Colourmaps are used throughout the thesis to present the large amount of data taken from the automated speckle measurement technique and the details of these plots and what they represent are introduced here. Experimental results are also presented on the lifetime and hysteresis for the LC device.

Following the proof-of-concept, the thesis then examines how the material parameters of the LC host influence the device performance in terms of speckle reduction and transmission, along with the electric field conditions required for optimum performance. Chapter 4 continues with an analysis of the importance of

the helical pitch, p, across a range of LC mixtures, with a variation of $224 \leq p \leq 2050$ nm. The results are analysed and compared to relevant published work and theoretical models. The chapter finishes by considering the importance of birefringence, Δn, of the nematic host on the resulting speckle contrast. Birefringence values tested in this chapter range from $0.091 \leq \Delta n \leq 0.274$. Unlike the pitch, it was not possible to vary the birefringence without a considerable change to other physical properties such as the dielectric anisotropy and viscosity. Despite this challenge, a qualitative relationship between birefringence and speckle reduction is proposed in this chapter.

Having considered the role of the material properties, Chapter 5 then explores whether the device performance can be enhanced through the addition of ionic dopants so as to increase the conductivity anisotropy of the LC mixture. This was achieved by introducing an ionic dopant into the chiral nematic LC mixture at various concentrations by weight. These dopants have long been used to facilitate and enhance EHDI and have been shown to increase light scattering from LC devices. It was hoped that their introduction would lead to an increase in the speckle reduction and/or reduce the electric field amplitude required for peak performance. However, it has been reported that these ionic compounds can cause cell deterioration through electrochemical reaction at the electrodes when high-amplitude, low-frequency fields are applied. For this reason, the lifetime and hysteresis of mixtures with ionic dopants is considered in depth in this chapter.

The next chapter (Chapter 6) considers how external factors and stimuli might aid or inhibit speckle reduction. The chapter begins with a study on the role of cell thickness, t. For this work, three cell thicknesses are tested: $t = 5, 9, 20$ μm.

It is expected that speckle contrast and transmission will decrease with increased cell thickness because of increased scattering as the light propagates through a greater volume of turbulent LC. It is also expected that the voltage required for peak performance will increase with cell thickness. Results on the lifetime and hysteresis of the switching properties for these cells are also presented. The chapter then continues by investigating whether the addition of scattering particles is a route to lower speckle contrast. Sub-micron sized particulates have been used previously to create a highly scattering, static state in LCs due to the number of defects in the director profile that they introduce. Nano-particles have also been shown to change the electro-optical properties of LC mixtures such as ion concentration and mobility and have even been used to reduce speckle contrast when mixed with water. Two types of scattering particle are considered in this study: 1 μm diameter silicon dioxide particulates and 25 nm titanium dioxide particulates.

The chapter concludes with a study of the effect of cell temperature on device performance. It is well known that the LC macroscopic properties are highly dependent on temperature. As the temperature increases, the degree of orientational order decreases, which causes a reduction in the bulk anisotropic properties. Furthermore, viscosity is known to decrease with temperature which should allow for faster response times, although the birefringence is also known to reduce which may lead to reduced light scattering.

In Chapter 7, an optical model for the LC speckle reducing device is presented. The theory of electromagnetic wave propagation in free space is considered, with a number of simplifications applied in order to obtain a numerical solution that is applicable to the experimental set-up used in this thesis. A model for

light interaction with a projection screen is also developed. Finally, a beam propagation method is used to model light propagation through the LC device, and a static model of the director orientation in the device is established.

Chapter 8 follows on directly by employing the simulation model developed in Chapter 7 to explore the relationships between device/material properties and device performance that have been studied in the preceding experimental chapters. Simulations are conducted on birefringence, cell thickness, the addition of scattering particulates, cell temperature and laser wavelength. Results from simulations are then compared with the experimental results. These comparisons are used to validate the simulation method used in this work.

The thesis closes with a conclusion and discussion of future work that could be carried out as a result of the progress made on the development of a LC speckle reducing device presented in this work.

2 Background and Literature Review

In this chapter, the origins and manifestations of laser speckle are presented, along with an overview of the statistical properties of speckle. A review of existing speckle reduction techniques is provided before introducing the materials used in this thesis for speckle reduction: liquid crystals (LCs). Existing speckle reduction techniques using LCs are reviewed, followed by a discussion of the volume scattering approach that is employed in this work. A more comprehensive overview of the speckle phenomenon can be found here [1] [2] [3].

2.1 Speckle

Speckle occurs when a coherent, or at least partially coherent, beam of light is scattered either by an optically rough reflecting surface or by travelling through a material with random variations in its refractive index. A material is considered optically rough when surface fluctuations are of the order of optical wavelengths or larger. Most surfaces are considered optically rough, with mirrors being a notable exception. Each point on a rough surface can be considered to be a secondary light source emitting a spherical wave $\boldsymbol{E} = Ee^{j\theta}$ that contributes to the reflected light field. An observer with a finite aperture samples this optical field at some point in space and the intensity (squared magnitude of the field at that point) is the integral of the complex fields (having both amplitude and phase) at that position, from each secondary emitter at the surface.

$$I = |\boldsymbol{E_{obs}}|^2 = \left| \frac{1}{\sqrt{N}} \sum_{n=1}^{N} E_n \, e^{j\theta_n} \right|^2 \tag{2.1}$$

The variation in amplitude and phase resulting primarily from path differences between the observer and these numerous secondary emitters has significant variation, which leads to a random amount of constructive and destructive interference. This causes a granular noise across the observed light field that has been given the name 'speckle' and an example of this can be seen in Figure 2.1.

Figure 2.1: Photograph of a typical laser speckle pattern

Speckle is observed in numerous applications including laser projectors [4] and optical coherence microscopy [5] where it is considered a nuisance that should be removed. However, as speckle is very sensitive to movement, it has found uses in a new field of coherent optics called speckle metrology for uses such as surface roughness measurements [6] and studies on surface vibrations [7]. Speckle is not limited to optical fields and is found in many other applications utilising coherent radiation such as radar [8], x-ray [9] and medical ultrasound [10].

Speckle can be observed with or without an image forming system. If a

detector (such as a charge-coupled device, CCD) is placed a distance from the scattering medium it captures the speckle field directly. This is known as objective speckle, whereas a speckle pattern that is obtained through image formation is referred to as subjective speckle. The properties of the imaging system have been shown to have a considerable effect on the observed speckle [11] and this is considered more thoroughly in Chapter 3.

2.1.1 Statistics of speckle

The degree of speckle present in an image with uniform average intensity is quantified by the speckle contrast C of the interference pattern. This is found by dividing the standard deviation of the intensity values σ_I by the average intensity value $\bar{I}$, and is the reciprocal of the signal to noise ratio [1].

$$C = \frac{\sigma_I}{\bar{I}} \tag{2.2}$$

Fully developed speckle occurs when a large number of statistically independent phasors are combined with phase uniformly distributed over $0 - 2\pi$ radians, and has a speckle contrast value of $C = 1$. This can be realised in practice by detecting the scattered light from a coherent laser incident upon a polarisation-preserving surface with spatially-random roughness of sufficient amplitude. The probability density function for intensity distribution in fully developed speckle is given by [1]:

$$P_I(I) = \frac{1}{\bar{I}} \exp\left(\frac{-I}{\bar{I}}\right) \tag{2.3}$$

2.2 Speckle reduction techniques

Speckle can be avoided altogether with the use of incoherent light sources. However, in applications such as holographic projection the properties of coherent light are essential. In these cases, speckle needs to be supressed.

Speckle contrast is reduced when two or more statistically independent, and at least partially decorrelated, speckle patterns are superimposed. Under these conditions the random intensity fluctuations due to speckle are 'averaged out' across the image to some extent. At the extreme that N completely uncorrelated speckle patterns are superimposed, the speckle contrast is given by [1]

$$C = \frac{\sqrt{\sum_{n=1}^{N} \bar{I}_n^{\,2}}}{\sum_{n=1}^{N} \bar{I}_n} \tag{2.4}$$

If all speckle patterns have equal mean intensity the minimum speckle contrast becomes $1/\sqrt{N}$.

Speckle reduction techniques can be separated according to whether the statistically independent speckle patterns are created instantaneously or time sequentially. Time sequential methods take advantage of the finite integration time of the observer. For example, the human eye has an integration time of approximately 50 ms [11]. They can also be further classified by the method by which these speckle patterns are mutually decorrelated. An overview of methods based on these characteristics can be found in Table 2.1, and the rest of this section takes a closer look at many of these options.

Decorrelation Method	Instantaneous	Time Sequential
Spectral	Array of lasers with varying wavelength	Laser wavelength chirping
Spatial	Low spatial coherence light source	Laser scanning
Angular	Array of sources with varying angles to screen	Rotating or vibrating diffuser
Polarisation	Depolarising screen	Source with quickly changing polarisation

Table 2.1: Overview of speckle reduction techniques using instantaneous or time sequential superposition of statistically independent and uncorrelated speckle patterns

2.2.1 Spectral decorrelation

When two independent, monochromatic sources with wavelength λ_1 and λ_2 illuminate a rough screen from the same position and angle, the resulting two speckle patterns will be decorrelated to some extent as a result of the wavelength variation $\Delta\lambda$, with decorrelation increasing with increased $\Delta\lambda$. It has been shown that $\Delta\lambda$ required for almost complete decorrelation is

$$\Delta\lambda \geq \frac{\bar{\lambda}^2}{2\sqrt{2}\pi\sigma_l} \tag{2.5}$$

where $\bar{\lambda}$ is the average wavelength of both sources and σ_l is the standard deviation of a gaussian distributed surface roughness [1]. From this it is clear that increased surface roughness reduces the variation in wavelengths for each source required for decorrelation of their respective speckle patterns. For N sources with sufficiently large $\Delta\lambda$ to achieve mutual decorrelation from the other sources, speckle contrast is reduced by $1/\sqrt{N}$. An example of this is shown using an array of lasers with different wavelengths for laser projection [12].

Alternatively, a broadband light source can be used to reduce speckle contrast in much the same way. A broadband source can be described as emitting light that is decomposed into single wavelengths. Two wavelengths that are very close will create quite correlated speckle patterns but the wider the broadband spectrum, the greater the decorrelation between these wavelengths. It has been shown that speckle contrast of a broadband light source with linewidth $\delta\lambda$ and average wavelength $\bar{\lambda}$ illuminating a surface with gaussian roughness with σ_l is [1]

$$C = \left[1 + 8\pi^2 \left(\frac{\delta\lambda}{\bar{\lambda}}\right)^2 \left(\frac{\sigma_l}{\bar{\lambda}}\right)^2\right]^{-\frac{1}{4}} \tag{2.6}$$

Once again increased surface roughness and an increase in the linewidth of the light source result in reduced speckle contrast. This has been shown experimentally using a broadband green laser source with a spectral bandwidth of 1.8 nm that has a speckle contrast reported to be $C = 0.04$ [13].

Time sequential speckle reduction can be achieved through wavelength chirping, varying the wavelength of laser emission within the integration time of the detector. There is very little difference in how this works with the instantaneous methods described above, except that the observer's integration time must also be considered.

2.2.2 Spatial Decorrelation

The ratio of observer spatial resolution to coherence area of light on the screen has a large impact on speckle contrast. The coherence area at the screen is the area over which a light source is considered spatially coherent. If the spatial resolution is smaller than or equal to the size of the coherence area the observer will be able to

observe every speckle spot fully. However, if the spatial resolution is larger, the observer will spatially integrate the light field across this region which will cause multiple speckle spots to be blurred together. Consequently, using a light source with low spatial coherence (and therefore very small coherence areas at the screen) will cause a reduction in speckle contrast. This has been shown using both an LED and random lasing [14].

Spatial decorrelation can be used in a time sequential manner through laser scanning, a method already used in the manufacturing of some laser pico-projectors [15]. In this case the coherence area is smaller than the observer's spatial resolution, but it is moved through the area of spatial resolution during the observer's integration time.

2.2.3 Angular decorrelation

Speckle contrast can be reduced instantaneously by illuminating the screen with multiple light sources that vary in illumination angle. The greater the variation in angle between sources, the more decorrelated the resulting speckle patterns will be. The size of the angle required for complete decorrelation between sources is strongly dependent on the ratio of surface roughness to wavelength, as well as the projection spot size [1]. Theoretically, if a surface with $\sigma_l = 100$ µm is illuminated with light $\lambda = 500$ nm to produce a spot with diameter $d = 4$ cm, the intensity covariance between two speckle patterns can be reduced to 0.1 with an angle difference of only $10 - 20$ µrad. With sufficient angular variation between N sources it is possible to reduce speckle contrast by $1/\sqrt{N}$.

A time sequential variation in angle can be achieved by passing light through a moving diffuser. The diffuser creates a time-varying spatially-random phase

perturbation across the beam of light. The most commonly cited method of time-sequential speckle reduction is achieved by passing coherent light through a rotating ground glass diffuser [16] [17] [12] and is capable of reducing speckle contrast to values of $C < 0.05$. Alternative approaches based on the same principle include the use of a rotating rectangular light pipe [18], a vibrating diffractive beam shaper [19], microelectromechanical diffuser [20] and fast scanning micro-mirrors [21], and further examples can be found in this summary [4]. Alternatively, the projection screen itself can be vibrated to achieve the same effect. While successful at reducing speckle contrast, each of these methods require additional bulky mechanical parts or expensive components, making them unsuitable or undesirable for applications that require a compact and vibration-free solution, such as laser-based pico-projectors.

2.2.4 Polarisation decorrelation

A typical projection screen exhibits volume scattering of light, with some light being diffuse scattered from the surface and some light undergoing multiple scattering as it penetrates a short distance into the surface. When a linearly polarised light is shone at such a screen the reflected light is shown to be depolarised, and this reduces speckle contrast in linearly polarised incident light by $1/\sqrt{2}$ [1]. This can be described as the result of two independent speckle patterns being created for each of the orthogonal polarisation components. Further, incident light polarisation can be changed between orthogonal components during the observer's integration time, and this combined with a depolarising screen can reduce speckle contrast further to $1/\sqrt{4}$.

2.2.5 Summary

Numerous methods for speckle reduction have been considered that all can be summarised as arising from the superposition of statistically independent and at least somewhat decorrelated speckle patterns. Multiple methods can be used together to further reduce speckle contrast, and the total speckle reduction is simply the product of the speckle reduction of each method, assuming each method produces speckle patterns in statistically independent ways. In this work, speckle reduction is achieved through time-sequential angular decorrelation and the instantaneous polarisation decorrelation of a depolarising screen. To avoid additional bulky mechanical parts, the angular decorrelation is achieved through the rapid, random movement of birefringent molecules in a diffuser device. This movement is driven by the application of an electric field to a LC mixture, resulting in a vibration-free device. The following sections introduce LCs, their relevant characteristics and their use in speckle reduction methods.

2.3 Liquid crystals

The term liquid crystal defines a mesophase of matter that exists in some materials. In this phase a material is capable of exhibiting characteristics of both a liquid and a crystalline solid. For example, the molecules of a LC are able to move relative to each other and form droplets. However, simultaneously these molecules exhibit some form of orientation and/or positional order, allowing them to show anisotropy in their optical and electrical properties. Although the unique behaviour of LCs was first discovered in 1888, it wasn't until the 1960s that a use was found that takes advantage of these crystalline characteristics, controlled by external stimuli. Since then, a huge amount of research has been committed to these

materials, leading to their domination in the flat-panel display industry.

LCs can be categorised by the physical conditions necessary for the mesophase to exist. Thermotropic LCs exist at a specific temperature range between the crystalline solid and isotropic liquid phases in certain materials. Lyotropic LCs require the correct temperature and concentration of solvent to exist. All the LCs considered in this thesis are thermotropic, thus lyotropic LCs are not considered further.

LCs can be further categorised by the type of order they exhibit, a characteristic controlled by the shape of the molecules and their resultant anisotropic electric interactions. All the LCs considered in this work are 'calamitic': rod-like in shape, but other mesophases can be made from disk-like (discotic) or bowl-like (bowlic) molecules, to name a few. 5CB is an example of a calamitic LC molecule which consists of two phenyl rings rigidly linked, with a flexible hydrocarbon chain and a cyano group as terminal units. This molecule is relatively long and thin, like a rod, and has a permanent dipole. The chemical structure is shown in Figure 2.2.

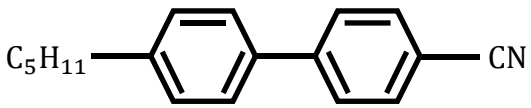

Figure 2.2: Chemical structure of 5CB. An example of a calamitic LC molecule

An overview of a selection of LC mesophases relevant to this thesis is now presented, with an illustrative diagram of their director alignment provided in Figure 2.3.

2.3.1 Nematic phase

The isotropic liquid phase exhibits no positional or orientational order, but when the temperature is reduced so that the nematic phase forms, the molecules arrange themselves with their long axes roughly parallel to each other. They are free to flow relative to each other and show no positional order. The average direction of the long axes of nematic molecules is represented by the director and is defined by the unit vector $\boldsymbol{n}$. There can be significant variation in the orientation of individual molecules around the director due to thermal motion and molecular interactions. This is quantified by the scalar order parameter, S. For a collection of calamitic molecules this is defined as

$$S = \frac{1}{2}\langle 3\cos^2(\theta - 1)\rangle \tag{2.7}$$

where θ is the angle between the long axis of a molecule and $\boldsymbol{n}$, and $\langle \dots \rangle$ represents an average over all molecules [22]. For perfect crystalline ordering $S = 1$ and for fully isotropic liquids $S = 0$. A typical nematic will have $0.3 < S < 0.8$ [23]. The order parameter varies with molecular constitution and is reduced with increasing temperature towards the clearing temperature (nematic to isotropic transition).

2.3.2 Chiral nematic phase

The chiral nematic phase is often called the cholesteric phase as it was first observed in cholesterol derivatives. It is similar to the nematic phase in that molecules exhibit long-range orientational order but no positional order. However, in contrast to the nematic phase, the director rotates about a helix axis which is perpendicular to the director. The distance over which the director rotates a full 2π is called the pitch. Due to the symmetry of the molecules the periodicity is half this value as $\boldsymbol{n}$ is

equivalent to $-\boldsymbol{n}$. The pitch of a chiral nematic changes with chemical composition, temperature and as a result of external stimuli such as electric fields.

The calamitic molecules that make up a chiral nematic differ from nematic molecules because they exhibit enantiomorphism: they have a distinct right- and left-handed form. A chiral nematic molecule either naturally exhibits enantiomorphism, or it is introduced to nematic molecules by doping with enantiomorphic compounds (commonly called chiral dopants). There is no phase transition between nematic and chiral nematic.

2.3.3 Smectic phase

The smectic phase differs from the nematic phase because the molecules are arranged in layers and exhibit some positional order. They exist at a temperature below the nematic or chiral nematic phase in certain materials. There is free movement of molecules within each layer, and the layers can slide freely over each other. There are many forms of smectic LC, classified by the molecular order in the layers. For example, the molecules in the smectic A phase arrange themselves perpendicular to the layers, whereas molecules in the Smectic C phase are tilted away from the layer normal. Chiral smectic phases also exist, for example a Smectic C* (* denotes chiral) has an azimuthal twist of the layer director from one layer to the next.

2.4 Liquid crystal physical properties

The chemical structure and shape of the calamitic molecules and their macroscopic orientation also result in LCs having interesting anisotropic physical properties. This section provides an overview of the important properties of relevance to this

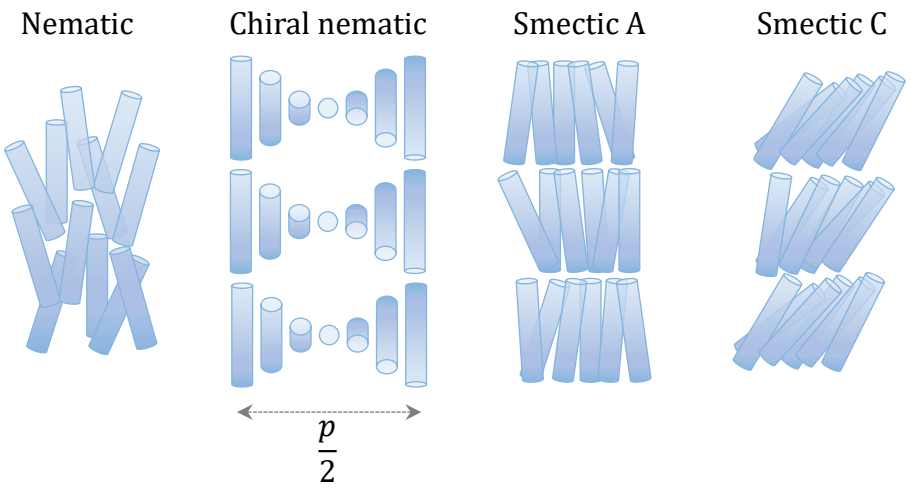

Figure 2.3: Molecular arrangements of the nematic, chiral nematic, smectic A and smectic C LC mesophases.

work.

2.4.1 Elastic behaviour

LC molecules align themselves relative to each other as a result of the Van de Waals forces between them, and as a result of their shape. In an unconstrained nematic, a uniform director through the bulk represents the minimum free energy arrangement and is thus the equilibrium state. If an external force is applied, it can force molecules to move from this position but elastic forces between molecules work to negate this effect. The elastic forces can be defined by three types of fundamental deformation, each described by a separate elastic constant: splay (K_{11}), twist (K_{22}) and bend (K_{33}). Splay deformation occurs when the top of a group of molecules are pulled away from each other, while the bottom of the group of molecules are pressed together (Figure 2.4). Twist deformation occurs when a torque causes a rotation in the director through a group of molecules and exists naturally in chiral nematic mixtures. Bend occurs when the top and bottom of a group of molecules are being pulled in the same direction. Diagrams of the three

types of fundamental deformation are shown in Figure 2.4.

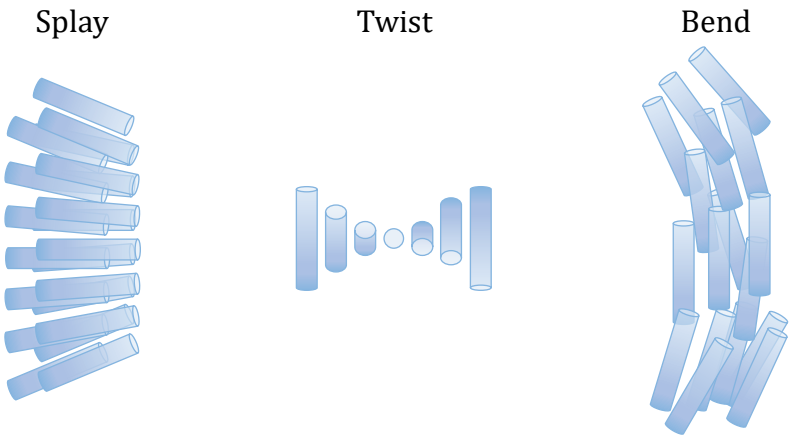

Figure 2.4: Three types of fundamental deformation: splay, twist and bend.

A typical value for the elastic constants in LCs is around 10 pN [24]. The energy density can be expressed by the Frank elastic energy density [25], ω_d (Nm^{-2}), in terms of these elastic constants as follows:

$$\omega_d = \frac{1}{2}K_{11}(\nabla.\boldsymbol{n})^2 + \frac{1}{2}K_{22}\left(\boldsymbol{n}.(\nabla\times\boldsymbol{n}) - \frac{2\pi}{p_0}\right) + \frac{1}{2}K_{33}(\boldsymbol{n}\times(\nabla\times\boldsymbol{n}))^2 \qquad (2.8)$$

where p_0 is the unperturbed pitch of the chiral nematic LC. Boundaries can be used to enforce an orientation on the molecules that are in contact with it through the use of alignment layers. These layers impose a predetermined orientation of the director at the surface when no field is applied. Elastic forces carry this orientation into the bulk of the material, therefore if two matching alignment layers are used that cause the director to lie parallel to the substrate, a nematic LC will align itself throughout a thin device in this way. Alternatively, the alignment layer may cause the local director to align perpendicular to the layer, or at some arbitrary tilt angle. Three standard device configurations are shown in Figure 2.5: planar alignment,

homeotropic alignment and twisted alignment. An electric field can be applied in conjunction with the surface alignment layers to form further types of alignment. In this thesis, all the glass cells that are used consist of planar alignment.

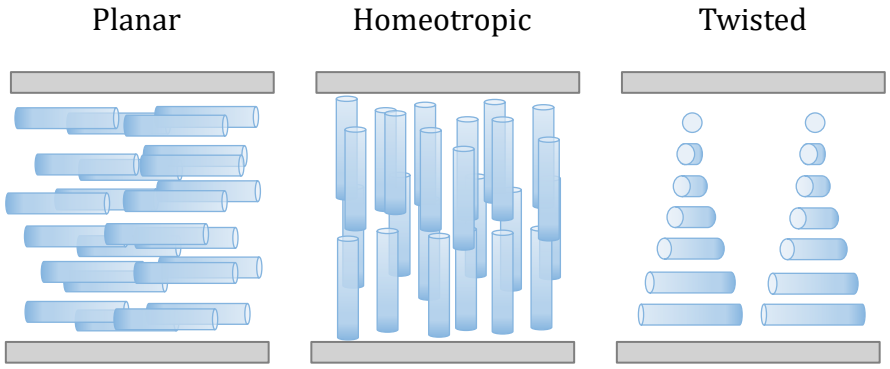

Figure 2.5: Examples of different nematic LC alignments in thin glass cells.

2.4.2 Dielectric properties

A dielectric permittivity can be described for each axis of an LC molecule, with the two short axes having approximately equal permittivities in calamitic molecules. The dielectric permittivity is thus defined as $\varepsilon_{\perp}$ (perpendicular to the director) and $\varepsilon_{\parallel}$ (parallel to the director), and the dielectric anisotropy is defined as $\Delta\varepsilon = \varepsilon_{\parallel} - \varepsilon_{\perp}$. This anisotropy arises as a result of an induced dipole, due to the polarisability of a molecule, and/or a permanent dipole, due to the chemical structure and shape of a molecule. For example, the cyano group at one end of the 5CB molecule attracts electrons from the rest of the molecule causing a permanent dipole. Meanwhile, an applied electric field can rearrange the free charges inside the phenyl rings to cause an induced electric dipole. Dielectric anisotropy is dependent on material properties such as polarisability and dipole angle, but also on the macroscopic orientational order of the bulk. 5CB has a strong permanent dipole that is almost parallel to the long axis and thus has a large positive value of $\Delta\varepsilon \approx 12$. Molecules

that have no permanent dipole, or where the dipole is inclined at a sufficient angle from the long axis can take negative values.

In the presence of a DC electric field, an LC with positive $\Delta\varepsilon$ will orient the director along the field direction as the free energy density is minimised in this case. On the other hand, an LC with negative $\Delta\varepsilon$ will orient the director perpendicular to the field direction for the same reason. If the applied field is AC, the director will reorient with the field, providing the frequency is low. Above the dielectric constant relaxation frequency, the molecules will no longer be able to reorient quickly enough.

In chiral nematic LCs the situation is slightly more complicated. A negative $\Delta\varepsilon$ material will align the helical axis parallel to the field as the rotating director will always be perpendicular with the field in this alignment. However, a positive $\Delta\varepsilon$ material cannot align such that all molecules are parallel with the field. At very low field amplitudes the helical axis will be aligned perpendicular with the field, and as the field amplitude is increased the molecules are increasingly rotated to align parallel with the field. This has the effect of lengthening the pitch, until a threshold voltage, the critical unwinding field E_c, is reached, above which the material enters a field-induced homeotropic nematic alignment [26]. This critical unwinding field can be expressed as

$$E_c = \frac{\pi^2}{p_0}\left(\frac{K_{22}}{\Delta\varepsilon}\right)^{\frac{1}{2}} \tag{2.9}$$

where p_0 is the unperturbed pitch of the chiral nematic LC.

2.4.3 Optical Properties

Light is an electromagnetic wave with oscillating electric and magnetic fields orthogonal to the direction of propagation. The refractive index n describes how quickly light can travel through a material (c/n), which is defined as $n = \sqrt{\varepsilon_r \mu_r}$. ε_r is the relative dielectric permittivity and μ_r is the relative magnetic permeability of the material. At optical frequencies, LCs are non-magnetic ($\mu_r \approx 1$) and the permanent dipole cannot couple to the electric field, so the relative dielectric constant is greatly reduced (ε_{r_opt}). As a result, the refractive index can be simplified to $n = \sqrt{\varepsilon_{r\_opt}}$. However, as shown in Section 2.4.2, the dielectric permittivity is anisotropic, thus the refractive index is anisotropic also and is defined as n_o, the ordinary refractive index, and n_e, the extraordinary refractive index. These are equivalent to the refractive index perpendicular and parallel to the director, respectively. Refractive index anisotropy is called birefringence and is defined in LCs as $\Delta n = n_e - n_o$. The materials used in this thesis have birefringence ranging from 0.091 (MLC-15900-100) to 0.274 (BL006). Refractive indices are temperature and wavelength dependent and the values quoted were measured at $T = 25$°C and $\lambda = 632.8$ nm.

The birefringence of LCs, combined with the ability to reorient the director with external fields, is what has made LCs of such interest for technological applications, especially in the display industry. For example, a simple planar aligned nematic cell can reorient the polarisation of incident light because the two orthogonal polarisation components of the light will experience a different refractive index, travel through the cell at different speeds and thus exit with an added phase difference. If a cell is sandwiched between an analyser and orthogonal

polariser, the linearly polarised light incident upon the cell can be rotated to pass fully through the polariser with the correct choice of birefringence, alignment and cell thickness. An electric field can be used to reorient the bulk into homeotropic alignment, such that the orthogonal polarisation components of light experience the same refractive index (n_o), causing no change to the polarisation state of the light and stopping transmission through the polariser. Varying the electric field amplitude to allow alignment between these extremes also allows for variable transmission through the device. This is the fundamental effect used in most LC-based displays to control the amount of light transmitted for each primary colour at each pixel.

In chiral nematics the birefringence leads to another interesting property: Bragg reflection. Light that travels along the helical axis of a chiral nematic mixture will experience a periodic change in refractive index. If the pitch of this material is of the order of optical wavelengths, this will cause reflection of light with circular polarisation of matching handedness to the chirality for the following range of wavelengths:

$$n_o p < \lambda < n_e p \tag{2.10}$$

where p is the pitch of the chiral nematic LC. This causes the cell to appear coloured, with the colour varying between transmitted and reflected light, with a change in observation angle, and with a change in pitch.

2.4.4 Conductivity properties

LCs are usually considered to be insulating dielectric materials, but there are often ionic impurities in the mixture as a result of the synthesis process. Nematic LCs

usually have a conductivity of $10^{-12} < \sigma < 10^{-8}\ \Omega^{-1}\text{cm}^{-1}$ [27]. Ions can also be introduced to a mixture through charge injection at the electrodes of a device, or intentionally added using ionic dopants. LCs have a macroscopic conductivity anisotropy because the ionic mobility is typically greater parallel to the director. Conductivity is thus defined by $\sigma_{\parallel}$ and $\sigma_{\perp}$.

2.5 Liquid crystals for speckle reduction

LCs appear to be an ideal medium for reducing speckle contrast as it is possible to change the optical properties externally with an electric field. This can be used to apply a phase, polarisation or intensity variation to incident light that varies in time and space. This in turn will create multiple statistically independent speckle patterns, reducing the appearance of speckle contrast. Furthermore, this can be achieved vibration free, LC devices are small, light and simple to make, and the power consumption is low due to the small conductivity.

The first use of LCs for speckle reduction that could be found in the literature was achieved using a nematic LC sandwiched between two substrates with a cell gap of 15 μm [28]. One substrate was coated in PVA to form an alignment layer, the other was coated in a mixture of PVA and azo dye molecules to form a controllable alignment layer. The application of UV light of wavelength close to the absorption maximum of the dye causes a rotation in in the double bond to transform the cell from its stable *trans* form to its unstable *cis* form. When this light is removed, the molecule will fall back into the *trans* form with either its original molecular shape, or one that differs by approximately 90°, preferring the direction that matches the polarisation of UV light. By exposing this layer to UV light with a checkerboard

pattern of orthogonal polarisations, the alignment layer forms a related checkboard pattern of orthogonal alignment properties. When filled with the nematic LC this creates a cell that aligns itself according to the alignment surface. They report a reduction in speckle contrast of $1/\sqrt{2}$ when used in conjunction with a stationary diffuser plate, as a result of the two simultaneous orthogonal polarisation states present in the transmitted light. Speckle contrast is measured with a CCD directly in the path of the laser, instead of in reflection from a screen. This approach cannot be improved without introducing movement to the diffuser or LC cell, as there are only two distinct polarisation states, and does not reduce speckle any further than a depolarising screen used in applications such as laser projection.

An alternative approach was proposed by Andreev et. al. with the use of a chiral smectic ferroelectric LC (FLC) [29] [30]. This mixture was filled into a 16 μm-thick glass cell, aligned with the smectic layer normal parallel to the substrates. With an electric field applied, the pitch begins to unwind as the molecules reorient themselves to align with the electric field. Molecules orient themselves with azimuthal angle of 0 or π, changing to the closest orientation to their unperturbed state. This creates spatially separated domains with domain walls between them at the point of molecular orientation variation of π. The most energetically favourable domains grow at the expense of the least favourable ones. When the field is reversed the most energetically favourable orientation flips, and with the correct alternating field applied these walls can be made to move rapidly backwards and forwards across the cell, thus creating a spatially and temporally random refractive index across the cell. Speckle reduction of 50% is reported with the application of a complicated electric field pattern composed of a low frequency (450 Hz) and high

frequency (3.5 kHz) component. A more recent paper from the same lab reports the use of a helix-free FLC that is also capable of 50% speckle reduction [31] but with a waveform of reduced complexity and amplitude, however it still requires the superposition of a low frequency (1 kHz) and high frequency (10 kHz) component.

Furue et. al. reports the use of FLC cells that are either surface or polymer stabilised [32]. Surface stabilisation was achieved using planar alignment layers, and the FLC mixture was bistable. The application of an electric field switches the LC between the two states quickly and is thus capable of reducing speckle contrast by $1/\sqrt{2}$ by creating two orthogonal polarisation states. The authors went on to use a mixture of FLC doped with a polymer that is capable of imposing a change in polarisation to incident light that can be varied continuously between the two orthogonal states. Unsurprisingly this did not provide further speckle reduction as all polarisation states can be decomposed into the two orthogonal states, and a maximum of only two statistically independent patterns can be made through a change in polarisation. Finally, they added a wedge cell with angle 0.35°, filled with 5CB. This was made to vary the incident angle of the two orthogonal polarisation components of laser light before it reached the FLC cell. This angular decorrelation increased speckle reduction to $1/\sqrt{3}$.

Later Furue et. al. went on to report a new cell design that consisted of the nematic E7 mixed with 20 wt.% NOA-65, a photocurable monomer [33]. UV radiation created domains whose size decreased with increased radiation exposure as a result of an increase in the number and volume of polymer networks. They claim that with the application of a simple applied field with $\pm$ 10 V and 100 Hz, and with 30 s of UV exposure, the electrically induced movement of these domains

scatter incident light sufficiently to reduce speckle by almost $1/\sqrt{2}$. This movement is expected to be a result of the competing orientational effects on the director of E7 of the alternating electric field and the polymer network.

An alternative method that utilises LCs would be the use of a LC spatial light modulator (SLM) that applies multiple random phase masks corresponding to the Hadamard orthogonal function [34]. This method utilises the minimum number of distinct phase masks to form statistically independent speckle patterns at the observer. This approach has the most efficient use of phase perturbation, reducing the number of distinct patterns that are required within the integration time of the observer, and has been shown to reduce speckle contrast by $1/\sqrt{64}$ when using 64 cyclic phase patterns. This approach has excellent speckle reduction but at the cost of using a very expensive and bulky LC SLM.

The approach that is used in this thesis is based on volume scattering of light in a thin (20 μm) cell filled with a chiral nematic LC. When exposed to a square-wave electric field of sufficient amplitude and frequency the cell becomes highly turbulent, with chaotic movement of molecules within the mixture. This creates a spatially random phase perturbation to incident light that varies quickly with time, reducing the appearance of speckle contrast to an observer with finite integration time. The physical process that causes this molecular turbulence is called electrohydrodynamic instability and is considered in the following section.

2.6 Electrohydrodynamic instability in LCs

Conductivity and dielectric anisotropy can be used to apply competing torques to LC molecules that create instability in the macroscopic alignment of a device. If a

thin layer (approximately $10 - 50$ μm) of nematic LC with negative $\Delta\varepsilon$ and positive $\Delta\sigma$ is exposed to a DC or low-frequency AC electric field perpendicular to the device substrates, the molecules will try to orient perpendicular to this field but the ionic impurities will try to move through the material towards the oppositely charged electrodes, applying a torque on the director back in the direction of the field. This causes a range of induced patterns that change with field amplitude and frequency [35].

At low voltages (< 1 V), the LC will align perpendicular to the field due to the negative $\Delta\varepsilon$. Above a certain threshold voltage, a periodic distortion of this planar alignment is seen that appears as a series of parallel lines perpendicular to the director. These are called Williams domains and are the result of a convective instability in the LC that causes material to flow in closed circles. The circles have diameters of approximately the cell thickness t, and thus the observed parallel lines have approximate periodicity of t. This happens because charged particles in the mixture are trying to move in the direction of the electric field but can only move parallel to the director as a result of conductive anisotropy. Although the nematic director has a set average direction, locally there is some distortion. Ionic charges therefore move normal to the field and accumulate in positions of local director distortion that are more energetically favourable. This creates a local electric field perpendicular to the applied electric field and serves to exaggerate the distortions in the planar alignment. Above a threshold voltage there is sufficient transverse electric field to rotate the local director and there is material flow as a result. This is the origin of the convection process that creates Williams domains and the steps are shown diagrammatically in Figure 2.6.

The observation of parallel lines is due to the convective flow causing a reorientation of the director to be perpendicular to the substrates where flow is perpendicular, and parallel where the flow is parallel.

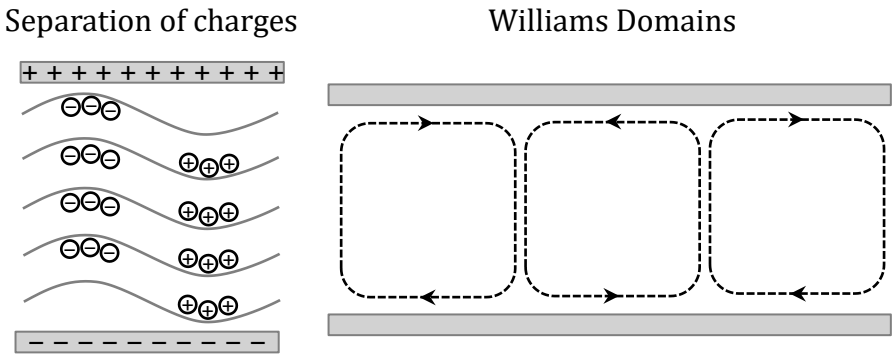

Figure 2.6: Diagram showing the lateral separation of charges due to conductive anisotropy in nematic LC under low voltage (left) and Williams domains formation in a nematic LC (right).

As the voltage is further increased these Williams domains become more agitated by increasing flow velocity until, above a larger threshold voltage, the flow becomes turbulent and completely disordered. In this state the director is randomly aligned both in space and time. This causes the material to become highly scattering, appearing opaque and with a milky white appearance to the eye. This is known as the dynamic scattering mode (DSM) [36].

For AC fields with higher frequencies, Williams domains reduce in periodicity, and above a threshold frequency a 'chevron' texture develops, and dynamic scattering is not observed with an increase in the voltage. Finally, above the ionic mobility relaxation frequency only the dielectric force remains, and the planar alignment returns. Below this frequency is the 'conduction regime' and above this frequency is called the 'dielectric regime'. Further information on EHDI-induced patterns in nematics can be found in an excellent recent review [37].

EHDI has been shown to occur in nematics [38], chiral nematics [39] and

smectics [40], with all three mesophases capable of exhibiting the DSM. In this thesis, speckle reduction is achieved through volume scattering of light that travels through a LC that is in the DSM. Chiral nematics are known to exhibit a highly scattering, stationary focal conic state, which is used for optical storage of information [41]. For this reason, chiral nematic mixtures are exclusively used to provide maximum scattering. To the author's knowledge, this is the first report of speckle reduction using DSM in LCs. Furthermore, it has been reported that chiral nematics can only exhibit EHDI with a negative $\Delta\varepsilon$ [39], and there have been many reports of experimental results that broadly agree with the accepted theory for LCs with negative $\Delta\varepsilon$. Despite this, there have recently been reports of EHDI observed in chiral nematics with positive $\Delta\varepsilon$ [42] [26], but there are no reports of the DSM being observed in these materials known to the author. However, it is shown in this thesis that chiral nematic mixtures with positive $\Delta\varepsilon$ are capable of exhibiting the DSM, and that it can be used to reduce laser speckle by up to 90%.

2.7 Concluding Remarks

In this chapter, the concept of laser speckle is introduced, describing the important statistics that describe and quantify the extent to which speckle is present in an image. An overview of the speckle reduction methods that have been reported in the literature is provided. An overview of the LC mesophases is then provided, with information about the physical properties that are of relevance to this thesis. The known uses of LCs for speckle reduction from the literature are presented, comparing each by speckle reduction method and effectiveness. Finally, the phenomenon of EHDI that occurs in certain LC mixtures is introduced. This effect is utilised in the devices developed in this thesis to create a LC speckle reducing device

that is capable of reducing speckle contrast by up to 90%. In the next chapter, an overview of the experimental methods that have been employed in this work, such as fabricating cells and measuring their effectiveness as speckle reducers, is provided.

3 Experimental Techniques

This chapter presents the experimental and analysis techniques used throughout this thesis, which describes the development of a liquid crystal (LC) speckle reducing device. A wide range of LC mixtures were prepared and characterised so as to study the effect of different optical, electrical and physical properties on the performance of a device in terms of speckle reduction and optical transmission. The measurement of speckle contrast is not a standard experimental procedure, particularly in relation to LC devices, and so it was necessary to develop a dedicated experimental set-up, taking care to understand the impact that various experimental conditions have on speckle measurements to ensure that the results obtained reflect the human perception of speckle as closely as possible.

3.1 Device Preparation

3.1.1 Liquid crystal mixture preparation

The mixture components used in this thesis were weighed using a precision micro-balance (Mettler Toledo AB104-S [43]) with an accuracy of ±0.05 mg. Mixture compositions are given throughout this thesis as a weight percentage (denoted *wt*. % to follow the typical convention). Mixtures were typically prepared in batches of 100 mg in total to ensure that the individual components could be weighed accurately with the precision balance. Each mixture was then heated to ~ 10°C above the clearing temperature and held at this temperature for at least 12 hours to

achieve complete thermally-assisted diffusive mixing of the components. Examination on a polarising optical microscope confirmed whether a uniform dispersion of the components had been achieved.

3.1.2 Liquid crystal glass cells

After thermal mixing, the LC mixtures were then filled into thin glass cells using capillary action. Most of the cells used in this thesis were the commercially-available INSTEC LC2 cells [44], which have a cell gap of d = 5.0 μm, 9.0 μm or 20.0 μm (an illustration of the cell architecture is shown in Figure 3.1). The cell spacing was achieved using spacer beads dispersed within the glue that holds both substrates together, and with further spacer beads distributed randomly throughout the cell. (These spacer beads can be clearly seen in the microscope images that will be shown later in this thesis.) These devices consisted of a transparent electrode coating of Indium Tin Oxide (ITO) (thickness 23 nm) that was patterned onto the inner surfaces of the glass substrates creating a 5 mm × 5 mm active region at the centre of the cell. On top of each ITO layer, a rubbed polyimide alignment layer was deposited onto the inner surface of each substrate. Upon assembling the two glass plates to form the cell, the rubbing directions were oriented such that they were aligned antiparallel to one another.

The actual thickness of a glass cell was determined using an interference method. The empty cell acts as an Fabry-Perot etalon under white light illumination at normal incidence. Constructive interference occurs when the condition $2d = m\lambda$ is satisfied, where d is the cell thickness, λ is the wavelength (nm) and m is the mode number (an integer). A MATLAB script was written that first extracted the corresponding wavelength for each peak in a plot of the transmission for white light

(Figure 3.2a) before plotting the inverse wavelength $(1/\lambda)$ as a function of the (arbitrary) mode number. The cell thickness was then extracted from the gradient of a linear best fit to this plot (as shown in Figure 3.2b). Cells that differ from the expected thickness, as defined by the spacer beads, by more than 5% were discarded. Also, the thickness of each cell was measured at three points across the active region to ensure that the thickness variation was minimal across each cell.

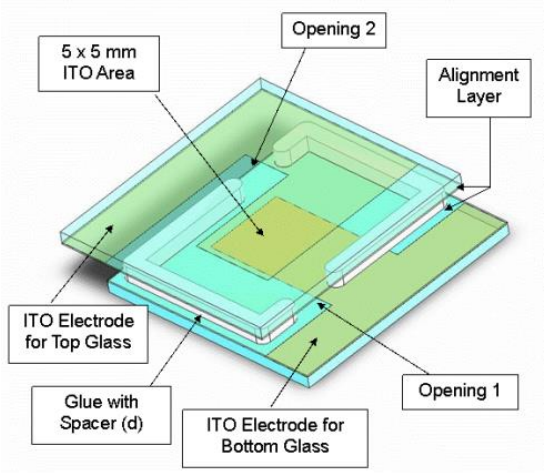

Figure 3.1: Diagram showing the structure of the INSTEC cells used to observe thin films (d μm) of LC with or without an applied electric field. (Figure taken from the INSTEC [44] catalogue of LC cells.)

3.2 Pitch measurements

The majority of the mixtures used in this thesis exhibit a right-handed chiral nematic LC phase. The nematic LCs used in this study are not inherently chiral and so they are mixed with a chiral dopant to induce a chiral nematic phase. An important property for comparison of different chiral mixtures is the pitch p, which is defined as the distance over which the director rotates by 2π. The pitch is related to the concentration of chiral dopant through the expression

$$p = (\beta c_w e_e)^{-1} \tag{3.1}$$

where β is the helical twisting power (HTP) (μm^{-1}), e_e is the enantiomeric purity

and c_w is the weight concentration of the chiral dopant. Chiral dopants with a range of HTPs were used in this thesis, from the low HTP dopant R811 (Merck) to the high HTP dopants R5011 and BDH1281 (Merck). The majority of work in the latter part of this thesis is undertaken with the dopants R5011 or BDH1281, both with high HTP. This is because a lower concentration of chiral dopant is required to obtain a pitch that is on a comparable lengthscale to the wavelength of light. Furthermore, the lower the concentration of chiral dopant, the more the known properties of the nematic host are retained.

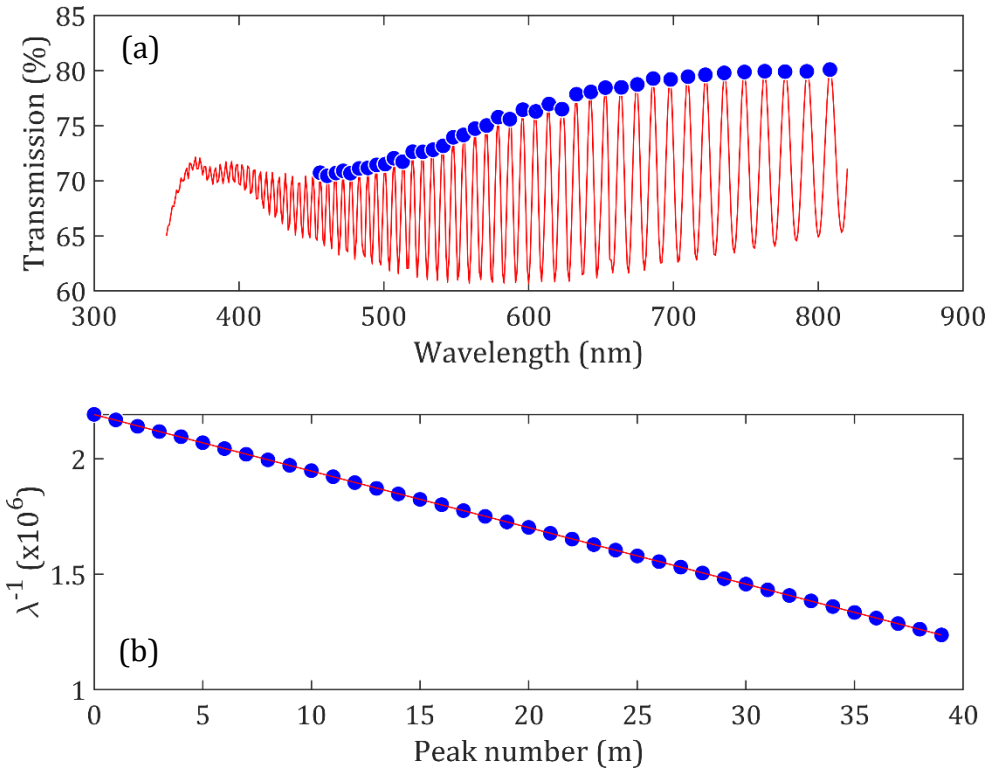

Figure 3.2: (a): Transmission spectrum of an empty cell showing that it acts as a Fabry-Perot etalon under white light illumination. The interference peaks are used to calculate the cell thickness. (b): Plot of successive interference peaks, the gradient of which is used to calculate cell thickness. In this example, the thickness is found to be 20.4 μm and is within 5% of the expected thickness quoted by the cell manufacturer (20 μm).

The HTP can vary depending on the combination of the nematic host and the chiral dopant and is therefore not known accurately for most mixtures. Also, the

weight percentage of the chiral dopant can be as low as 1 wt.%, which requires the measurement of <1 mg of material using the microbalance as mixtures are typically prepared in 60 – 100 mg batches. This can result in an inaccuracy of more than 5% in the measured weight of the chiral dopant. Consequently, an alternative method of pitch measurement is used that doesn't use equation 3.1.

In this thesis, the pitch for each mixture was determined by observing the position of the photonic (reflection) band-gap (PBG) using an ultra-violet-visible (UV-Vis) spectrometer (Agilent Cary 8454 UV-Vis [45]). This method requires knowledge of the refractive indices of the host material. A glass cell with anti-parallel rubbed polyimide alignment layers (Instec LC2) was first filled with a chiral nematic LC mixture and was carefully annealed to produce a well-aligned and uniform Grandjean texture, which was confirmed using optical polarising microscopy (this process is described in more detail in Section 3.3). The transmission spectrum of the cell for white light was then measured using the UV-Vis spectrometer across the wavelength range 190 – 1100 nm, as shown in Figure 3.3. This wavelength range is obtained using the combination of a low-pressure deuterium gas lamp (190 – 800 nm) and a tungsten lamp (370 – 1100 nm). The spectrometer diode array consists of 1024 photodiodes, which over the specified wavelength range, leads to a sampling interval of 0.9 nm. The ITO layer attenuates most of the light below 350 nm, which limits the observable range to approximately 350 – 1100 nm. For each device, three spectra were taken from different positions across the electrode area of the cell and cells with a variation in the PBG position of > 10 nm were then discarded. The temperature at which measurements were conducted is noted (and checked to be within 2°C of the required temperature for

the study) as the refractive indices of these materials are temperature dependent.

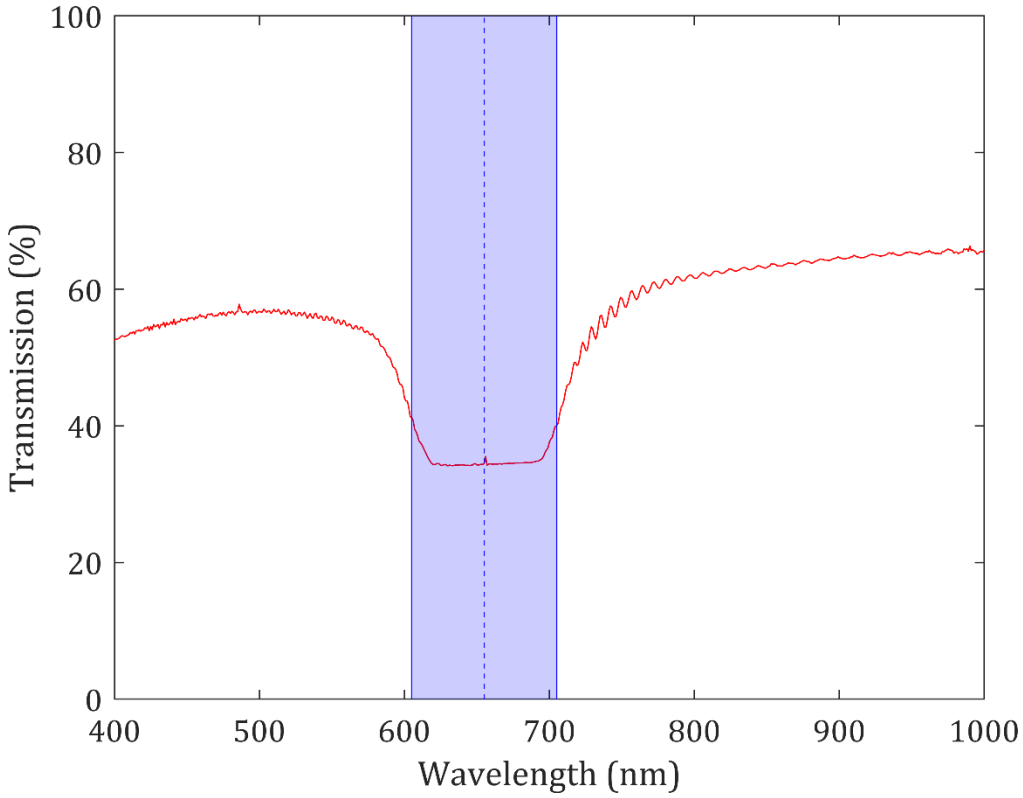

Figure 3.3: Transmission spectrum for a 20 μm-thick, chiral nematic liquid crystal cell containing the nematic host, E7, dispersed with 3.3 wt.% chiral dopant (BDH1281). The cell temperature during measurement was T = 25°C. The PBG position is highlighted in light blue, with the PBG centre λ_c marked with a dashed blue line.

A MATLAB script was written that performs a cross-correlation of the transmission spectrum with an inverted top-hat function. The resulting peak is then taken as the central wavelength of the PBG, λ_c, and the pitch is calculated from:

$$p = \frac{2\lambda_c}{n_o + n_e} \tag{3.2}$$

where n_o and n_e are the ordinary and extraordinary refractive indices of the host nematic LC, respectively. For mixtures of the same nematic and chiral dopant, the reciprocal of the pitch is plotted as a function of the concentration of chiral dopant to confirm the inverse proportionality stated in equation 3.1 and is shown in Figure

3.4. In the case of a mixture that has a PBG outside of the measurable range of the UV-Vis spectrometer, the pitch is estimated by extrapolating this linear plot.

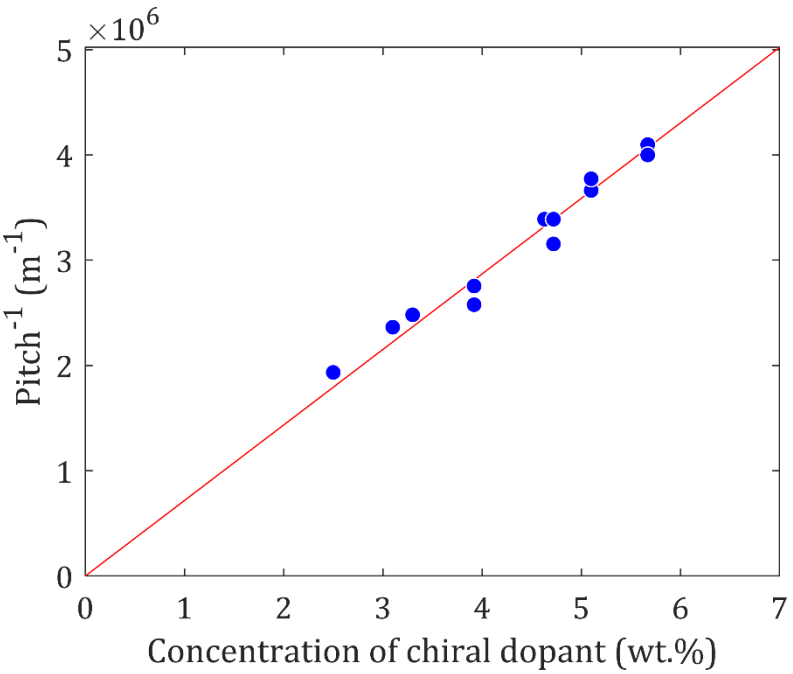

Figure 3.4: Plot of the reciprocal of the pitch (μm^{-1}) as a function of the chiral dopant concentration (wt.%) for chiral nematic mixtures consisting of the nematic LC, E7, dispersed with different concentrations of the high twisting power chiral dopant (BDH1281). A line of best fit is shown in red.

3.3 Polarising microscopy observations

A polarising optical microscope (Olympus BX51-P [46]) was used throughout this study to identify and confirm the LC phase, check the quality of the alignment of the phase in the INSTEC glass cells, and to confirm that the constituent molecules have sufficiently mixed during the preparation procedure. It was also used to record the transition temperatures of the mixtures.

A halogen filament light bulb provides white light illumination that passes through a condenser lens and then a linear polariser. The optical spectrum of this bulb is given in Figure 3.5. This can be used in conjunction with an analyser placed after the objective turret that can be rotated relative to the first polariser so that

birefringent materials can be studied. This combination was used to observe the different optical textures of the LC crystal cells placed on the stage or platform between the two polarisers.

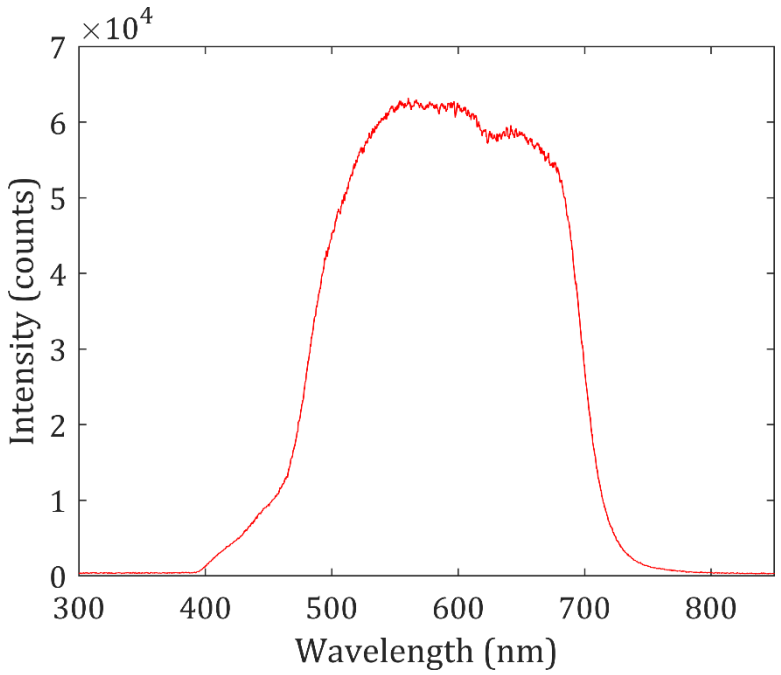

Figure 3.5: Optical spectrum of halogen filament light bulb used in Olympus BX51-P polarising optical microscope. Measured using Ocean Optics USB2000+ spectrometer.

Optical textures of the LC devices were recorded on the optical polarising microscope when subjected to an a.c. electric field of various frequencies and amplitudes. Examples of four different textures relevant to this study are shown in Figure 3.6.

The sample was placed on a hot-stage that was mounted onto the rotation stage of the microscope. Temperature control was provided by a hot-stage connected to a controller (INSTEC mK1000 [44]). This experimental arrangement was used to observe the clearing temperature of the LC mixtures, to aid in the alignment process for transmission measurements and to keep the cell at a constant temperature throughout the experiments. Temperatures used in this work vary

from 20°C to 150°C. Based upon the information provided by the hot-stage manufacturer, the hot-stage/controller combination is quoted as being stable to 0.1°C and capable of a maximum temperature resolution of 0.001°C.

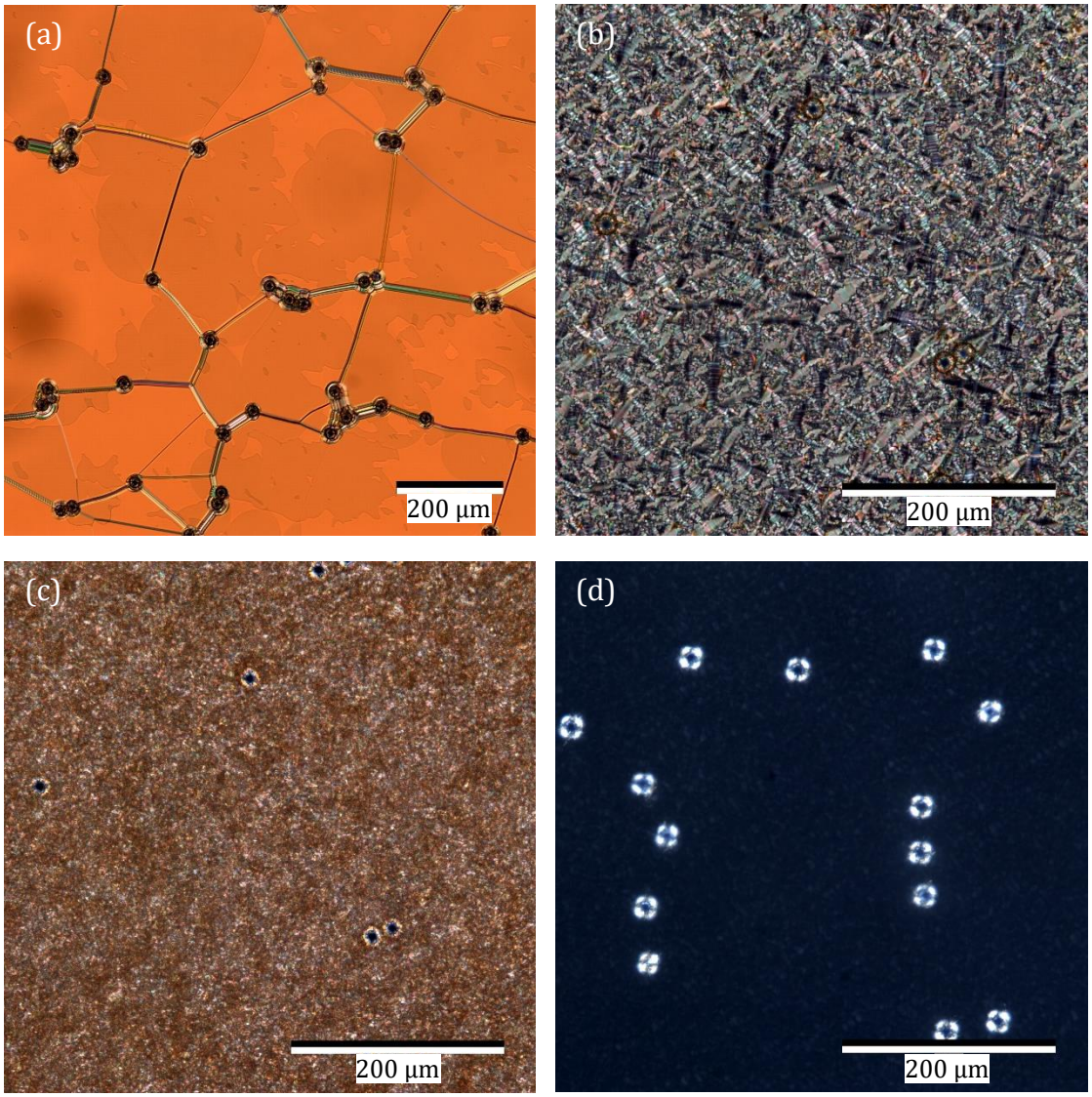

Figure 3.6: Polarizing optical microscope images of (a) annealed Grandjean texture, (b) focal conic texture, (c) dynamic scattering mode (8 V/µm, 40 Hz) with camera exposure time at 5 ms, (d) electric field-induced nematic homeotropic texture (11 V/µm, 20 Hz) at (a) 10 ×, (b-d) 20 × magnification with crossed polarisers of a 20 μm-thick, chiral nematic liquid crystal cell containing the nematic host, E7, dispersed with 2.5 wt.% chiral dopant (BDH1281). The cell temperature was T = 25°C. The scale bar depicts a distance of 200 μm in all images. 20 µm spacer beads are clearly visible in (a) and (d).

A range of microscope objectives were used to observe the cell at different magnifications, ranging from 4× to 50×. The specifications of each objective used is

given in Table 3.1.

Magnification	Numerical Aperture	Fluorite aberration correction	Working Distance (mm)
4 ×	0.10	No	22.0
10 ×	0.30	Yes	10.0
20 ×	0.45	Yes	7.4-8.3
50 ×	0.70	Yes	2.2-3.0

Table 3.1: Microscope Objective specification for objectives used throughout this thesis

A moveable prism above the objective turret then directs light to either the eyepieces of the microscope or to the phototube (or both), which was typically equipped with a 6.0MP CCD camera (QImaging Retiga R6 [47]) that was used to record micrographs of the optical textures. Alternatively, a fibre-coupled spectrometer (Ocean Optics USB2000+ [48], 1.5 nm resolution) could also be mounted in the phototube depending upon the measurement requirements.

An alternating electric field was supplied to the cell during observation by a dual channel function generator (Tektronix AFG 3022 [49]), amplified by a 10× voltage amplifier (FLC Electronics F10AD [50]) capable of supplying voltage amplitudes of up to ± 200 V when both channels are combined. The output of the function generator was controlled via a PC running a MATLAB script that was written specifically for this application and is capable of applying the same field conditions that are used later in the speckle contrast experiment.

3.4 Measuring speckle contrast

To quantify the amount of speckle present in laser light, and to measure by how

much this reduces with the addition of the LC devices, a dedicated experiment had to be designed and constructed with which to measure the so-called speckle contrast, which is an important parameter that quantifies speckle and was introduced in more detail in Section 2.1.1 of Chapter 2.

The speckle contrast C of an image with uniform average intensity is defined as [1]:

$$C = \frac{\sigma}{\bar{I}} \tag{3.3}$$

where σ is the standard deviation of the image intensity and $\bar{I}$ is the mean image intensity. From this relationship, it is clear that an image without speckle will have a value of $C \approx 0$, whereas an image that is dominated by speckle will possess a value of C close to 1.

As discussed in Goodman [1] there are two ways of observing speckle: objective and subjective speckle. Objective speckle is observed directly with no imaging optics involved; for example, when laser light passes through a ground-glass diffuser and is captured in free-space by a lens-less CCD. Humans observe speckle subjectively; the speckle pattern being formed on the retina by the lens in the eye. This work is focussed entirely on subjective speckle as it is intended for direct comparison with human perception. However, the additional imaging optics that are typically needed have a considerable effect on the observed speckle contrast, which makes it very difficult to compare the measured speckle values reported in the literature as there is no single, standardised setup for speckle measurements. To best correlate the results found in this thesis with human perception, the parameters that most effect the measurement of speckle are studied first and subsequently these parameters are selected to match the human eye as

closely as possible.

3.4.1 Experimental setup

The basic experimental setup is shown in diagram (Figure 3.7) and photograph (Figure 3.8) form. A single mode, continuous wave, linearly polarised Helium-Neon laser (JDS Uniphase 1122P, $\lambda = 632.8$ nm, beam diameter at the output of the laser = 0.63 mm, beam divergence = 1.3 mrad [51]) was used as the coherent light source. An LC-filled cell was placed on a hot-stage connected to a controller (INSTEC mK1000 [44]), which is used to keep the cell at a constant temperature throughout each experiment. Temperatures used in the study of the speckle contrast vary from 20°C to 100°C. The controller has a maximum temperature resolution of 0.001°C.

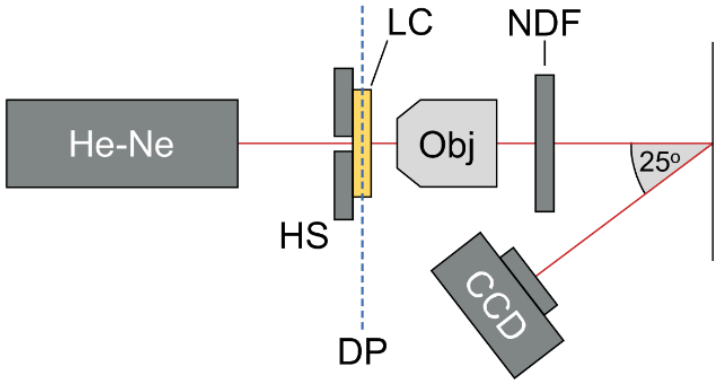

Figure 3.7: Diagram of the experimental setup for measuring the speckle contrast of a laser source in this work. (HS) Hot Stage, (DP) Diffuser Plane, (LC) Liquid Crystal device, (Obj) Microscope Objective, 10×, 0.3 NA, (NDF) Neutral Density Filter with optical density varied from 0.1 - 2.0, (CCD) Cooled, monochrome, 12-bit camera with 3.2 mm iris and focusing lens (f = 33 mm)

An alternating electric field was supplied to the cell by a dual channel function generator (Tektronix AFG 3022 [49]), amplified by a 10× voltage amplifier (FLC Electronics F10AD [50]) capable of supplying voltage amplitudes of up to $\pm$ 200 V when both channels are combined. The output of the function generator was controlled via a PC running a MATLAB script that was written specifically for

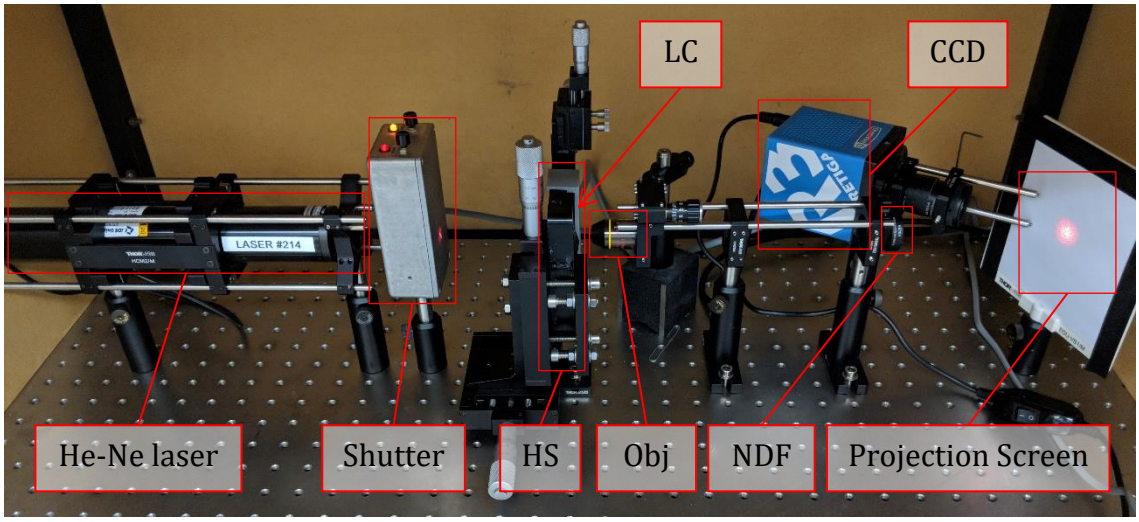

Figure 3.8: Photograph of the experimental setup for measuring the speckle contrast of a laser source used in this work. Acronyms are the same as those defined in Figure 3.7.

this experiment, a screenshot of which is shown in Figure 3.9. The waveforms used in these experiments are limited to square-wave forms only.

A 10× microscope objective (Olympus UPlanFL N, NA = 0.3 [46]), placed directly after the LC device, was used to limit the divergence of the scattered beam transmitted through the LC cell. An absorptive neutral density filter (NDF) (Thorlabs NEK01 [52]) was also used to reduce the intensity of the beam observed at the camera (CCD) to ensure that the sensor was not over-exposed, while retaining maximum use of the dynamic range available to avoid the loss of accuracy caused by discretisation errors.

The camera used in this work was a cooled, monochrome CCD (QImaging QICAM 12-bit [47]) with 1392 × 1040 pixels, 4.65 µm × 4.65 µm pixel size and 1/2" optical format. The camera was cooled to reduce the dark noise generated by the camera that would otherwise artificially increase the measured speckle contrast. A monochrome sensor was preferred because the light source was monochromatic. A camera sensor simply measures the intensity of light, irrespective of wavelength,

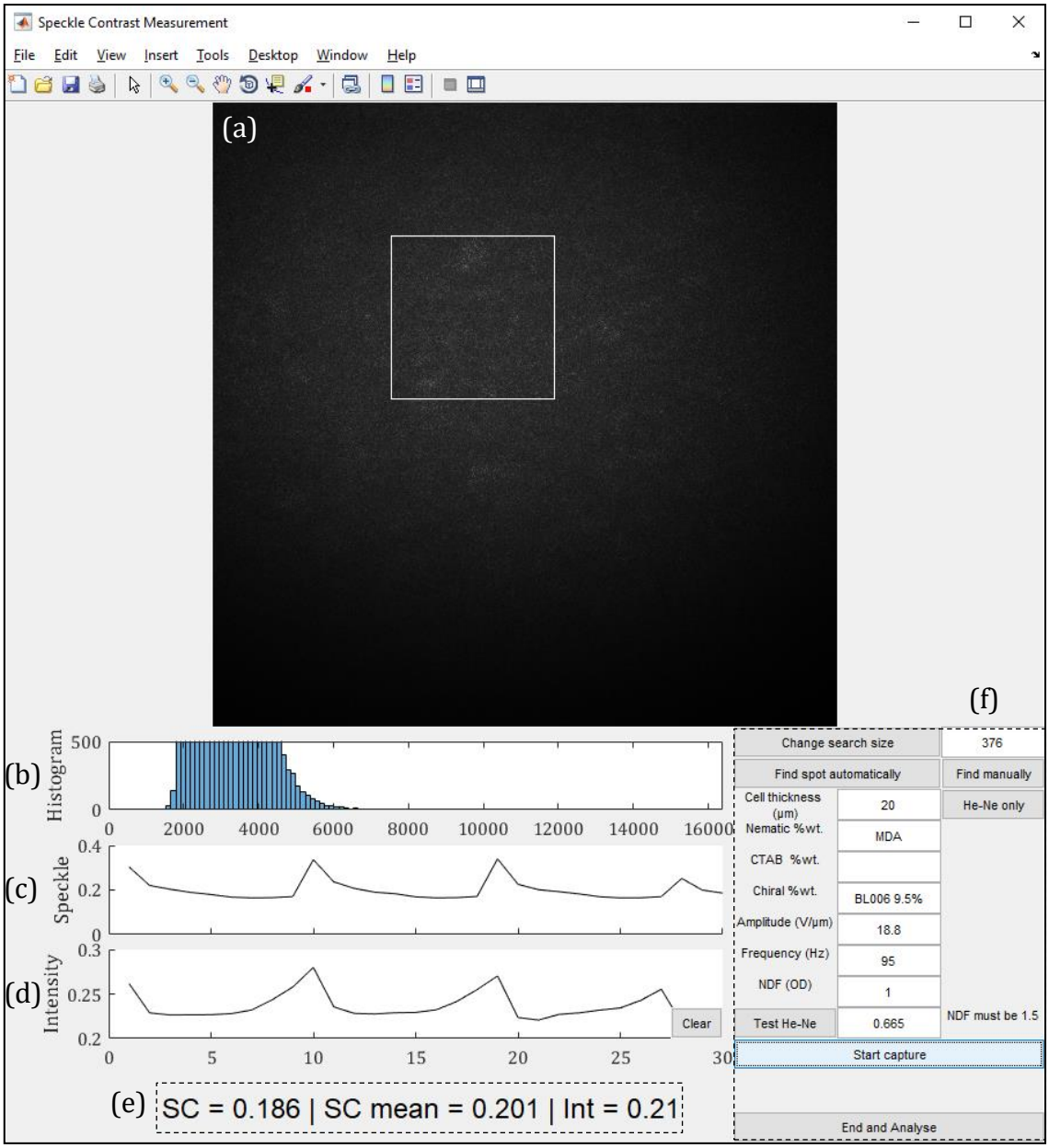

Figure 3.9: Screenshot of the user-facing screen of the MATLAB program that was written for the speckle contrast measurements. (a) Live camera view of the projection screen. The white box shows the region over which measurements are taken, (b) histogram of the pixel values used to avoid over-exposure of the camera, (c) real-time plot of the measured speckle contrast (d) real-time plot of intensity, (e) the current speckle contrast and intensity values, (f) Input boxes for mixture and setup conditions along with buttons to perform a range of experimental procedures.

that falls upon it using the photoelectric effect. A colour sensor differs from a monochrome sensor with the addition of band-pass filters (for each of the primary colours red, green and blue) placed in front of the sensor array, usually in the form of a Bayer pattern. This setup would only allow light at 633 nm to reach a quarter of

the sensors and interpolation would then be required to estimate the intensity of red light falling on the sensors in between. A monochrome sensor is incapable of distinguishing wavelength, but in the case of single wavelength emission, as in this experiment, this is not a problem and it avoids the need to interpolate data. An imaging lens was used in conjunction with the camera, the parameters of which are discussed in more detail in the following sections.

It is important to use a camera with unity gamma correction for a true linear relationship between the optical intensity and pixel value. Without this condition, a change in optical intensity will result in an unwanted change in the measured speckle contrast.

3.4.2 Camera properties for consideration

The physical properties of the camera sensor cannot be adjusted, but it is important to consider the effect of changing the camera position relative to the screen as well as the properties of the imaging lens and the integration time of the sensor.

3.4.2.1 *Imaging lens*

Most lenses are diffraction-limited, especially those with a small clear aperture. This means that the angular resolution is limited more by diffraction rather than by aberrations. The angular resolution, $\sin\theta$, of a circular aperture is defined by the Rayleigh criterion as:

$$sin\theta = 1.22\frac{\lambda}{D} \tag{3.4}$$

where λ is the wavelength of light and D is the size of the aperture. As such, the aperture is directly related to the angular resolution of the detector.

If the angular resolution of the projection system is larger than the detector, spatial decorrelation occurs. Goodman [53] showed that speckle can be reduced by $\sqrt{N_1}$ in such a system if the coherence of the laser beam has been significantly reduced. In turn, N_1 is defined as:

$$N_1 = \frac{\Omega_P}{\Omega_D} \tag{3.5}$$

where Ω_P is the solid angle subtended by the exit pupil of the projection system to the screen and Ω_D is the solid angle subtended by the entrance pupil of the detector to the screen. Figure 3.10 gives a visual representation of spatial decorrelation caused by an increase in Ω_P with no change in Ω_D.

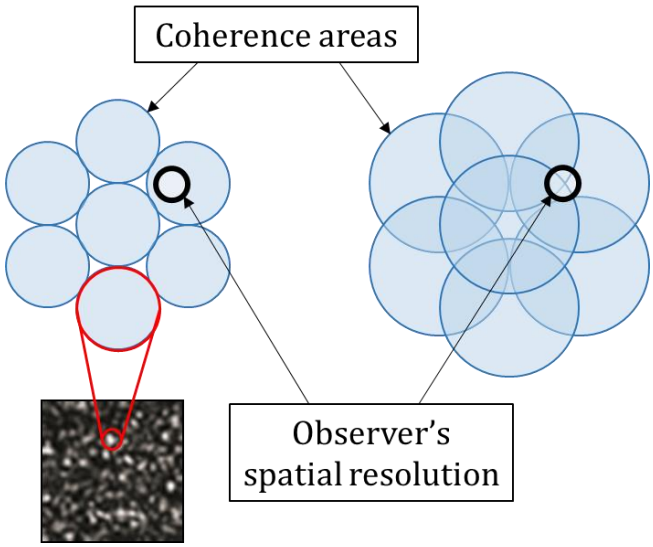

Figure 3.10: Visual representation of spatial decorrelation caused by an increase in Ω_P for constant Ω_D. The coherence areas increase in size and overlap, which would have the effect of blurring together otherwise distinct areas of uniform coherence and therefore lower the speckle contrast.

In his study, Goodman showed that the average speckle size A_C observed by a detector with an imaging lens is given by

$$A_C = \frac{\lambda^2}{\Omega_l} \tag{3.6}$$

where Ω_l is the solid angle subtended by the exit pupil of the camera lens as seen by the CCD sensor. For a circular aperture this becomes:

$$A_C = \frac{4\lambda^2 F^2}{\pi} \tag{3.7}$$

where F is the *f*-number of the lens, the ratio of the focal length to the aperture size. If the average speckle size is smaller than the pixel size, A_P, speckle is reduced by $\sqrt{N_2}$ through spatial averaging:

$$N_2 = \frac{A_P}{A_C} \tag{3.8}$$

Figure 3.11 illustrates the spatial averaging that would be caused by a large pixel size when compared to the speckle grain size.

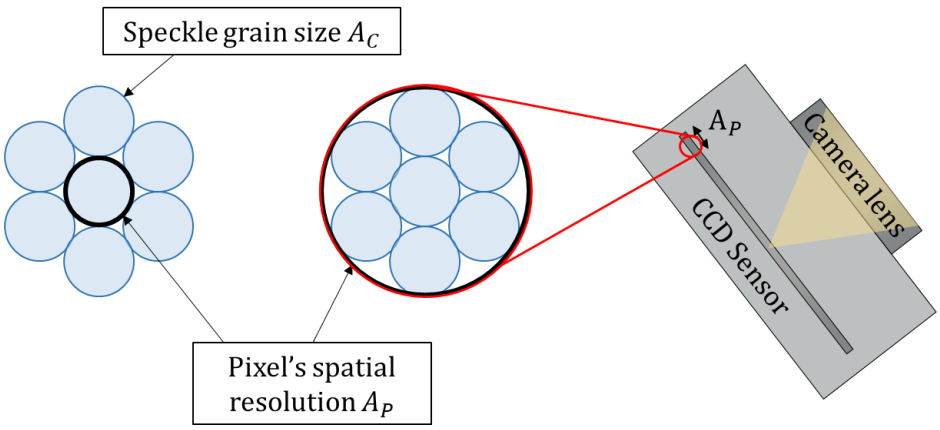

Figure 3.11: Visual representation of spatial averaging that would result when the speckle grain size A_C is much smaller than the sensor pixel size A_P. Multiple speckle 'grains' with different intensities, due to interference, will be spatially averaged thus lowering the perceived value of the speckle contrast.

The camera lens has, therefore, been shown to artificially reduce the appearance of speckle in two ways. A small *f*-number can cause spatial averaging

and a large *f*-number can cause spatial decorrelation. This is shown experimentally in Figure 3.12 using a 75 mm focal length lens and varying the aperture with an adjustable iris. It is shown that in this specific configuration an *f*-number of 12.5 provides the most accurate measurement of speckle as it corresponds to the highest measurement of C for otherwise unchanged experimental conditions. The same dependence on the *f*-number was also shown experimentally in the literature by Roelandt et. al. [11].

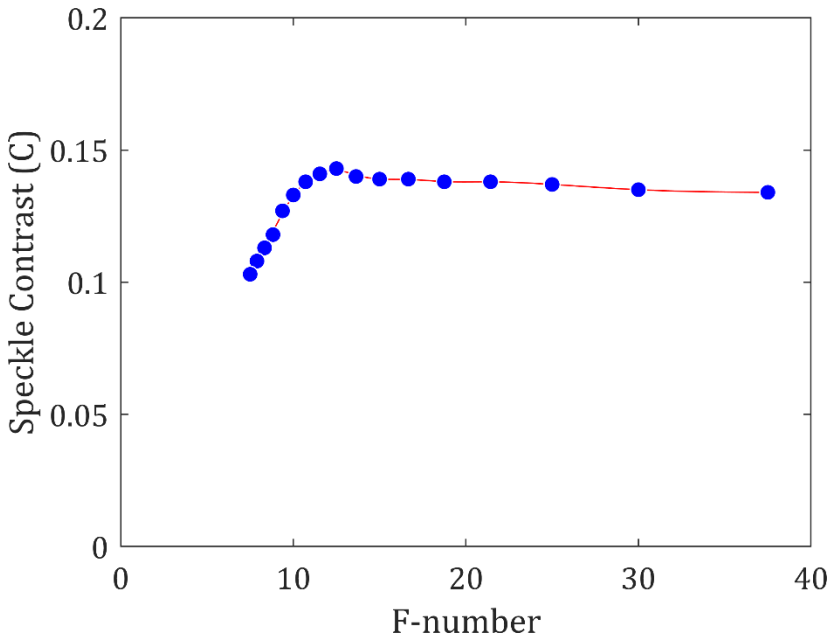

Figure 3.12: Speckle contrast measured as a function of the camera lens *f*-number. A He-Ne is directed through an LC cell under maximum speckle reduction conditions (E = 14.2 $V/\mu m$, 95 Hz square wave). The LC mixture was E7 + 4.7 wt.% BDH1281, the cell thickness was 20 μm, and the cell temperature was held at 25°C. A 75 mm plano-convex camera lens was used in conjunction with an adjustable iris with a variable aperture from 2 – 10 mm so as to vary the *f*-number. The data points were obtained from the measurements and the line is a smoothing spline fit used to guide the eye.

3.4.2.2 *Camera distance*

Moving the camera relative to the screen only serves to change the angle subtended by the entrance pupil of the detector to the screen, Ω_D, in equation 3.5. The effect of refocussing the camera lens to compensate for the change in position can be ignored if the distance between the screen and camera, l, is considerably larger than the

laser spot size on the projection screen. So as l increases, the amount of spatial decorrelation increases and the observed speckle contrast decreases. This is shown experimentally in Figure 3.13 using the same 75 mm plano-convex camera lens and varying the distance between the camera and the projection screen. The camera lens position is carefully adjusted for every measurement to ensure the camera is correctly focussed. It is shown that there is a clear positive linear correlation between speckle contrast and the reciprocal of l. As a result, it is concluded that the camera position should be chosen at the beginning of the experiment and left unchanged throughout. Also, to measure the highest possible speckle contrast value the camera should be placed as close to the screen as possible, without blocking the laser.

3.4.2.3 *Camera integration time*

Speckle contrast can be reduced if a number of speckle patterns are superimposed upon each other within the integration time of the detector. Passing the laser beam through a moving surface or volume scatterer such as a rotating ground glass diffuser (RGGD) or a LC cell undergoing electrohydrodynamic instabilities (EHDI) has the effect of applying a time-varying spatially-random phase perturbation on the wavefront. Goodman [1] showed that for N statistically independent speckle patterns superimposed during one integration period, the speckle contrast is reduced by $\sqrt{N}$. This can be observed in Figure 3.14, which is a plot of the speckle contrast measured over a range of camera integration times with a LC cell in place. The cell is under constant electric field conditions for each measurement, but the observed speckle contrast reduces as the integration time of the CCD camera increases.

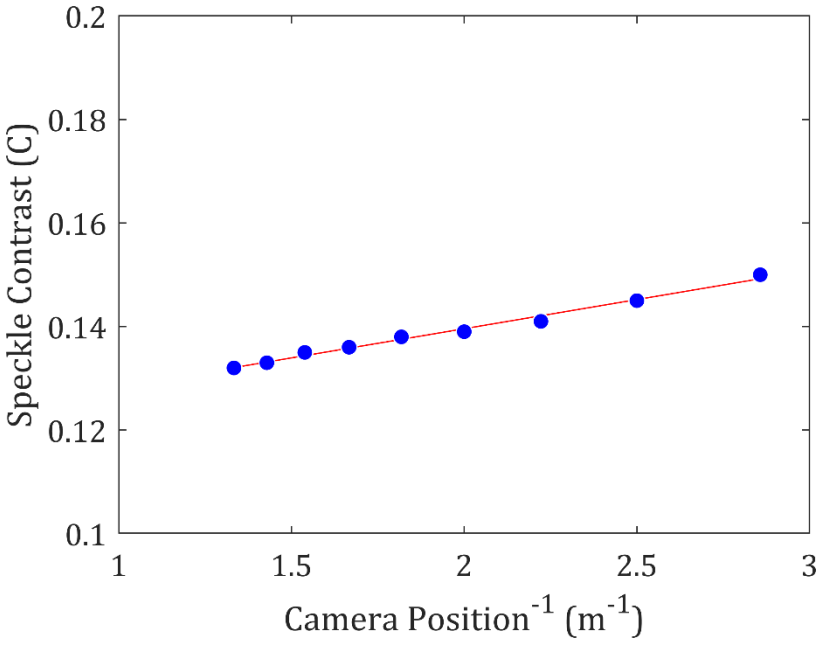

Figure 3.13: Speckle contrast measured for a distance range from 0.35 - 0.75 m between the camera and the projection screen. Laser light from a He-Ne is directed through an LC cell under maximum speckle reduction conditions (E = 14.2 $V/\mu m$, 95 Hz square wave). The LC mixture was E7 + 4.7 wt.% BDH1281, cell thickness 20 μm, cell temperature 25°C. The camera lens is refocussed for each position by measuring the speckle contrast over a range of lens positions and selecting the highest contrast recorded. The data points were obtained from the measurements and the line is a linear fit.

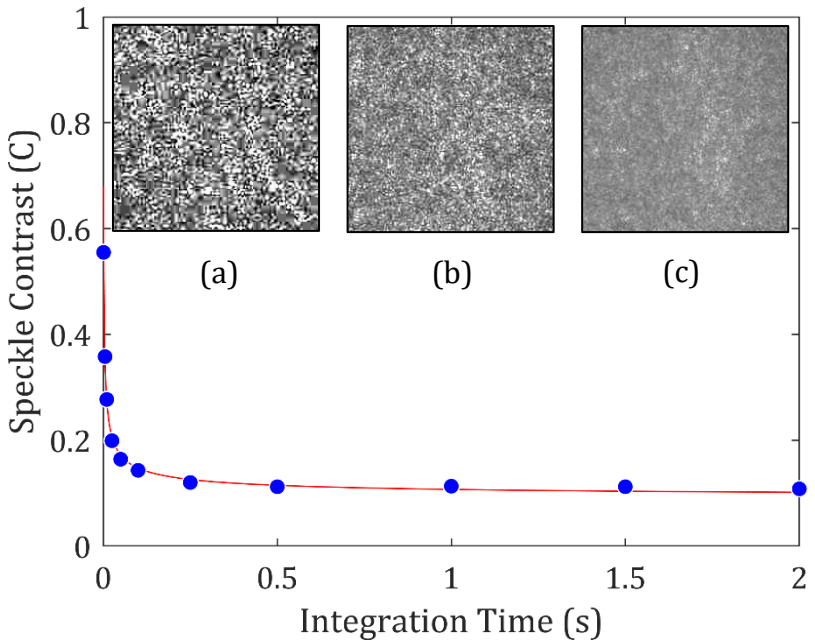

Figure 3.14: Speckle contrast measured after passing through a 20 μm-thick cell filled with E7 + 4.7 wt.% BDH1281 under a square wave electric field of amplitude 13.6 $V/\mu m$ and a frequency of 75 Hz at a range of camera integration times. The cell thickness was d = 20 μm, cell temperature T = 25°C. The data points were obtained from measurements and the line is a fit of the form $ax^{-0.5} + b$ which shows that C reduces approximately by $1/\sqrt{N}$ as expected from Goodman [1]. Inset speckle images shown for (a) 1 ms, C = 0.555, (b) 10 ms, C = 0.277, (c) 2 s, C = 0.108 integration time and speckle contrast values respectively.

3.4.2.4 *Camera focus*

Incorrect focussing of the camera lens can significantly reduce the measured speckle contrast as shown in Figure 3.15. Speckle contrast is measured as the camera lens is moved over a range of 40 mm. Speckle contrast quickly drops from its peak value with a small adjustment of the camera lens position and is shown to be reduced by up to 24% at the extremes of the positions tested. As such, it is essential that the camera is always correctly focussed on the screen.

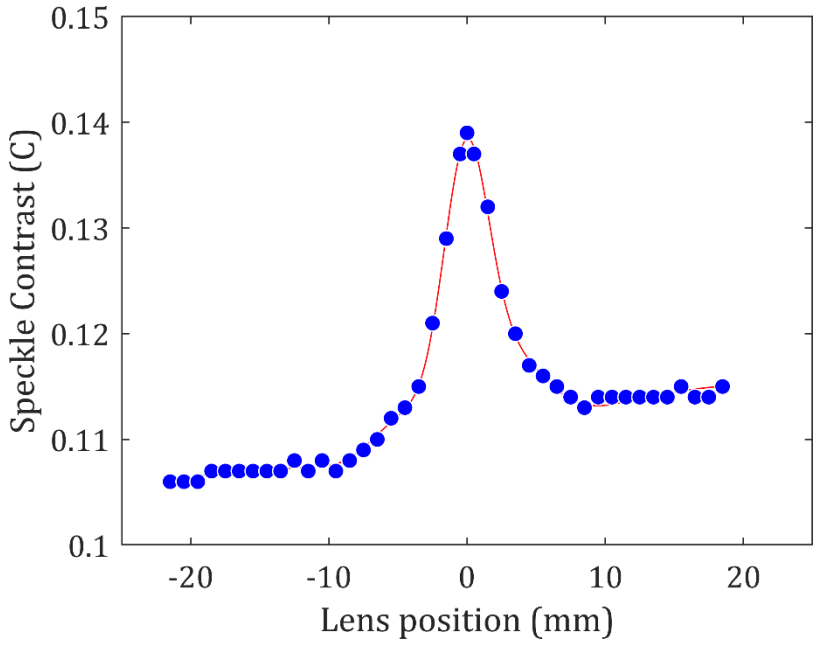

Figure 3.15: Speckle contrast measured as a function of the camera lens position. Laser light from a He-Ne is directed through an LC cell under peak speckle reduction conditions (E= 14.2 $V/\mu m$, 95 Hz). The mixture used for these measurements was E7 + 4.7 wt.% BDH1281, the cell thickness was d = 20 μm and the cell temperature T = 25°C. The data points were obtained from the measurements and the line is a gaussian fit to guide the eye.

3.4.3 Human Perception

It is only possible to derive equations that directly link speckle contrast to properties such as camera position and the lens *f*-number under ideal conditions with a complete understanding of the speckle reduction methods being used. In a practical experiment it is not readily possible to decouple the effect of different

measurement configurations on the resulting speckle contrast that is observed.

Instead, it is essential that the same configuration is used for all measurements conducted in this study. The work in this thesis is therefore undertaken with the goal of supressing the appearance of speckle from the subjective perception of the human eye. As a result, the above parameters are now considered with the aim of selecting those which correspond most closely to the human imaging system.

First, the iris size is considered. The size of the pupil is predominantly dependent on the luminance of the scene being observed, in this case the projected image. The industry standard for an indoor cinema projection system is that the luminance is a value of L = 48 cd/m^2 [54]. Equation 3.9 from [55] is therefore used to estimate the pupil diameter d based upon the luminance L:

$$d = 5 - 3\tanh(0.4 \log L) \tag{3.9}$$

From this equation, the required pupil diameter is estimated to be d = 3.2 mm. Therefore, a 3.2 mm iris was used in front of the camera lens for the work presented in this thesis.

Next, the spatial averaging the eye would experience under these conditions is considered using equation 3.8. For this study, the speckle size A_C was calculated based upon a 3.2 mm aperture and the image focal length of the eye, which is reported to be 22.8 mm [56]. From these values, the average speckle size was estimated to be approximately A_C = 18.29 μm^2.

For the level of luminance considered in this work (e.g. L = 48 cd/m^2),

photopic vision (cones) dominates over scotopic vision (rods) at the retina. It is reported in [57] that the peak foveal cone density is at least 100,000 cones/mm^2 among humans. This high density occurs in an area known as the fovea centralis, and the eyeball moves to ensure that light from the point of primary interest falls on to the fovea centralis. Consequently, this corresponds to a human pixel size of A_P = 10 μm^2. Using equation 3.8 it is found that $N_2 = 0.386$.

In order to obtain similar conditions in the experimental setup it is necessary to select the right focal length for the camera lens. The sensor pixel size is set at 4.65 μm wide, or 21.62 μm^2, by the choice of camera. Rearranging the relevant equations allows an estimation of the required focal length:

$$f = \sqrt{\frac{(3.2 \times 10^{-3})^2 \times \pi \times (4.65 \times 10^{-6})^2}{0.386 \times 4 \times (632.8 \times 10^{-9})^2}} = 33.54 \text{ mm} \tag{3.10}$$

and thus, for this work a lens with a focal length of $f = 35$ mm was selected.

As described in Section 3.4.2.2, the camera distance is inversely proportional to the speckle contrast. As a result, the camera was set at a distance of 160 mm from the screen and at an angle of 25° from the optical axis for all measurements presented in this thesis. This position was chosen as it was sufficiently close to the screen and the optical axis to ensure minimum spatial decorrelation while avoiding being so close to the screen as to partially block the path of the laser beam.

Following the discussion presented in Section 3.4.2.3, the camera integration time clearly has a significant effect on the speckle contrast. The integration time of the eye differs greatly at distinct positions on the retina. For example, rod cells are very sensitive to low levels of light and consequently integrate over a longer period

than the less sensitive cones. Integration time for both photoreceptor cells decreases with increased illumination intensity and varies considerably across the visible spectrum [58]. As a result, it isn't possible to select an integration time that perfectly matches complete human perception, but it has been reported that photopic vision at long wavelengths has a temporal integration time of approximately 50 ms [59]. As the eye directs light from its point of interest onto the cone-dense fovea centralis, this integration time was used throughout the thesis unless otherwise stated.

Finally, it is important to ensure that the camera has sufficient dynamic range to avoid discretisation errors. It has been reported that a minimum bit-depth of 6 bits is adequate for sampling the speckle pattern [11] and was easily satisfied by the camera used in this work, which had a bit-depth of 12 bits.

3.4.4 LC Cell conditions

It is well known that macroscopic LC properties such as viscosity and refractive indices are temperature dependent. As a result, a variation in the operating temperature is expected, and later shown, to influence the performance of the LC device. To control temperature variations, the cell was placed on a hot-stage which was held at a constant temperature throughout each experiment. Unless otherwise stated, every experiment was conducted at T = 25°C as this is close to ambient room temperature.

3.4.5 Ambient lighting

A high level of ambient lighting can significantly lower the measured speckle contrast as it increases the mean intensity without having much effect on the standard deviation in the intensity values. To ensure that any unwanted influence

from ambient lighting is avoided, the experimental apparatus was fully enclosed and experiments were performed in a dark lab. Sufficiently dark conditions were confirmed by ensuring the ambient light measured by the CCD was smaller than the least significant bit of the dynamic range.

3.4.6 Measurement area

As previously noted, speckle contrast should be measured over an image with a uniform intensity profile. However, a laser spot has an approximately gaussian intensity profile, as shown in Figure 3.16. Consequently, measuring over a larger area artificially increases the speckle contrast due to an increase in the standard deviation of the intensity values. Conversely, measuring over a smaller area samples less intensity values and leads to greater variation between consecutive measurements taken under the same circumstances.

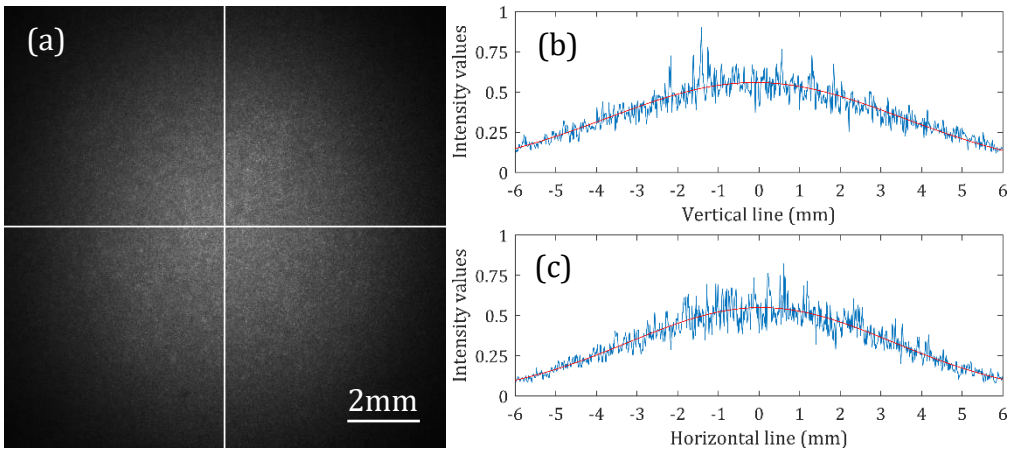

Figure 3.16: (a) Photograph of the laser spot on the projection screen taken by the cooled-CCD camera, scale bar indicates 2 mm at the projection screen (b) Intensity values along the vertical white line shown in (a) with a Gaussian fit plotted in red and (c) Intensity values along the horizontal white line in (a) with a Gaussian fit plotted in red.

To illustrate the importance of a uniform intensity profile, a set of 10 images were taken of the laser spot after passing through a LC cell under constant experimental conditions. The mixture was the nematic LC (E7) + 4.7 wt.% chiral

dopant (BDH1281) that was driven with a square-wave a.c. electric field at an amplitude of $E = 14.2$ V/μm and a frequency of $f = 95$ Hz. A MATLAB algorithm was written to find the centre of the laser spot and by fitting it to a Gaussian curve it is possible to calculate its size. The width of a gaussian curve is related to the constant c defined in equation 3.11, which represents a gaussian function:

$$f(x) = ae^{-\left(\frac{x-b}{c}\right)^2} \tag{3.11}$$

The speckle contrast was then measured for each image by analysing a square region of pixels at the centre of the laser spot. A range of square box sizes were analysed to see how the speckle contrast, C, varied with box size, and to see how this value varied across all 10 images for the same box size. The results can be seen in Figure 3.18 and the speckle image that was used to obtain these results is shown in Figure 3.17. This experiment was repeated for a range of spot sizes and a range of LC cells, including without a LC cell as shown in Figure 3.19.

As expected, the speckle contrast, C, is artificially increased with increasing box size and the error between images is increased for smaller box sizes. As a result, it was decided that a box size of $0.5c$ be used throughout all the images tested as this combined minimal error with minimal artificial increase in C.

3.5 Calibration of setup

To benchmark measurements from this setup against existing literature the speckle contrast of a highly coherent He-Ne laser without a diffuser was tested and found to be 0.625 ± 0.008, close to the theoretical value of $1/\sqrt{2}$ reported in Section 2.2.4 of Chapter 2. Another measurement was taken with a RGGD in the diffuser plane

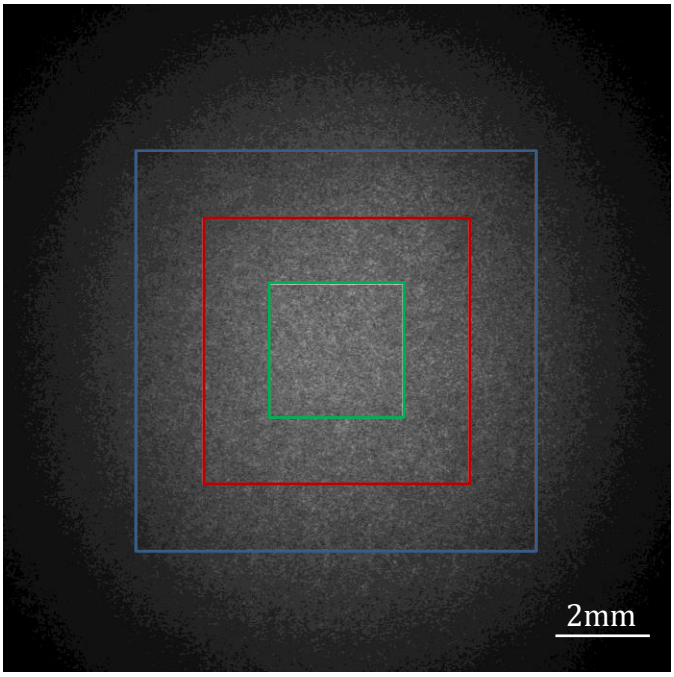

Figure 3.17: Speckle image for E7 + BDH1281 4.7 wt.% (used in Figure 3.18) with three example box sizes highlighted: 0.5c in green, 1c in red and 1.5c in blue. These sizes correspond to the vertical lines of the same colour in Figure 3.18.

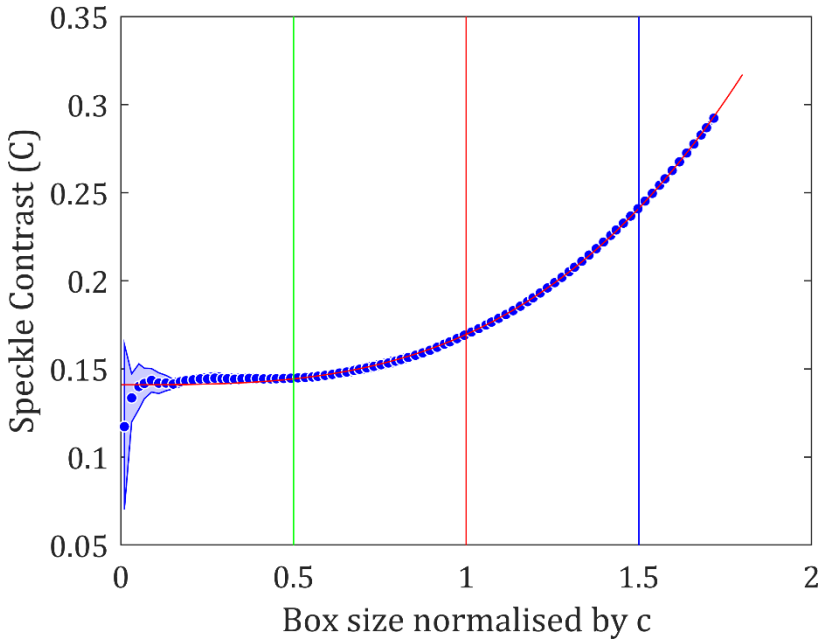

Figure 3.18: Plot of speckle contrast dependence on the box size. The blue circles are the speckle contrast averaged over 10 images taken under the same experimental conditions with an LC cell at optimum operating conditions (E = 14.2 $V/\mu m$, f = 95 Hz square wave) for a range of box sizes. The LC device consisted of the nematic LC (E7) and 4.7 wt.% chiral dopant (BDH1281), cell thickness of d = 20μm, and temperature of T = 25°C. The error present in the speckle contrast measurement is highlighted by the blue shaded regions around the data points. A fitted line of the form $ax^b + c$ is shown in red to guide the eye. The green, red and blue vertical lines correspond to three example box sizes shown in Figure 3.17.

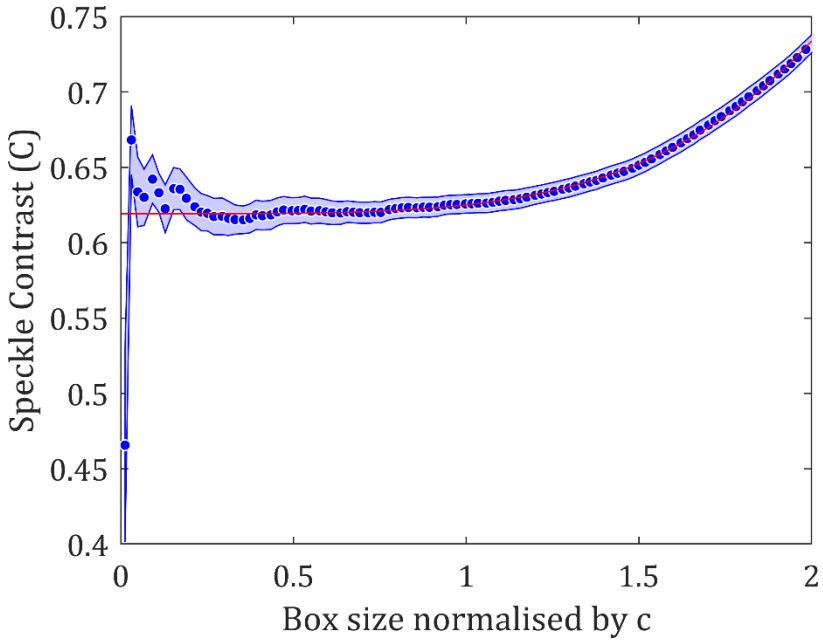

Figure 3.19: Plot of speckle contrast on the box size. The blue circles are the measured speckle contrast averaged over 10 images taken under the same experimental conditions without an LC cell for a range of box sizes. The error present in the speckle contrast is shown by the blue shaded regions around the data points. A fitted line of the form $ax^b + c$ is shown in red to guide the eye.

(Figure 3.7) tested at 40-200rpm. It was found that, in this case, $C = 0.04 \pm 0.003$, which is in good agreement with previously published results for similar devices [4]. Images of the resultant speckle in both cases are shown in Figure 3.21.

3.6 Error Analysis

Throughout this thesis every effort has been made to reduce the error in measurements of speckle contrast and transmission. The dominant sources of random error are discussed in the following sections along with the methods used to reduce their impact.

3.6.1 Speckle contrast and transmission measurements

There are several potential sources of error that would be present during the measurement of speckle contrast and transmission for each individual cell. The noise associated with the camera is minimised through the use of a cooled CCD.

Fluctuations in laser intensity or coherence are avoided by using a stable He-Ne laser. The laser is switched on and left for at least 30 minutes before every experiment to ensure its output has reached a steady state during use. Cell temperature is shown to have a great impact on device performance, so all LC cells are mounted to a hot stage with PID feedback control. The hot stage is switched on at least 30 minutes before every experiment to ensure the cell temperature has reached a steady state during use, with fluctuations of less than ± 0.1°C. Mechanical vibrations and changes to ambient light were minimised by running all experiments in an unlit lab with no other experiments taking place and nobody present from start to finish. The MATLAB code was written such that experiments were fully automated and could be started remotely.

In each experiment throughout the thesis, minimum speckle contrast is measured over a period of at least 5 minutes with at least 100 consecutive speckle photographs taken. This is referred to as the 'steady state test'. The value quoted is the average of all these measurements along with the maximum range around the average that was measured throughout the experiment. A histogram of the values measured in the 60-minute steady state test conducted in the proof-of-concept experiment in Section 4.1 is shown in Figure 3.20. The mean speckle contrast is calculated to be $C = 0.157$, with a standard deviation across all measurements of 0.002 and a range of 0.014. Consequently, the speckle contrast is presented as $C = 0.157 \pm 0.007$.

The following sections describe sources of error that will not vary throughout the experiments undertaken on each cell but represent the random error that may exist between measurements taken on multiple cells.

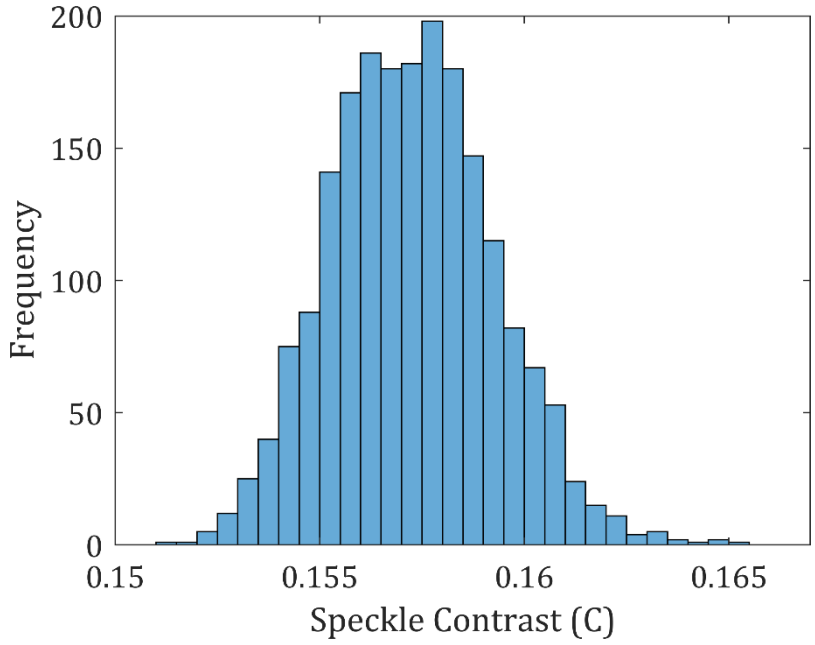

Figure 3.20: Histogram of speckle contrast values measured during steady state test undertaken in Section 4.1 with a 20 µm cell containing the nematic E7 with 2.5 wt.% chiral dopant BDH1281. 2000 measurements were taken over a period of 60 minutes.

3.6.2 Cell thickness

The cells used are quoted to have a cell gap of 5 µm, 9 µm and 20 µm. Every cell gap is measured as described in Section 3.1.2 and any that are more than 5% from the quoted size are discarded.

3.6.3 Pitch measurement

The PBG position of each cell is measured using a UV-Vis spectrometer and the MATLAB code described in Section 3.2. The pitch is then calculated using information about the refractive indices of the material. Each result is checked by eye to ensure the MATLAB code has correctly located the PBG position. The inverse of the measured pitch for all mixtures based on the same nematic and chiral dopant is plotted against the concentration of chiral dopant and a line of best fit that intersects the origin is used to check that all mixtures have pitch that is less than 5% removed from this line. Mixtures that are more than 5% from the line are discarded.

3.6.4 Optical component positioning

It has been shown throughout this chapter that the position of the optical components in the experimental set up can have a significant impact on the measurement of speckle contrast. Consequently, the position of all optical components was set at the start of this work and was not changed at any point.

3.6.5 Systematic errors

Systematic errors may arise from sources such as incorrectly positioned optical components, an unstable or low-coherence laser, thermal noise added by the camera etc. However, the work described above to reduce random noise is expected to minimise systematic error also. The speckle contrast of the He-Ne was also measured every 1-2 months and was found to vary from C = 0.625 by less than 0.01 throughout the experiments. The values of speckle contrast for the He-Ne (C = 0.625) and the RGGD (C = 0.04) were also found to match up with those reported in the literature and expected from the theory. In conclusion, systematic errors are shown to have been minimised throughout this work.

Finally, error bars are shown in plots of electric field amplitude and frequency. These show the resolution in amplitude and frequency values that each cell was exposed to throughout the experiments.

3.7 Summary

This chapter has described the various apparatus and methods developed and used throughout this thesis. A range of liquid crystal mixtures were prepared, inserted into commercially-available glass cells and characterised using a number of experimental techniques. A method of measuring speckle contrast of laser light was

developed, with the intention of matching to human perception, and used to observe the reduction in speckle that is present after passing through one of the liquid crystal devices under a range of applied electrical and physical conditions. Careful consideration was given to the camera properties and experimental setup to better

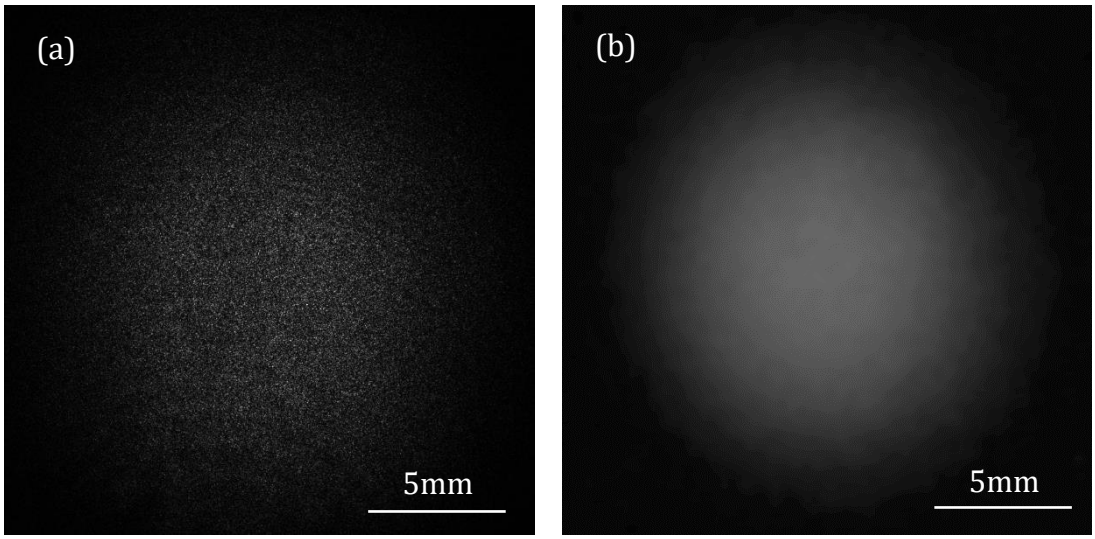

Figure 3.21: Examples of speckle pattern for (a) a highly coherent He-Ne laser without a diffuser ($C = 0.625$) and (b) the same laser after passing through a rotating ground glass diffuser ($C = 0.04$).

understand and avoid speckle reduction that did not result from the liquid crystal device.

The system was calibrated using a He-Ne laser and RGGD as they represent the known extremes of the speckle contrast and the values obtained were in good agreement with those reported in the literature. The following chapters document the experiments carried out with this experimental setup and the results that were obtained. It is shown that a chiral nematic liquid crystal device can be used to reduce the speckle contrast when in the dynamic scattering state and that, through careful consideration of the material parameters and the applied electric field conditions, it is possible to optimise the performance of these devices.

4 Study of liquid crystal parameters on speckle reduction

Having developed the experimental tools for measuring the speckle contrast ratio, C, of a laser source in the previous chapter, in this chapter reduction of the parameter, C, using a chiral nematic liquid crystal (LC) with positive dielectric anisotropy is demonstrated. Contrary to the published literature [39] [60], positive dielectric anisotropy mixtures with short pitches (typically below 1 μm) exhibit a dynamic scattering mode (DSM) when subjected to a low frequency (< 100 Hz) square wave electric field of sufficiently large amplitude. In this DSM, the rapid movement of the LC molecules causes a spatially and temporally random phase perturbation to the incident laser light, which results in a reduction in the observed speckle contrast. The performance of the device is quantified in terms of the reduction (given as a percentage) in the speckle contrast value, C.

Following the presentation of results that demonstrate the proof-of-principle of the device, the influence that a range of different LC material parameters have on the speckle contrast is investigated by subjecting different mixture formulations to a wide range of electric field conditions to observe those required for peak device performance (defined in terms of the maximum reduction in the speckle contrast, C). In this way, results are presented on the dependence of the device performance on parameters such as the pitch of the chiral nematic LC helix, birefringence, electric field amplitude and applied frequency of the external electric field. It is shown that a reduction in the pitch, p, results in significantly reduced speckle contrast, but that

the transmission of the laser light through the device reaches a minimum for p = 0.5 – 1 µm before increasing with a further reduction in the pitch. The results indicate that there is an inverse relationship between the pitch and both the electric field amplitude and frequency required for peak device performance. Afterwards, the influence of increasing the birefringence on the speckle contrast ratio is considered.

4.1 Proof-of-concept

One approach to reducing the speckle contrast is to produce multiple, statistically-independent speckle patterns within the integration time of the detector. In this study, a chiral nematic LC cell was employed as the time varying, spatially-random phase perturbation element to the incident laser light as it is known to produce bi-stable scattering states [61] [62] [41]. The scattering state is known as the focal conic state and in this state the LC molecules assume many helical units whose axes are randomly oriented relative to each other.

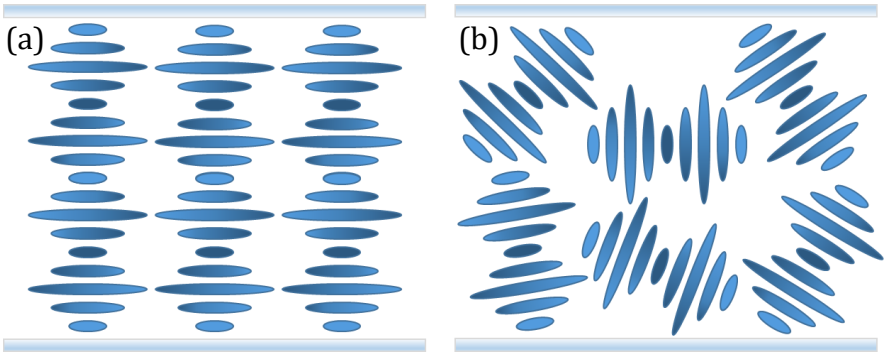

Figure 4.1: Schematic diagram of (a) the chiral nematic LC phase and (b) the focal conic scattering state.

It has been shown that shorter pitch mixtures are better suited to forming the focal conic state under an electric field, with longer pitch mixtures tending to exhibit the fingerprint texture instead [26]. As a result, a high twisting power chiral dopant

capable of producing short pitch helices was chosen for this proof-of-concept demonstration. A chiral nematic with positive dielectric anisotropy will also assume a homeotropic nematic state under a sufficiently high amplitude electric field. Consequently, it was the intention to subject a chiral nematic mixture to an alternating electric field in order to switch the mixture between independent scattering states within the integration time of the human eye, thus reducing the appearance of speckle.

To prove the concept, E7 (Synthon) was chosen as the nematic host as it is liquid crystalline at room temperature and its macroscopic physical properties such as the refractive indices, dielectric permittivities and elastic constants are well known. The E7 mixture was dispersed with the high twisting power chiral dopant BDH1281 (Merck) at a concentration of 2.5 wt.% to form a chiral nematic phase with a right-handed helical structure. This mixture was then capillary-filled into a glass cell with a known thickness of 20 μm. The pitch of the mixture was determined using the method described in Section 3.2 and was found to be p = 517 nm at a temperature of $T = 25°C$. An optical polarising microscope image is shown in Figure 4.2 of the cell after mixing and annealing prior to the measurement of the pitch. The figure shows the typical Grandjean texture, which indicates that the axis of the helix is aligned parallel to the surface normal of the glass substrates. In the image, oily streaks can be seen emanating from the glass spacer beads (20 μm) that are dispersed randomly throughout the cell. The corresponding transmission spectrum for white light at normal incidence (i.e. parallel to the helical axis) is shown in Figure 4.3.

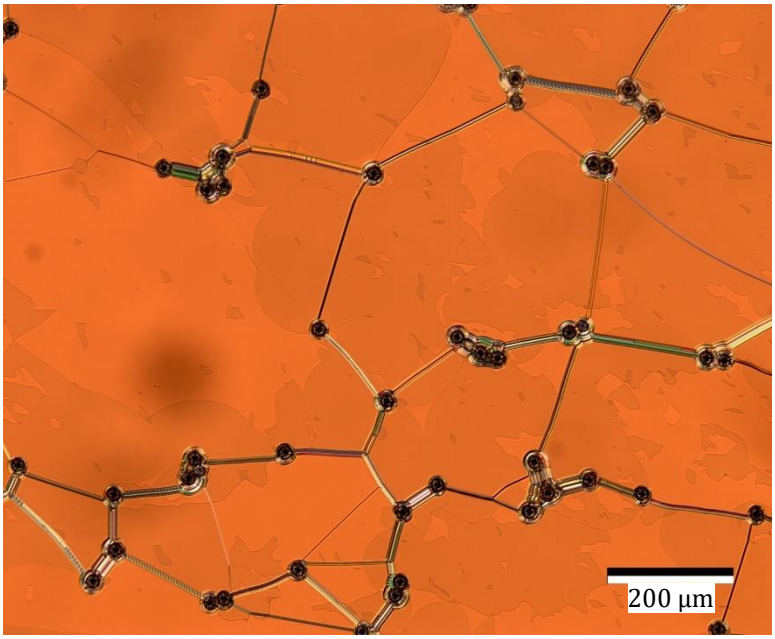

Figure 4.2: Microscope image at 10 × magnification with crossed polarisers of a 20 μm-thick, chiral nematic liquid crystal cell containing the nematic host, E7, dispersed with 2.5 wt.% chiral dopant (BDH1281). The cell temperature was T = 25°C. The scale bar depicts a distance of 200 μm. Spacer beads can be seen throughout the cell.

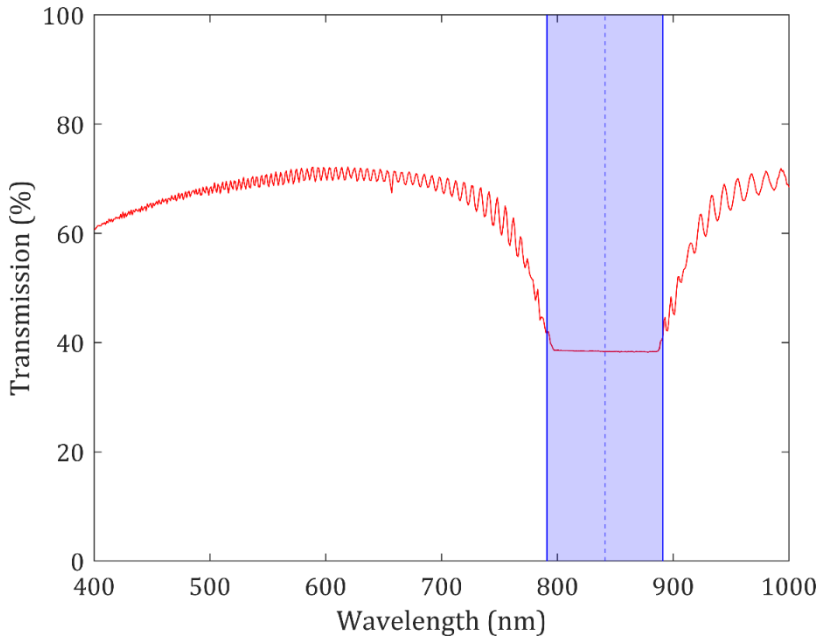

Figure 4.3: Transmission spectrum for a 20 μm-thick, chiral nematic liquid crystal cell containing the nematic host, E7, dispersed with 2.5 wt.% chiral dopant (BDH1281). The cell temperature during measurement was T = 25°C. The reflection band position is highlighted in light blue, with the centre estimated to be $\lambda_c = 841\ nm$ marked with a dashed blue line.

In order to characterise the range of field-induced optical textures that this mixture can exhibit, the cell was subjected to a square-wave electric field whose amplitude

was varied from 1 – 20 V/μm at a frequency of 20 - 200 Hz and observed under a polarising optical microscope. The textures that were observed are shown in Figure 4.4. As expected this mixture exhibits a focal conic texture instead of the fingerprint texture under electric fields above $E = 1$ V/μm and throughout the range of frequencies tested. The critical field required for the field-induced homeotropic nematic texture was found to be $E_c = 10$ V/μm. It was also found that, over time, the cell returns to the focal conic texture once released from any of the electric field amplitudes applied in this study.

According to the published literature on EHDI in chiral nematic LCs, the dynamic scattering mode is only expected to be present in materials with negative dielectric anisotropy and is a direct result of the competition between the conductivity and dielectric torques [26] [39] [63] [64]. However, contrary to the conventional wisdom, above a threshold of $E_{th} = 3$ V/μm the mixture considered in this study was found to enter a dynamic scattering mode, which manifested itself as a random, rapid movement of small domains only several microns wide. No regular optical pattern could be observed. At $E = 3$ V/μm this dynamic scattering nucleated from small regions across the device which grew slowly with time. With an increase in the electric field amplitude, dynamic scattering was observed to replace the focal conic texture throughout the entire active area of the device (defined by the area of the glass cell coated with indium tin oxide electrodes) and the scattering intensified, making the device appear milky white to the naked eye. Scattering was strongest just below the critical electric field amplitude required to unwind the helical structure and induce a homeotropic nematic texture. Photograph Figure 4.4.b was taken with an integration time of 5 ms. Photographs taken with longer integration

times appear blurred and relatively featureless due to the fluctuation frequency of the LC director within the cell.

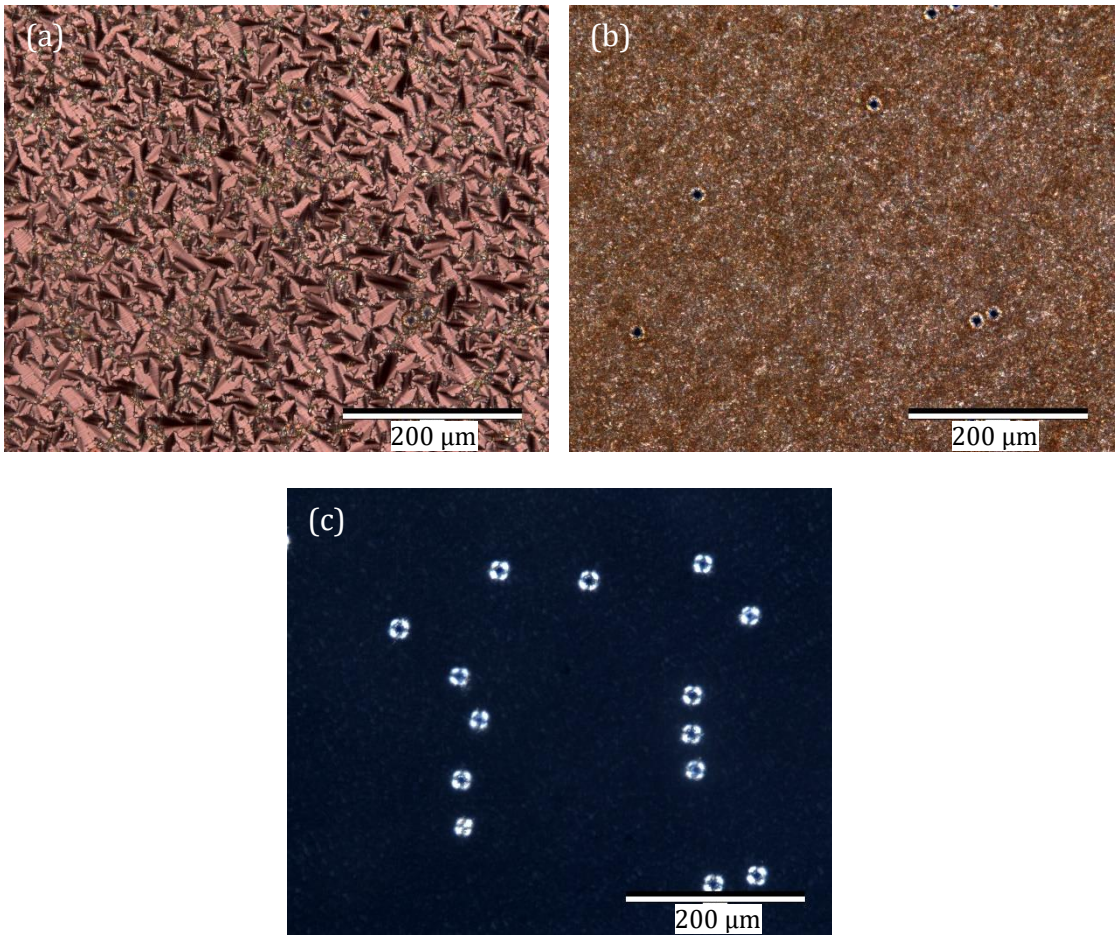

Figure 4.4: Polarizing optical microscope images of (a) focal conic texture (2 V/µm, 100 Hz), (b) dynamic scattering mode (8 V/µm, 40 Hz), (c) electric field-induced nematic homeotropic texture (11 V/µm, 20 Hz) at 20 × magnification with crossed polarisers of a 20 μm-thick, chiral nematic liquid crystal cell containing the nematic host, E7, dispersed with 2.5 wt.% chiral dopant (BDH1281). The cell temperature was held at T = 25°C. The scale bar depicts a distance of 200 μm in all images. The spacer beads are present in all images and are particularly visible in image (c).

The dynamic scattering mode is well suited to speckle reduction as the fluctuation in the LC director is fast and random, thus a sufficiently birefringent material is capable of subjecting incident light to a time-varying, spatially-random phase perturbation. Also, switching between different scattering states is limited by the small number of distinct states the mixture can adopt, and by the response time of the LC [29] [33] [32]. As a result, all subsequent work in this thesis employs the use

of the dynamic scattering mode in LCs.

To test how effective DSM is in speckle reduction of a coherent laser source, the cell was inserted into the experimental rig for measuring the Speckle Contrast, C, as described in Chapter 3, Section 3.5. The MATLAB script was set up to test the cell at a range of electric field conditions, from 1 – 20 $V/\mu m$ in increments of 1 $V/\mu m$, and from 20 – 100 Hz square-wave in increments of 20 Hz. At each electric field condition, the MATLAB code that was written to control the experiment switches the signal generator off for 5 s to allow the LC device to relax. It then switches the signal generator on at the correct amplitude/frequency and waits 5 s more for the cell to reach a steady-state response. It then takes three photographs of the speckle pattern generated at the projector screen with a 1 s delay in between each shot. The mean and range of the speckle contrast and transmission are then recorded before restarting the cycle at the next electric field condition. Photographs of the speckle pattern and corresponding LC textures are shown in Figure 4.5 with increasing electric field amplitude at a frequency of 40 Hz.

In Figure 4.6 a plot of the speckle contrast, C, is plotted as a function of the electric field amplitude for a square wave of frequency 40 Hz. For comparison, the speckle contrast observed without an LC device in place is presented (blue line) along with the speckle contrast observed with a rotating ground glass diffuser (RGGD) in the diffuser plane (green line).

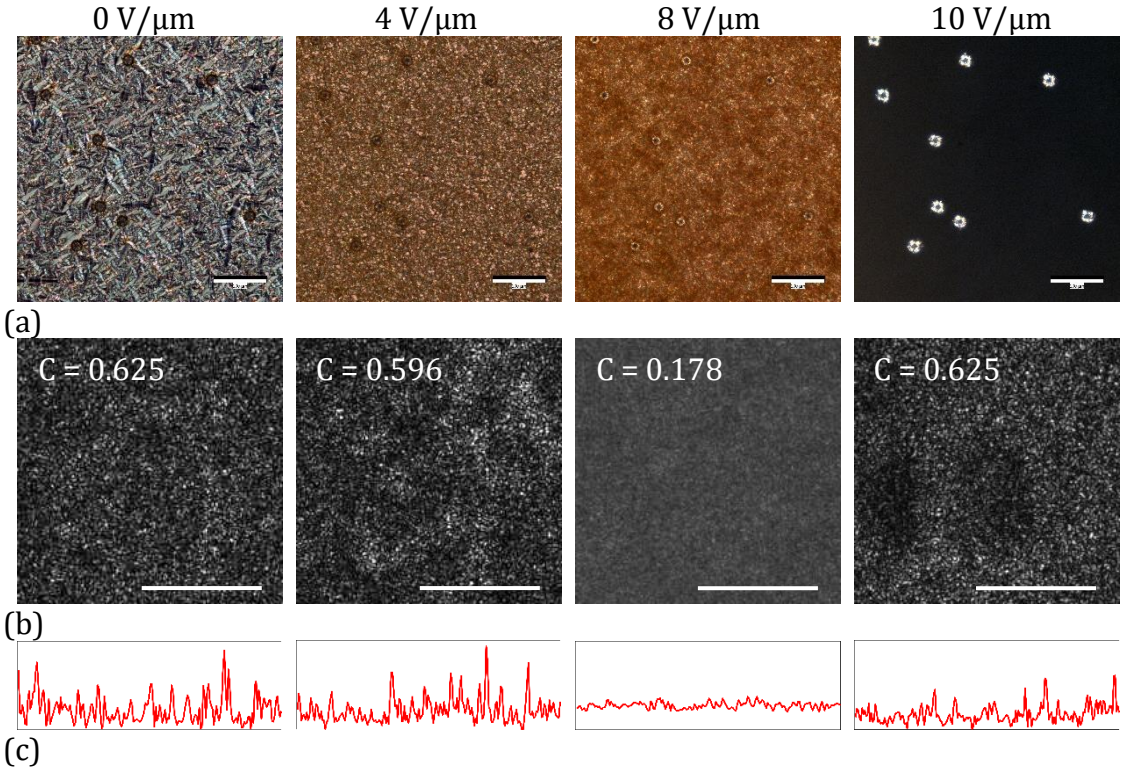

Figure 4.5: (a) Polarizing optical microscope images (crossed polarizers, 20x objective) of a chiral nematic LC cell at different E-fields. Scale bars represents a distance of 200 µm (b) Corresponding images of the speckle pattern formed on the projection screen that was subsequently recorded by the CCD with a 50 ms exposure time and normalized by the average intensity. The scale bar represents a distance of 1 mm on the projection screen. (c) Plots of the intensity distribution of the central line of pixels across the width of each image (red).

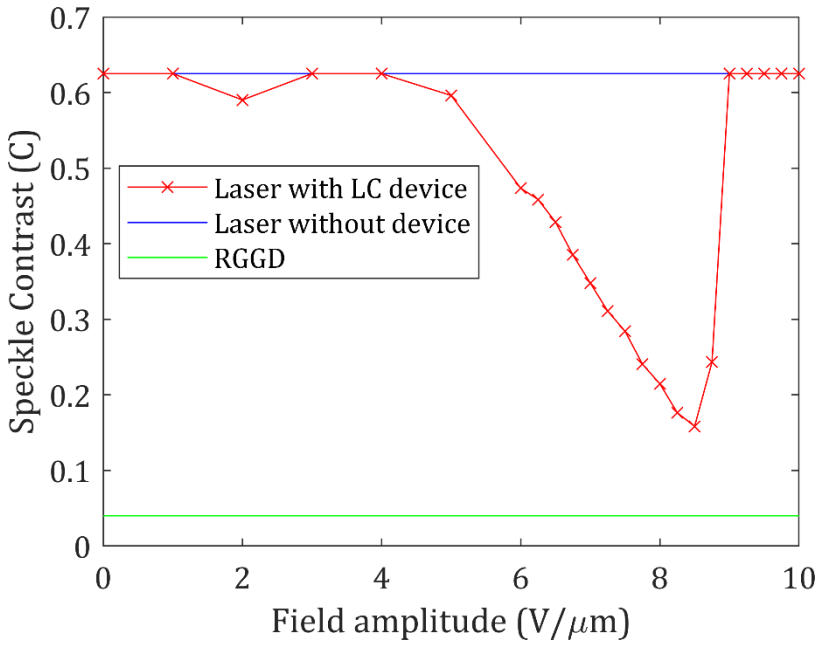

Figure 4.6: Plot of the speckle contrast parameter, C, as a function of the electric field amplitude for a chiral nematic LC device (red). The solid blue line represents the value of C for the He-Ne laser without a diffusing element (C = 0.625), whereas the green line shows the value of C for an RGGD (C = 0.04). All measurements are taken with a 50 ms exposure time.

At $E = 0$ V/μm there is no observable turbulence and consequently no observable reduction in the speckle contrast. As the electric field amplitude increases above $E = 3$ V/μm the difference between the bright spots corresponding to constructive interference and the dark spots corresponding to destructive interference reduces significantly. At $E = 8$ V/μm the speckle contrast is at a minimum value of $C = 0.18$. This is most clearly demonstrated by the intensity distributions plotted in Figure 4.5(c). Above 9 V/μm the cell appears transparent as it is in a field-induced homeotropic nematic texture and thus is no longer able to reduce the speckle contrast.

The complete speckle contrast results of this test are shown in Figure 4.7 in the form of a colourmap. Red sections in the map represent little-to-no speckle reduction while dark blue regions represent high-levels of speckle reduction. From this map it is clear that the peak speckle reduction occurs at an electric field amplitude of $E = 8\ V/\mu m$ and a frequency of $f = 40$ Hz, which corresponds to a speckle contrast of $C = 0.19$.

The results for the proportion of laser light transmitted through the cell and collected using the optical components in the experimental apparatus are shown in Figure 4.8. Red sections in the map represent maximum transmission through the LC cell whereas dark blue sections show the electric field conditions for which there was very little transmission. It is clear from this colourmap that the conditions for peak speckle reduction typically coincide with low transmission properties due to the magnitude of the scattering.

Once a ball-park estimate of the electric field conditions required to achieve maximum speckle reduction had been identified, the next step was to study the cell

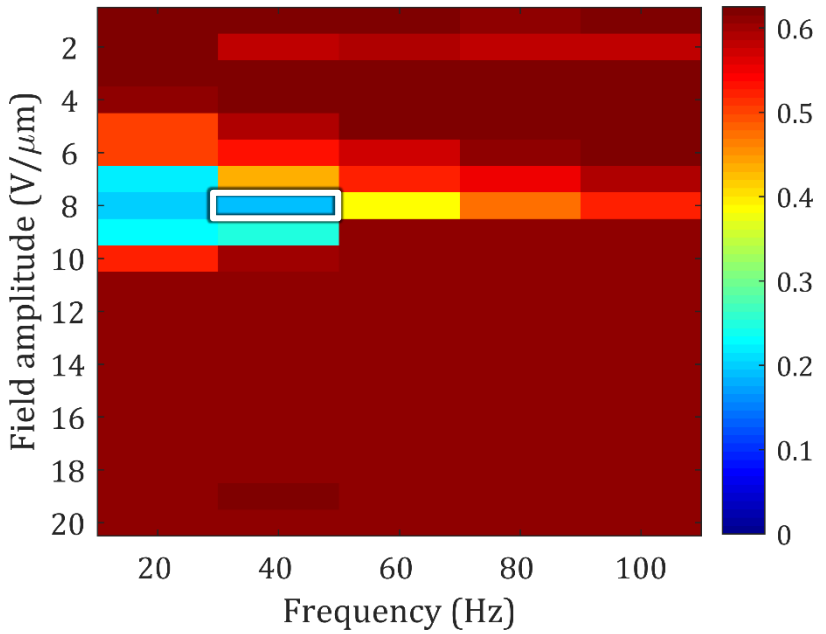

Figure 4.7: Map of the speckle contrast, C, for a range of applied electric field conditions; field amplitude from $1-20\ V/\mu m$ and square-wave frequency from $20-100$ Hz. The cell tested was a 20 μm-thick, chiral nematic liquid crystal cell containing the nematic host, E7, dispersed with 2.5 wt.% chiral dopant (BDH1281). The cell temperature during measurement was T = 25°C. Peak performance conditions are highlighted in a white box.

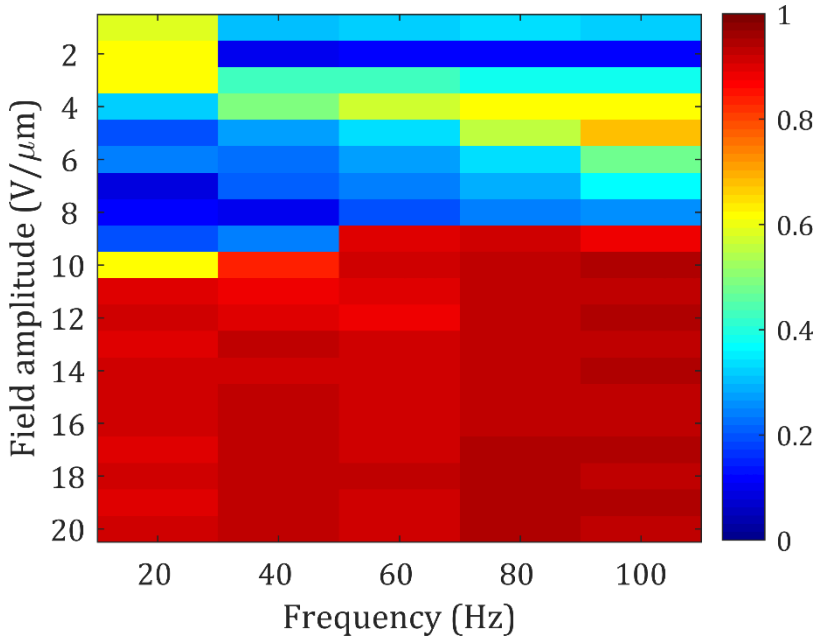

Figure 4.8: Transmission map for a range of applied electric field conditions; field amplitude from $1-20\ V/\mu m$ and square-wave frequency from $20-100$ Hz. The cell tested was a 20 μm-thick, chiral nematic liquid crystal cell containing the nematic host, E7, dispersed with 2.5 wt.% chiral dopant (BDH1281). The cell temperature during measurement was T = 25°C.

at a higher resolution of field conditions close to the region where the peak speckle reduction was observed. In this case, the electric field amplitude was varied from

$7.8 - 9.0\ V/\mu m$ in increments of $0.2\ V/\mu m$, and the frequency is varied from $30 - 50$ Hz in increments of 5 Hz. The resulting colourmap is shown in Figure 4.9. With this finer resolution, peak speckle reduction is now found to occur at $8.4\ V/\mu m$ and 40 Hz, which corresponds to a speckle contrast of $C = 0.14$.

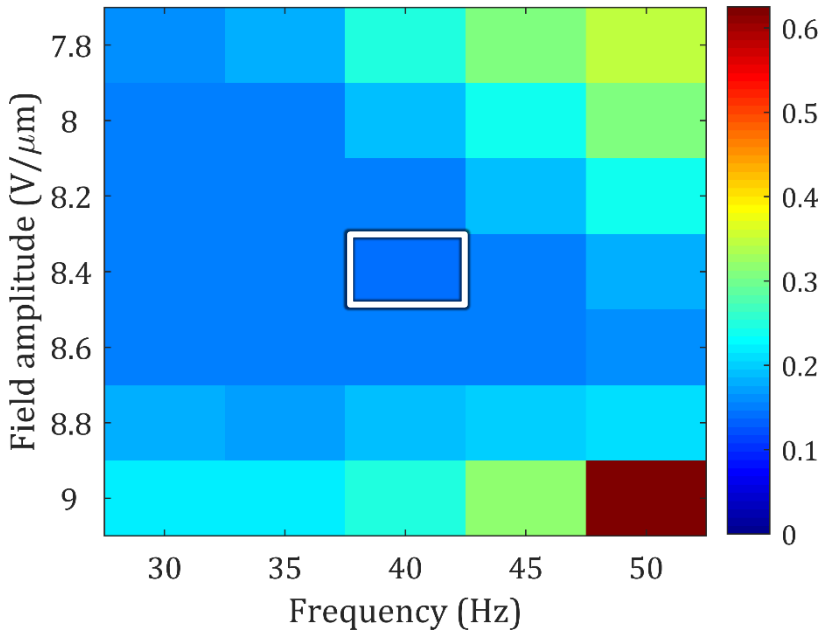

Figure 4.9: High resolution speckle contrast map for a range of applied electric field conditions; field amplitude from $7.8 - 9.0\ V/\mu m$ and square-wave frequency from $30 - 50$ Hz. The cell tested was a 20 μm-thick, chiral nematic liquid crystal cell containing the nematic host, E7, dispersed with 2.5 wt.% chiral dopant (BDH1281). The cell temperature during measurement was T = 25°C. Peak performance conditions are highlighted in a white box.

Next, the cell undergoes a steady-state response test. The MATLAB code sets the signal generator to apply the peak speckle reduction electric field conditions that have been identified from these measurements over a period of 60 minutes. A photograph of the speckle at the projector screen is taken every 1 s and the speckle contrast and transmission are then recorded. An example of a plot of the speckle contrast, *C,* taken over a period of 60 minutes is shown in Figure 4.10. Throughout all the experiments the cell is secured to a hot plate held at a temperature of $T = 25°\,\mathrm{C}$. The average speckle contrast measured during this experiment was $C = 0.157 \pm 0.07$.

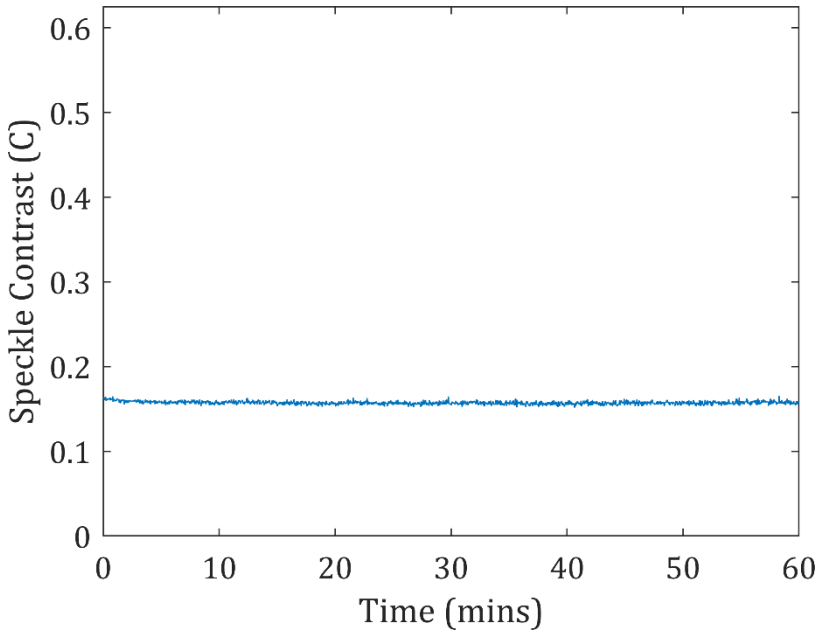

Figure 4.10: Plot of speckle contrast taken over a period of 60 minutes for a 20 μm-thick, chiral nematic liquid crystal cell containing the nematic host, E7, dispersed with 2.5 wt.% chiral dopant (BDH1281). The electric field conditions required for peak speckle reduction were applied throughout (8.4 $V/\mu m$, 40 Hz square-wave). The cell temperature during measurement was T = 25°C.

Finally, the cell undergoes two hysteresis tests. In the first test, the frequency is set to 40 Hz (corresponding to the frequency for peak performance) and the electric field amplitude is cycled from 6 – 10 V/μm in steps of 0.25 V/μm, and back from 10 – 6 V/μm. This process is repeated 5 times. At each electric field condition, the signal generator holds the current amplitude and frequency for 5 s so that the cell reaches a steady-state response. It then takes 3 photographs of the speckle pattern generated at the projector screen with a 1 s delay in between each shot. The mean and range of speckle contrast and transmission are recorded before restarting the cycle at the next field condition. The results of such an experiment are plotted in Figure 4.11.

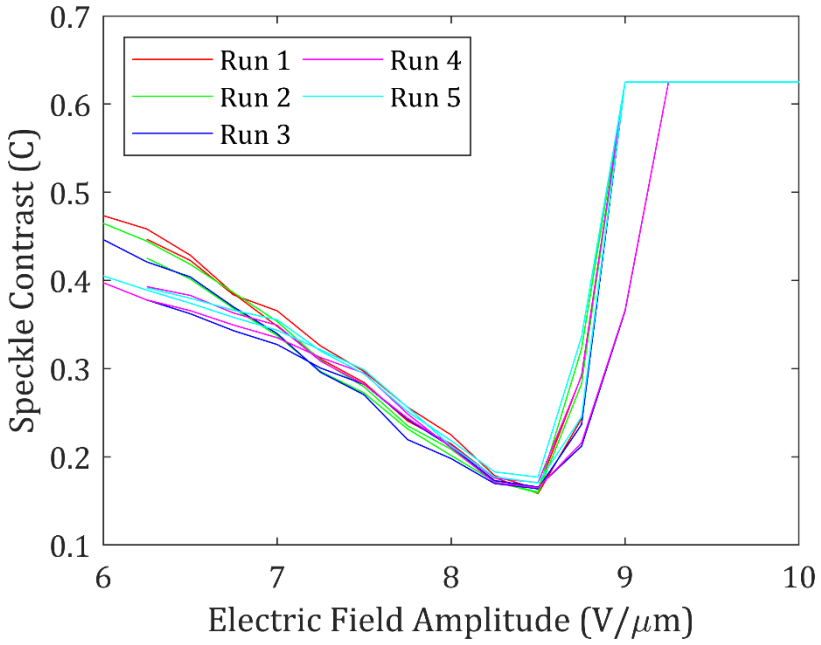

Figure 4.11: Plot of speckle contrast as the electric field amplitude is cycled from 6 – 10 V/μm and back in increments of 0.25 V/μm a total of 5 times. The frequency is set to 40 Hz throughout. The cell temperature during measurement was T = 25°C. Each colour represents a complete cycle, the order of which is given in the legend.

This data shows that there was limited variation in the speckle contrast recorded at a set field amplitude as the experiment was carried out. At peak performance in terms of speckle reduction ($E = 8.5$ V/μm) the speckle contrast varied from $C = 0.158$ to 0.177, a maximum variation of 12%. At electric field amplitudes below peak performance the variation in the speckle contrast value increased. A clear trend is seen as the speckle contrast reduces with each consecutive sweep. An initial speckle contrast of $C = 0.474$ dropped to $C = 0.405$ by the final sweep. This represents a reduction in speckle contrast of 17%.

Following this test, the cell was then subjected to a second hysteresis test, the equivalent of running 10 consecutive high-resolution sweeps of the electric field conditions. This allowed the identification any hysteresis effects over a range of frequencies. The results for scans 1, 5 and 10 are shown in Figure 4.12.

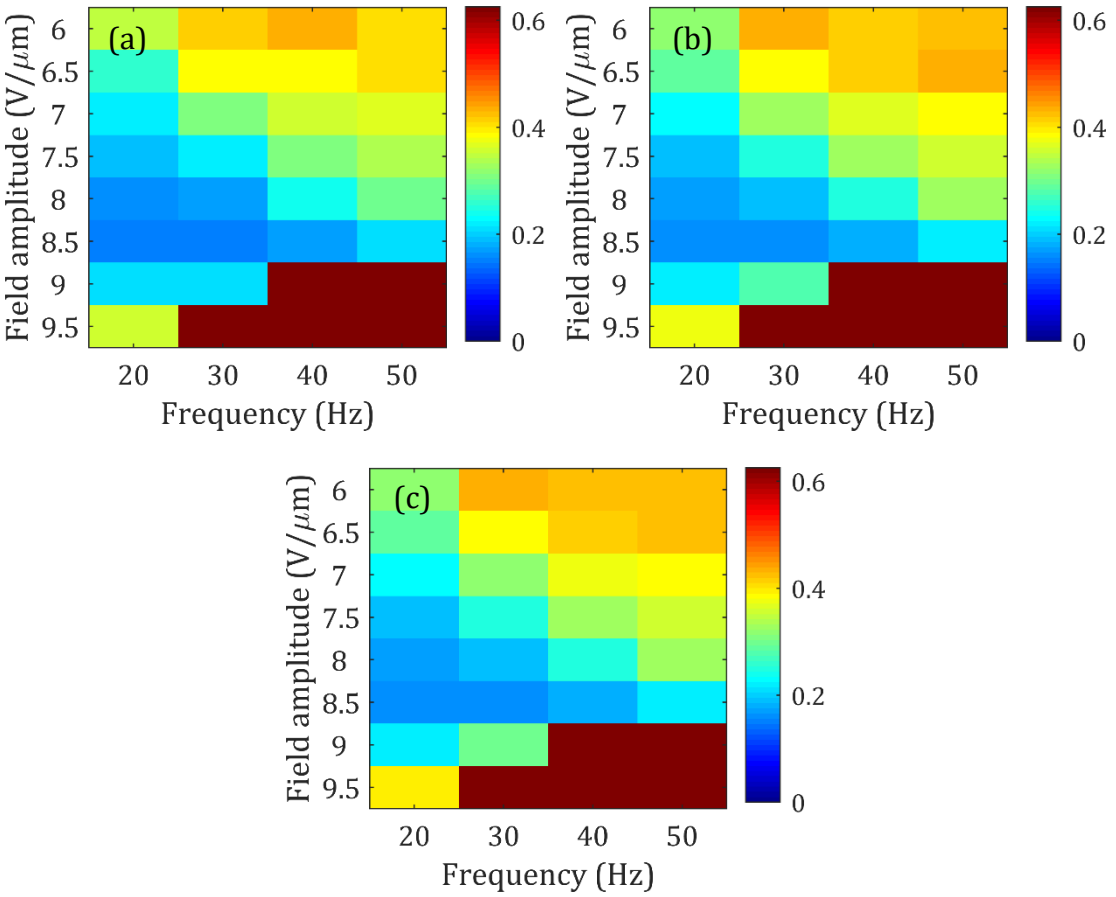

Figure 4.12: Plot of speckle contrast as a function of the electric field for a 20 μm-thick, chiral nematic liquid crystal cell containing the nematic host, E7, dispersed with 2.5 wt.% chiral dopant (BDH1281). The same test was carried out 10 times consecutively with results shown for (a) run 1, (b) run 5 and (c) run 10. The cell temperature during measurement was T = 25°C.

These plots show that there is very little change in the speckle contrast measured under any set of electric field conditions as the cell is continuously cycled through a range of field conditions. At peak speckle reduction conditions ($E = 8.5$ V/µm, $f = 20$ Hz) the speckle contrast ranged from $C = 0.156$ to $C = 0.162$, a variation of approximately 4%. Variation at most other electric field conditions was limited to less than 10%.

In summary, it has been shown that a chiral nematic mixture, consisting of E7 with the chiral dopant BDH1281 (2.5 wt.%) with pitch $p = 517$ nm, applies maximum speckle reduction to an incident He-Ne laser beam with an applied

square-wave electric field of amplitude $E = 8.4$ V/μm and a frequency of $f = 40$ Hz. At this electric field condition, the cell enters a dynamic scattering mode that, due to the birefringent nature of the LC molecules, has the effect of significantly reducing the appearance of speckle. Under these conditions it is shown that the speckle reduces from $C = 0.625$ to $C = 0.157 \pm 0.014$. It is also shown that this speckle reduction remains constant over a period of 60 minutes and does not suffer from significant hysteresis when cycling the cell through a large range of electric field amplitudes and frequencies.

4.2 Role of the Helical Pitch

Having shown that a chiral nematic LC can reduce the speckle contrast of coherent laser light, the effect that a change in the helical pitch has on the performance of the cell is now explored. In this material study, experimental results for a range of pitch values are presented for mixtures consisting of different nematic hosts (E7 and BL006) and different chiral dopants (BDH1281, R811, R5011). The influence of a change in pitch on the field amplitude and frequency required for maximum speckle reduction is explored, as well as the minimum speckle contrast value and corresponding transmission that each mixture can achieve.

4.2.1 *Preparation of mixtures*

In total, 21 mixtures were prepared for this experiment. The mixture concentrations and corresponding pitch values are shown in Table 4.1. The pitch of each mixture was determined using the relevant experimental procedure described in Section 3.2. Mixtures with photonic bandgaps outside the detection range of the UV-Vis spectrometer were estimated by extrapolation of the line of best fit taken from the

other concentrations of the mixture in question, as shown in Figure 4.13. From these fits it is possible to estimate the macroscopic helical twisting power (HTP), β, of each chiral dopant in each nematic host using equation 3.1.

$$p = (\beta c_w e_e)^{-1} \tag{4.1}$$

where e_e is the enantiomeric purity, p is pitch and c_w is the weight concentration of the chiral dopant. (For these estimations it is assumed that $e_e = 1$.) The values calculated are in line with what one would expect as the chiral dopant, BDH1281, is a high twisting power dopant, whereas R811 is a low twisting power chiral dopant.

Nematic	**Chiral Dopant**	**wt.%**	**Pitch (nm)**	**HTP (μm^{-1})**
E7	BDH1281	0.5 – 6.4	244 – 2700	71.579
E7	R811	5.1 – 19.9	518 – 1980	9.918
BL006	R811	4.9 – 25.4	410 – 2050	9.802
BL006	R5011	unknown	224 - 263	unknown

Table 4.1: Mixture concentration summary for the 21 mixtures used in this study, along with corresponding pitch. The weight percentage of the BL006 with R5011 mixture was unknown as it arrived pre-mixed from Merck.

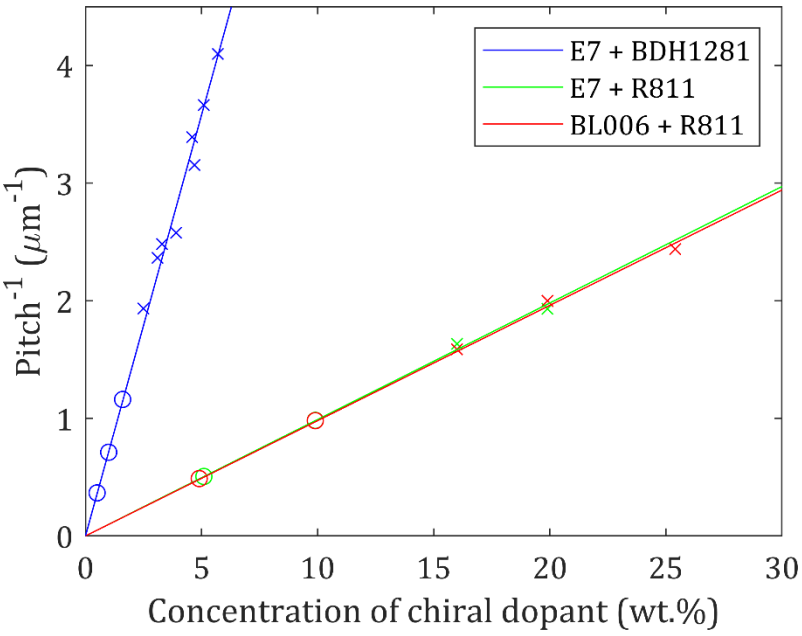

Figure 4.13: Plot of the reciprocal of the pitch (μm^{-1}) as a function of the chiral dopant concentration (wt.%) for chiral nematic mixtures consisting of the nematic LCs, E7 and BL006, dispersed with different concentrations of the chiral dopants BDH1281 (high twisting power) and R811 (low twisting power). Crosses represent measured data points. A line of best fit is shown for each mixture. Circles represent values extrapolated from the best fit.

Each cell was subjected to a low-resolution electric field parameter sweep, then a high-resolution sweep around the point of peak performance in terms of speckle reduction, before a 5-minute steady-state test was carried out at the optimum speckle reduction electric field conditions. The individual colourmaps are not shown in this thesis for the sake of space. Instead, four graphs that highlight the salient details extracted from these experiments are presented.

Unfortunately, the cells consisting of BL006 with the chiral dopant R5011 with pitch values of 224 and 230 nm exhibit peak speckle reduction at an electric field amplitude above the maximum value of 20 V/µm that the apparatus employed in this study could deliver. Consequently, results from these mixtures are not presented in the subsequent sections of this chapter. Also, mixtures of E7 with the chiral dopant BDH1281 for concentrations above 5.7 wt.% (pitch values below 244

nm) did not appear to mix properly and are therefore also omitted.

4.2.2 Speckle Contrast

In Figure 4.14 the minimum speckle contrast values measured for every mixture are presented as a function of pitch. The values shown are the average speckle contrast measured during the 5-minute steady state test at peak speckle reduction electric field conditions. It is clear from this data that shorter pitches are most suitable for maximum speckle reduction, with all mixtures showing a reduction in minimum speckle contrast achievable with a reduction in pitch.

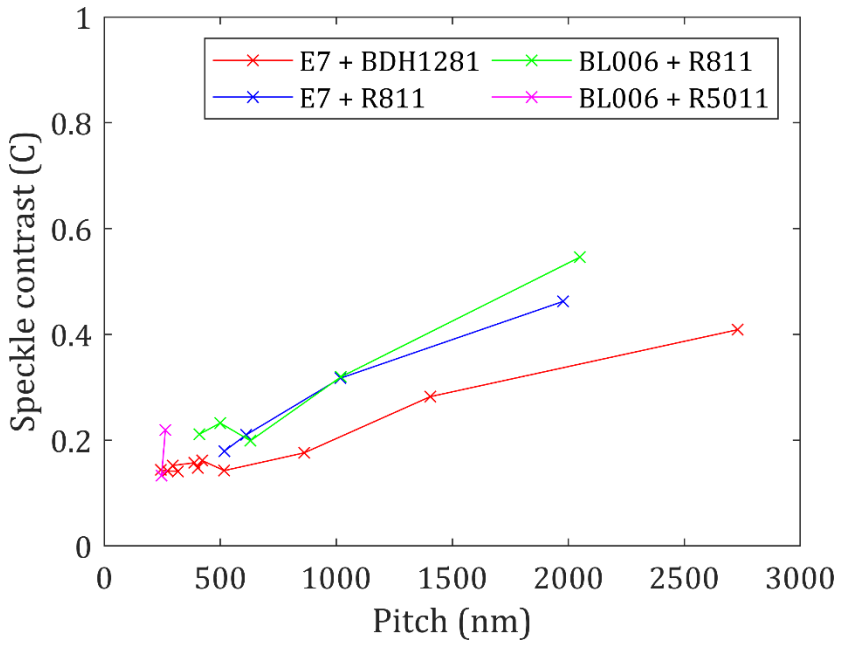

Figure 4.14: Plot of minimum speckle contrast for a range of mixtures with different pitch values. Each cell was 20 μm thick and the cell temperature throughout measurements was held at $T = 25°C$. Data points correspond to measured values and the lines are a linear interpolation to guide the eye.

As this is the first study on the use of DSM in chiral nematics for speckle reduction there is no directly relevant data to compare these findings to. However, literature on EHDI in chiral nematic mixtures can be used to identify two interesting points. The size of the stationary patterns that exist at lower electric field amplitudes has been shown to be of the order of the pitch of the mixture [65]. Therefore, one would

expect a mixture with a shorter pitch to exhibit more spatial variation of birefringence across the cell, which would lead to increased scattering. Also, mixtures with long pitches (> 4 μm) exhibit an electric field-induced fingerprint texture rather than the focal conic state [26] [66] , which will result in less scattering. This is consistent with the limited speckle reduction achieved for the long pitch mixtures considered in this study.

4.2.3 Transmission

In Figure 4.15 transmission data for the same set of mixtures is presented as a function of pitch. In this case the transmission percentage is calculated as a ratio of light intensity at the projection screen in comparison to that which is present without a LC cell in place. The values shown are the average transmission measured over the 5-minute steady state test at peak speckle reduction electric field conditions.

From this plot one can see that initially the transmission reduces with a reduction in pitch. Each mixture reaches a minimum transmission at a pitch between 0.5 – 1 μm and at shorter pitches the transmission appears to improve, in some cases by more than a factor of two, from the minimum value. The point of minimum transmission does not coincide with a band-gap that overlaps with the laser source wavelength for any mixture tested.

The same reasoning applied to speckle reduction can be applied to the transmission behaviour at long pitches. However, the existence of a transmission minima that varies depending on the mixture is more difficult to explain. When considering using a LC cell for speckle reduction in imaging, maximum transmission would be highly desirable while retaining minimum speckle contrast. As a result,

pitch values below this transmission minimum are very appealing, and chiral dopants with a higher HTP should be considered for future studies in order to obtain very short pitch mixtures.

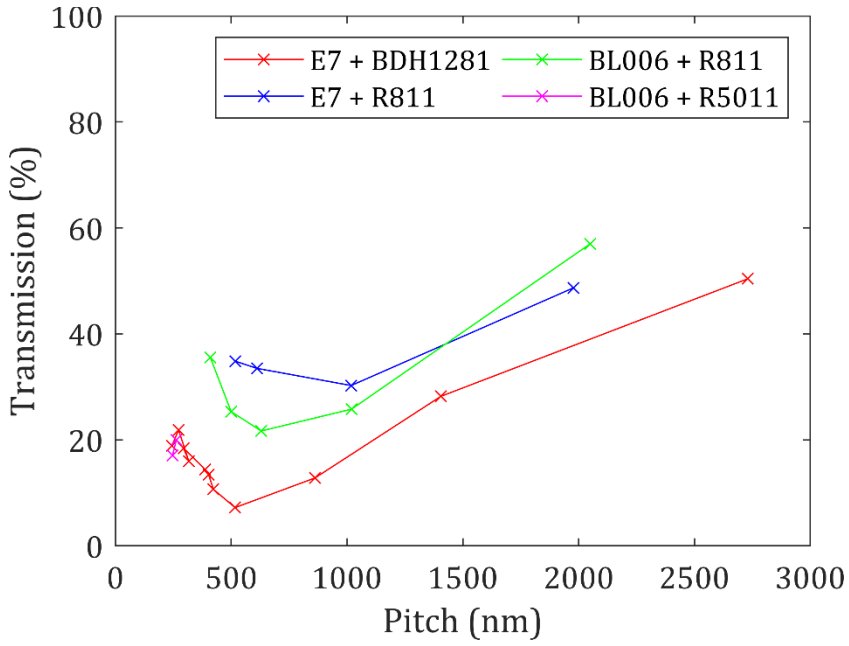

Figure 4.15: Plot of the transmission when minimum speckle contrast is achieved for a range of mixtures with different pitch values. Each cell was 20 μm thick and the cell temperature throughout measurements was $T = 25°C$. Data points are measured values and the lines are a linear interpolation to guide the eye.

4.2.4 Electric Field Amplitude

In Figure 4.16 the electric field amplitude at which each mixture exhibits maximum speckle reduction is presented as a function of the pitch of the chiral nematic LC. The peak electric field amplitude is obtained from the high-resolution scan of the electric field parameters (i.e. amplitude and frequency). It is important that this performance is consistent, therefore, every cell was subjected to a 5-minute steady-state test under peak speckle reduction conditions.

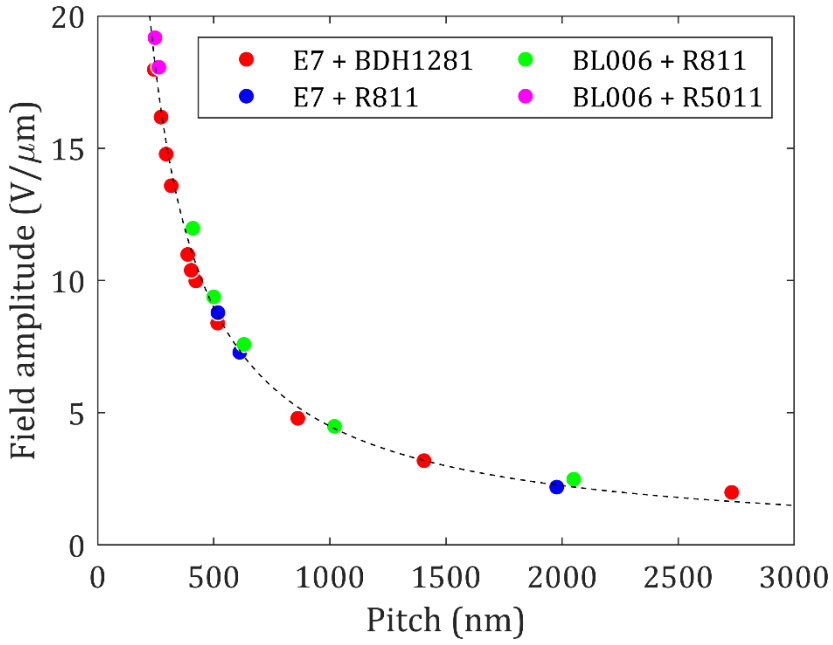

Figure 4.16: Plot of the electric field amplitude at minimum speckle contrast (maximum speckle reduction) for four different chiral nematic LC mixtures covering a range of pitch values. Each cell was 20 μm-thick and the cell temperature throughout the measurements was held at $T = 25°C$. Data points are measured values and the dashed black line is a fit of the form ax^{-1}.

From the data presented in Figure 4.16 it is clear that there is an inverse relationship between the pitch of the chiral nematic LC mixture and the electric field amplitude required for maximum speckle reduction. At short pitches, the electric field amplitude required becomes quite large and any small decrease in the pitch requires a large increase in the electric field amplitude. Indeed, the two mixtures with the shortest pitch values that were tested (BL006 with R5011: $p = 224$ and $p = 230$ nm, respectively) were found to exhibit a peak speckle reduction at electric field amplitudes above $E = 20$ V/μm, which is the maximum value that the equipment could deliver and are thus omitted from these results.

Once again, it is difficult to compare the experimental observations relating the pitch and electric field amplitude to theory as very little information is available in the literature that is dedicated to the theoretical treatment of such systems. Indeed, there appears to be no reports on the electric field required to produce

maximum scattering, with studies instead focused on characterising the threshold fields for EHDIs in chiral nematic LCs.

Helfrich [39] was the first to develop a theoretical basis for the understanding of EHDI in chiral nematic LCs, which was later extended by Hurault [67]. The theory predicts an inverse relationship between the threshold field required to generate EHDI and the square root of the pitch, and this relationship was demonstrated experimentally in a number of subsequent papers [67] [63]. In the case of maximum speckle reduction, the required electric field is considerably larger than this threshold field. In fact, when you consider the speckle contrast maps for each mixture it is clear that the field required for maximum speckle reduction is always just below the threshold field required for the chiral nematic-nematic phase transition. The relationship between the threshold unwinding field and the pitch is $E \propto p^{-1}$ (equation 2.9), which is the same as the relationship shown in Figure 4.16. Also, the threshold field required for a long pitch chiral nematic LC with a positive dielectric anisotropy to realign in a fingerprint texture is reported to be [66] $E \propto p^{-1}$. As discussed previously, long pitch mixtures realign in the fingerprint texture at electric field amplitudes that are smaller than that observed for short pitch mixtures, which instead collapse into the focal conic texture. Consequently, it is believed that the inverse relationship observed between the pitch and the electric field amplitude for maximum speckle reduction is consistent with the most relevant theory presented in the literature.

4.2.5 Frequency of the applied electric field

In Figure 4.17 the frequency for which each mixture exhibits peak speckle reduction is presented as a function of the pitch of the chiral nematic LC. The peak frequency

is obtained in the same way as that described in Section 4.2.4. The electric field conditions required for maximum speckle reduction are determined from the high-resolution electric field parameter scan and these conditions are tested in the 5-minute steady state test to ensure performance is consistent.

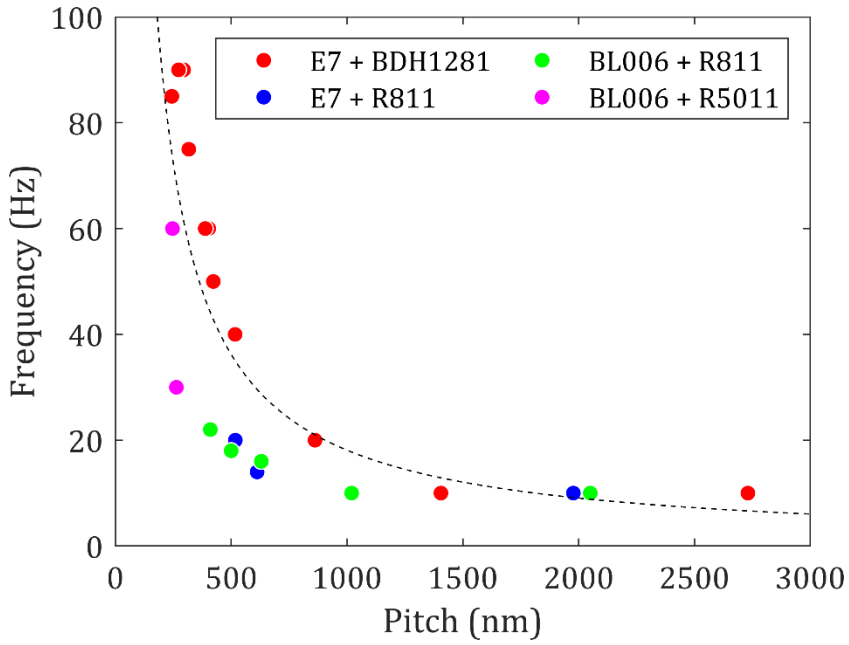

Figure 4.17: Plot of the square-wave frequency of the applied electric field at minimum speckle contrast for a range of mixtures with a range of pitch values. Each cell was 20 μm-thick and the cell temperature throughout measurements was $T = 25°C$. Data points are measured values and the dashed black line is a fit of the form ax^{-1}.

In this plot, it is shown that frequency for maximum speckle reduction is approximately inversely proportional to the pitch. The data points show more variation about the line of best fit than observed in Figure 4.16; however, this could be in part due to the lower resolution increments of 5 Hz between frequency measurements compared to the resolution of 0.2 V/µm used for the electric field amplitude during the high-resolution field parameter scan. Also, frequencies of the applied field below 10 Hz were not tested because at such low frequencies, DC effects from carrier injection can become significant, and this frequency is already below the video frame rate of 20 Hz, which can result in the video frames suffering

from flashing.

Once again there is little information provided in the literature for a direct comparison with this experimental data, however, in the work of Hurault a relaxation frequency, ω, for positive dielectric anisotropy chiral nematic LCs is provided, which follows the form [67]:

$$\omega = \bar{K}\frac{\pi}{d}\frac{2\pi}{p}\frac{1}{\gamma} \tag{4.2}$$

where $\bar{K}$ is the average value of the Frank elastic constants, d is the cell thickness, p is the pitch and γ is the rotational viscosity coefficient. With typical values for E7 of $\bar{K} = 14e^{-12}$ N and $\gamma = 0.15$ Pa. s inserted, along with $d = 20$ μm and $p = 0.5$ μm, a relaxation frequency of $f \approx 50$ Hz is obtained. This value is remarkably close to the frequency recorded for peak speckle reduction of a chiral nematic LC mixture consisting of E7 and BDH1281 with a pitch of $p = 500$ nm, which was found to be $f = 40$ Hz. Further, equation 4.2 follows the same inverse proportionality between frequency and pitch as was shown in Figure 4.17.

4.2.6 Summary

It is clear from the data presented in Section 4.2 that short pitch chiral nematic LCs are most suitable for maximum speckle reduction. Even though the transmission through the device, collected over a narrow solid angle, initially reduces with a reduction in pitch, each mixture reaches a minimum transmission for pitch values between $0.5 - 1$ μm and at shorter pitch values the transmission appears to improve; in some cases, by more than a factor of two from the minimum value. There is clearly a strong dependence between the field conditions, such as the electric field amplitude and the applied frequency, and the pitch of the chiral nematic helix. At

shorter pitch values the field amplitude required for maximum reduction in the speckle contrast tends to larger values, as do the required frequencies.

The device that was found to give the largest reduction in the speckle contrast in this study was the nematic LC, E7, doped with the high twisting power chiral dopant BDH1281 (4.7 wt.%, $p = 317$ nm at $T = 25$°C). Specifically, this device was found to be capable of reducing the speckle contrast to $C = 0.141$ at $E = 13.6$ V/μm and $f = 75$ Hz: a reduction of 77% from $C = 0.625$. The corresponding transmission through the device at these field conditions was found to be 16.0%. The same host nematic mixture, E7, dispersed with a larger concentration of chiral dopant, leading to a shorter pitch (5.1 wt.%, $p = 273$ nm) was found to reduce the speckle contrast to almost the same level ($C = 0.142$) but with an improved transmission of 21.9%.

4.3 The role of birefringence of the nematic host

In this section, the influence of the birefringence of the nematic LC host on the speckle contrast ratio C is considered. For this work, two separate studies were carried out. In the first study, three different nematic LC mixtures are compared with a range of birefringence values (low, medium, and high), each one mixed with the high twisting power chiral dopant, BDH1281, to form a chiral nematic phase. The mixtures were prepared so that they had the same pitch (425 nm $\pm$ 5 nm) at $T = 25$°C because it has already been shown that the speckle contrast, C, can vary significantly with pitch.

In the second study presented in this section, mixtures of nematics E7 and BL006 with the low-power chiral dopant R811 are compared. This is a comparison

of two moderately birefringent materials, with $\Delta n_{BL006} > \Delta n_{E7}$. Mixtures from each nematic host are compared over a range of pitch values.

4.3.1 Variation in birefringence for a fixed pitch

In this experiment, three mixtures were prepared with the following nematic host LCs: E7, MDA-02-2419 and MLC-15900-100. Each mixture was obtained from Merck Ltd and used without further purification. To form a chiral nematic phase at room temperature, the high twisting power chiral dopant BDH1281 (3.0 wt.%) was dispersed into each mixture. According to the literature, the birefringence of these mixtures range from $\Delta n = 0.091$ to $\Delta n = 0.223$ at $\lambda = 589.8$ nm and $T = 20$°C, as shown in Table 4.2. Each mixture was capillary filled into 20 µm INSTEC cells at 70°C and cooled to room temperature. A polarising optical microscope was used to confirm the existence of a chiral nematic phase with a right-handed helical structure with the helix axis parallel to the surface normal. The pitch of all three mixtures was determined using UV-Vis spectroscopy as described in Section 3.2 and was found to be 425 nm $\pm$ 5 nm.

Subsequently, each cell was subjected to a low-resolution (large increments in the amplitude and frequency) sweep of the electric field parameters as described in Section 4.1. The speckle contrast results from the low-resolution tests are shown in Figure 4.18 in the form of a colourmap for each mixture. As before, the red sections represent little-to-no speckle reduction while dark blue regions represent high-levels of speckle reduction.

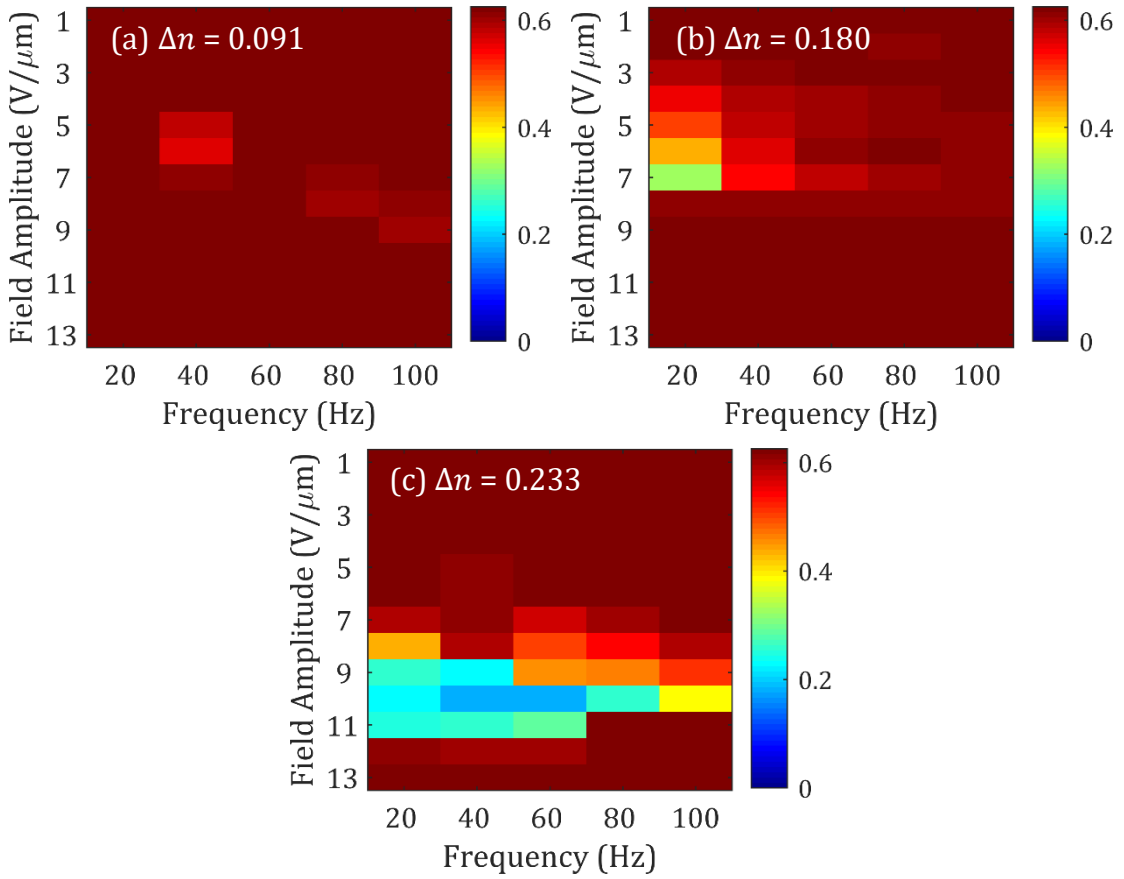

Figure 4.18: Colour maps of the speckle contrast for a range of applied electric field conditions; electric field amplitude from 1 − 13 V/μm in increments of 1V/μm and square-wave frequency from 20 − 100 Hz in increments of 20 Hz. The devices tested were all 20 μm-thick planar aligned glass cells, the details of which are described in Chapter 3, chiral nematic liquid crystal cells containing the nematic host, (a) MLC-15900-100 (b) MDA-02-2419 (c) E7, dispersed with 3.0 wt.% chiral dopant (BDH1281). The cell temperature during measurements was held at T = 25°C.

	MLC-15900-100	**MDA-02-2419**	**E7**
Δn	0.091	0.180	0.233
$\Delta \varepsilon$	10.1	38.5	13.7
γ (mP. s)	unknown	500 (22°C)	224 (20°C)
V/μm	6	7	10
Hz	40	20	50
C	0.566	0.327	0.161
Transmission	47%	21%	11%

Table 4.2: Birefringence (Δn) of the nematic hosts MLC-15900-100 [68], MDA-02-2419 [69] and E7 [70], measured at λ = 589.8 nm and 20°C, dielectric anisotropy measured at 1 kHz and 20°C and viscosity γ (mP.s) measured at given temperatures for comparison [71] [72]. Also shown is the electric field amplitude and square-wave frequency for peak speckle reduction for each mixture, along with the speckle contrast and transmission under these conditions.

The birefringence of each nematic host LC is shown in Table 4.2 alongside the electric field conditions required for peak speckle reduction. The colourmaps show that MLC-15900-100, which has a very small birefringence of $\Delta n = 0.091$, exhibits very little speckle reduction across the field parameter space tested. An increase in birefringence appears to lead to an increase in the speckle reduction and a decrease in the transmission through the device collected over a narrow solid angle. Also, in this case, the electric field amplitude required increases with the birefringence. This suggests that, for maximum speckle reduction, a nematic host with a high birefringence is preferred, albeit it at the cost of lower transmission through the device. These results are consistent with the simulations that are presented later in the thesis in Chapter 8, Section 8.3.

As shown in Table 3.2, the birefringence is not the only parameter that changes across these mixtures as there is a wide variation in other material parameters that could also potentially influence the speckle contrast (such as the dielectric anisotropy or viscosity), which should be taken into account when considering these results. However, of all the parameters listed in Table 4.2, only the birefringence varies in a concomitant way with the speckle contrast under peak speckle reduction field conditions.

4.3.2 Birefringence comparison for a range of pitch values

In this experiment, two mixtures with different birefringence values are compared across a range of pitch values. Five mixtures were prepared consisting of the nematic host, BL006 at various concentrations of the low twisting power chiral dopant, R811. The concentration of R811 was varied from 4.9 – 25.0 wt.% to produce mixtures with a wide range of pitch values. Another four mixtures were

then prepared with varying concentrations of the nematic E7 with the low twisting power chiral dopant R811. The concentration of R811 in these mixtures varied from 5.1 – 19.9 wt.% resulting in a similarly wide range of pitch values to the mixtures with BL006 for comparison. E7 has the lower birefringence of the two nematic hosts as shown in Table 4.3.

	BL006	**E7**
$\boldsymbol{\Delta n}$	0.274	0.212
$\boldsymbol{\Delta \varepsilon}$	15.3	13.7
$\boldsymbol{\gamma}$ $(\mathbf{mP.s})$	426	224

Table 4.3: Birefringence (Δn) measured at 623.8 nm and 25°C, dielectric anisotropy ($\Delta \varepsilon$) measured at 1 kHz and 20°C and rotational viscosity coefficient (γ) measured at 20°C of nematic hosts BL006 and E7, for comparison [70] [73].

At room temperature, all mixtures were found to exhibit a chiral nematic phase with a right-handed helical structure. The pitch of each mixture was determined using the method described in Section 3.2 and the results for the speckle contrast as a function of the pitch can be seen in Figure 4.19. The individual colourmaps are not shown for the sake of space. Instead, four graphs that show the salient details obtained from the experiment are presented.

Figure 4.19 is a plot of the minimum speckle contrast achieved for each mixture as a function of pitch. The peak speckle reduction is similar for the two nematic hosts, with minimum speckle contrast obtained at comparable pitch values, with a variation in speckle contrast of less than 0.08. Both mixtures exhibit the lowest speckle contrast at short pitch values of around 500 nm.

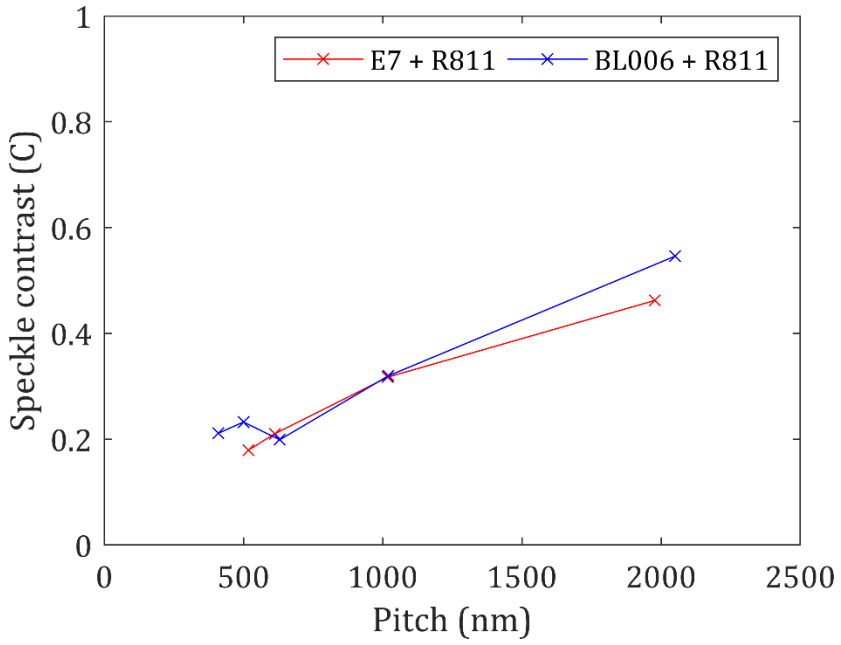

Figure 4.19: Plot of the minimum speckle contrast as a function of the pitch for two different nematic-chiral dopant combinations. Mixtures with the nematic host, E7, are plotted in red whereas mixtures with BL006 are plotted in blue. Each cell was 20 μm thick and the cell temperature throughout measurements was held at $T = 25°C$. Data points are measured values and the lines are a linear interpolation to guide the eye.

Figure 4.20 is a plot of the optical transmission for each mixture at the maximum reduction in the speckle contrast as a function of the pitch. It is found that the transmission through the device is lower for the mixtures with a larger birefringence, with the transmission dropping as low as 21.7% in the cell with a 630 nm pitch. The lowest transmission observed with the E7-based mixtures is 30.3% at $p = 1018$ nm. These results are consistent with those presented in Section 4.3.1, and are in good agreement with the simulation results presented in Chapter 7, Section 7.4.

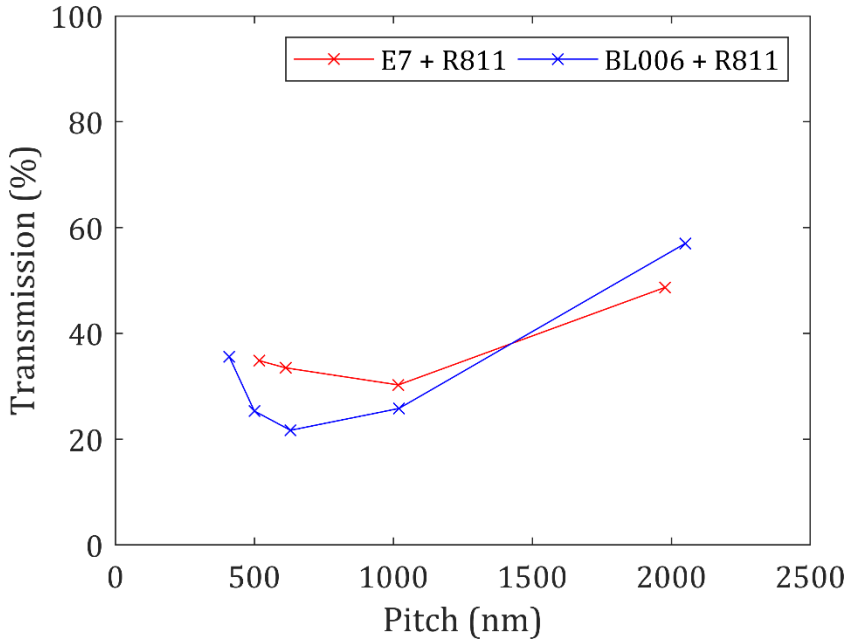

Figure 4.20: Plot of transmission at the maximum reduction in the speckle contrast as a function of the pitch for two different nematic-chiral dopant combinations. Mixtures with the nematic host E7 are plotted in red whereas mixtures with BL006 are plotted in blue. Each cell was 20 μmthick and the cell temperature throughout measurements was held at $T = 25°C$. Data points are measured values and the lines are a linear interpolation to guide the eye.

Figure 4.21 is a plot of the electric field amplitude and square wave frequency for maximum speckle reduction as a function of pitch. These results show little difference in the field conditions required for optimum speckle reduction between the mixtures. From this it is surmised that the electric field conditions are more strongly related to the pitch of the LC mixture than any other physical property. Once again, as in Section 4.2 an inverse relationship between the electric field conditions and pitch of the helix is seen.

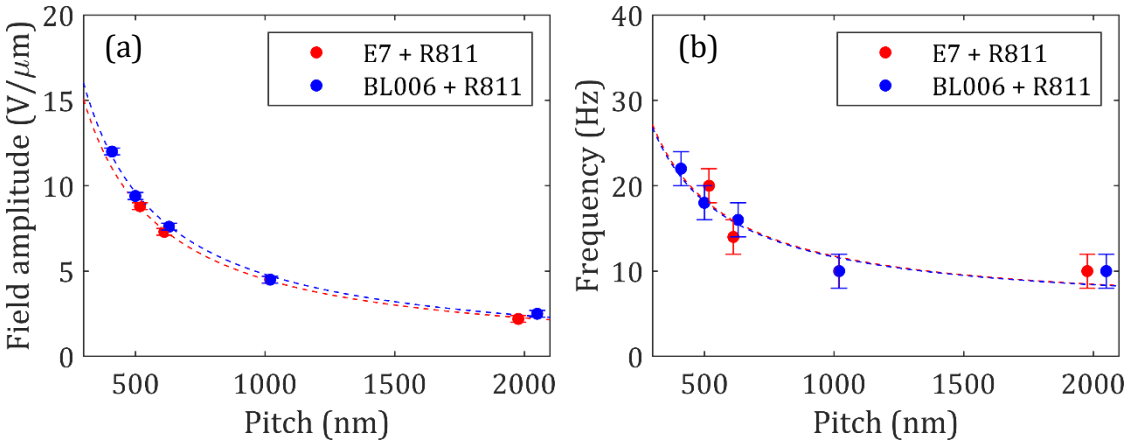

Figure 4.21: Plot of (a) the electric field amplitude and (b) the square wave frequency at peak speckle reduction as a function of the pitch for two different nematic-chiral dopant combinations. Mixtures with the nematic host, E7, are plotted in red whereas mixtures with the nematic host, BL006, are plotted in blue. Each cell was 20 μm -thick and the cell temperature throughout measurements was held at $T = 25°C$. Data points are measured values and the lines are a linear interpolation to guide the eye.

4.3.3 Summary

It is difficult to draw unequivocal comparisons for nematic LCs with different birefringence values because this parameter is not the only material property that varies between each mixture. However, across all mixtures presented in this section, the transmission through the device was shown to be lower in mixtures with higher birefringence values. Furthermore, the minimum speckle contrast was found to be reduced with an increase in the birefringence values for the mixtures presented in Section 4.3.1, but it was found to be very similar between the two mixtures in Section 4.3.2. It is possible that speckle reduction due to increased birefringence reaches a maximum for $\Delta n \approx 0.2$ and above.

4.4 Concluding Remarks

In this chapter, it has been shown that under the correct applied electric field conditions, a device filled with a chiral nematic LC exhibits dynamic scattering that can be used to reduce the speckle contrast ratio, C, of incident coherent laser light.

It has been shown that the frequency and amplitude of the applied electric field required for maximum speckle reduction are inversely proportional to the pitch of the nematic LC host. While there are no direct comparisons to make with the literature in terms of comparable experiments or underlying theoretical analysis, these findings have been considered in the context of theory that has been developed for EHDI in nematic and chiral nematic LCs with negative dielectric anisotropies, which appears to support the findings at least qualitatively. In general, short pitch chiral nematic LCs appear to be best suited for speckle reduction, with pitch values below 1 μm being capable of reducing the speckle contrast to at least $C = 0.2$ across a range of mixtures. It is also found that the transmission through the device appears to decrease with pitch down to a minimum value before increasing with a further decrease in the pitch. The pitch corresponding to the minimum transmission is found to depend on the exact mixture composition. Consequently, there is a trade-off between the requirements for a low electric field amplitude, low speckle contrast and good transmission at low pitch values.

In section 4.3, it was shown that an increase in birefringence tends to reduce the transmission and the speckle contrast. However, further study with a larger range of material parameters is required to determine the precise structure-property relationship, and it is difficult to compare directly the birefringence values between mixtures as other material properties tend to vary significantly as well. However, these results serve as a useful guide and design motif and, importantly, are consistent with the simulations that are presented later in the thesis in Chapter 7, Section 7.4. In the next chapter, the impact of doping the chiral nematic mixtures with ionic compounds on the resulting speckle reduction is considered.

5 Ionic Doping and Device Lifetime

In the previous chapter, a proof-of-concept device has been presented that uses the dynamic scattering state of a thin liquid crystal (LC) film to reduce the speckle contrast of an incident laser beam. Applying a low frequency ($f < 100$ Hz) square wave electric field to a chiral nematic LC with positive dielectric anisotropy induces electrohydrodynamic instabilities (EHDI) due to the ionic impurities present in the mixture. After having demonstrated the proof-of-principle, it was then shown that chiral nematic LC mixtures with a short pitch ($p \approx 250$ nm) are preferred for maximum speckle reduction, and that the electric field amplitude and frequency required for peak performance in terms of speckle reduction are inversely proportional to the pitch. It was also shown that an increase in the birefringence of the nematic LC host typically results in a reduction in the transmission as defined in Section 4.2.3 of Chapter 4.

In this chapter, the effect of increasing the ionic conductivity of the mixture on the resulting reduction in the speckle contrast is considered; this is achieved through the addition of an ionic dopant. Ionic compounds have long been used to facilitate or improve dynamic scattering in LCs because the disruptive transport of ions, which result from the application of an electric field, is necessary to generate EHDI [40] [74] [75] [76] [77]. Ionic dopants serve to increase mixture conductivity and have subsequently been shown to lead to stronger light scattering [78]. To first approximation, the conductivity of an isotropic liquid is determined by the ionic

charge, the ionic concentration, and the mobility. In this chapter, an ionic dopant is dispersed into the host LC mixture, which effectively increases both the ionic charge and the concentration thereof. In turn, this serves to reduce the threshold field required for EHDI. The dopant used exclusively throughout this study was the compound cetyltrimethylammonium bromide (CTAB), an ionic material that is commonly added to smectic A LCs to facilitate electrically-induced dynamic scattering [40] [79] [80] [81].

In the following sections, the performance of a mixture of the nematic BL006 with the high-twisting power chiral dopant R5011 (Merck) is compared with and without the addition of 1.1 wt.% of CTAB. It is shown that the threshold for EHDI is significantly reduced but that the device lifetime is severely limited, especially when the device is exposed to large electric field amplitudes. Where possible, the potential origins of the electric field-induced cell deterioration are considered. Subsequently, the concentration of CTAB added to a LC mixture is varied and it is shown that a concentration of 0.2 wt.% is sufficient to reduce the threshold voltage (electric field), without significantly degrading the performance of the device. Finally, an in-depth study of cell performance, lifetime and hysteresis effects are conducted for a number of mixtures with and without 0.2 wt.% of CTAB.

5.1 Mixture Preparation

In total, 30 mixtures were prepared for this study. The mixture concentrations and corresponding pitch values are summarised in Table 5.1. The pitch of each mixture (without CTAB) was determined using the relevant experimental procedure described in Section 3.2. Mixtures with photonic bandgaps outside the detection range of the UV-Vis spectrometer were estimated by extrapolation of the line of best

fit taken from the other concentrations of the mixture in question, as shown in Figure 4.13. Once each mixture was characterised, a portion of the mixture was dispensed into separate vials and the required amount of CTAB was then added.

Nematic	Chiral Dopant	wt.%	Pitch (nm)	CTAB (wt.%)
BL006	R5011	unknown	230 - 267	1.1
E7	BDH1281	4.6	295	0.2 - 1.1
E7	R811	5.1 – 25.4	518 – 1980	0.2
BL006	R811	4.9 – 25.4	410 – 2050	0.2

Table 5.1: Components and corresponding concentrations for the 30 mixtures used in this study, along with the pitch at a temperature of 25°C. The weight percentage of the BL006 and R5011 mixture was unknown as it was received already dispersed from Merck.

5.2 Initial device characterisation

5.2.1 Chemical degradation

In the first study, three different mixtures of BL006 with the high twisting power chiral dopant, R5011, were tested for pitch values ranging from 230 - 267 nm. For each mixture, two cells were prepared: one with and one without 1.1 wt.% of CTAB added. After the pitch had been determined, each cell was subjected to a low-resolution electric field parameter sweep of 1 – 20 V/μm and 20 – 100 Hz. All three cells with CTAB were observed to undergo an irreversible change that prevents the cells exhibiting turbulence and therefore speckle reduction when subjected to electric field amplitudes above 12 V/μm for a prolonged period. These cells were observed to turn a shade of yellow-brown, often with large gas bubbles present, as shown in Figure 5.1.

It is believed that at high electric field amplitudes the bromide ions present

in the CTAB compound undergo an electro-chemical reaction at the electrode to form molecules of bromine gas (Br_2), while also forming other unknown non-ionic molecules. It should be stressed that the formation of these molecules has not been confirmed directly through chemical analysis, but the hypothesis is consistent with observations of browning, because bromine is brown in colour, and the reduction in turbulence as a result of ionic purification. This process has been noted previously both with CTAB doping [79] [81] [82], and in other LC mixtures consisting of ionic dopants [74] [83] [84] [85].

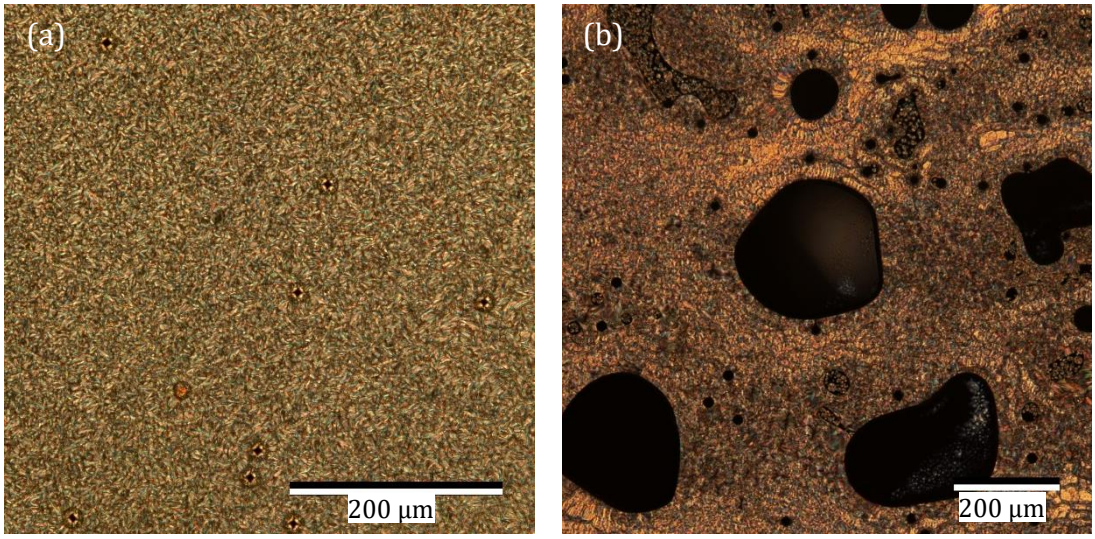

Figure 5.1: Microscope image of a 20 μm-thick, chiral nematic liquid crystal glass cell between crossed polarisers. The cell contained the nematic host, BL006, dispersed with chiral dopant (R5011) with a pitch of 247 nm at a temperature of T = 25°C. (a) Before to the application of an electric field, 20 × magnification, (b) After the application of an electric field of $E > 12\ V/\mu m$, 10 × magnification. Images were taken when the cell was held at a temperature of T = 25°C. The scale bars depict a lengthscale of 200 μm.

5.2.1 Speckle reduction comparison

After the change in colour and appearance of gas bubbles was confirmed to have occurred in all three cells, new cells were then prepared. The low-resolution electric field sweep was repeated for each cell, but with an electric field amplitude limited to the range 1 – 12 V/µm for the cells containing CTAB. Figure 5.2 shows the

resulting colourmaps for each mixture (230 nm, 247 nm and 267 nm pitch) with and without CTAB. The grey region in colourmaps for the CTAB-doped samples represents field conditions above 12 V/μm that were not probed.

For cells without CTAB, turbulence is generally only observed at high electric field amplitudes and low applied frequencies. The 'active range' of electric field conditions for speckle reduction is therefore relatively small. In contrast, LC cells with the ionic dopant, CTAB, have a larger active region over which the speckle contrast is reduced, extending to much smaller electric field amplitudes and higher frequencies than that observed for non-CTAB doped devices. In these experiments, speckle reduction is seen to occur in CTAB cells at a frequency of up to 500 Hz without a reduction in the device performance. Meanwhile, the threshold field amplitude for EHDI, which was determined to be the lowest electric field amplitude at which the speckle contrast is reduced, decreases from 16.5 V/μm to 6 V/μm for the cell with a 230 nm pitch. Qualitatively, this reduction in electric field amplitude is consistent with an increase in conductivity of the mixture in the context of theoretical studies on EHDI in LC materials [39].

As the electric field amplitude is limited to only $E = 12$ V/μm, the speckle contrast is unable to drop to the low values that are obtained at the higher field amplitudes with the non-CTAB cells. For example, the device with a pitch of $p = 247$ nm achieves a minimum speckle contrast of $C = 0.133 \pm 0.002$ at $E = 19.2$ V/μm and $f = 60$ Hz. However, the same chiral nematic mixture doped with CTAB was found to give a larger value of the speckle contrast of $C = 0.230 \pm 0.001$ at $E = 12.0$ V/μm and $f = 350$ Hz, which is the maximum field strength that can be reliably applied to the device without there being any degradation.

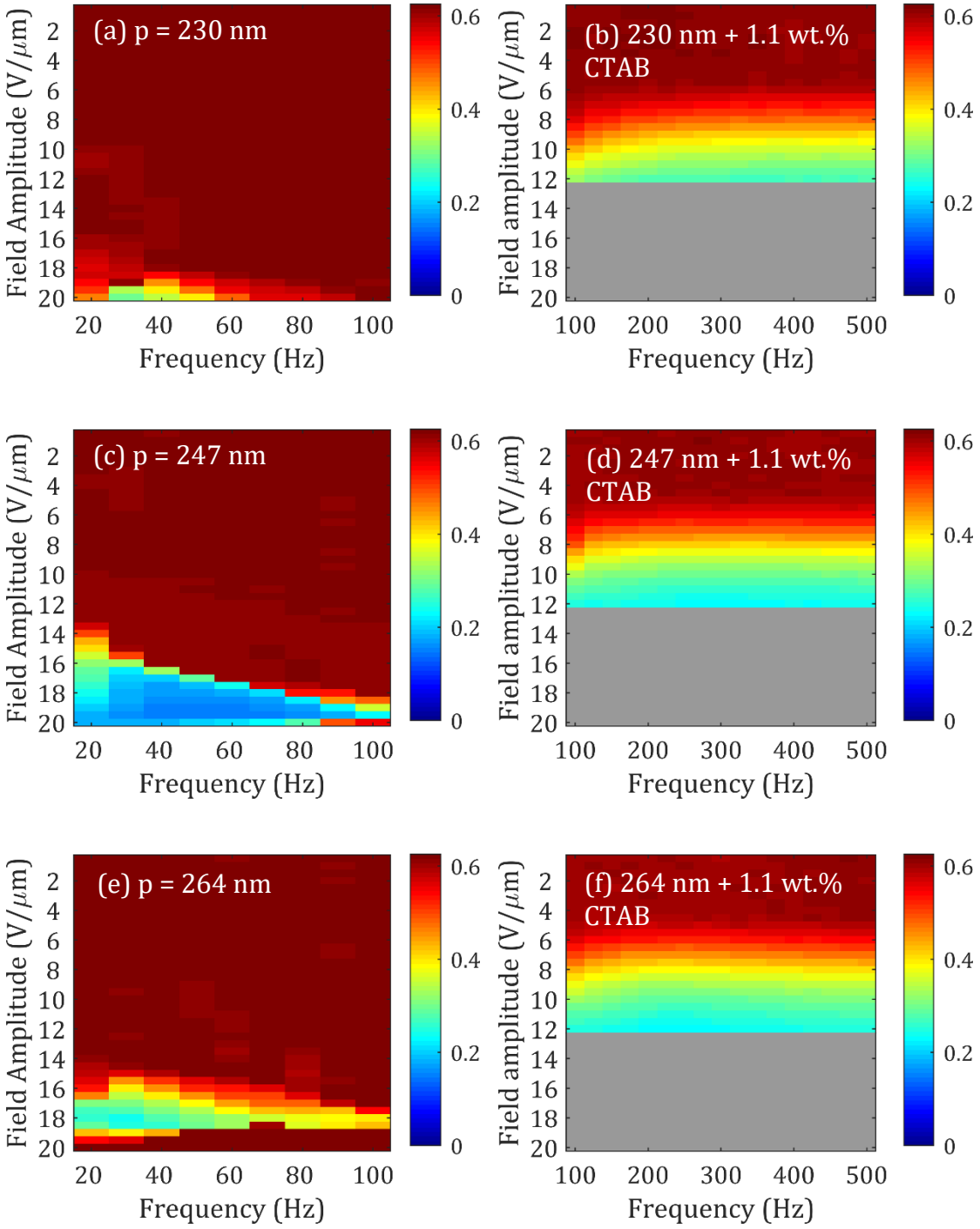

Figure 5.2: Speckle contrast maps (colour code is provided on the right-hand side of each plot) for a range of LC cells under different applied electric field conditions. The devices tested were 20 μm-thick, chiral nematic LC glass cells containing the nematic host, BL006, dispersed with chiral dopant (R5011) at different concentrations to produce a pitch of (a) 230 nm (b) 230 nm + 1.1 wt.% CTAB (c) 247 nm (d) 247 nm + 1.1 wt.% CTAB (e) 264 nm (f) 264 nm + 1.1 wt.% CTAB. The cell temperature throughout measurements was held at T = 25°C.

5.3 CTAB concentration

5.3.1 Speckle reduction comparison

Thus far, it has been shown that the addition of 1.1 wt.% of CTAB decreases the threshold voltage required for speckle reduction to occur, which is desirable. However, the downside is that it severely reduces the lifetime of the device when it is subjected to large electric field amplitudes (in this case above 12 V/μm). In the next study, the influence of the concentration of CTAB in the host chiral nematic mixture on the electro-optic characteristics of the LC speckle reducer is considered. For this study, CTAB is added at various concentrations to a chiral nematic mixture consisting of E7 (Synthon) doped with 4.6 wt.% of the high-twisting power chiral dopant, BDH1281 (Merck). The performance of four different cells with concentrations of CTAB ranging from 0 wt.%, to 1.0 wt.% is compared. This chiral nematic host was chosen as it has a longer pitch of 295 nm, which results in a lower electric field amplitude of 15 V/μm for maximum speckle reduction. This lower electric field amplitude should allow a comparison of each mixture at peak performance without an immediate, irreversible degradation of the cell. Each cell is subjected to a low-resolution field parameter sweep. Figure 5.3 shows speckle contrast colourmaps for each cell. Due to the damage caused to cells as reported in Section 5.2, at higher voltages the CTAB cells were limited to a maximum field amplitude of 17 V/μm as the non-CTAB cell exhibit no speckle reduction at larger amplitudes.

The conditions for peak speckle reduction are presented in Table 5.2 for each cell. It is shown that 0.2 wt.% CTAB achieves a similar minimum speckle contrast, C, and transmission at $E = 15$ V/μm as that of the same mixture without CTAB.

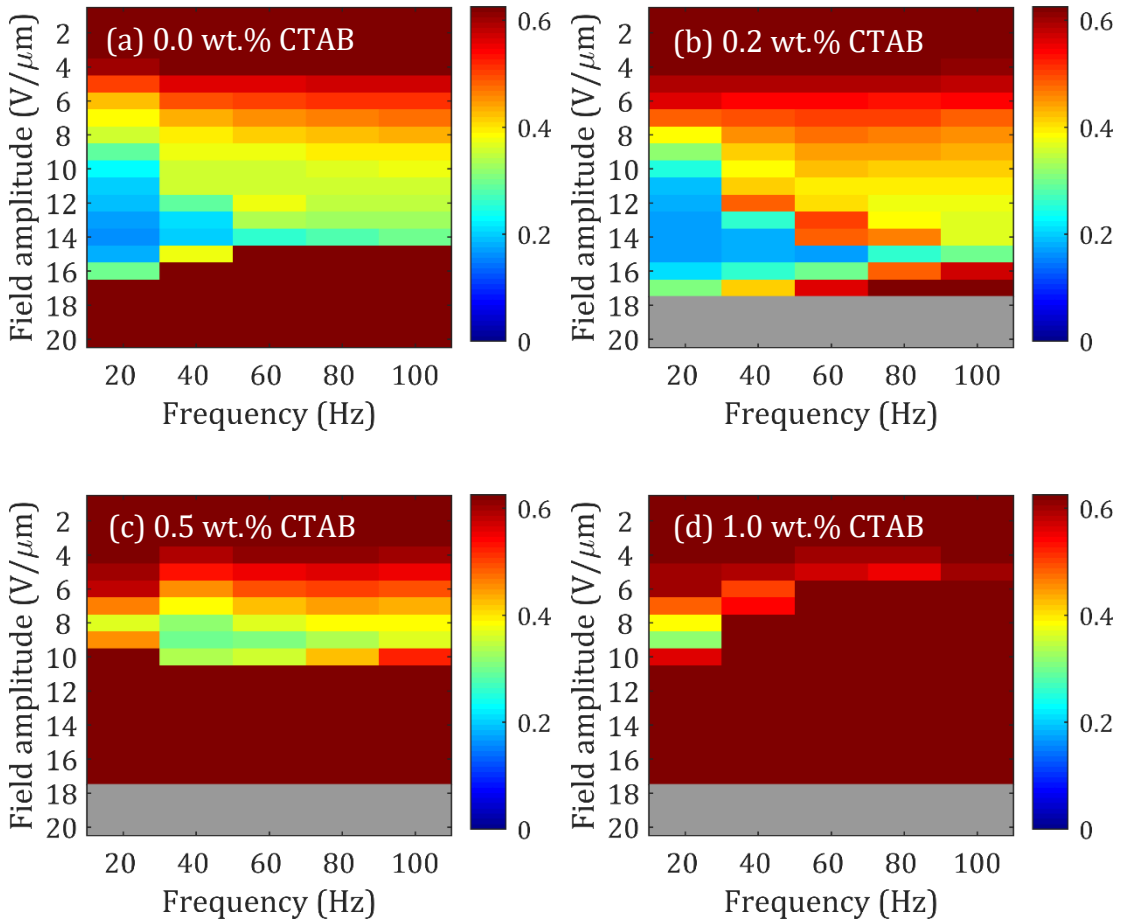

Figure 5.3: Speckle contrast maps for a range of applied electric field conditions. The cells tested were 20 μm-thick, chiral nematic LC cells containing the nematic host, E7, dispersed with 4.6 wt.% chiral dopant (BDH1281) to produce a pitch of (a) 295 nm (b) 295 nm + 0.2 wt.% CTAB (c) 295 nm + 0.5 wt.% (d) 295 nm + 1.0 wt.% CTAB. The cell temperature throughout measurements was held at T = 25°C.

However, maximum speckle reduction is found to occur at lower frequencies for the 0.2 wt.% CTAB cell. This could be because the parameter-sweep cycles through incremental voltages at the lowest frequency and then repeats at each subsequent higher frequency being tested. If the mixture has deteriorated slightly at the high voltages it is subjected to at 20 Hz, it would then limit the speckle reduction possible at higher frequencies. However, it has been reported that ionic movement due to CTAB dominates at lower frequencies [82].

CTAB concentration	0.0%	0.2%	0.5%	1.0%
Electric field (V/μm)	15	15	9	9
Frequency (Hz)	80	20	40	20
Speckle Contrast (C)	0.16	0.17	0.29	0.31
Transmission	18%	19%	11%	11%

Table 5.2: Peak speckle reduction results for four cells of E7 with BDH1281 (with a pitch of 295 nm) and varying amounts of CTAB.

As can be seen, the cells with higher concentrations of CTAB do not exhibit any speckle reduction above $E = 10$ V/μm, suggesting that these cells immediately suffer from the irreversible degradation at electric field amplitudes above this threshold. Further, the 1.0 wt.% CTAB cell is clearly affected the most at higher electric field amplitudes. The speckle reduction is significantly reduced and limited to lower amplitudes with each increment in frequency during the test. A potential chemical change of the CTAB dopant is identified both by eye and under an optical polarising microscope after the low-resolution test.

5.3.2 Low voltage hysteresis test: 0.2 wt.% CTAB

A new set of undamaged cells were then prepared and subjected to 10 consecutive low-resolution sweeps with a maximum electric field amplitude of 10 V/μm. The aim of this experiment was to understand whether a CTAB-doped device is damaged under constant cycling at lower electric field amplitudes. Figures 5.4(a)-(c) shows colourmaps for the first, fifth and tenth sweeps of the electric field conditions for the 0.2 wt.% CTAB cell. In addition, a plot of the speckle contrast recorded at the different driving field conditions as a function of the number of runs (low-resolution sweep of 1 – 10 V/μm and 20 – 100 Hz) is presented in Figure 5.4(d).

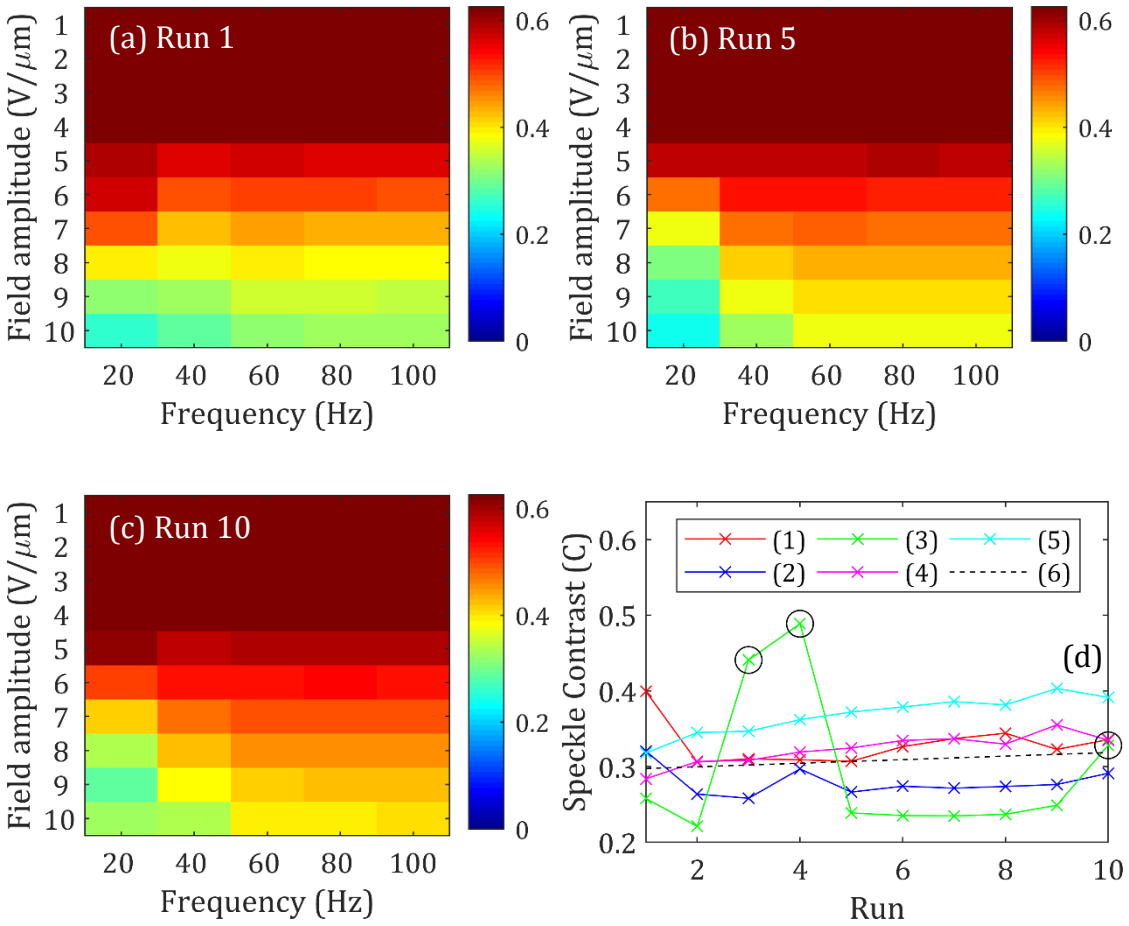

Figure 5.4: Speckle contrast maps for a range of applied electric field conditions. The cells tested were 20 μm-thick, chiral nematic LC cells containing the nematic host, E7, dispersed with chiral dopant (BDH1281) to produce a pitch of 295 nm, with 0.2 wt.% added CTAB. (a), (b) and (c) are speckle contrast maps taken from 10 consecutive runs, with runs 1, 5 and 10 shown here, respectively. (d) Plot of the speckle contrast, C, for five selected electric field conditions over 10 separate runs. (1) 8 V/µm, 20 Hz, (2) 9 V/µm, 20 Hz, (3) 10 V/µm, 20 Hz, (4) 10 V/µm, 40 Hz, (5) 10 V/µm, 60 Hz, (6) Dotted black line shows the average trend for all data. Circled data points represent measurements when it was assumed that a gas bubble was present within the electrode region. The cell temperature throughout measurements was held at T = 25°C.

It is seen that there is little variation between runs for the electric field conditions that provide the largest speckle reduction with this mixture, and the speckle contrast values are consistent with those measured in Section 5.3.1. The one exception is $E = 10$ V/µm, $f = 20$ Hz during runs 3 and 4; however, this is expected to be due to the presence of a small gas bubble moving through the active region of the cell and is confirmed by observing the speckle photographs taken for these readings. As shown in Figure 5.5, a bright spot is present in the centre of the images

taken during runs 3 and 4. Laser light incident on part of the cell with a gas bubble present will not be scattered thus causing a bright spot on the projection screen that greatly increases the measured speckle contrast value.

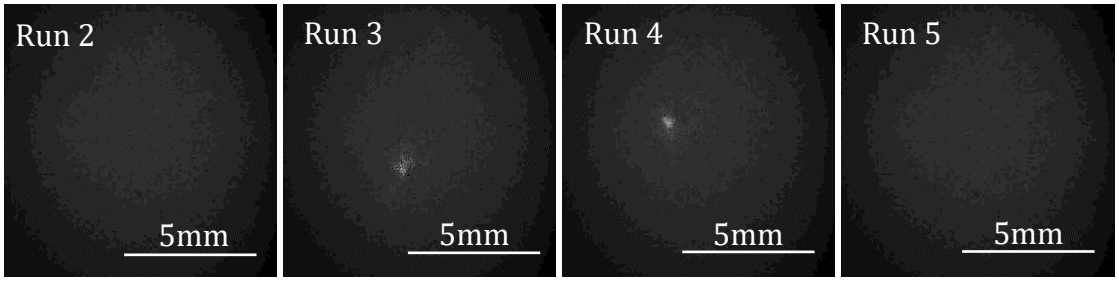

Figure 5.5: Photographs of the speckle pattern taken during runs 2-5 of the experiment shown in Figure 5.4 at 10 $V/\mu m$ and 20 Hz. Note the bright spots in runs 3 and 4 indicating the presence of a small gas bubble. Scale bars represent a distance of 5 mm at the projection screen.

Overall, the 0.2 wt.% CTAB cell shows very little hysteresis between subsequent runs. The average change in speckle contrast for the 5 chosen electric field conditions between runs is calculated to be $+0.002$, less than a 1% increase. This was calculated by fitting a line of best fit to each dataset, ignoring images with bubbles present, and finding the average gradient of all fits. Thus, it is shown that there is little hysteresis exhibited by this mixture when electric field amplitudes are limited to amplitudes below $E = 10$ V/μm.

5.3.3 Low voltage hysteresis test: 0.5 wt.% CTAB

The same test was conducted using a new cell of 0.5 wt.% CTAB and the results are presented in Figure 5.6. It is shown that the performance reduces slightly after the first 2 runs but then remains constant until the final three runs. During these runs, there is a large gas bubble growing in the centre of the cell which is confirmed by observing the speckle photographs and a microscope image of the cell taken after the 10 runs had been completed, as shown in Figure 5.7. The speckle photographs

shown represent the cell under peak speckle reduction conditions as well as the condition when no electric field was applied. The large bright spot is present in both photographs, unaffected by the change in the electric field conditions. Ignoring measurements with bubbles present, the average change in speckle contrast for the 5 chosen electric field conditions between runs is calculated to be +0.012. This represents approximately a 3% increase in speckle contrast between runs.

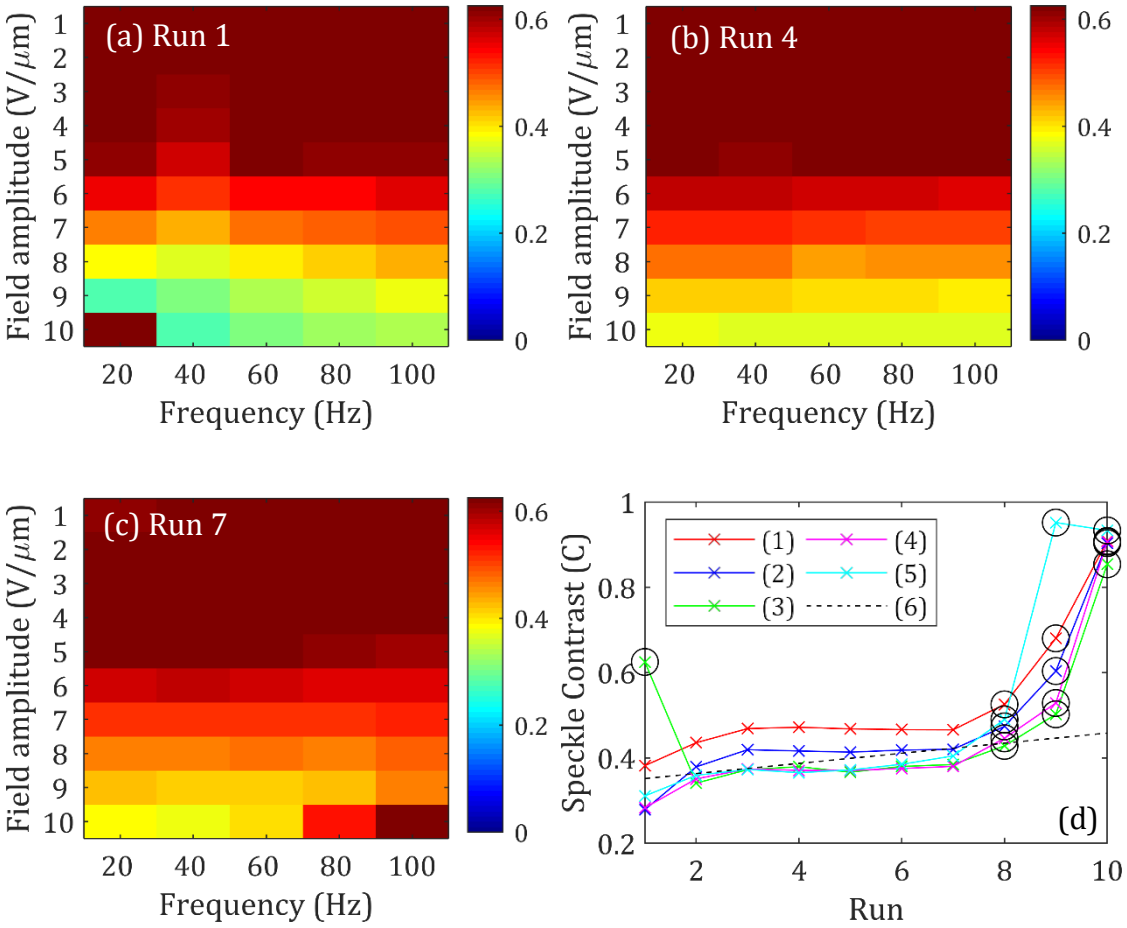

Figure 5.6: Speckle contrast maps for a range of applied electric field conditions. The cells tested were 20 μm-thick, chiral nematic LC cells containing the nematic host, E7, dispersed with chiral dopant (BDH1281) to produce a pitch of 295 nm, with 0.5 wt.% of CTAB. (a), (b) and (c) are speckle contrast maps taken from 10 consecutive runs, with runs 1, 4 and 7 shown, respectively. (d) Plot of speckle contrast under 5 selected electric field conditions from the 10 consecutive runs. (1) 8 V/µm, 20 Hz, (2) 9 V/µm, 20 Hz, (3) 10 V/µm, 20 Hz, (4) 10 V/µm, 40 Hz, (5) 10 V/µm, 60 Hz, (6) Dotted black line shows the average trend for all data. Circled data points represent the presence of a gas bubble in the active region. The cell temperature was held throughout measurements at T = 25°C.

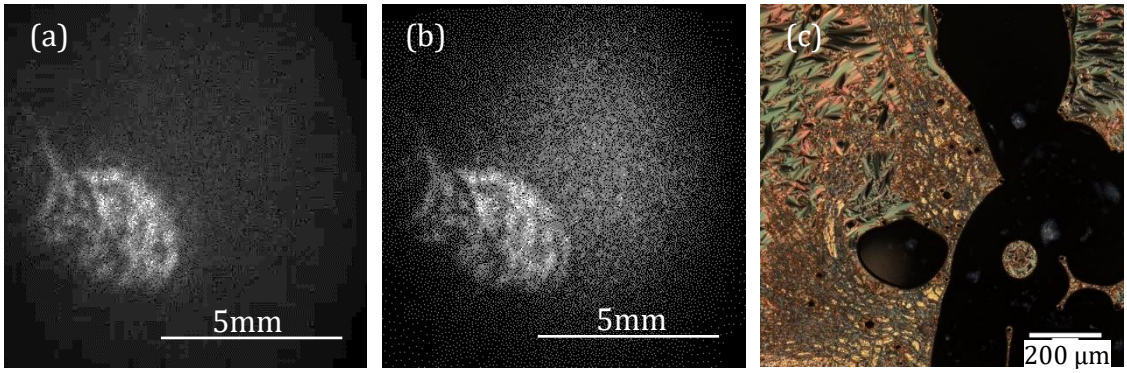

Figure 5.7: Speckle photographs taken during run 10 of the experiment shown in Figure 5.6 at (a) 9 $V/\mu m$ and 60 Hz and (b) 3 $V/\mu m$ and 80 Hz. Scale bars represent a distance of 5 mm at the projection screen. (c) Microscope image at 10 × magnification with crossed polarisers taken after 10 consecutive runs. The cell temperature was T = 25°C. The scale bar depicts a distance of 200 μm.

5.3.4 Low voltage hysteresis test: 1.0 wt.% CTAB

The same test was also conducted using a new cell of 1.0 wt.% CTAB and the results are presented in Figure 5.8. It is shown that performance reduces slightly during the first 2 runs but remains consistent after this until completion of the field parameter sweeps. The average change in speckle contrast, C, for the 5 chosen field conditions between runs is calculated to be $\Delta C = +0.008$. This represents approximately a 2% increase in speckle contrast between each run.

5.3.5 High voltage hysteresis and lifetime tests: all concentrations

Having tested for hysteresis in all three CTAB mixtures, it has been shown that each mixture suffers slightly from a deterioration of the speckle reduction between runs even when limiting the maximum electric field amplitude to $E = 10\ V/\mu m$. Also, two of the three mixtures suffered from the presence of gas bubbles in the active electrode region of the cell, limiting or removing the cell's ability to reduce speckle contrast. Further, after the hysteresis tests had been carried out, none of these cells could reduce the speckle contrast to a value of $C = 0.16$, which is the level attained using the non-CTAB-doped mixture, or even to the speckle contrast values that were

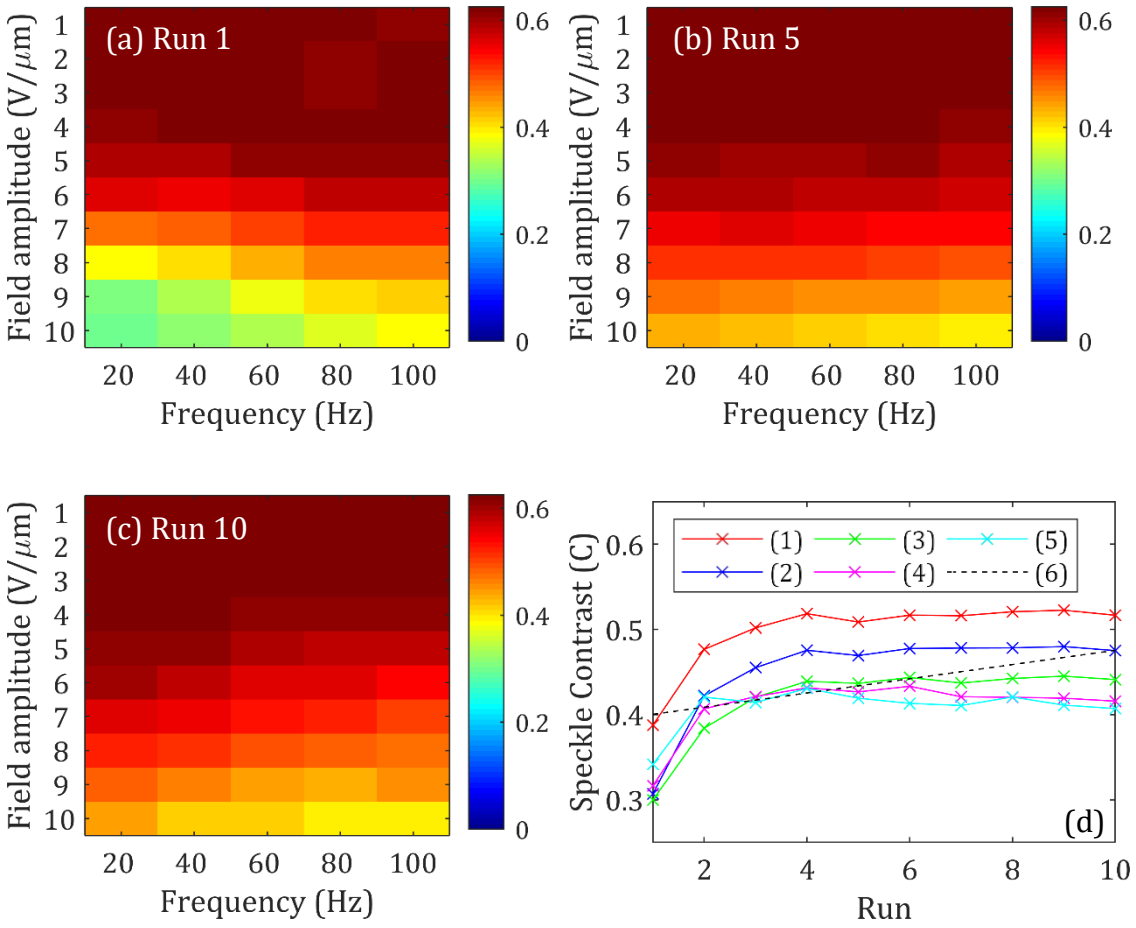

Figure 5.8: Speckle contrast maps for a range of applied electric field conditions. The cells tested were 20 μm-thick, chiral nematic LC cells containing the nematic host, E7, dispersed with chiral dopant (BDH1281) to produce a pitch of 295 nm, with 1.0 wt.% CTAB. (a), (b) and (c) are speckle contrast maps taken from 10 consecutive runs with runs 1, 5 and 10 shown, respectively. (d) Plot of speckle contrast under 5 selected field conditions during the 10 consecutive runs. (1) 8 V/μm, 20 Hz, (2) 9 V/μm, 20 Hz, (3) 10 V/μm, 20 Hz, (4) 10 V/μm, 40 Hz, (5) 10 V/μm, 60 Hz, (6) Dotted black line shows the average trend for all data. The cell temperature was held at T = 25°C throughout the measurements.

obtained during the initial tests with the CTAB-doped mixtures (summarised in Table 5.2). These findings are, in part, due to the limited electric field amplitudes that were employed to drive each cell. As a result, a third set of devices was prepared, and the hysteresis tests were repeated with a new maximum electric field amplitude of 17 V/μm.

Figure 5.9 shows plots for each cell of the speckle contrast through each run at 5 salient field conditions. Also shown is a plot of the steady-state response for

mixtures with three different concentrations of CTAB (0, 0.2 and 0.5 wt.%) under peak speckle reduction conditions. This test was conducted immediately after the hysteresis test. For the sake of space, no colourmaps are shown in this case.

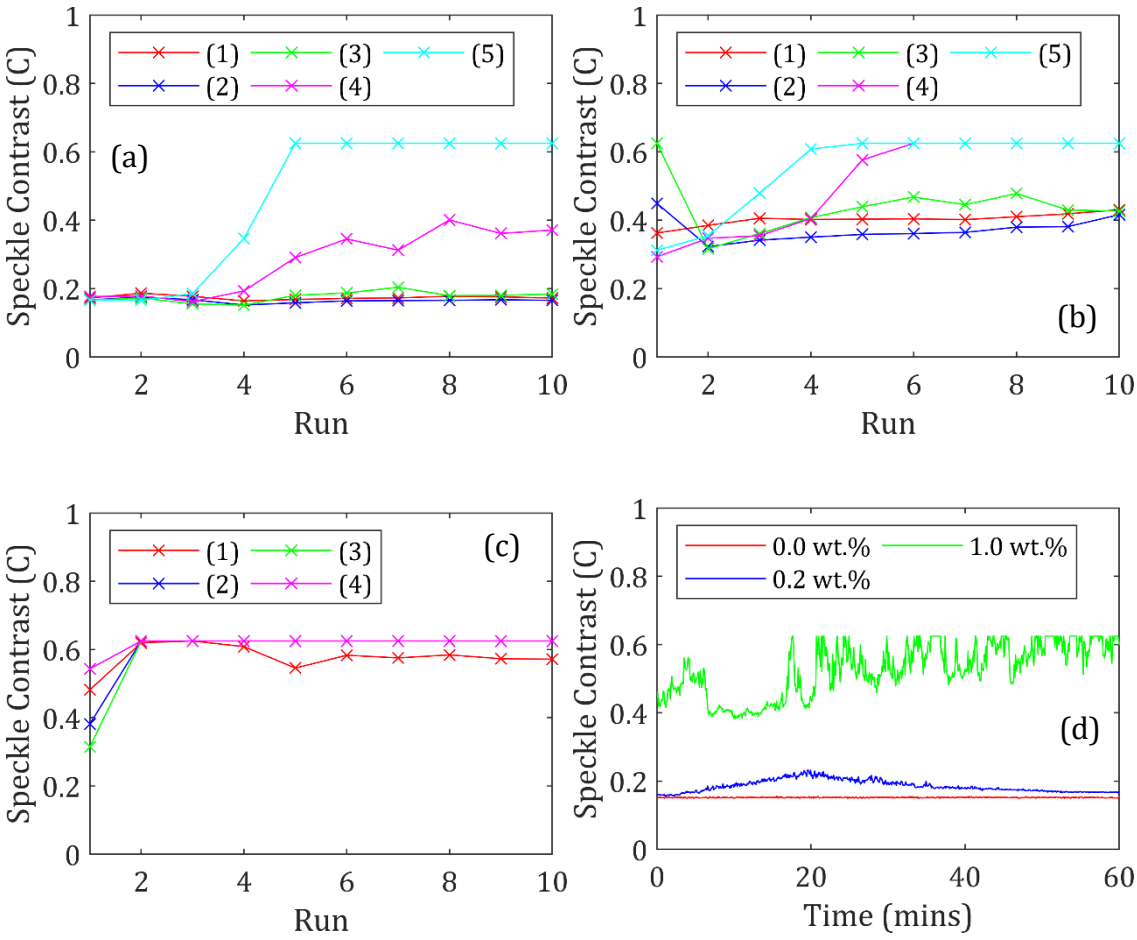

Figure 5.9: Plot of the speckle contrast for 5 selected field conditions over 10 consecutive sweeps of the electric field parameters for (a) 0.2 wt.% CTAB: *(1) 13 V/µm 20Hz, (2) 14 V/µm 20Hz, (3) 15 V/µm 20Hz, (4) 15 V/µm 40Hz, (5) 15 V/µm 60Hz,* (b) 0.5 wt.% CTAB: *(1) 8 V/µm 20Hz, (2) 9 V/µm 20Hz, (3) 10 V/µm 20Hz, (4) 9 V/µm 40Hz, (5) 9 V/µm 60Hz* and (c) 1.0 wt.% CTAB: *(1) 7 V/µm 20Hz, (2) 8 V/µm 20Hz, (3) 9 V/µm 20Hz, (4) 7 V/µm 40Hz*. (d) Plot of the speckle contrast recorded over a period of 60 minutes for cells with 0.0, 0.2 and 0.5 wt.% CTAB. The electric field conditions for peak speckle reduction were applied throughout. The cell temperature during all measurements was held at T = 25°C.

The results from this experiment, presented in Figure 5.9, clearly shows that the 0.2 wt.% CTAB mixture (Figure 5.9a) does behave consistently for the applied electric field conditions corresponding to peak speckle reduction, even when subjected to electric field amplitudes of > 12 V/µm. However, it is observed that for higher

frequencies of the applied field (greater than 20 Hz) the speckle reduction appears to deteriorate after only 3 runs, with the speckle reduction at 60 Hz diminishing completely by run 6. During the 1-hour steady-state test (Figure 5.9d, blue line), the speckle contrast rose slightly from $C = 0.17$ to $C = 0.23$ before settling back down to $C = 0.17$ in the final 10 minutes.

The 0.5 wt.% (Figure 5.9b) cell once again exhibited no turbulence above 10 $V/\mu m$ and thus never reduced the speckle contrast to values below $C = 0.29$. Throughout the 10 runs this minimum value increased to $C = 0.42$, and in a similar way to the 0.2 wt.% cell, higher frequencies resulted in rapid deterioration of the cell, resulting in no speckle reduction above a frequency of 20 Hz from the 6th run of the field parameters onwards. During the steady-state test (Figure 5.9d, green line), the speckle contrast was found to increase from $C = 0.42$ to $C = 0.63$ due to the formation of gas bubbles in the cell. This was confirmed by carefully examining the speckle photographs captured during the measurements as well as microscope images taken after the test.

The 1.0 wt.% cell (Figure 5.9c) also exhibited no turbulence above 10 V/μm and again reduced speckle contrast to only $C = 0.31$ in the initial run. Almost no speckle reduction was observed after the initial run as the active electrode region of the cell suffered from the presence of large gas bubbles. This was confirmed by checking speckle photographs and microscope images taken after the test. The cell was not subjected to a steady state test due to its poor condition after the hysteresis test.

5.4 0.2 wt.% concentration of CTAB

In the previous section, it was shown that the addition of CTAB to short-pitch chiral nematic LC mixtures should be limited to a concentration of 0.2 wt.% or below to avoid potential chemical changes that purify the ionic dopants present in the mixture, which subsequently inhibit EHDI-based dynamic scattering. Next, cells with 0.2 wt.% CTAB over a range of mixtures are tested, all of which have helical structures with a sufficiently long pitch so as to exhibit peak speckle reduction at or below $E = 12$ V/μm.

5.4.1 Importance of pitch in ionic-doped chiral nematic speckle reducers

In the following study, the performance of cells containing different nematic LC hosts in the form of E7 and BL006 are considered, both of which were doped with the low twisting power chiral dopant, R811. Furthermore, mixtures were prepared both with and without a concentration of 0.2 wt.% CTAB. Each cell was subjected to an initial low-resolution parameter sweep, followed by the high-resolution sweep around the point of peak performance before a 5-minute steady-state test was carried out under field conditions that correspond to maximum speckle reduction.

For comparison, a selection of speckle contrast colourmaps from three of the E7 with R811 mixtures, both with and without CTAB, are presented in Figure 5.10. This data clearly shows that the addition of CTAB increases the range of electric field conditions that induce EHDI and consequently light scattering necessary for speckle reduction, especially at higher frequencies of the applied electric field. However, it can also be sees that the field conditions for peak speckle reduction are largely unaffected by the addition of CTAB, along with the minimum speckle contrast value achieved. This was the case for all 10 mixtures tested in this experiment, though the

other colourmaps are omitted for the sake of space.

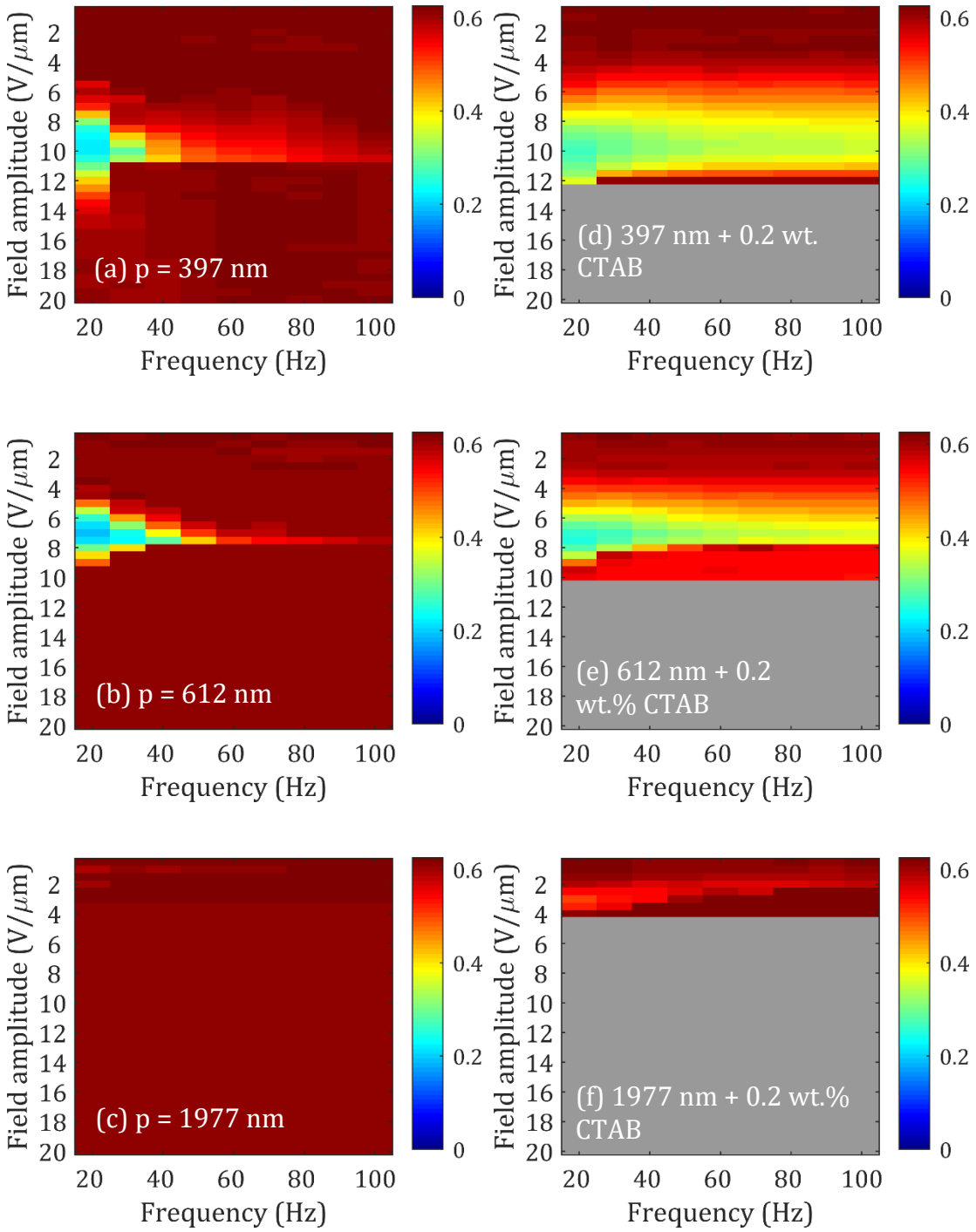

Figure 5.10: Speckle contrast maps for cells consisting of the chiral nematic LC mixture E7 + R811 with different pitch values and with (a-c) and without (d-f) 0.2 wt.% CTAB under a range of applied electric field conditions. The cells tested were 20 μm-thick, and the pitch values were (a,d) 397 nm, (b,e) 612 nm and (c,f) 1977 nm. The cell temperature during measurements was T = 25°C.

5.4.1.1 *Dependence of transmission on the pitch*

A complete comparison of each parameter is now presented. Figure 5.11 shows the transmission through the cells for peak speckle reduction field conditions as a function of the pitch. The values shown represent an average value taken from the 5-minute steady state test.

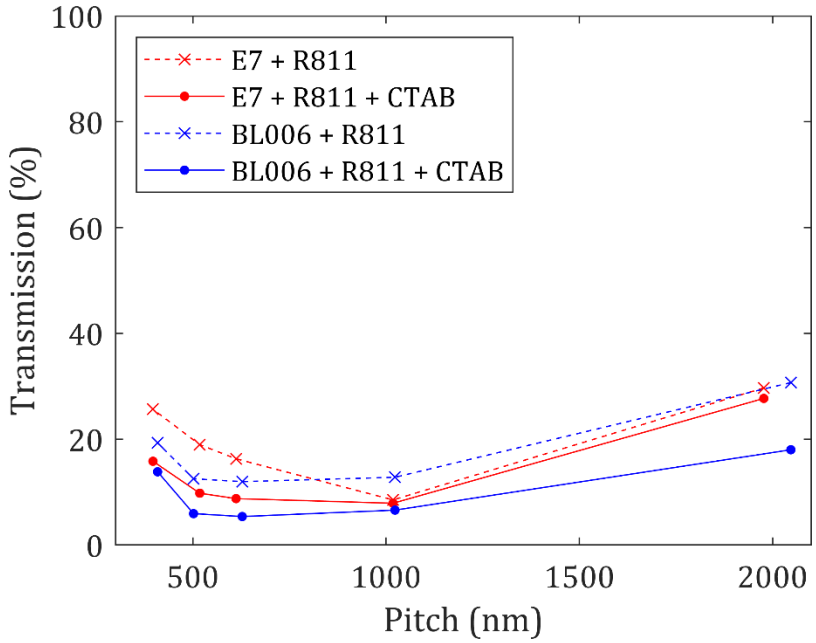

Figure 5.11: Plot of transmission at minimum speckle contrast for mixtures of E7 (red) and BL006 (blue) with R811 at a range of pitch values. Mixtures without CTAB are plotted with crosses and a dashed line, mixtures with 0.2 wt.% CTAB are plotted with circles and a solid line. Each cell was 20 μm thick and the cell temperature throughout measurements was held at $T = 25°C$. Data points are measured values and the lines are a linear interpolation to guide the eye.

All ten mixtures showed a reduction in the transmission, as defined in Section 4.2.3 of Chapter 4, with the addition of CTAB. This is largely in agreement with the literature, which reports stronger scattering, as measured by a reduction in transmission, with the addition of ionic dopants [40] [78] [81].

5.4.1.2 *Dependence of the speckle contrast variation with pitch*

In Figure 5.12 the minimum speckle contrast measured for each mixture is presented as a function of pitch. Once again, the values shown represent the average value extracted from the 5-minute steady-state test at peak speckle reduction electric field conditions.

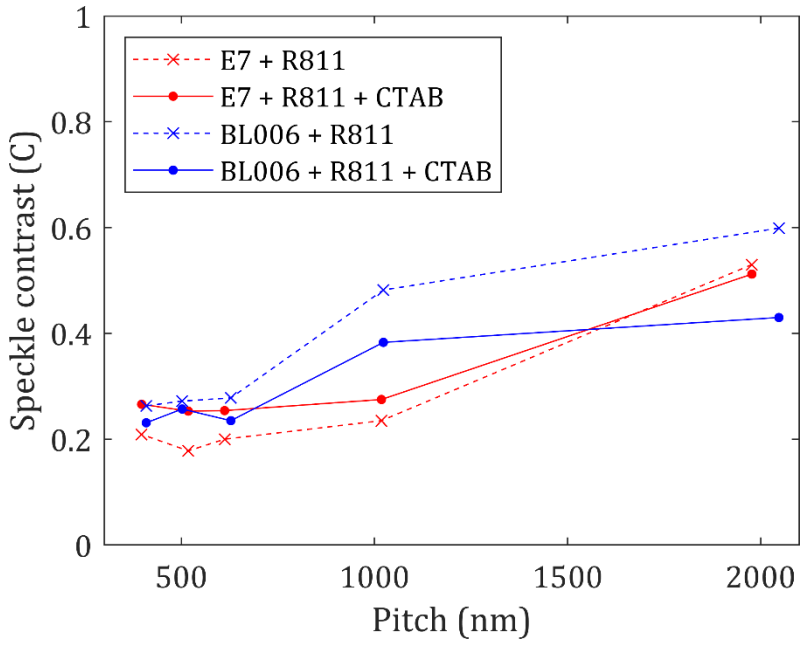

Figure 5.12: Plot of minimum speckle contrast for mixtures of E7 (red) and BL006 (blue) with R811 as a function of the pitch. Mixtures without CTAB are plotted with crosses and a dashed line, mixtures with 0.2 wt.% CTAB are plotted with circles and a solid line. Each cell was 20 μm-thick and the cell temperature throughout measurements was held at $T = 25°C$. Data points represent measured values and the lines are a linear interpolation to guide the eye.

Again, the minimum speckle contrast attainable by a mixture increases with helical pitch which is in agreement with the results presented in Section 4.2. The mixtures consisting of the nematic host LC, BL006, showed improved performance with the addition of CTAB. Each cell achieved a smaller speckle contrast under peak electric field conditions with 0.2 wt.% CTAB. On the other hand, mixtures that consisted of the host nematic LC, E7, showed the opposite trend, with most performing worse with the addition of CTAB. Reports in the literature that claim that stronger

scattering can be obtained with the addition of ionic dopants have typically quantified the degree of scattering through measurements of transmission through the devices [40] [78] [79]. The results presented in this chapter, however, indicate that the process of speckle reduction is more complex and simply increasing the number of ions present in the mixture so as to increase turbidity does not always correlate with increased speckle reduction, despite the decrease in transmission.

5.4.1.3 *Dependence of the electric field threshold on the pitch*

Figure 5.13 is a plot of the electric field threshold for each mixture as a function of pitch. In the literature, the threshold voltage is often taken as the voltage at which the transmission begins to reduce [86]; however, in this case, the threshold voltage is marked as the point at which speckle contrast begins to decrease as the cells are not being driven into a scattering state from a transparent state. The data shows a marked decrease in the threshold electric field for dynamic scattering as the pitch is increased. Furthermore, it appears that the addition of the CTAB dopant also serves to reduce the electric field threshold, which can be explained by the increased conductivity that arises due to the presence of the ionic dopant. The theoretical equations for EHDI threshold voltage in chiral nematics are related both to dielectric and conductivity properties of the mixture, with an inverse relationship between threshold voltage and conductivity [39] as shown in equation 5.1.

$$E_c = 2\pi \left(\frac{(2K_{22}K_{33})^{\frac{1}{2}} 2\pi}{\Delta\sigma . \varepsilon_{\parallel h} / \sigma_{\perp h}} (p_0 d)^{-1} \right)^{\frac{1}{2}} \tag{5.1}$$

where K_{22} and K_{33} are the elastic constants for twist and bend deformation, respectively, p_0 is the unperturbed pitch, d is the cell thickness, $\Delta\sigma$ is conductive anisotropy, $\sigma_{\perp h}$ is conductivity perpendicular to the helical axis and $\varepsilon_{\parallel h}$ is dielectric

permittivity parallel to the helical axis. The assumptions made when deriving this equation are that the mixture has a positive conductive anisotropy, no charge injection and $p_0 \ll d$, all of which apply to these cells. In general, the data follows the relationship $E_c \propto p_0^{-1/2}$ well.

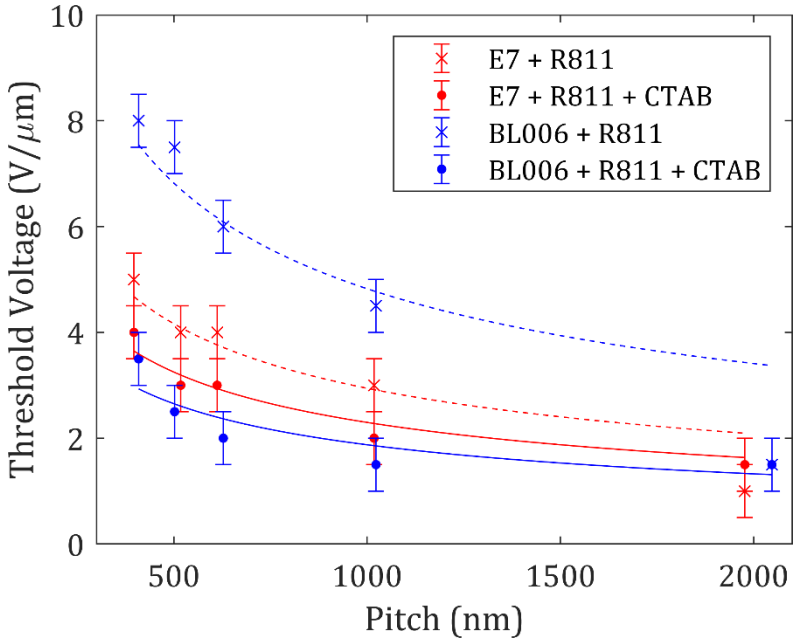

Figure 5.13: Plot of electric field threshold for mixtures of E7 (red) and BL006 (blue) with R811 as a function of pitch. Mixtures without CTAB are plotted with crosses and a dashed line whereas mixtures with 0.2 wt.% CTAB are plotted with circles and a solid line. Each cell was 20 μm-thick and the cell temperature throughout measurements was held at $T = 25°C$. Data points represent measured values, error bars represent uncertainty due to resolution of electric field amplitude increments and the lines are a fit of the form $ax^{-1/2}$.

5.4.1.4 *Dependence of the electric field amplitude required for peak speckle reduction as a function of the pitch*

Figure 5.14 is a plot of the electric field amplitude required for peak speckle reduction as a function of the pitch of the chiral nematic helix for each mixture. It is clear from this plot that the electric field amplitude required for peak performance in terms of speckle reduction shows very little variation with the addition of the ionic dopant, CTAB. As reported previously in Section 4.2.4 of Chapter 4, peak speckle reduction appears to occur at electric fields close to the field-induced chiral

nematic-homeotropic nematic transition. Unlike the equations derived for the threshold for EHDI to take place, the threshold for the chiral nematic-to-nematic transition is dependent on the dielectric properties of the mixture and not the conductivity [26], as shown in equation 2.9:

$$E_c = \frac{\pi^2}{p_0}\left(\frac{K_{22}}{\Delta\varepsilon}\right)^{\frac{1}{2}} \tag{5.2}$$

where K_{22} is the elastic constant for twist deformation, p_0 is the unperturbed pitch and $\Delta\varepsilon$ is dielectric anisotropy. Gardiner [81] showed that the addition of CTAB influences the dielectric anisotropy in a smectic A at higher applied frequencies than are used in this study, but in this case the addition of ionic dopants do not appear to have a large effect on the dielectric properties.

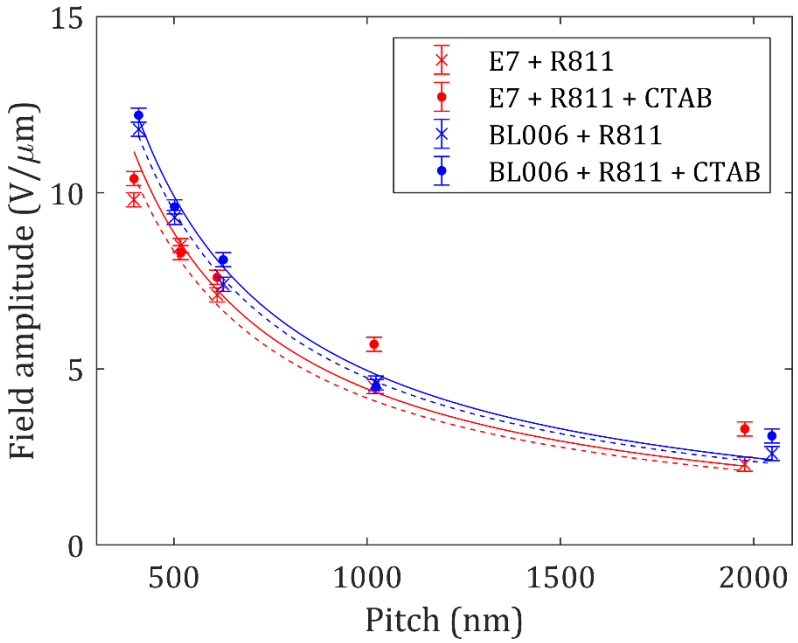

Figure 5.14: Plot of the electric field amplitude corresponding to the minimum speckle contrast value for chiral nematic mixtures of E7 (red) and BL006 (blue) with the chiral dopant, R811, as a function of the pitch. Mixtures without CTAB are plotted with crosses and a dashed line whereas mixtures with 0.2 wt.% CTAB are plotted with circles and a solid line. Each cell was 20 μm thick and the cell temperature throughout measurements was held at $T = 25°C$. Data points represent measured values and the lines are a fit of the form ax^{-1}.

A plot of the frequency required for peak speckle reduction is not shown here

because all the mixtures tested in this experiment were found to perform best at 20 Hz, the lowest frequency tested. (Frequencies below this were not tested as they would be below the average frequency of the eye (20 Hz) thus resulting in observable flicker making such a device unusable.) This finding is in agreement with the literature, which reports that the ionic-driven motion of CTAB molecules dominates at low frequencies, causing maximum distortion of the microscopic texture of the LC [82].

5.4.2 Low voltage hysteresis test

Next, a hysteresis test was undertaken on a mixture of E7 with 19.9 wt.% R811, with and without 0.2 wt.% CTAB. This mixture was chosen as it exhibits peak speckle reduction at an electric field amplitude of approximately 9 V/μm, well below the damage threshold of 12 V/μm discussed in 5.2. This permits an analysis of the hysteresis and lifetime tests on mixtures with and without the ionic dopant CTAB, without the doped cells undergoing rapid deterioration.

The cell was exposed to a field parameter sweep of 5 – 11 V/μm in steps of 1 V/μm, with a square wave frequency of 20 – 100 Hz in steps of 10 Hz. This range of field parameters was chosen as it represents the conditions under which turbulence is seen in both types of devices and avoids the high amplitude electric fields that cause rapid electro-chemical reactions in the mixture that have been observed previously. Colourmaps from the first, fifth and tenth run are shown in Figure 5.15, with non-CTAB cells displayed on the left, next to CTAB-doped cells on the right. Figure 5.16 is a plot of the speckle contrast recorded at three different driving field conditions as a function of the number of runs. The three chosen field conditions correspond to those that show maximum speckle reduction throughout

all 10 runs.

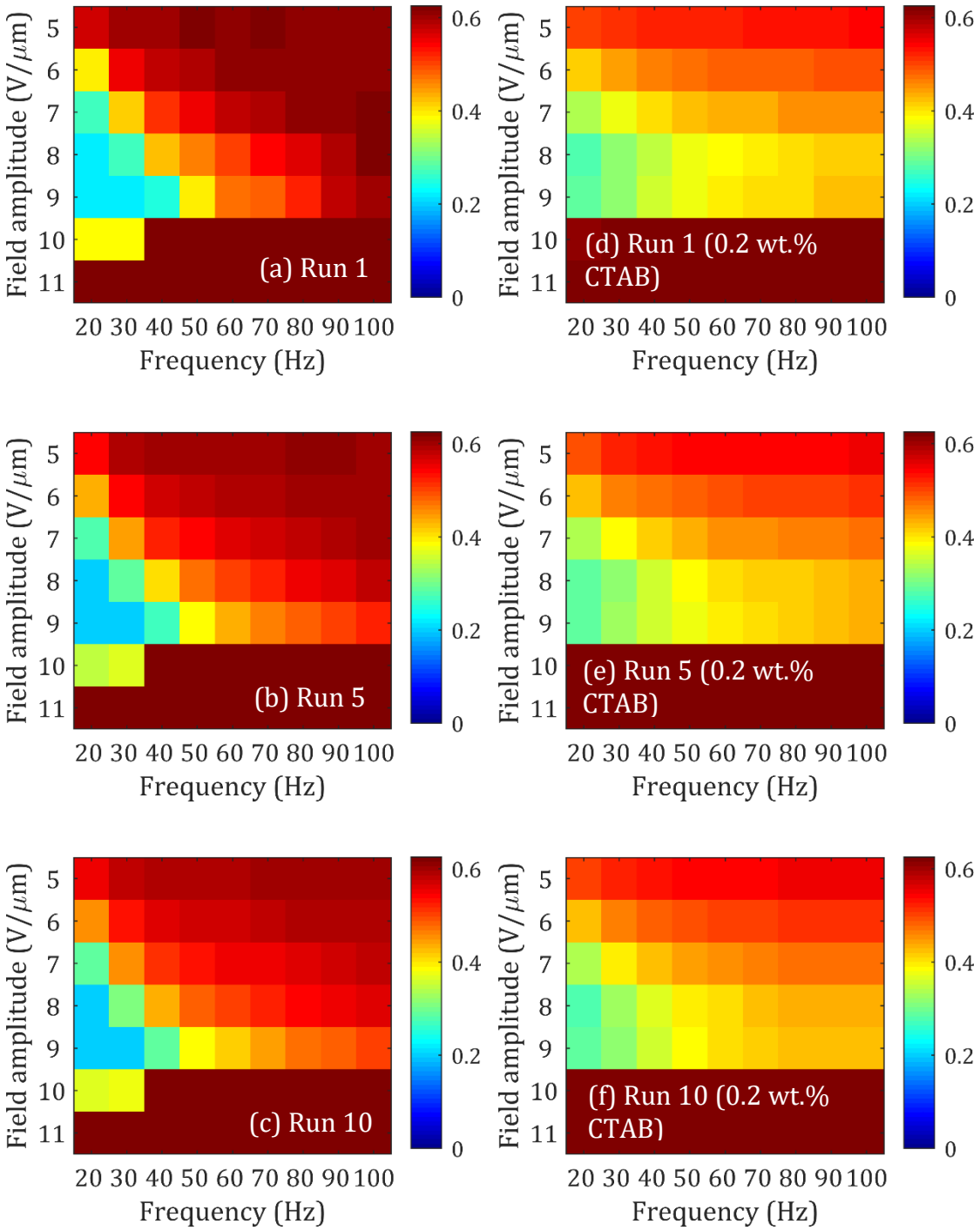

Figure 5.15: Speckle contrast maps for a range of applied electric field conditions. The cells tested were 20 μm-thick, chiral nematic LC cells containing the nematic host, E7, dispersed with chiral dopant (R811) to produce a pitch of 518 nm. (d-f) have 0.2 wt.% of CTAB added. (a,d) First run, (b,e) fifth run, (c,f) tenth run. Cell temperature throughout was T = 25°C.

As before, speckle reduction is seen over an extended range of electric field parameters with the CTAB-doped cells. Microscope observations also reveal that the EHDI regime is extended over the same range. However, the CTAB-doped cells do not exhibit the same level of speckle reduction as the undoped samples, indeed speckle contrast is significantly higher for the CTAB-doped cells across all runs. It is found that there is very little hysteresis for both mixtures, with and without CTAB. The mixture without CTAB improves in performance over the 10 runs, with the speckle contrast reducing from $C = 0.217 \pm 0.008$ to $C = 0.199 \pm 0.006$. Meanwhile, the CTAB-doped cell exhibits a speckle contrast of $C = 0.280 \pm 0.002$ for the first run, and a slightly increased value of $C = 0.281 \pm 0.001$ for the final run. This is further evidence that supports the hypothesis that CTAB does not undergo any significant deterioration when the electric field amplitude that is applied to the device is limited to below 12 V/µm.

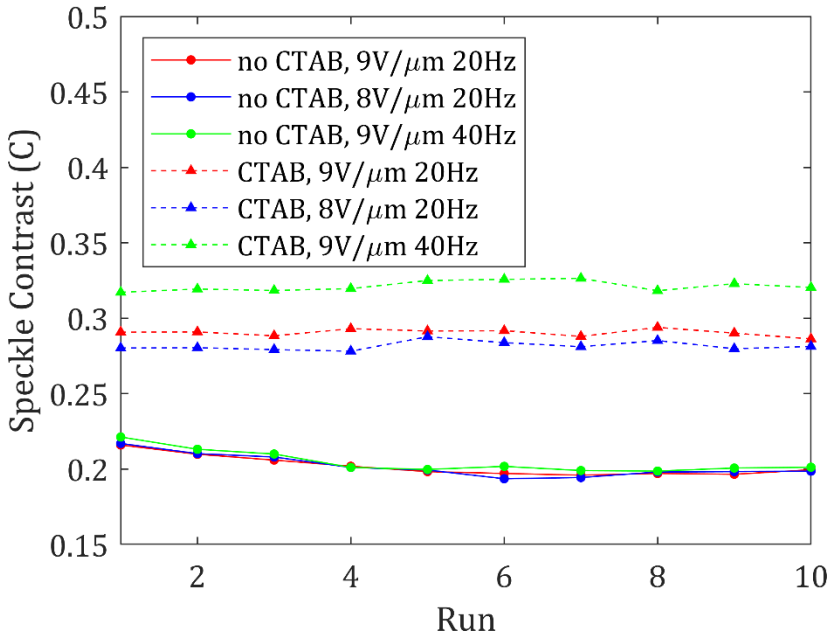

Figure 5.16: Plot of speckle contrast for 3 selected electric field conditions over 10 runs. The cells tested were 20 μm-thick, chiral nematic LC cells containing the nematic host, E7, dispersed with chiral dopant (R811) to produce a pitch of 518 nm. The temperature throughout measurements was held at T = 25°C. Cells without CTAB are shown with a solid line and circle data points whereas cells with CTAB are shown with a dashed line and triangle data points.

5.4.3 High voltage hysteresis test

Following the low voltage hysteresis test in 5.4.2, a very similar hysteresis test was undertaken for the same cells but with electric fields of $5 - 20$ V/μm and frequency of 20 – 100 Hz to observe the rate at which they deteriorate when subjected to large electric field amplitudes. In this experiment, each cell was subjected to the electric field parameter sweep 40 times consecutively. Figure 5.17 shows colourmaps from runs 1, 20 and 40, with non-CTAB cells displayed on the left, next to CTAB cells on the right. Figure 5.18 is a plot of the speckle contrast recorded at three different driving field conditions as a function of the number of runs. The three chosen field conditions are the same as those shown in Figure 5.16.

From the 5th run onwards the non-CTAB cell shows consistent speckle reduction at the peak electric field conditions, with the speckle contrast rising slightly from $C = 0.206 \pm 0.003$ to $C = 0.213 \pm 0.008$. This represents a slight deterioration in performance, likely due to electro-chemical reactions at the electrodes with the ionic impurities present in the base LC mixture. It is suspected that the presence of gas bubbles in the active electrode region may account for the anomalous rise in speckle contrast for runs 2-4 as discussed previously in Sections 5.2.1 and 5.3.2.

The two other field conditions shown exhibit a greater deterioration in performance throughout measurements. This suggests that for optimum device lifetime, each cell should be limited to the electric field conditions that result in maximum speckle reduction.

Evidently, the device with CTAB deteriorates more significantly, with the speckle contrast rising from $C = 0.265 \pm 0.006$ to $C = 0.305 \pm 0.013$ from run 1 to

run 40 under peak speckle reduction electric field conditions. This is further evidence that the addition of CTAB significantly reduces the lifetime of the device, as reported in the literature [79], especially when subjected to large electric field amplitudes.

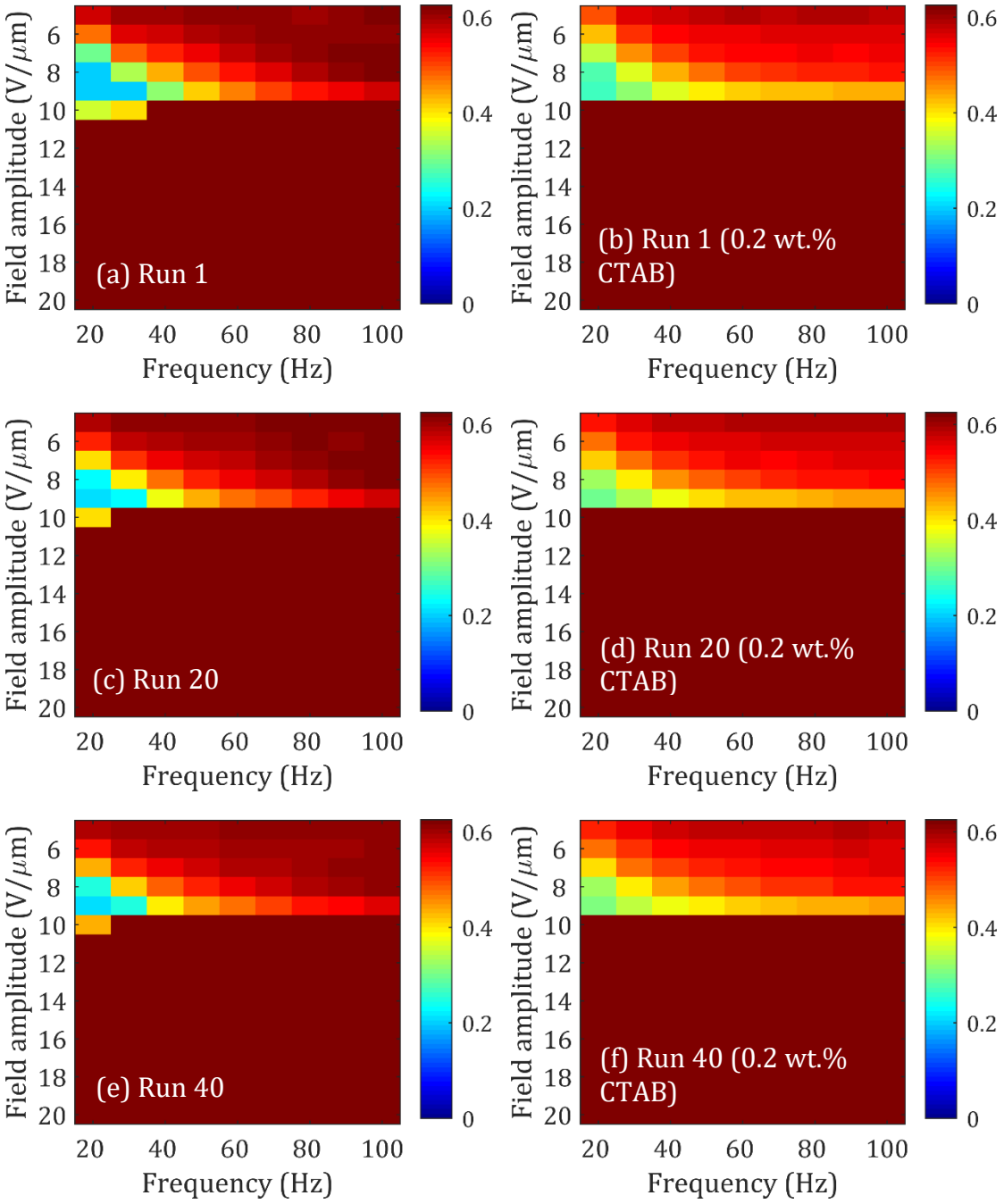

Figure 5.17: Speckle contrast maps for a range of applied electric field conditions. The cells tested were 20 μm-thick, chiral nematic LC cells containing the nematic host, E7, dispersed with chiral dopant (R811) to produce a pitch of 518 nm. (d-f) have 0.2 wt.% of CTAB added. (a,d) First run, (b,e) twentieth run, (c,f) fortieth run. Cell temperature throughout was T = 25°C.

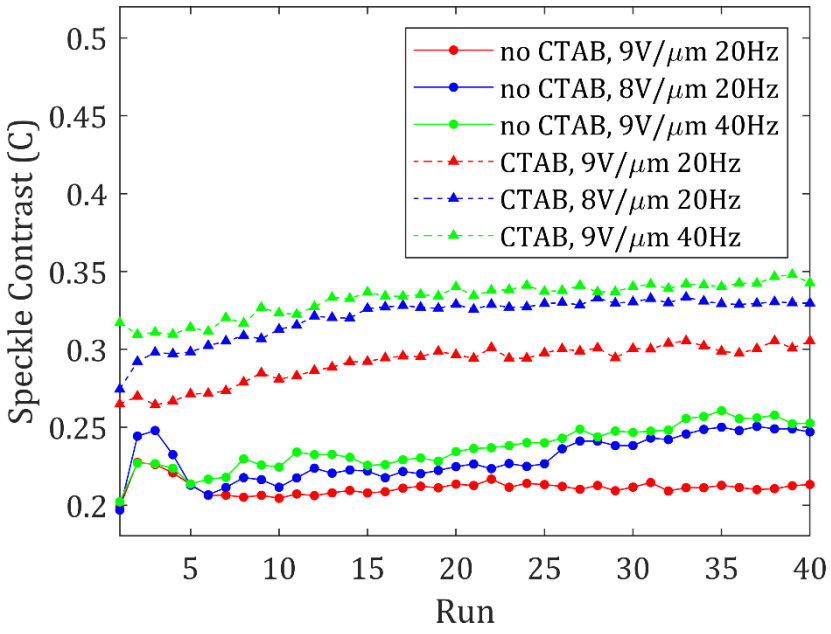

Figure 5.18: Plot of speckle contrast under 3 selected electric field conditions over 40 runs. The cells tested were 20 μm-thick, chiral nematic LC cells containing the nematic host, E7, dispersed with chiral dopant (R811) to produce a pitch of 518 nm. The temperature throughout measurements was held at T = 25°C. Cells without CTAB are shown with a solid line and circle data points whereas cells with CTAB are shown with a dashed line and triangle data points.

5.4.4 Lifetime test

Finally, both cells were subjected to a steady-state experiment, with each cell being exposed to the electric field conditions required for peak speckle reduction over a prolonged period of time. The results are shown in Figure 5.19 where it is shown clearly that, despite each cell having undergone deterioration to some degree, when subjected only to the low electric field amplitude required for peak performance, both devices exhibit no further deterioration over 60 minutes.

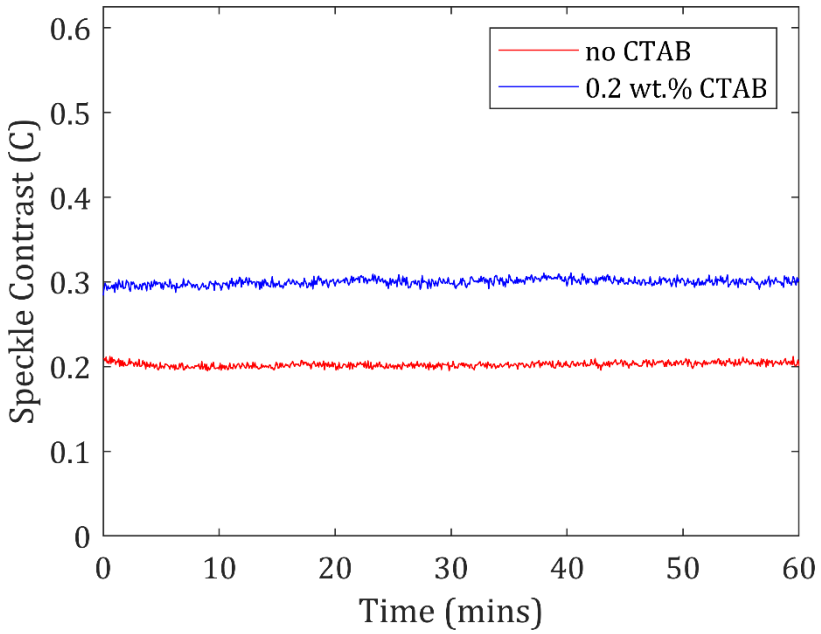

Figure 5.19: Plot of speckle contrast taken over a period of 60 minutes for a 20 μm-thick, chiral nematic LC cell with and without 0.2 wt.% CTAB. The host chiral nematic mixture contained the nematic host, E7, dispersed with a low twisting chiral dopant (R811) to produce a pitch of 518 nm at 25°C. The electric field conditions required for peak speckle reduction were applied throughout (9 $V/\mu m$, 20 Hz square-wave). The cell temperature during measurement was T = 25°C.

5.5 Summary

In this Chapter, it has been shown that adding the ionic compound CTAB to a chiral-nematic LC will increase the range of electric field conditions under which a device exhibits speckle reduction. Speckle reduction is seen at higher frequencies and lower electric field amplitudes than the equivalent mixtures without CTAB. However, maximum speckle reduction generally occurs under the same field conditions as non-CTAB mixtures and the presence of CTAB does not necessarily increase the amount by which the speckle contrast is reduced, despite the apparent decrease in transmission.

Increasing the concentration of CTAB limits the maximum electric field amplitude the cell can withstand before undergoing permanent electro-chemical reactions that restrict turbulence in the cell. Also, an increase in CTAB concentration is likely to produce larger gas bubbles in the active region of the cell, again limiting

light scattering and the lifetime of the cell. It has been shown that the CTAB concentration should be limited to < 0.2 wt.% and electric field amplitudes to $<$ 12 V/μm in order to ensure that the cell exhibits a similar lifetime to an equivalent chiral nematic LC mixture without CTAB.

As a result of this study, it is clear that the disadvantages of limited electric field amplitude and long-term deterioration outweigh the advantages of adding CTAB to a mixture for the purpose of speckle contrast reduction. The exact cause and nature of the browning of CTAB mixtures is not yet fully understood, but it was speculated that the bromide ions present in CTAB may be oxidised to form bromine gas, known to be a similar colour, under high electric field amplitudes. This could in turn cause the formation of the bubbles that completely inhibit speckle reduction.

It is clear that the degradation of the LC mixture is related to the irreversible electro-chemical reactions occurring at the electrodes [87] either to the ionic dopant or the ionic impurities already present in the base LC mixture. As a result, further work could involve studying the effect of adding redox dopants to the mixture instead of ionic dopants such as CTAB. Redox dopants consist of donors and acceptors that readily undergo reversible electrochemical reactions at lower voltages than the irreversible reactions of the LC components. These dopants have been shown to improve lifetime, threshold voltage and scattering when compared to salt-type ionic dopants [82] [83] [85] [86] [87] [88].

6 Study of geometrical and environmental parameters on speckle reduction

In the previous chapter, it was shown that adding the ionic dopant, CTAB, in small quantities by weight up to 1.1 wt.% into a chiral nematic mixture increases the range of electric field conditions under which a device reduces speckle contrast when compared to the equivalent non-ionic-doped mixtures. The results showed that while the electric field threshold for EHDI was reduced, the field amplitude and frequency for maximum speckle reduction was largely unaffected. Doping with CTAB generally served to decrease transmission but did not necessarily increase the amount by which speckle is reduced. Finally, it is shown that CTAB-doped cells undergo an irreversible chemical reaction that inhibits EHDI, reducing the lifetime of the device, especially at concentrations above 0.2 wt.% and when exposed to electric field amplitudes that were greater than $E = 12$ V/μm. It was therefore concluded that the disadvantages far outweighed the advantages of CTAB-doping and instead that redox dopants should be considered as an alternative in future work.

In this chapter, results were presented on the impact that other device parameters have on the resulting speckle-reduction performance of the chiral nematic device. Specifically, the effect of cell thickness, the introduction of additional scattering particles and the role of cell temperature were considered. It is shown that an increase in the cell thickness leads to increased light scattering and reduced speckle contrast. The scattering particles that are employed in this study

do not appear to reduce speckle contrast at low concentrations but are shown to aid speckle reduction at concentrations by weight of 5 wt.%. Finally, an increase in the operating temperature is shown to decrease speckle contrast, increase transmission, decrease field amplitude for peak speckle reduction and increase square-wave frequency for peak speckle reduction.

6.1 Cell Thickness

In this section, the effect of cell thickness on the performance of a LC cell in terms of speckle reduction and transmission, electric field parameters for maximum speckle reduction and hysteresis is investigated. The cells tested were the commercially available INSTEC LC2 with nominal cell gaps of 5.0, 9.0 and 20.0 μm. This range is achieved using spacer beads dispersed throughout the cell of the desired size. In this study, results are presented for aforementioned cell thicknesses for a range of concentrations of the following mixtures to obtain chiral nematic LCs with different pitch values. In particular, mixtures consisting of the nematic host, BL006, doped with the chiral dopant R5011 or mixtures consisting of the nematic host, E7, dispersed with the chiral dopant, BDH1281, are studied.

6.1.1 Mixture Preparation

In total, six mixtures were prepared for this study, each one filled into 5 μm, 9 μm and 20 μm cells. The mixture concentrations and corresponding pitch values are summarised in Table 6.1**.** The pitch of each mixture was determined using the relevant experimental procedure described in Section 3.2 of Chapter 3. At room temperature, all mixtures were found to exhibit a chiral nematic phase with a right-handed helical structure. The precise thickness of each cell was determined using

an interference method as described in Section 3.2 of Chapter 3. Cells that differ from the manufacturers quoted thickness, as defined by the spacer beads, by more than 5% were discarded.

Nematic	Chiral Dopant	wt.%	Pitch (nm)
BL006	R5011	unknown	223 – 264
E7	BDH1281	2.5 – 5.1	273 – 517

Table 6.1: Components and corresponding concentrations for the six mixtures used in this study, along with the pitch at a temperature of 25°C. The weight percentage of the BL006 and R5011 mixture was unknown as it was received already dispersed from Merck.

6.1.2 Initial Results

After determining the pitch of each mixture, each cell was subjected to a low-resolution field parameter sweep, then a high-resolution sweep around the point of peak performance as described in Section 4.1 of Chapter 4. The 20 μm-thick cells were limited to a maximum field amplitude of 20 V/μm due to the limitations of the electronic equipment available. As a result, the two shortest pitch BL006 + R5011 cells ($p = 223$ nm and 230 nm) are not exposed to a field amplitude that is sufficiently large enough as to reach maximum speckle reduction. Figure 6.1, Figure 6.2 and Figure 6.3 show examples of 18 colourmaps from the low-resolution field parameter sweep of each mixture in cells of thicknesses $d = 5.0$, 9.0 and 20.0 μm.

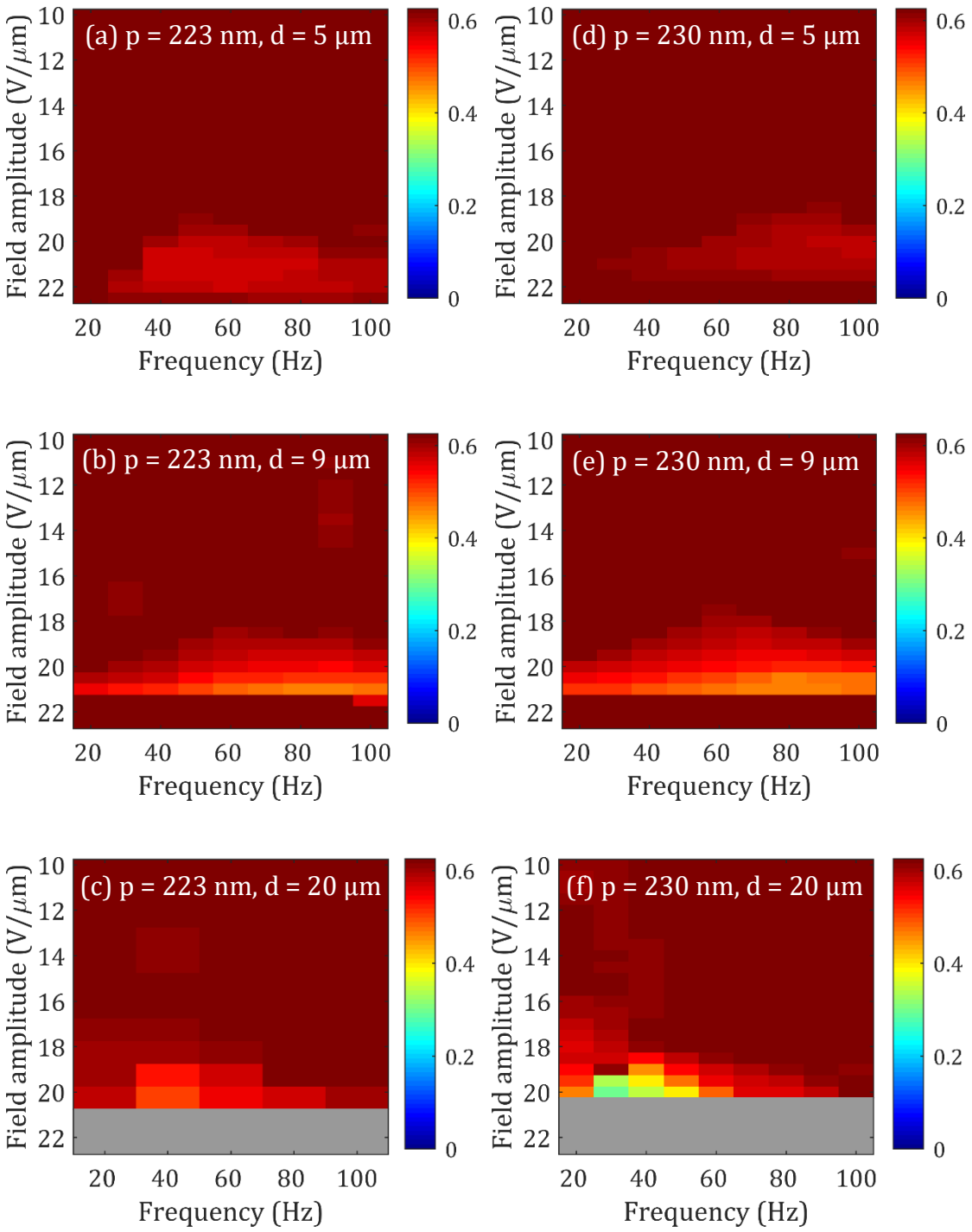

Figure 6.1: Speckle contrast maps for a range of applied electric field conditions; electric field amplitude from E = 1 − 22.5 $V/\mu m$ and square-wave frequency from 20 − 100 Hz. The cells tested are chiral nematic LC cells containing the nematic host, BL006, dispersed with the chiral dopant (R5011). The cell temperature during measurements was T = 25°C.

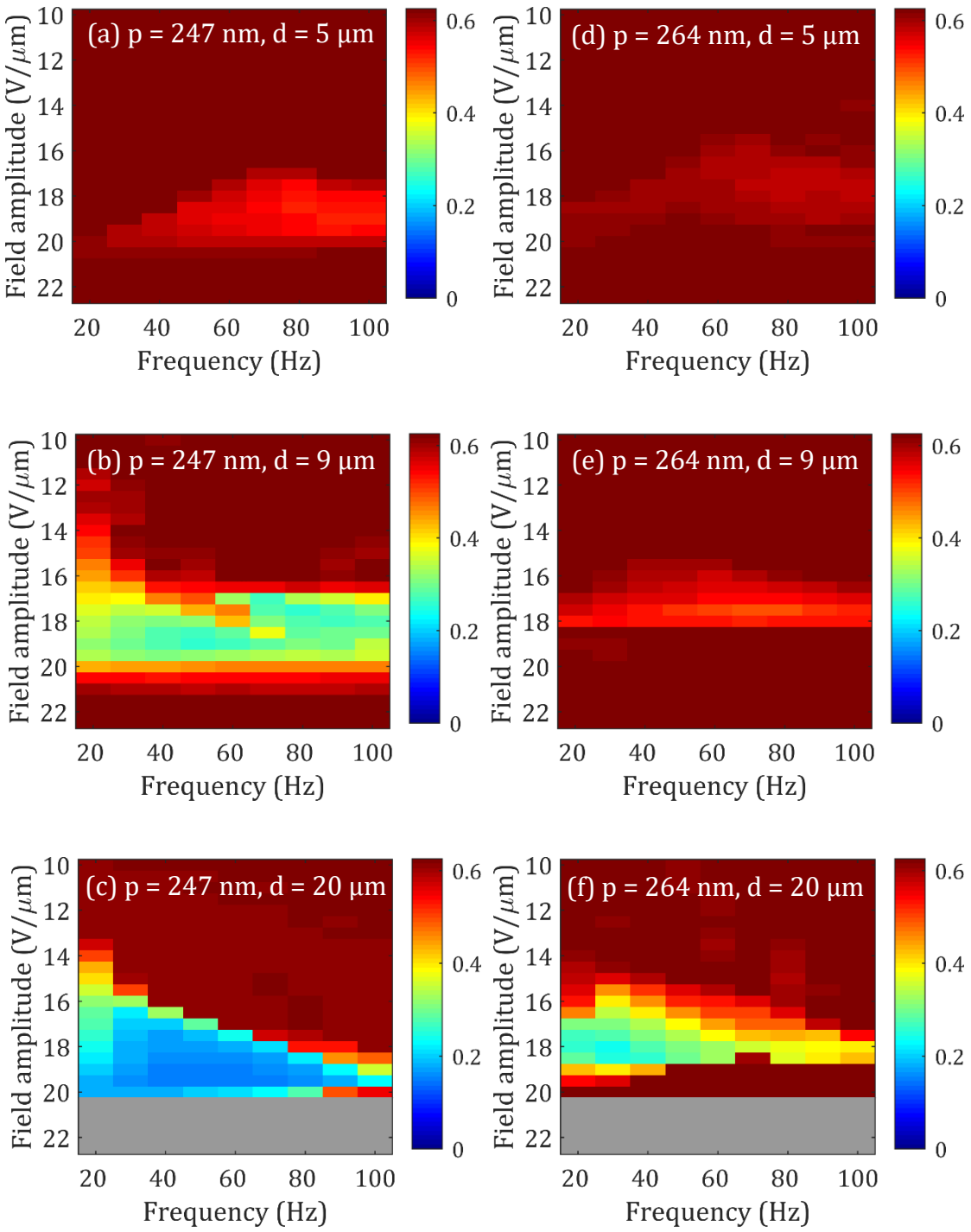

Figure 6.2: Speckle contrast maps for a range of applied electric field conditions; electric field amplitude from E = 1 – 22.5 $V/\mu m$ and square-wave frequency from 20 – 100 Hz. The cells tested were chiral nematic LC cells containing the nematic host, BL006, dispersed with chiral dopant (R5011). The cell temperature during measurements was T = 25°C.

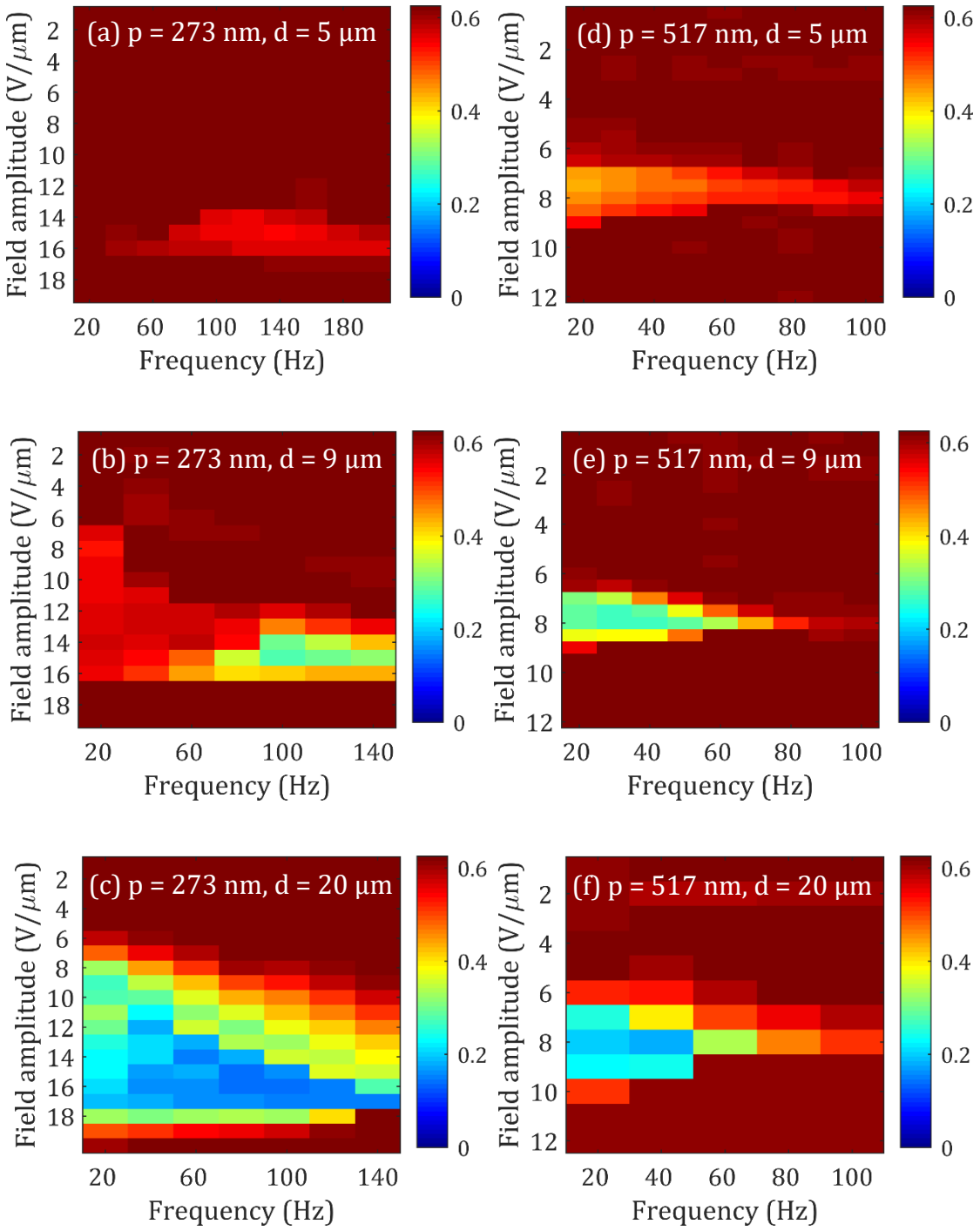

Figure 6.3: Speckle contrast maps for a range of applied field conditions. The cells tested were chiral nematic LC cells containing the nematic host, E7, dispersed with chiral dopant (BDH1281). The cell temperature during measurements was T = 25°C.Dependence of the speckle contrast on cell thickness

Figure 6.4 is a plot of the minimum speckle contrast achieved for each mixture during the high-resolution field parameter sweep as a function of cell thickness. The results for the 20 µm cells are consistent with those shown in Section 4.2.2 of

Chapter 4. It can be seen that, in general, an increase in the cell thickness results in a reduction in minimum speckle contrast. This is likely to be due to an increase in light scattering with thicker LC films, as shown through the transmission measurements presented in Figure 6.4 and as reported in the literature for light scattering in helix-free ferroelectric LCs [89] and polymer-stabilised chiral nematic LCs [90]. Also, it has been reported that a cell thickness of at least 6 µm is required for light scattering through a LC film [78], which would explain the particularly poor performance of the 5 µm cells observed in this study.

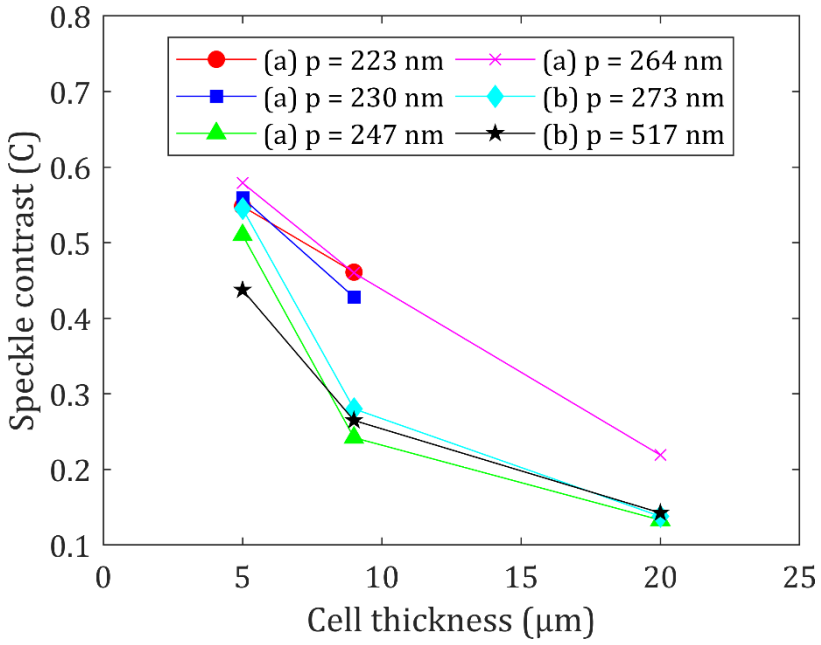

Figure 6.4: Plot of minimum speckle contrast for a range of cell thicknesses, at a range of pitch values for a mixture of (a) the nematic BL006 with the chiral dopant R5011 or (b) the nematic E7 with the chiral dopant BDH1281. Cell temperature throughout measurements was $T = 25°C$. Solid lines are linear interpolation to guide the eye.

6.1.3 Dependence of transmission on cell thickness

Figure 6.5 is a plot of transmission, as defined in Section 4.2.3 of Chapter 4, at minimum speckle contrast for all six mixtures as a function of cell thickness. It is clear that an increase in cell thickness results in a reduction in transmission, a trend that has also been reported in the literature [89] [90] for cell thicknesses between

8 and 30 µm.

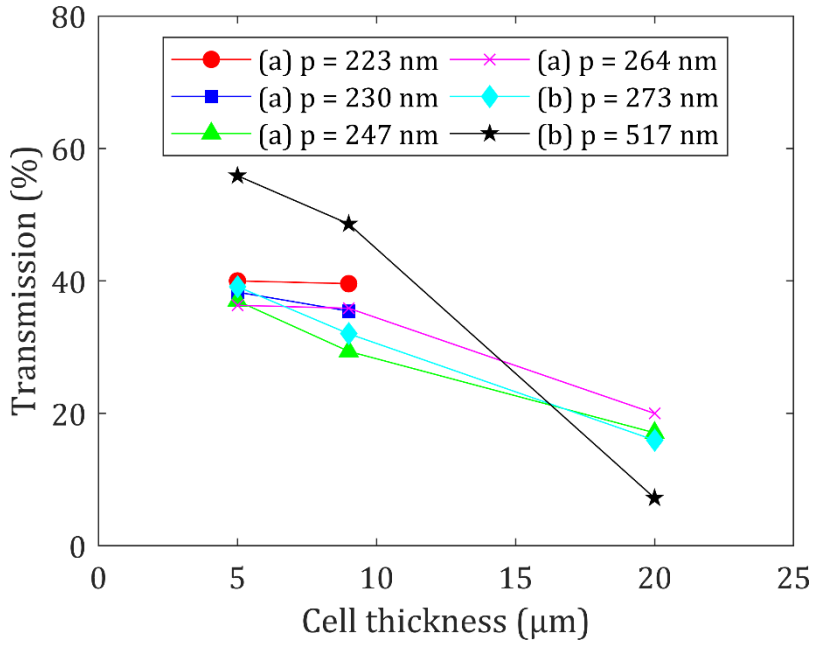

Figure 6.5: Plot of transmission at peak speckle reduction for a range of cell thicknesses, at a range of pitch values for a mixture of (a) the nematic BL006 with the chiral dopant R5011 or (b) the nematic E7 with the chiral dopant BDH1281. Cell temperature throughout measurements was $T = 25°C$. Solid lines are linear interpolation to guide the eye.

6.1.4 Dependence of threshold voltage on cell thickness

Figure 6.6 is a plot of the peak-to-peak threshold voltage for light scattering in all six mixtures as a function of cell thickness. As the threshold voltage is significantly lower than the voltage required for peak speckle reduction, it was possible to measure threshold voltage for both mixtures with the smallest pitches as they were below the amplitude limit accessible with the equipment used in this thesis. The results show that there is a clear linear relationship between the threshold voltage and the cell thickness, which is in accord with previous studies on DC scattering in nematic LCs [91], and experimental studies on AC scattering in smectic A mixtures [82] [40] [80].

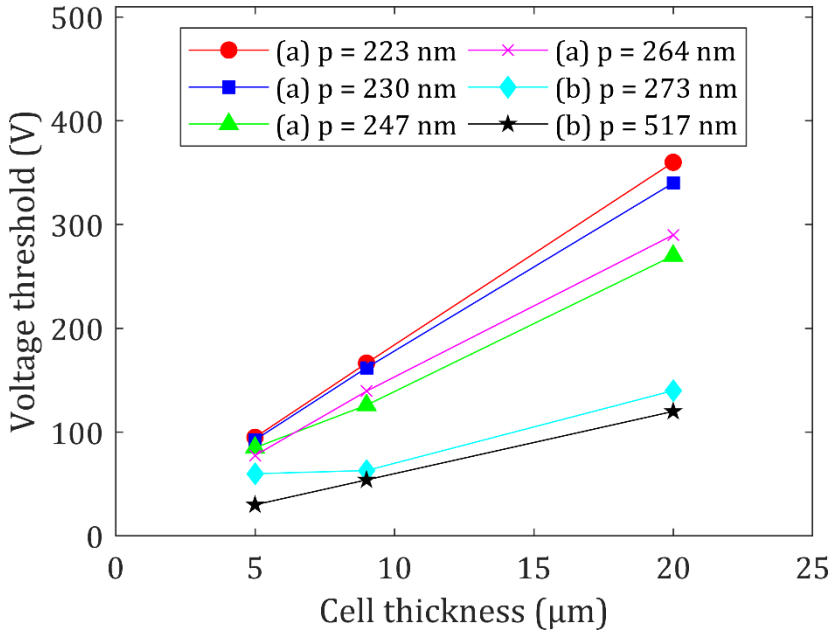

Figure 6.6: Plot of peak-to-peak threshold voltage for light scattering for a range of cell thicknesses, at a range of pitch values for a mixture of (a) the nematic BL006 with the chiral dopant R5011 or (b) the nematic E7 with the chiral dopant BDH1281. Cell temperature throughout measurements was $T = 25°C$. Solid lines correspond to linear interpolations to guide the eye.

6.1.5 Dependence of the electric field amplitude required for peak speckle reduction as a function of cell thickness

Figure 6.7 is a plot of the electric field amplitude required for peak speckle reduction as a function of cell thickness for all six mixtures. All mixtures show very little dependence on cell thickness, with most cells increasing in electric field amplitude only slightly (≤ 1 V/μm) with an increase in cell thickness. This independence from the cell gap supports the hypothesis that the field conditions for peak speckle reduction are very close to the threshold for the field-induced chiral nematic-homeotropic nematic transition, which is in accord with existing theory which shows no dependence on cell thickness, as demonstrated in equation 5.2.

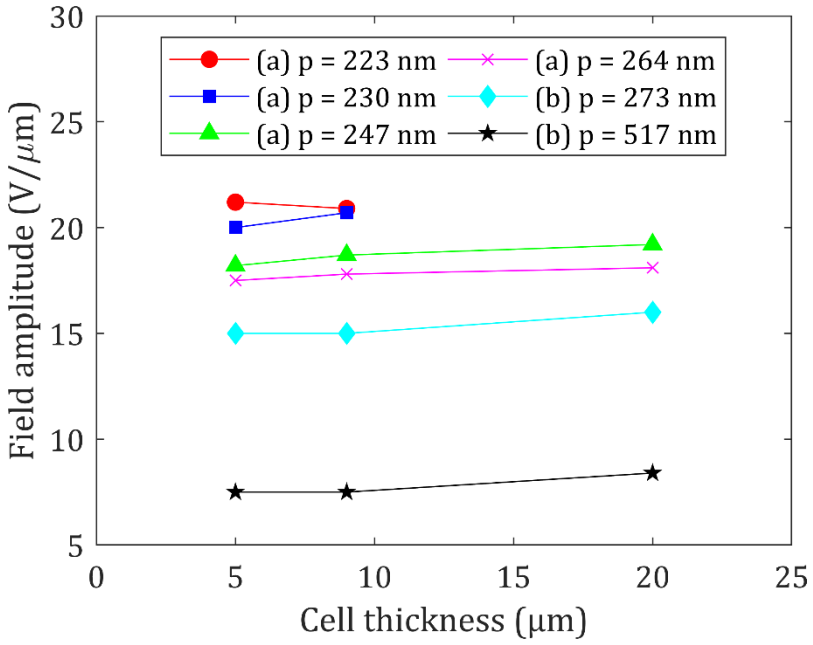

Figure 6.7: Plot of the electric field amplitude for peak speckle reduction for a range of cell thicknesses, at a range of pitch values for a mixture of (a) the nematic BL006 with the chiral dopant R5011 or (b) the nematic E7 with the chiral dopant BDH1281. Cell temperature throughout measurements was $T = 25°C$. Solid lines are linear interpolation to guide the eye.

6.1.6 Hysteresis and cell thickness

To further study the effect of varying the cell thickness, a new set of cells were made and subjected to 10 consecutive low-resolution sweeps of the electric field parameters, following a similar procedure to that described in Chapter 3, Section 3.4.2. The aim of this experiment is to discover whether constant cycling of the field conditions alters the speckle reducing capabilities of the cells of different thicknesses. The mixture used exclusively for this experiment consisted of the nematic E7 with 5.1 wt.% chiral dopant BDH1281. Figure 5.4 shows colourmaps for runs 1, 5 and 10 from the sweep for the 5 μm cell, alongside a plot of how 5 salient field conditions vary throughout the runs.

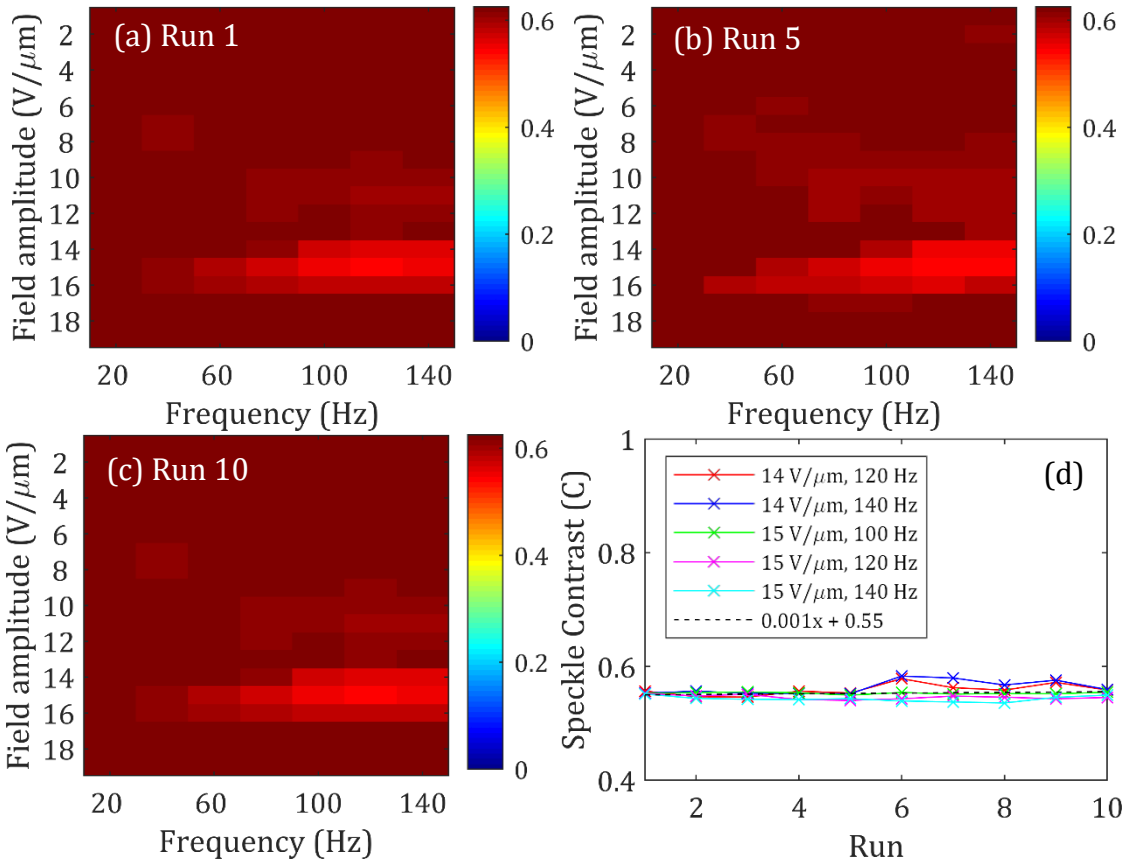

Figure 6.8: Speckle contrast maps for a range of applied electric field conditions. The cells tested were 5 μm-thick, chiral nematic LC cells containing the nematic host, E7, dispersed with the chiral dopant (BDH1281) to produce a pitch of 517 nm. (a), (b) and (c) are speckle contrast maps taken from 10 consecutive runs, with runs 1, 5 and 10 shown, respectively. (d) Plot of the speckle contrast for 5 selected electric field conditions from the 10 consecutive runs. The dotted black line shows the average trend for all data. The cell temperature throughout measurements was held at T = 25°C.

In this case, there is almost no increase in speckle contrast at the electric field conditions that provide the largest speckle reduction with this mixture throughout the 10 runs tested. The average increase in the speckle contrast between runs is only 0.001 and the minimum speckle contrast remains at 0.55 throughout measurements. The same test was then conducted using a new 9 µm cell and the results are presented in Figure 6.9.

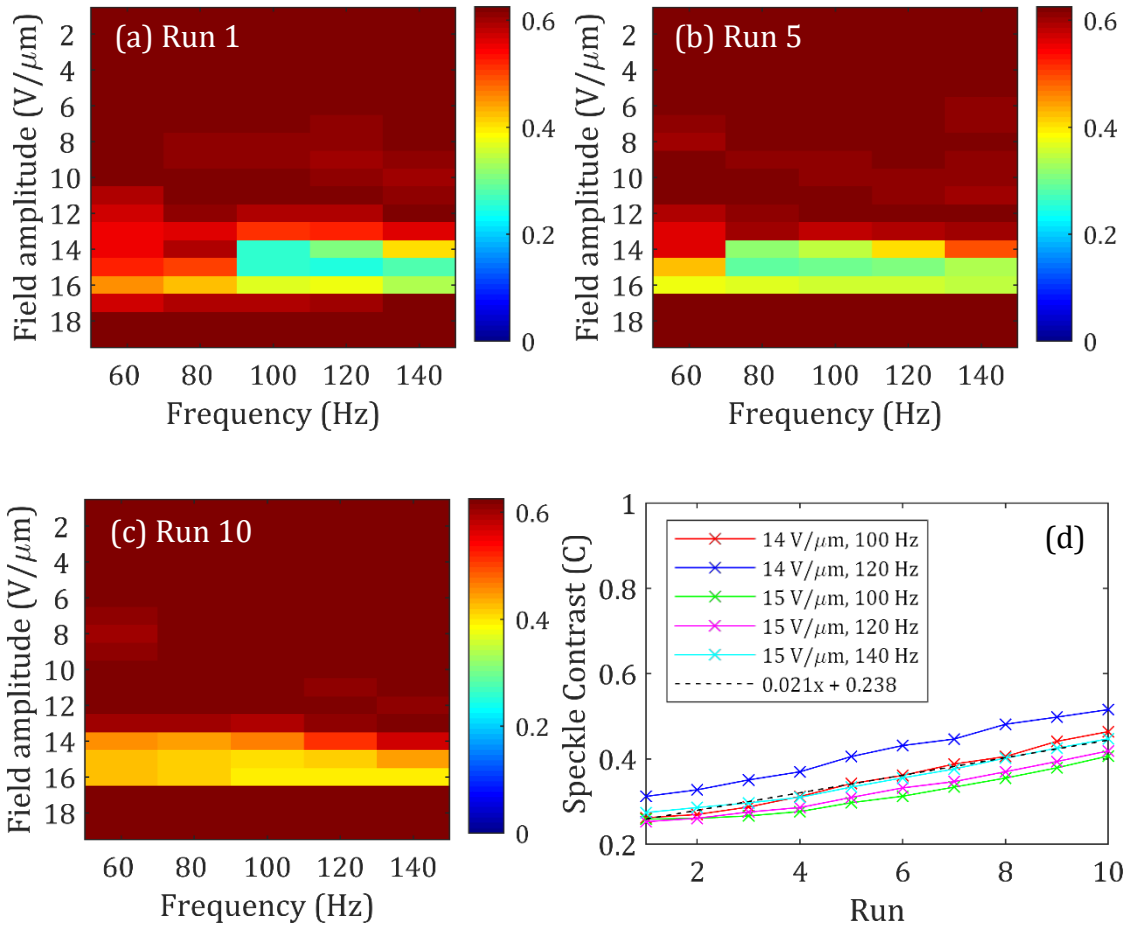

Figure 6.9: Speckle contrast maps for a range of applied electric field conditions. The cells tested were 9 μm-thick, chiral nematic LC cells containing the nematic host, E7, dispersed with the chiral dopant (BDH1281) to produce a pitch of 517 nm. (a), (b) and (c) are the speckle contrast maps taken from 10 consecutive runs, with runs 1, 5 and 10 shown, respectively. (d) Plots of the speckle contrast for 5 selected electric field conditions from the 10 runs. The dotted black line shows the average trend for all data. The cell temperature throughout was held at T = 25°C.

From these measurements it is clear that there is an increase in the speckle contrast at constant field parameters over the 10 runs, with the minimum speckle contrast increasing from $C = 0.25$ to $C = 0.41$. On average, the speckle contrast is found to increase by $\Delta C = 0.021$ between runs. A second cell was then made and tested following the same procedure as that employed before to ensure there was no isolated issue with the INSTEC cell used and the results were consistent with the previous findings.

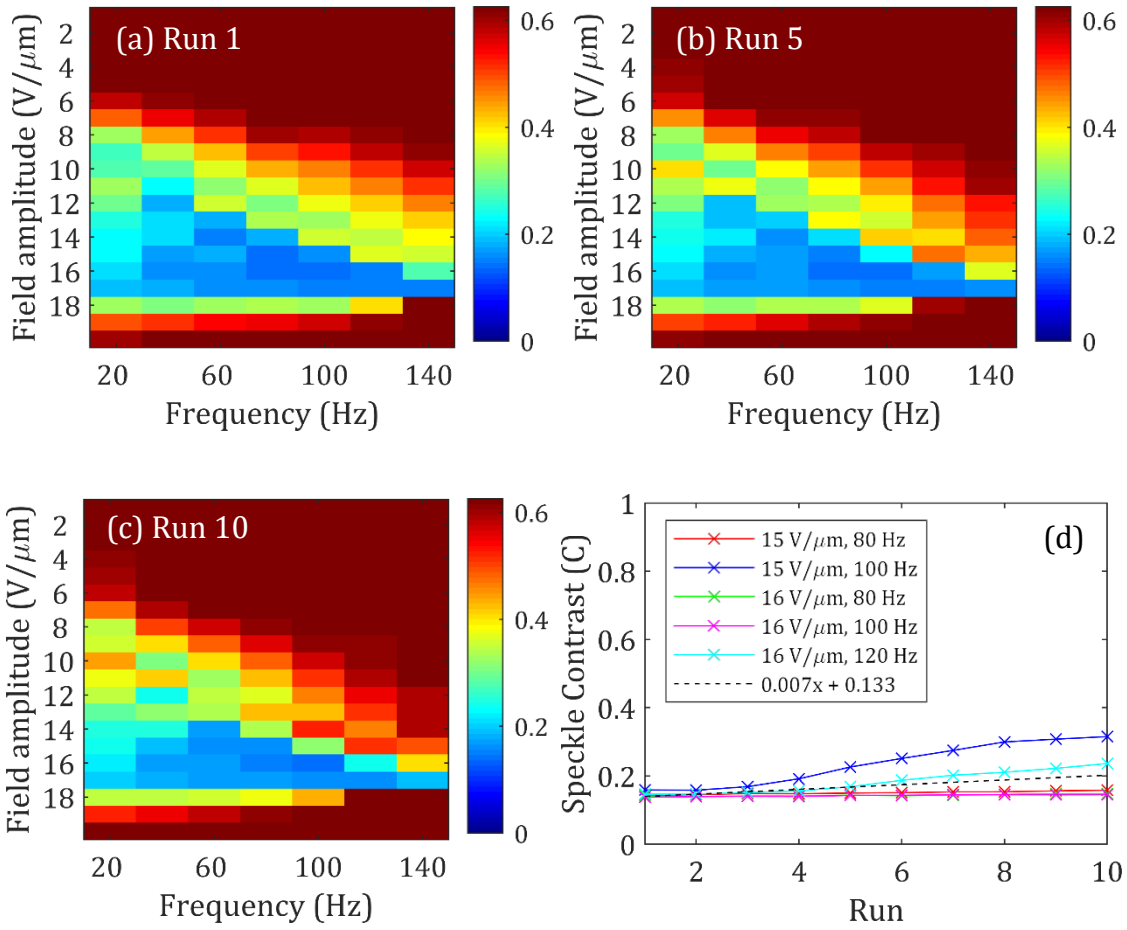

Figure 6.10: Speckle contrast maps for a range of applied electric field conditions. The cells tested were 20 μm-thick, chiral nematic LC cells containing the nematic host, E7, dispersed with chiral dopant (BDH1281) to produce a pitch of 517 nm. (a), (b) and (c) are the speckle contrast maps taken from 10 consecutive runs, with runs 1, 5 and 10 shown, respectively. (d) Plot of the speckle contrast for 5 selected field conditions from the 10 runs. The dotted black line shows the average trend for all data. The cell temperature throughout measurements was held at T = 25°C.

Finally, the same hysteresis test was applied to the 20 µm-thick cell, the results of which are presented in Figure 6.10. In this case, there is a degradation in performance for electric field conditions with frequencies of the applied field higher than that required to generate minimum speckle contrast in the laser image. However, for field conditions at or close to the peak performance observed in this case at $E = 16$ V/µm and 100 Hz, the speckle contrast was found to remain constant at $C = 0.141 \pm 0.004$ throughout the hysteresis tests. This is consistent with the performance seen in Section 5.4.3 in Chapter 5 for the non-ionic-doped cell

consisting of the nematic E7 host dispersed with the chiral dopant R811 to form a chiral nematic phase with a pitch of 518 nm. The cell tested also exhibited constant speckle reduction at the electric field parameters corresponding to peak speckle reduction, with the speckle contrast increasing over time for field parameters slightly outside of that required for optimum device performance.

6.1.7 Summary

In this section, it has been shown that an increase in the cell thickness from 5 μm to 20 μm causes a reduction in the minimum speckle contrast of around 40 – 60% and a decrease in the transmission of at least 50% due to an increase in the magnitude of the light scattering. The electric field amplitude required for minimum speckle contrast appears largely independent of cell thickness whereas, in general, the applied frequency decreases. The threshold voltage for light scattering showed a linear increase with cell thickness.

The hysteresis tests conducted in section 6.1.6 showed that the 5 μm and 20 μm cells exhibited little-to-no reduction in performance through 10 sweeps of a range of field amplitudes and square-wave frequencies. However, the 9 μm cell suffered badly from hysteresis over 10 runs in both tests carried out, with minimum speckle contrast rising by a factor of 2 in the second test.

6.2 Scattering Particles

Scattering particles (SP) such as silicon dioxide (SiO_2) have been added to nematic LCs previously in order to create a static, highly scattering state [92] [93] [94] [95]. When uniformly dispersed, these particles cause a large number of orientational defects, such that a LC with high birefringence becomes highly scattering without

the need for an applied electric field [96]. Typically, these devices are used as an optical switch because the application of an electric field can reorient the LC molecules into a homeotropic nematic alignment, thus making the device appear transparent because the silicon dioxide has a refractive index that is matched to the ordinary refractive index of the nematic LC host.

It is known that nano-particle doping can also be employed to change the electro-optic properties of an LC mixture. For example, titanium dioxide (TiO_2) doping has been shown to decrease the concentration of ions present in a LC mixture, thus reducing the ion diffusion constant [97]. This effect is increased through the use of smaller particles (~5 nm) as this increases the surface area per unit volume of the dopant [98], which can be used to reduce the threshold voltage for display and photovoltaic devices [99].

Additionally, nano-particles have also been used in microfluidic flows as a weak light scatterer for the reduction of laser speckle [100]. In this work, 500 nm-sized particles of poly(methyl methacrylate) with a refractive index of $n = 1.49 - 1.59$ were dispersed in water and pumped through thin tubes. A laser beam was then expanded onto the device with a 5 mm diameter and it was shown that this configuration could be used to reduce the laser speckle observed directly to $C = 0.04$.

In this section, the influence of SPs in a chiral nematic LC mixture on the resulting performance of the laser speckle-reducer device is considered. For this study, microparticles of SiO_2 with a diameter of 1 μm and refractive index of $n = 1.457$ at 633 nm and nanoparticles of TiO_2 with average diameters of 25 nm and refractive index $n = 2.584$ at 633 nm are dispersed into the host chiral nematic

mixture. Initially, a low concentration of 0.25 wt.% of SP are dispersed into a mixture consisting of the nematic LC host, E7, with the high twisting power chiral dopant, BDH1281. Subsequently, a higher concentration of 5 wt.% SiO_2 dispersed in the nematic BL006 with chiral dopant R5011 is considered.

6.2.1 0.25 wt.% concentration of SiO_2 and TiO_2 particles

According to the published literature, the optimum concentration of 25 nm TiO_2 particles in terms of minimum rotational viscosity when dispersed in a nematic LC is 0.25 wt.% [101]. Concentrations of 0.1 – 0.25 wt.% show the quickest response times whereas concentrations above 0.5 wt.% have been shown to suffer from aggregation of particles and poor dispersion [102]. For these reasons, a 0.25 wt.% concentration of both the SiO_2 and TiO_2 particles were added separately to a mixture of the nematic E7 with 4.3 wt.% of the high-twisting power chiral dopant BDH1281. This mixture was found to have a pitch of 320 nm at $T = 25°C$. The SP (either SiO_2 or TiO_2) was added to the chiral nematic host at a temperature of $T = 70°C$ (above the clearing temperature) and were sonicated for 90 minutes to aid dispersion within the mixture. Previous work has shown that particles disperse best at high temperature and in the isotropic liquid phase [103]. Microscope images of each mixture are shown in Figure 6.11.

Subsequently, the cells were subjected to a low-resolution electric field parameter sweep, followed by a high-resolution sweep around the conditions required for peak speckle reduction before a 5-minute steady-state test at peak speckle reduction field conditions was carried out, as described in more detail Section 4.1 of Chapter 4. The speckle contrast colourmaps for the low-resolution sweep are also shown in Figure 6.11. The peak speckle reduction results are

summarised in Table 6.2.

Mixture	(a)	(b)	(c)
Field amplitude (V/μm)	14.5	14.0	14.0
Frequency (Hz)	77.5	65	70
Speckle Contrast (C)	0.169	0.248	0.201
Transmission (%)	16.5%	26.1%	21.6%

Table 6.2: Peak speckle reduction properties for three cells for (a) E7 with BDH1281 with (b) 0.25 wt.% of SiO_2 particles and (c) 0.25 wt.% of TiO_2 particles. All three cells are 20 μm-thick and the temperature throughout all experiments was held at 25°C. These values are taken from a 5-minute steady-state test at optimum speckle reduction field conditions.

These results show that in both cases the addition of SP at a weight concentration of 0.25 wt.% serves to impede speckle reduction considerably when compared to the performance of the base mixture. LC mixtures such as E7 contain molecules with cyano groups, which have been shown to form hydrogen bonds with SiO_2 particles [93]. It is thought that these bonds may increase viscosity, thus reducing the turbulence achieved in the mixture under EHDI conditions. Also, the simulations in Section 8.5.1 of Chapter 8 have shown that concentrations below 2 wt.% of SP typically serve to increase the speckle contrast not decrease it. Unfortunately, these simulations are unable to model the behaviour of the electrical and visco-elastic properties that occurs as a result of the introduction of the SPs, but the model does describe changes in the optical properties.

The electric field amplitude and frequency for peak speckle reduction with the addition of either SP is found to be reduced slightly. This is likely to be because the addition of nanoparticles at such low concentration has been shown to increase ion concentration and reduce rotational viscosity [102] which should serve to

reduce the electric field amplitude for peak speckle reduction.

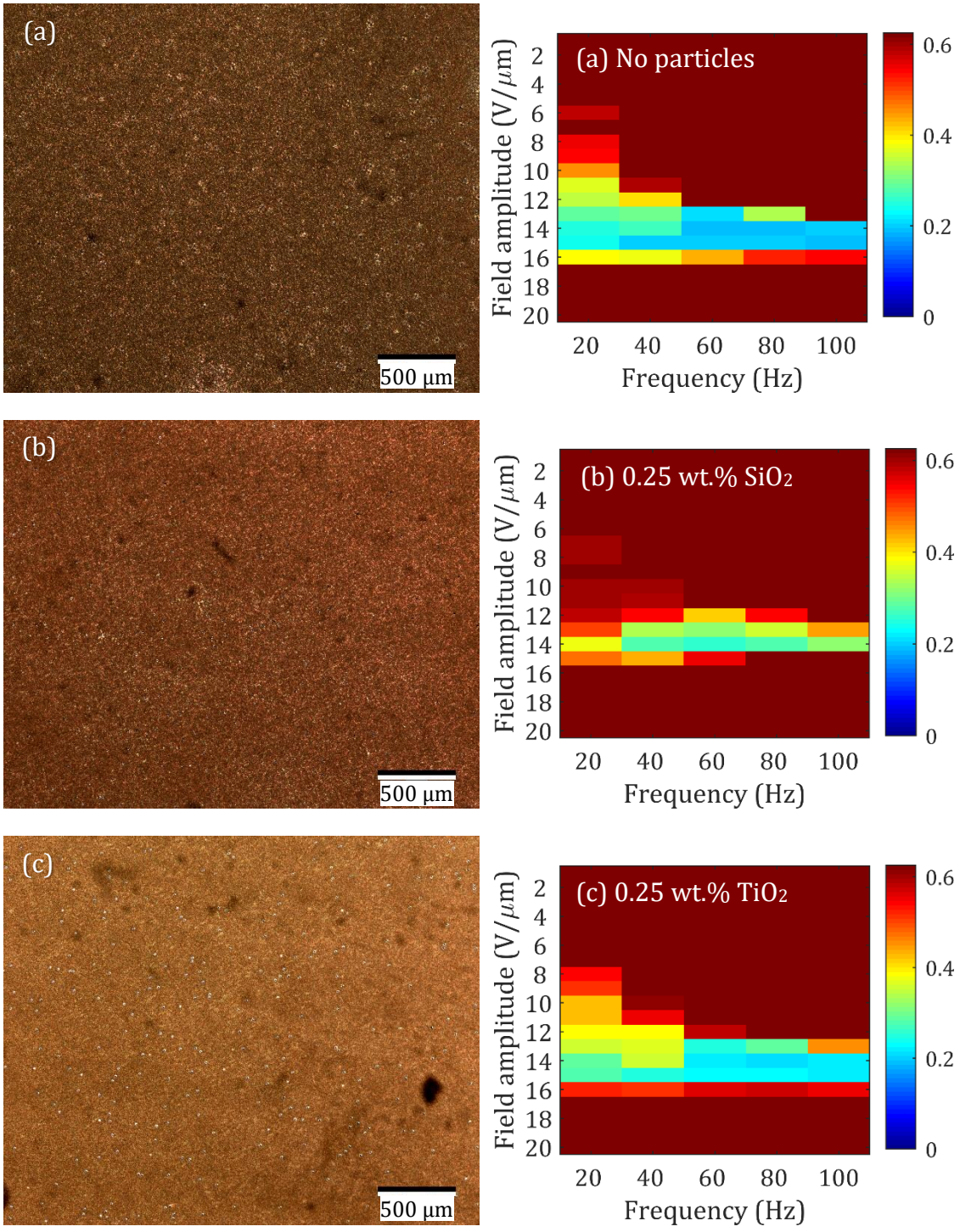

Figure 6.11: (Left) Microscope images at 4 × magnification with crossed polarisers with the application of an electric field for peak speckle reduction. The scale bar depicts a distance of 500 μm. (Right) Speckle contrast maps for a range of applied electric field conditions. The cells tested were 20 μm-thick, chiral nematic LC cells containing the nematic host, E7, dispersed with the chiral dopant (BDH1281) to produce a chiral nematic with a pitch of p = 320 nm. (a) Base chiral nematic mixture without the addition of SP, (b) base mixture with 0.25 wt.% SiO_2 (c) base mixture with 0.25 wt.% TiO_2. The cell temperature throughout measurements was $T = 25°C$.

The increase in transmission seen in both cells doped with SPs is likely to be linked to the reduced light scattering which is in accord with the reduced speckle reduction performance. It is thought that light scattering reduces with SiO_2 particles due to the reduction in spatial frequency of refractive index variation that they introduce in short pitch mixtures due to their comparatively large size and low concentration.

6.2.2 5 wt.% concentration of SiO_2 particles

In this experiment, the effect on the magnitude of the speckle reduction for a chiral nematic device with a larger concentration of SPs is considered. A mixture only capable of moderate (26%) speckle reduction was chosen as the base so that the effect of adding SPs may be expected to be more apparent. The base mixture consisted of the nematic LC, BL006, and chiral dopant, R5011, with a pitch of $p = 270$ nm at 25°C was prepared and Silicon Dioxide particles of diameter 1 μm and refractive index $n = 1.457$ at 633 nm were added at a temperature of 125°C. At this temperature, the mixture was in the isotropic liquid phase. The mixture was then sonicated for 90 minutes before being filled into a 20 μm-thick glass cell. A second cell was made from the base chiral nematic mixture, without SPs for comparison.

Mixture	**(a)**	**(b)**
Field amplitude (V/μm)	15.4	18.6
Frequency (Hz)	40	30
Speckle Contrast (C)	0.46	0.43
Transmission (%)	34.5%	30.5%

Table 6.3: Peak speckle reduction parameters for two devices consisting of base chiral nematic mixture (BL006 with R5011) with (b) and without (a) silicon SP. Cells with SP were filled through capillary action at 125°C. These values are taken from high resolution sweeps of the cells presented in Figure 6.12.

The cells were subjected to a low-resolution field parameter sweep as described previously in Section 4.1 of Chapter 4. Speckle contrast colourmaps presented in Figure 6.12 show the results of these tests, and the results for peak speckle reduction are summarised in Table 6.3. Figure 6.12 also shows microscope images of each cell after filling, before being subjected to the low-resolution electric field parameter sweep. Each photograph was taken with 50 × magnification objective. The small dark specks present throughout photograph in Figure 6.12(b) are the additional silica micro-particles. (Note that the faint specks present in (a) are a result of dust on the objective, not the presence of micro-particles.)

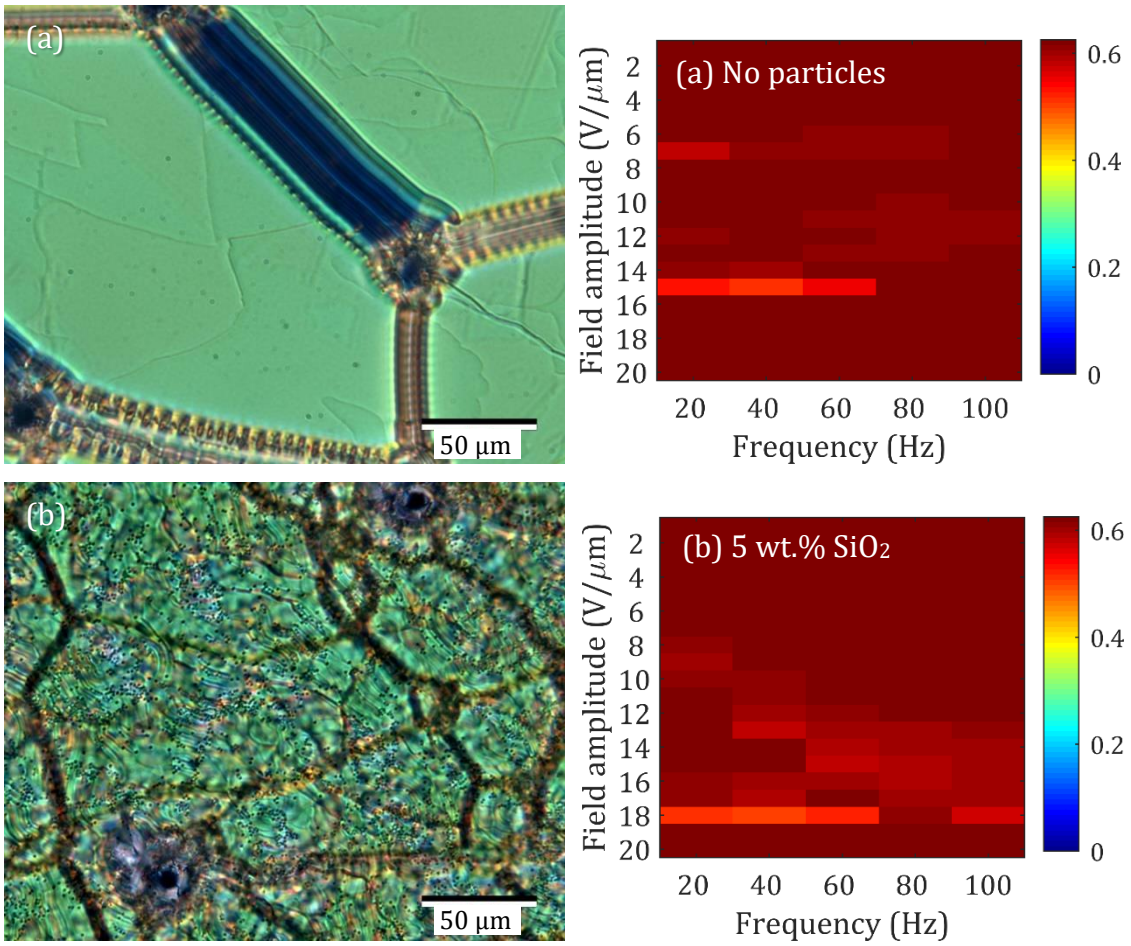

Figure 6.12: (Left) Microscope images at 50 × magnification with crossed polarisers for each chiral nematic LC mixture after filling, before the application of an electric field. The scale bar depicts a distance of 50 μm. (Right) Speckle contrast maps for a range of applied electric field conditions. The cells tested were 20 μm-thick, chiral nematic LC cells containing the nematic host, BL006, dispersed with the chiral dopant (R5011) to produce a pitch of p = 270 nm. (a) Base mixture without SP, (b) base mixture with SP added at 125°C. The cell temperature throughout measurements was held at $T = 25°C$

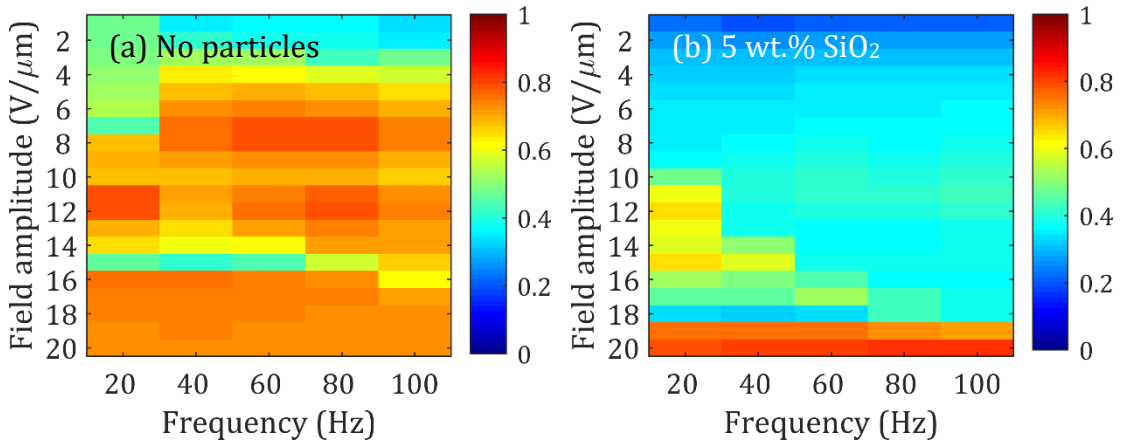

Figure 6.13: Transmission maps for a range of applied electric field conditions. The cells tested were 20 μm-thick, chiral nematic LC cells containing the nematic host, BL006, dispersed with chiral dopant (R5011) to produce a pitch of p = 270 nm, (b) with 5.0 wt.% added silicon dioxide particles and (a) without added silicon dioxide. Cell temperature throughout was T = 25°C.

Figure 6.13 presents transmission values recorded during the low-resolution parameter sweeps. As expected, the cells with the SP show transmission as low as 15% at electric field amplitudes below the threshold required for EHDI, in comparison to 35% for the cell without SP. However, there is only a small decrease in the minimum speckle contrast and the transmission at peak speckle reduction for the cells with SP when compared to the base mixture. This is likely to be because the refractive index of SiO_2 particles ($n = 1.457$) is very similar to that of E7 ($n_o = 1.519, n_e = 1.731$) and therefore the addition of these particles does not cause a significant increase in light scattering from that obtained when driven into the EHDI texture. Nevertheless, as predicted in the simulations, at a concentration of 5 wt.%, the SiO_2-doped mixture achieves significantly better speckle reduction than is seen for a device with only 0.25 wt.% of the SiO_2 scattering particles.

The electric field amplitude for peak speckle reduction increases with the addition of SP from $E = 15.4$ V/μm to $E = 18.6$ V/μm. This corresponds to an increase in the threshold field amplitude for the field-induced homeotropic state.

The threshold electric field amplitude is found to increase from $E = 16$ V/μm to $E = 19$ V/μm providing further evidence that peak speckle reduction occurs at amplitudes of the electric field that are just below that required to induce the homeotropic nematic texture and unwind the helical structure of the chiral nematic phase. It is believed that the higher electric field threshold for the chiral nematic-nematic transition is due to the extra energy required to reorient the molecules that have formed bonds directly with the SP.

6.2.3 Summary

In this section, the effect of adding scattering particles to the chiral nematic LC mixtures on the resulting speckle contrast properties has been investigated. At a low concentration of 0.25 wt.% both SP had the effect of increasing speckle contrast and transmission. It is thought that the introduction of SPs serves to increase viscosity, and at this low concentration there is not sufficient increase in light scattering to compensate for this change and improve device performance.

In contrast, a higher concentration of 5 wt.% of SiO_2 particles caused a slight reduction in speckle contrast in comparison to base chiral nematic mixture from $C = 0.46$ to $C = 0.43$. This was accompanied by a reduction in the transmission, which leads to the conclusion that this is a result of increased light scattering in the device. The improved performance at this concentration is consistent with simulations using short-pitch chiral nematic mixtures presented in Chapter 8. Furthermore, it is noted that both chiral nematic mixtures used in this experiment have high birefringence of $\Delta n > 0.2$. Optical simulations show that scattering particles only increase light scattering in materials with small birefringence of $\Delta n < 0.2$. Future work should be undertaken to test the performance of devices with low

birefringence when scattering particles are added.

6.3 Temperature

The physical properties of a thermotropic LC are known to vary considerably with temperature. In this section, the effect a change in temperature has on speckle reduction for three different compositions is considered. For this study, measurements are carried out at room temperature up to the chiral nematic-isotropic liquid transition temperature.

In general, the pitch decreases slightly with temperature [104] in a chiral nematic LC. The order parameter described in Chapter 2 also reduces with temperature, which in turn causes a reduction in the birefringence and dielectric anisotropy [105], while viscosity reduces with temperature in accordance with the Arrhenius equation as shown in equation 6.2. It has already been shown that the pitch and birefringence of a mixture influence light scattering considerably. Here it is shown that cell temperature has a significant effect on speckle reduction, transmission and peak field conditions. Initial results are presented in Section 6.3.2 before an analysis is carried out in the following sections.

6.3.1 Mixture preparation

Three mixtures were used in this experiment. The concentration, pitch and transition temperature for each mixture is presented in Table 6.4. Each mixture was prepared so that they had a pitch of approximately $p = 250$ nm at $T = 25$°C as this has been shown to reduce speckle effectively in Chapter 4.

Nematic host	Chiral Dopant	wt.%	Pitch (nm)	Clearing temperature (°C)
5CB	BDH1281	5.2	248	35
E7	BDH1281	5.1	273	60
BL006	R5011	unknown	250	115

Table 6.4: Components and corresponding concentrations for the three mixtures used in this study, along with the pitch at a temperature of 25°C and chiral nematic-isotropic liquid transition (clearing) temperature. The weight percentage of the BL006 and R5011 mixture was unknown as it was received already dispersed from Merck.

The pitch of each mixture was determined using UV-vis spectroscopy as described in Section 3.2 of Chapter 3. At room temperature, all mixtures were found to exhibit a chiral nematic phase with a right-handed helical structure. The thickness of each cell was checked using an interference method as described in Section 3.2 of Chapter 3. Cells that differ from the expected thickness, as defined by the spacer beads, by more than 5% were discarded. Table 6.5 summarises the relevant macroscopic physical parameters including the birefringence, rotational viscosity and dielectric anisotropy values for the nematic LC hosts used in this study.

Nematic	Birefringence	Rotational Viscosity (Pa s)	Dielectric Anisotropy
5CB	0.1717 (25°C)	0.091 (25°C)	11.5 (25°C)
E7	0.2116 (25°C)	0.208 (25°C)	13.7 (20°C)
BL006	0.2739 (25°C)	0.43 (20°C)	15.3 (20°C)

Table 6.5: Birefringence (at 633 nm), rotational viscosity and dielectric anisotropy (at 1 kHz) measurements for each nematic used in this section at the specified temperatures (in brackets) provided for comparison. Taken from the literature [105] [70] [73] [106].

Figure 6.14 shows plots of the birefringence as a function of reduced temperature (a) as well as the logarithm of the rotational viscosity as a function of the inverse of

the absolute temperature (b). Both graphs include plots for the devices with nematic LC hosts 5CB, E7 and BL006. Unfortunately, data at high temperatures for BL006 was not available. Reduced temperature is defined here as

$$\text{Reduced Temperature} = \frac{T_{actual}\,(K)}{T_{transition}(K)} \tag{6.1}$$

This enables a presentation of the results on a temperature scale normalised to the transition temperature for each mixture.

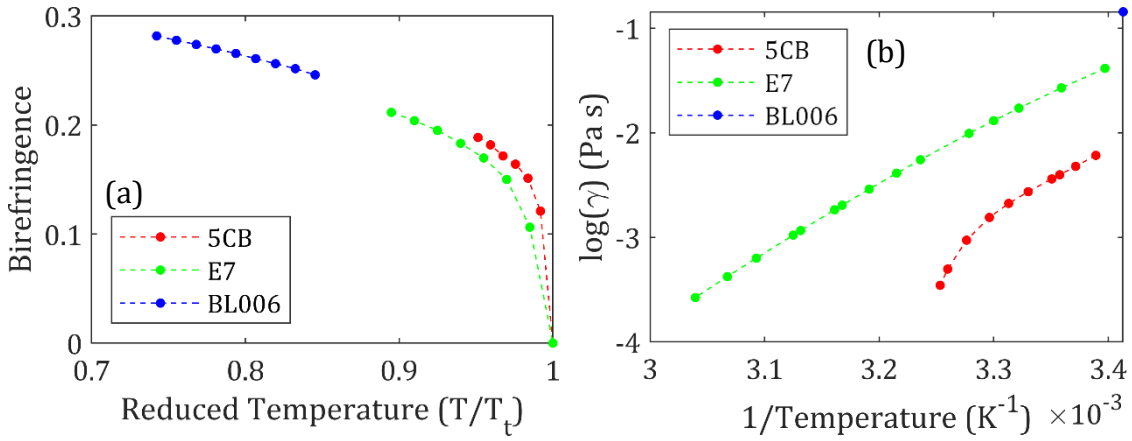

Figure 6.14: Plot of (a) birefringence [70] [107] and (b) the logarithm of the rotational viscosity [105] for the nematic LCs 5CB, E7, and BL006 as a function of the reduced temperature and the inverse of the absolute temperature, respectively. Data points are measured values taken from the literature. Dashed lines are fits used to guide the eye.

In the following sections, the measurements of speckle contrast, transmission, electric field amplitude and frequency are plotted as functions of both the reduced temperature and the inverse of the absolute temperature. In doing so, it should be possible to elucidate whether the LC material parameter in question is dominated by the order parameter (and by extension related properties such as birefringence and dielectric anisotropy) or by the rotational viscosity.

6.3.2 Initial results

Each cell was subjected to a low-resolution electric field parameter sweep as

described in Section 4.1 of Chapter 4. Speckle contrast colourmaps from these experiments are presented for each mixture in Figure 6.15, Figure 6.16 and Figure 6.17. A selection of colourmaps are shown for each mixture from across the range of temperatures tested.

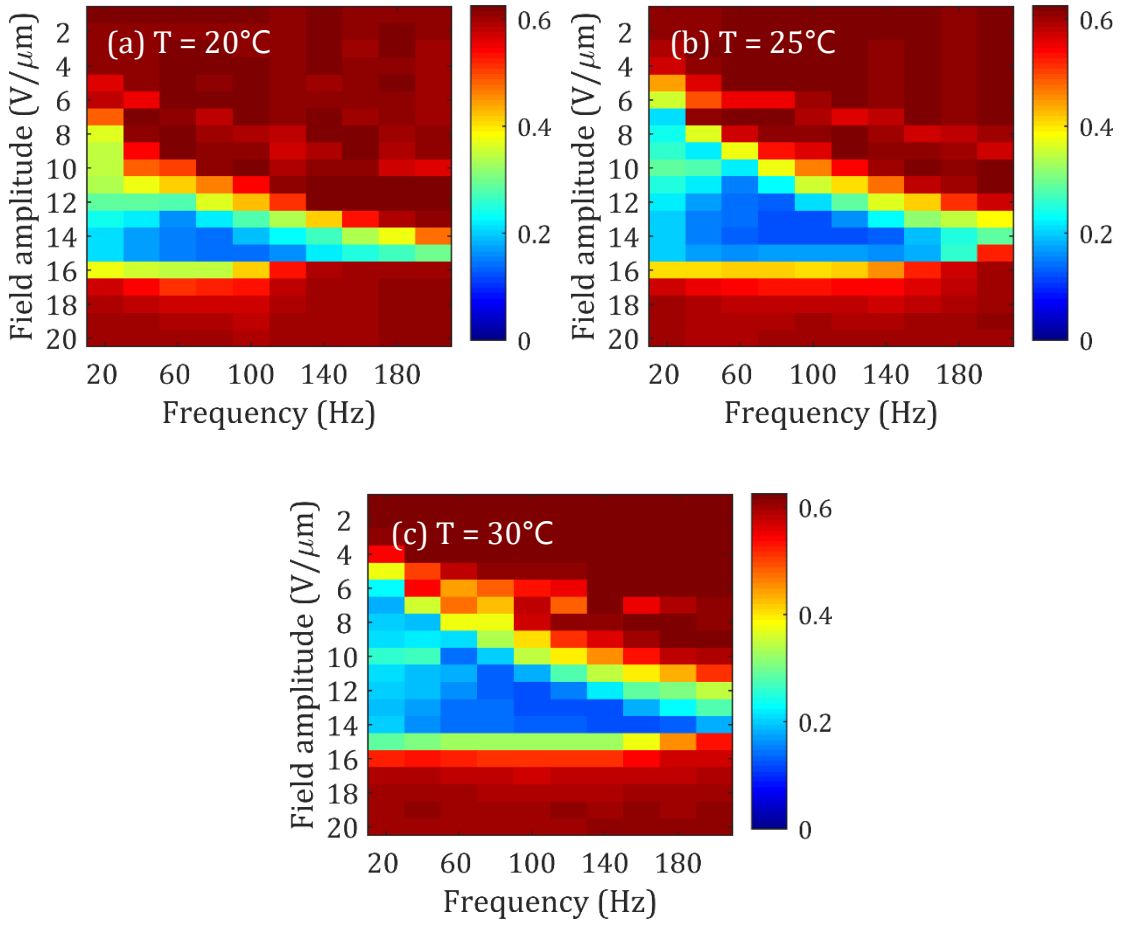

Figure 6.15: Speckle contrast maps for three different operating temperatures. The cells tested were 20 μm-thick, chiral nematic LC cells containing the nematic host, 5CB, dispersed with the chiral dopant (BDH1281) to produce a chiral nematic with a pitch of p = 248 nm. The cell temperature throughout was (a) T = 20°C, (b) T = 25°C, (c) T = 30°C.

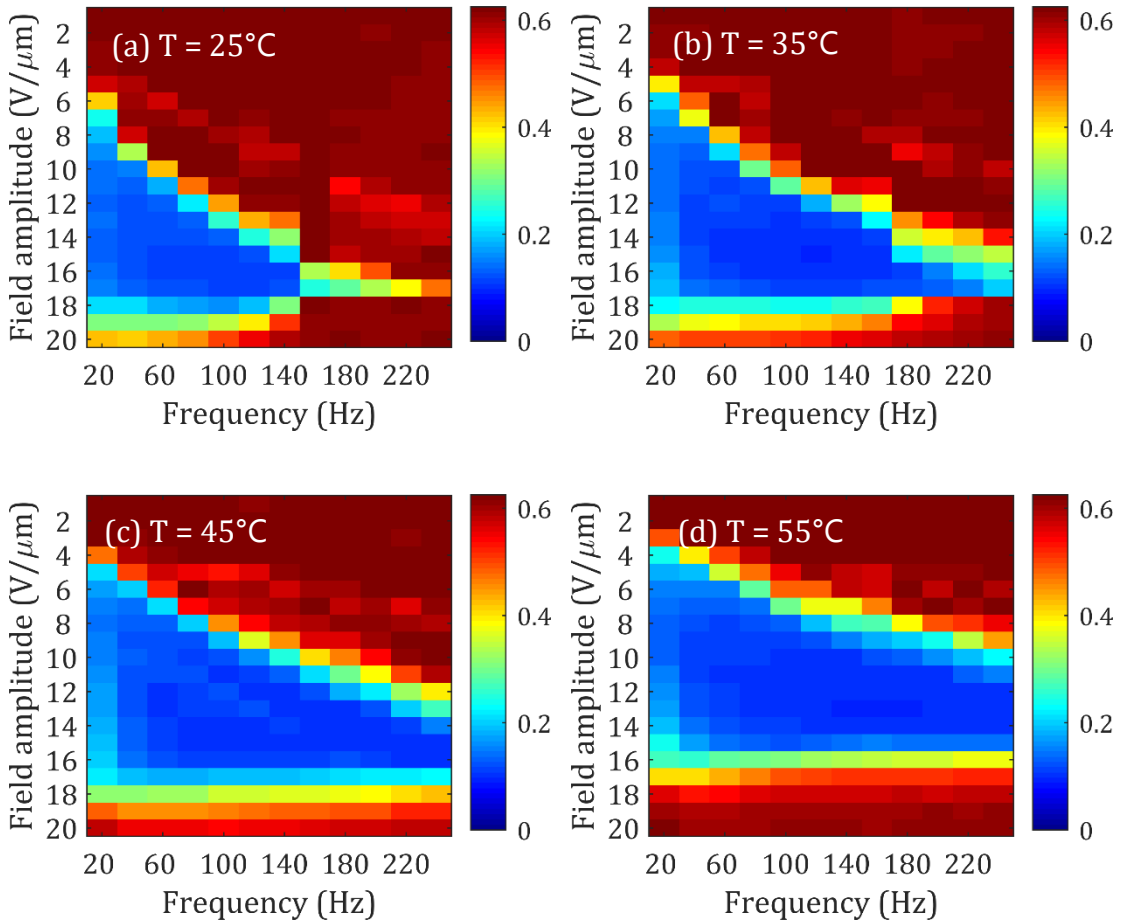

Figure 6.16: Speckle contrast maps for three different operating temperatures. The cells tested were 20 μm-thick, chiral nematic LC cells containing the nematic host, E7, dispersed with the chiral dopant (BDH1281) to form a chiral nematic phase with a pitch of p = 273 nm. Cell temperature throughout was (a) T = 25°C, (b) T = 35°C, (c) T = 45°C, (d) T = 55°C.

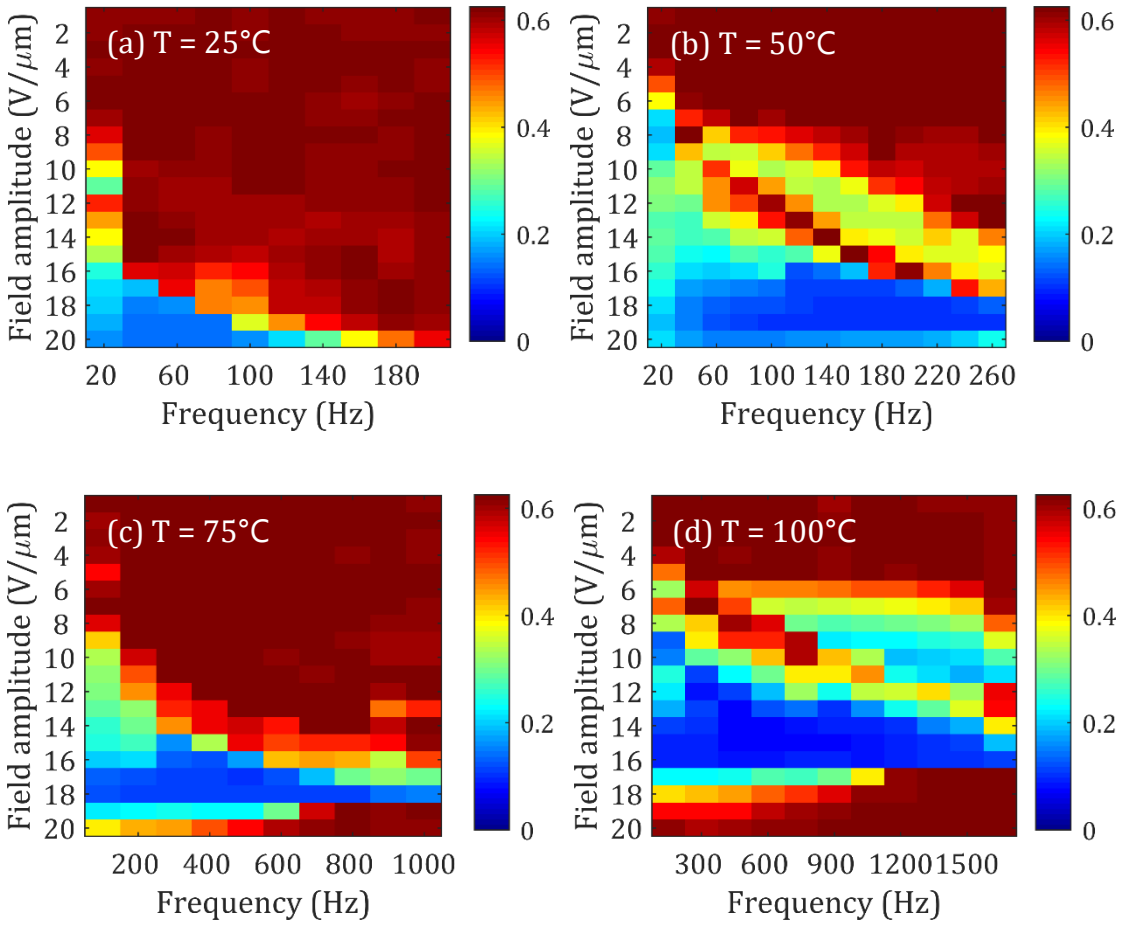

Figure 6.17: Speckle contrast maps for three different operating temperatures. The cells tested were 20 μm-thick, chiral nematic LC cells containing the nematic host, BL006, dispersed with chiral dopant (R5011) to form a chiral nematic phase with a pitch of p = 250 nm. The cell temperature throughout was (a) T = 25°C, (b) T = 50°C, (c) T = 75°C, (d) T = 100°C. Note the change in scale on the x-axis between plots.

6.3.3 Dependence of speckle contrast on temperature

Figure 6.18 shows a plot of the minimum speckle contrast achieved for each mixture during the electric field parameter sweep as a function of reduced temperature (a) and the inverse of the absolute temperature (b). It is clear from these plots that speckle reduction increases with temperature up to the transition temperature for each mixture, with a slight decrease just below the transition temperature. It is well-known that the birefringence reduces with increased temperature [70]. The change in birefringence is considered in the simulations presented in Section 8.3 of Chapter 8 and has already been considered experimentally in Section 4.3.1 of Chapter 4,

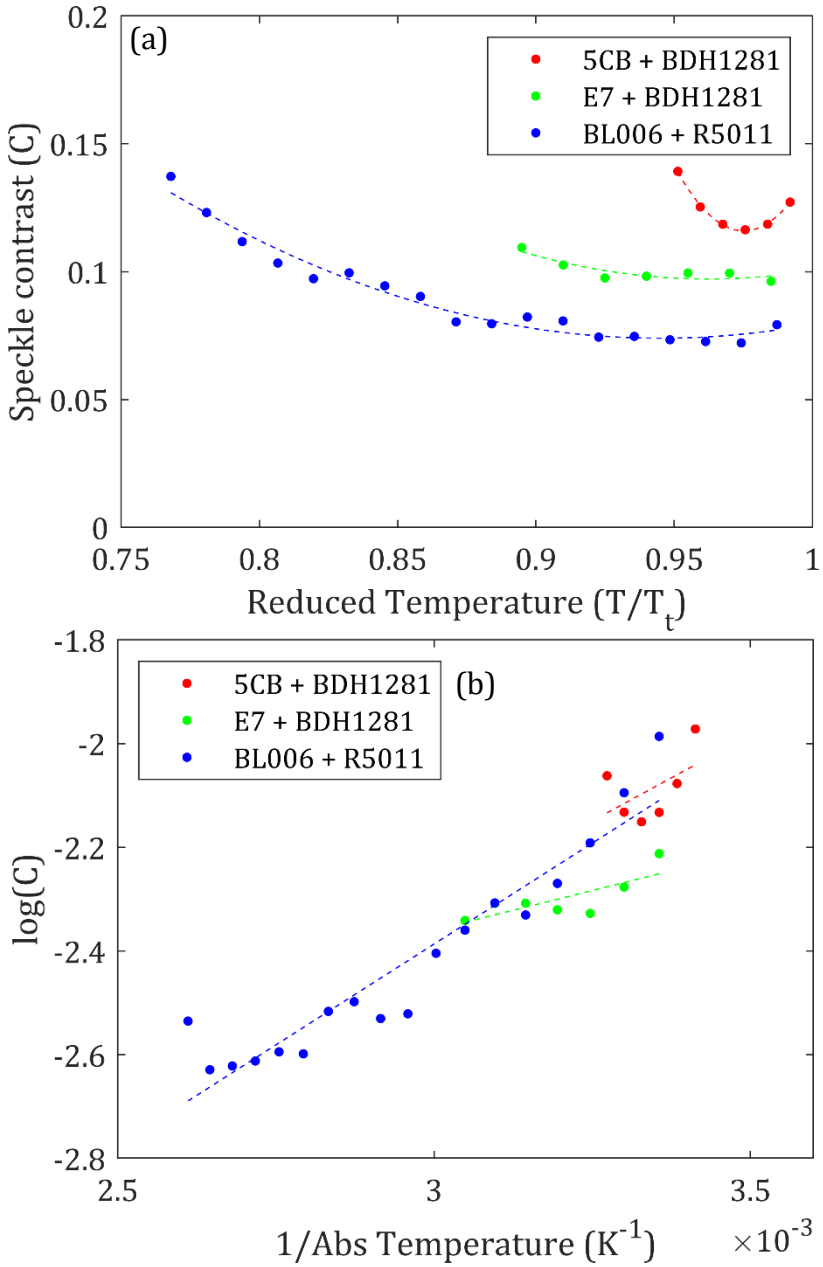

Figure 6.18: Plots of the minimum speckle contrast for three different mixtures at a range of temperatures. (a) Speckle contrast is plotted against reduced temperature. (b) The logarithm of the speckle contrast is plotted against the inverse of the absolute temperature. Each cell was 20 μm-thick. Data points represent measured values whereas the dashed lines are (a) fits of the form $ax^2 + bx + c$ and (b) linear fits to guide the eye.

where, as a general rule of thumb, a decrease in the birefringence leads to a decrease in the speckle reduction as a result of reduced light scattering. However, it is also well-known that the viscosity decreases with an increase in temperature [105], which would allow the local director to move more freely during the EHDI process thus increasing the rate of fluctuations across the device. This effect is analogous to

increasing the exposure time of the camera in experiments and is studied further in Section 6.3.7. This has been shown in other LC devices, with transition and delay times reducing with increased temperature [108]. Effectively, a decrease in the viscosity would serve to increase the number of independent speckle patterns per unit time, which would reduce the magnitude of the speckle contrast. The speckle contrast plots presented here suggest that a reduction in viscosity has a larger effect on the speckle contrast than the reduction in birefringence with increased temperature. This hypothesis is supported by the linear trends that are presented in Fig 6.18(b) in accordance with the Arrhenius dependence. This is further borne out by the fact that E7 has a lower birefringence and rotational viscosity than 5CB at the same reduced temperature, yet the speckle contrast values for the E7 chiral nematic mixture are found to be lower than that of the 5CB chiral nematic mixture.

6.3.4 Dependence of transmission on temperature

Figure 6.19 is a plot of transmission, as defined in Section 4.2.3 of Chapter 4, at minimum speckle contrast of all three mixtures as a function of reduced temperature (a) and the inverse of the absolute temperature (b). There is a clear increase in transmission with increased temperature, despite the reduction in speckle contrast shown in Figure 6.18. This is likely due to the reduction in birefringence as shown in Table 6.5 and Figure 6.14(a) and is consistent with experimental results shown in Section 4.3 and the simulations that will be presented in Section 8.4. Furthermore, the trends shown in Figure 6.19 (a) are very similar for each mixture while the trends in Figure 6.19 (b) do not appear to correlate, indicating that the transmission at peak speckle reduction is dominated by parameters that change with the order parameter, such as the birefringence.

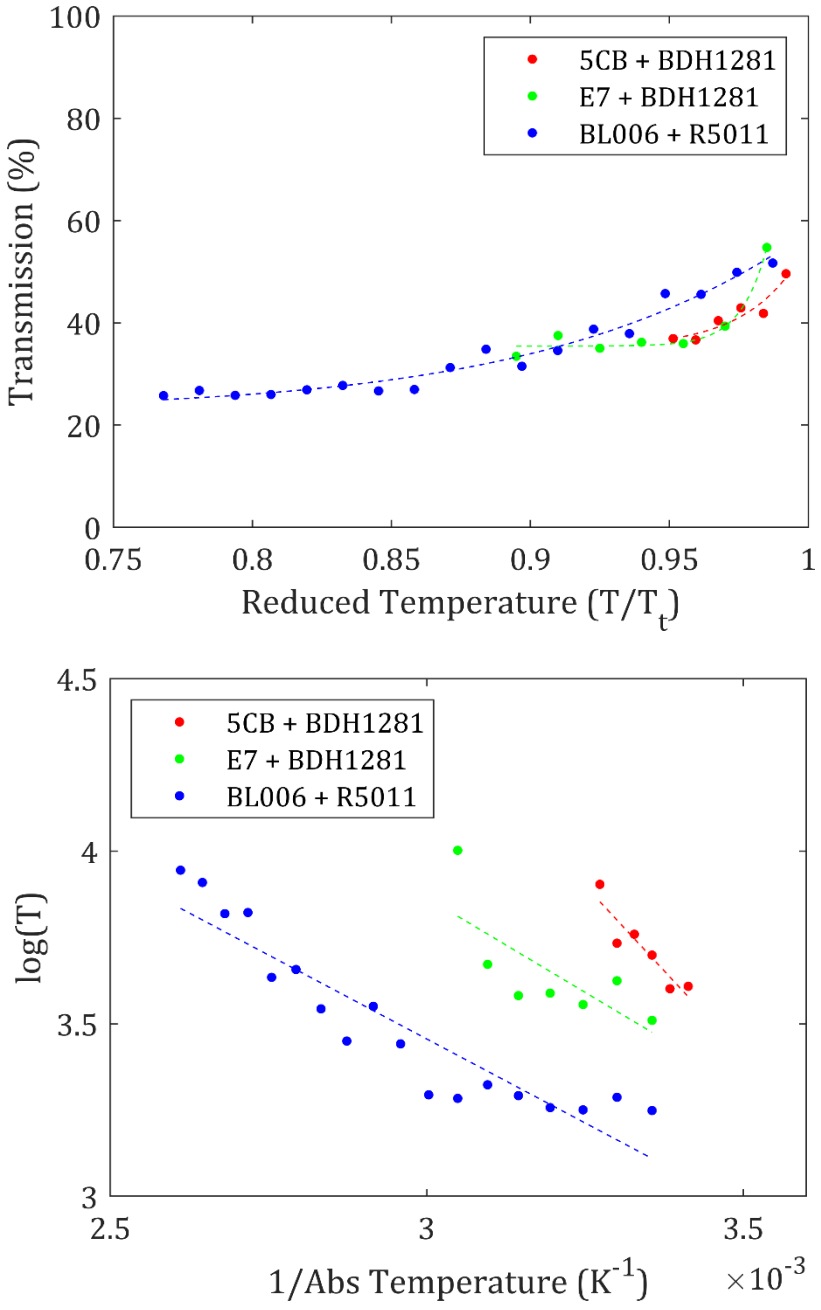

Figure 6.19: Plots of the transmission at minimum speckle contrast for three different mixtures at a range of temperatures. (a) Transmission is plotted against reduced temperature. (b) The logarithm of the transmission is plotted against the inverse of the absolute temperature. Each cell was nominally 20 μm-thick. Data points represent measured values whereas the dashed lines are (a) fits of the form $ax^b + c$ and (b) linear fits in order to guide the eye.

6.3.5 Dependence of field amplitude at peak speckle reduction on temperature

Figure 6.20 is a plot of the electric field amplitude required for peak speckle reduction for each cell as a function of reduced temperature (a) and the inverse of the absolute temperature (b).

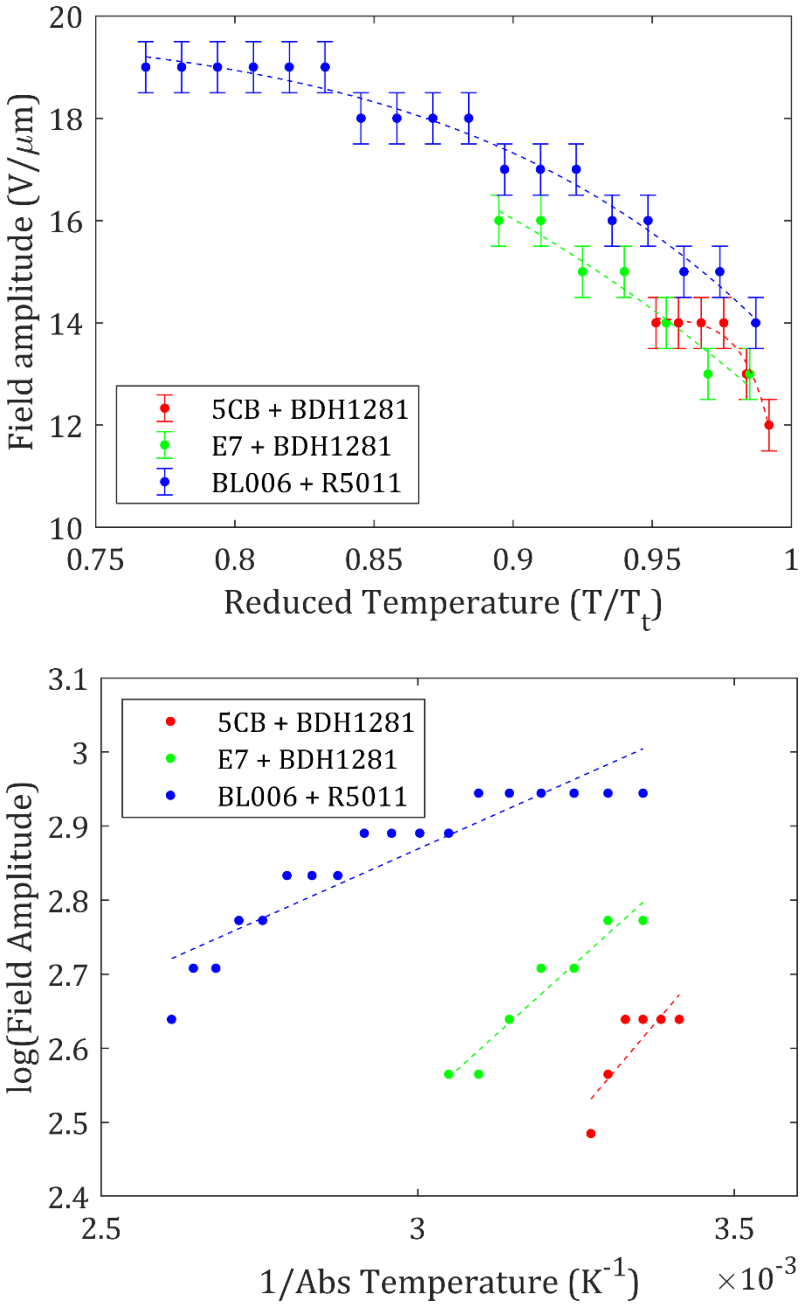

Figure 6.20: Plots of the electric field amplitude at minimum speckle contrast for three different mixtures at a range of temperatures. (a) Electric field amplitude is plotted against reduced temperature. (b) The logarithm of the electric field amplitude is plotted against the inverse of the absolute temperature. Each cell was 20 μm-thick. Data points represent measured values whereas dashed lines are (a) fits of the form $ax^b + c$ and (b) linear fits in order to guide the eye. Error bars represent the resolution of field amplitudes used in this experiment.

The electric field amplitude for peak speckle reduction reduces for all mixtures with an increase in temperature. The plots in Figure 6.20(a) show a similar reduction for all three mixtures and follow the behaviour of the order parameter with

temperature.

It is expected that this is mainly due to the reduction in the elastic constant for twist deformation K_{22} that each mixture experiences with increased temperature [109] as less electromotive force is required to move ions through the mixture. As previously shown in equation 5.2, this causes a reduction in the threshold field for field-induced homeotropic orientation and has been shown to reduce with the square of the order parameter. As noted in Section 5.4.1.4 the electric field amplitude for peak speckle reduction appears to be closely related to this threshold field, so the results presented here are consistent with this hypothesis.

Conversely, it has been shown that increased temperature causes a reduction in dielectric anisotropy in LCs [106] [110] which, according to equation 5.2, would serve to increase the threshold field. Consequently, it is speculated that the reduction in the magnitude of the elastic constants is of much greater importance than the reduction in dielectric anisotropy.

Figure 6.20(b) does not reveal an obvious relationship between the electric field amplitude and the absolute temperature for the three mixtures considered in this study. These findings suggest that the reduction in electric field amplitude required for peak speckle reduction is dominated by the reduction in the order parameter, and not by the reduction in viscosity. This is in good agreement with the theory that the electric field amplitude required for peak speckle reduction is related to the electric field amplitude for the chiral nematic-nematic transition, in accordance with equation 5.2, which does not dependent on viscosity.

It is interesting to note that the room temperature measurements taken for the BL006 and E7 mixtures (the lowest reduced temperature data point in each set) match well with the experimental results given in Section 4.2.4. It was shown that the electric field amplitude for peak speckle reduction followed a close inverse relationship with the pitch for mixtures based on the nematic hosts, BL006 and E7. However, the 5CB mixture has a slightly smaller pitch than the BL006 mixture, but considerably smaller electric field amplitude for peak speckle reduction at room temperature. This could be a result of the significantly lower viscosity of 5CB at room temperature.

6.3.6 Dependence of frequency at peak speckle reduction on temperature

Figure 6.21 is a plot of the square wave frequency required for peak speckle reduction for each mixture as a function of reduced temperature (a) and the inverse of the absolute temperature (b). It is clear from this data that the frequency for peak speckle reduction increases with increasing temperature. This is likely again to be a result of the decreased viscosity, which is in accord with equation 4.2: the Hurault relaxation frequency of chiral nematic LCs. Figure 6.21(b) supports this hypothesis as the relationship between frequency and absolute temperature is consistent throughout the three mixtures, whereas there is no clear relationship shown in Figure 6.21(a) when comparing frequency to reduced temperature. The frequencies for the 5CB mixture are slightly smaller than those for the E7 mixture at similar reduced temperatures, which again is likely due to 5CB being slightly more viscous than E7, as shown in Figure 6.14(b). The significantly higher frequencies required for peak speckle reduction in the BL006 mixture are liekly a result of significantly reduced viscosity at the higher temperatures of the chiral nematic phase of BL006

before the phase transition to an isotropic liquid.

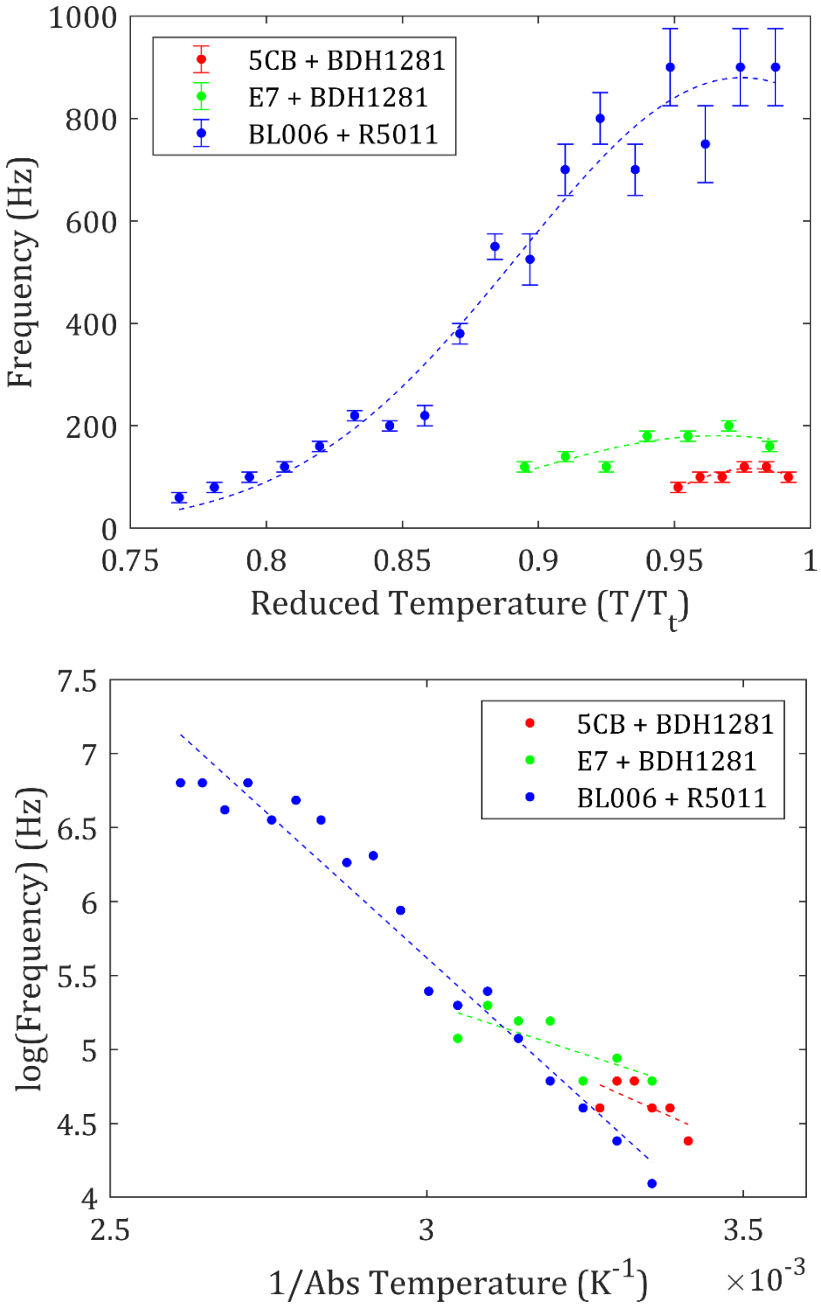

Figure 6.21: Plot of square-wave frequency at minimum speckle contrast for three different mixtures at a range of temperatures. (a) Frequency is plotted against reduced temperature. (b) The logarithm of the frequency is plotted against the inverse of the absolute temperature. Each cell was 20 μm thick. Data points are measured values. Dashed lines are (a) gaussian fits and (b) linear fits to guide the eye. Error bars represent the resolution of frequencies used in this experiment.

6.3.7 Exposure test

In Section 3.4.2.3 the speckle contrast of a cell at peak speckle reduction field

conditions was presented as a function of the camera exposure time. In Section 6.3.3, the idea that a decrease in viscosity would be similar to increasing the exposure time of the camera was discussed as it allows the molecules (director) to move more freely thus providing a greater number of independent speckle patterns per unit time. In this section, this idea is explored further by measuring the speckle contrast of a LC cell across a range of exposure times and across a range of temperatures.

The device used in this experiment was a mixture of the nematic LC, E7, with 4.3 wt.% of the chiral dopant BDH1281, resulting in a chiral nematic LC with a pitch of 320 nm. As before, the cell underwent a low-resolution electric field parameter sweep, followed by a high-resolution sweep around the conditions of peak speckle reduction. Measurements concluded with a 5-minute steady-state test at the optimum field conditions to ensure that the cell behaved consistently, at each temperature tested. Figure 6.22 is a plot of speckle contrast under these conditions as a function of exposure time at temperatures of $T = 25°C$, 35°C, 45°C and 55°C. the inset is a graph that only scales $0 - 50\ ms$ to show the behaviour over this range more clearly.

It is clear from the inset that speckle contrast reduces more quickly with increased exposure time as the temperature is increased. This is consistent with the data presented in 6.3.3. Also, the lowest speckle contrast values reached by each temperature at an exposure time of 2 seconds increases with temperature. This is also consistent with the previous reasoning as the increased viscosity does appear to allow the director to move more freely, but the maximum reduction is lower due to a decrease in the birefringence with increased temperature.

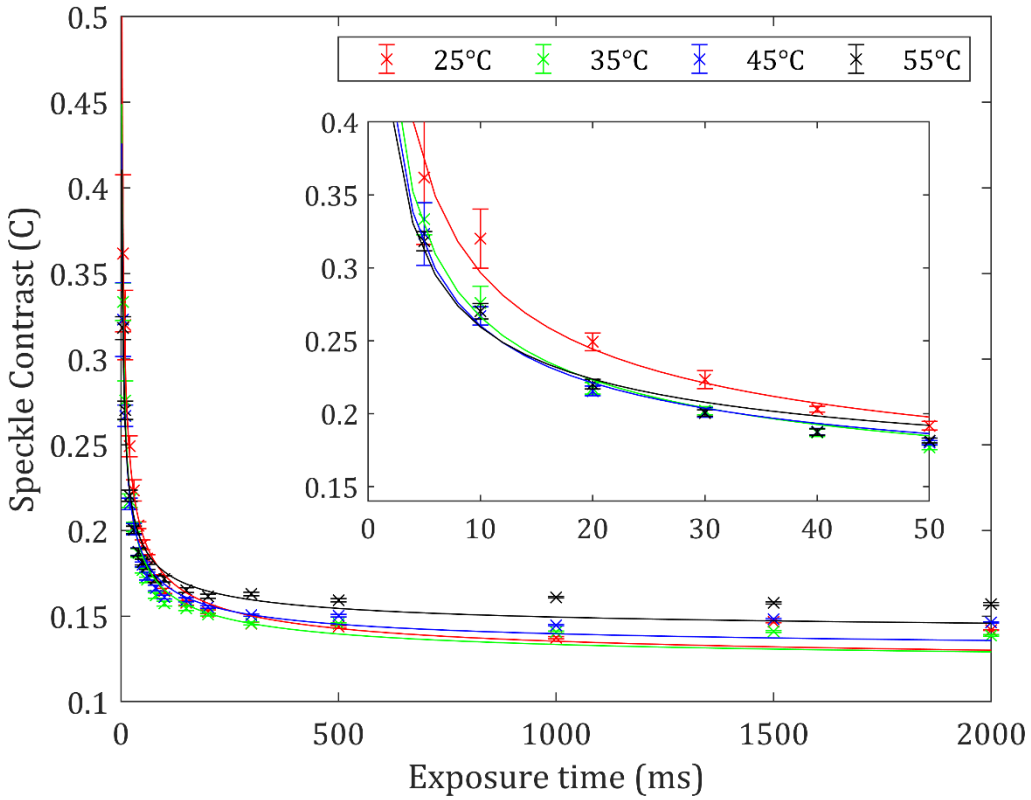

Figure 6.22: Plot of the speckle contrast as a function of exposure time for a range of operating temperatures. Each cell was 20 µm-thick and contained the nematic LC E7 with 4.3 wt.% of chiral dopant BDH1281. The electric field conditions required for peak speckle reduction at each temperature was applied throughout the experiment. Data points are measured values. Error bars represent the range of values measured over 20 separate readings. Lines of best fit are of the form $ax^{-0.5} + b$.

To test this hypothesis further the fact that viscosity is known to follow the Arrhenius equation of the form is considered:

$$\gamma = Ae^{-\frac{B}{T_{abs}}} \tag{6.2}$$

where γ is the rotational viscosity and A and B are constants. The data presented in Figure 6.22 includes lines of fit of the form $C = ax^{-0.5} + b$ where x is the exposure time. If one expects the speckle contrast for increased temperature to scale in the same way as it does with exposure time, as a result of a decrease in viscosity, then

one can relate the constant a with γ as such:

$$a = Ce^{-\frac{B}{T_{abs}}} \tag{6.3}$$

where C is a constant. Rearranging one gets

$$\ln a = \ln C - \frac{B}{T_{abs}} \tag{6.4}$$

Therefore, if one plots $\ln a$ as a function of $1/T_{abs}$ one would expect a straight line. This plot is presented below in Figure 6.23. Unfortunately, there are only a small number of data points for the comparison, nevertheless, the data does show the expected linear relationship within experimental error, but future work is required to verify this hypothesis.

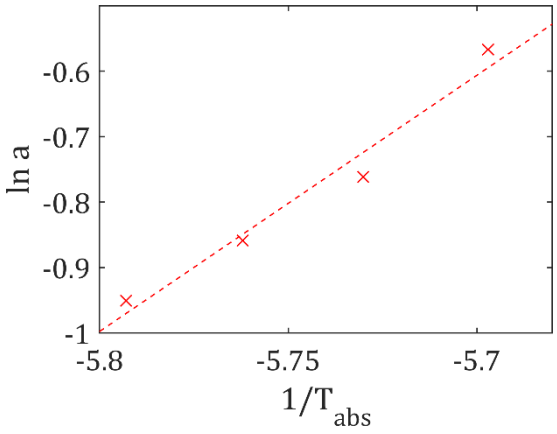

Figure 6.23: Plot of $\ln a$ as a function of $1/T_{abs}$ for the data fits presented in Figure 6.22. Data points are calculated from the fitting constants and temperature conditions. The dashed line is a line of best fit.

6.3.8 Summary

In this section, results on the speckle contrast, transmission and field conditions required for peak speckle reduction over a range of operating temperatures were presented. It has been shown that an increase in temperature serves to decrease the speckle contrast, increase transmission, reduce the field amplitude required for

peak speckle reduction and also increases the frequency for peak speckle reduction. These changes have been explained, at least qualitatively, by considering the reduction in birefringence, viscosity and dielectric anisotropy as the operating temperature is increased. It was also shown that an increase in the temperature is analogous to increasing the camera exposure time as a result of a reduction in the viscosity.

It would appear that the viscosity has the largest effect on speckle reduction and future work should be focussed on using LCs with low viscosity, or using viscosity reducing agents. While an increase in birefringence does increase scattering, it does so at the expense of transmission, likely due to an increase in scattering angle and the proportion of light that is backscattered. Devices appear to perform best at temperatures just below the transition to the isotropic liquid phase, where they have very low viscosity and birefringence. For this reason, a mixture could be chosen that has a transition temperature just above the operating temperature at which it is intended to be used.

6.4 Concluding remarks

In this chapter, the influence of the cell thickness, scattering particles and cell temperature on the performance of an LC device was presented in terms of the magnitude of the speckle reduction, transmission and electric field parameters. This has helped to optimise not only these environmental parameters, but also to gain further understanding of the role of the LC parameters.

The study on cell thickness showed that an increase from 5 μm to 20 μm resulted in increased light scattering, which was evidenced through a decreased

speckle contrast ratio and transmission. The electric field amplitude required for peak speckle reduction was shown to be independent of cell thickness and the frequency was, in general, found to be inversely proportional to the cell thickness. Further tests showed that a 9 μm cell gap appeared to be highly susceptible to hysteresis, with almost no speckle reduction observed after 10 cycles of the electric field parameters. 5 μm and 20 μm-thick cells, on the other hand, appeared to perform consistently at peak speckle reduction field conditions, but speckle reduction decreased at conditions close to peak performance. This is likely to be due to the shielding effect when ions collect at an electrode. At optimum field conditions, the electric field would reverse before too many ions reach the electrode thus limiting this effect. It is unlikely that there is a permanent electro-chemical reaction occurring at the electrodes, particularly for the 5 μm and 20 μm-thick cells because the performance is consistent throughout the parameters sweeps at peak speckle reduction field conditions, despite the reduction in performance at the other field conditions. However, at this stage the reason for the reduction in performance observed for the 9 μm-thick cells is not known and further studies are required to elucidate the cause of the degradation.

The study on scattering particles showed that increasing the refractive index contrast does not necessarily reduce the speckle contrast beyond that seen with the base chiral nematic mixtures. It is likely that the small concentration (0.25 wt.%) of micro- or nano-particle failed to further reduce speckle contrast over the base LC mixture simply because the concentration was too low. This will also be considered in the simulations to be presented in Chapter 8 for SiO_2 particles. These additional particles have been reported to form bonds with LCs which is expected to increase

viscosity. The higher concentration of 5 wt.% of SiO_2 was shown to reduce speckle contrast more than the base mixture it was added to. However, the improvement in the speckle reduction was small, corresponding to a decrease in the speckle contrast from $C = 0.46$ to $C = 0.43$. Further work is required to gain more understanding on the effect of adding SPs.

Finally, a study on cell temperature showed that an increase in temperature serves to decrease speckle contrast, increase transmission, decrease field amplitude for peak speckle reduction, and increase frequency for peak speckle reduction. This was true for all three mixtures tested despite their nematic temperature ranges varying considerably, as well as other properties such as birefringence and viscosity at room temperature. It is well-known that the viscosity, birefringence, dielectric anisotropy and elastic constants all reduce with an increase in temperature, but it was shown that the property expected to have the largest effect on speckle contrast appears to be the viscosity. In all cases, each device performed best at just below the transition temperature to the isotropic liquid phase. At this temperature, the low viscosity allows the molecules (director) to move more freely, thus increasing the number of independent speckle patterns that are created per unit time. This was shown to be analogous to increasing the exposure time of the camera. At these temperatures, the birefringence was also at a minimum, which has been shown experimentally (and will be considered in simulations in Chapter 8) to decrease light scattering, and hence speckle contrast. Also, the dielectric anisotropy is at its lowest at this temperature, which has been shown to increase the field amplitude required for peak speckle reduction. However, both effects were clearly overwhelmed by the effect of the reduction in viscosity.

In conclusion, it has been shown in this chapter that the optimum LC mixture would exhibit minimal viscosity for increased speckle reduction and decreased electric field amplitude. Under these circumstances it is possible to use a mixture with relatively low birefringence to improve transmission. Cell thickness should be at least 20 μm as this avoids the reduced performance of thinner cells with regards to speckle reduction, lifetime and hysteresis. Scattering particles do not appear to aid speckle reduction in mixtures with high birefringence, and if used should be mixed at a relatively high concentration. A LC device shows optimum performance at a temperature just below the clearing temperature. Consequently, a mixture could be chosen with clearing temperature just above the expected operating temperature of the device.

7 Simulating the Speckle Contrast of a Liquid Crystal Scattering Device

In this chapter, a model for the LC speckle reduction system is developed to improve understanding of the process by which the device reduces the speckle contrast and to investigate the effect of varying a range of properties specific to the LC mixture, the cell architecture and the position of the optical components. This section begins with a review of Maxwell's equations and, with the help of necessary simplifying assumptions, derives a set of formulae that describe wave propagation through a thin LC film, through free-space and through the relevant optical components. These equations are then implemented in to a purpose-built MATLAB code.

This chapter provides a detailed overview of the important steps that progress from Maxwell's equations to the convolution and Fourier transform approach adopted in the MATLAB code. For a more rigorous derivation of the principles highlighted here the following work of [111] and/or [112] should be consulted.

7.1 Propagation in free-space

7.1.1 From Maxwell's equations to the wave equation

Maxwell's equations define the interaction between magnetic and electric fields. As such, the fundamental physics underpinning electromagnetic radiation can be derived from these ubiquitous equations. The four well-known Maxwell's equations

in an isotropic medium, in differential form, can be written as:

$$\nabla \times \mathbf{E} = -\frac{\partial \mathbf{B}}{\partial t} \tag{7.1}$$

$$\nabla \times \mathbf{B} = \mu \mathbf{J} + \mu\varepsilon \frac{\partial \mathbf{E}}{\partial t} \tag{7.2}$$

$$\nabla \cdot \mathbf{E} = \frac{\rho}{\varepsilon} \tag{7.3}$$

$$\nabla \cdot \mathbf{B} = 0 \tag{7.4}$$

These show that an oscillating electric field **E** is induced by a magnetic flux density **B** that varies in time (from Faraday's law of induction, equation 7.1), and that a divergent electric field is induced by a point charge of charge density ρ (according to Gauss' law for electrostatics, equation 7.3). Alternatively, an oscillating magnetic field can be induced both by the flow of charge (with current density **J**) and a time-varying electric field (Ampere's law with Maxwell's correction, equation 7.2). There is no way of creating a divergent magnetic field because there is no such thing as a 'magnetic monopole' (Gauss law for magnetostatics, equation 7.4). These relationships are also influenced by the constitutive equations involving the magnetic permeability μ and the dielectric permittivity ε of the material in which the electromagnetic waves propagate.

If it is assumed the wave is propagating in a dielectric medium there would be no free electric charges and therefore also no electric current, equations 7.2 and 7.3 then become:

$$\nabla \times \mathbf{B} = \mu\varepsilon \frac{\partial \mathbf{E}}{\delta t} \tag{7.5}$$

and

$$\nabla \cdot \mathbf{E} = 0, \tag{7.6}$$

respectively. It is further assumed that the propagation medium is linear, isotropic, homogenous (with constant ε) and non-dispersive. Considering now the curl of equation 7.1 and substituting like terms from equation 7.5 leads to

$$\nabla \times (\nabla \times \mathbf{E}) = -\mu\varepsilon \frac{\partial^2 \mathbf{E}}{\partial t^2} \tag{7.7}$$

Using the vector calculus identity $\nabla \times (\nabla \times \mathbf{E}) = \nabla(\nabla \cdot \mathbf{E}) - \nabla^2\mathbf{E}$ and equation 7.6, simplifies to the wave equation:

$$\nabla^2 \mathbf{E} - \frac{n^2}{c^2} \frac{\partial^2 \mathbf{E}}{\partial t^2} = 0 \tag{7.8}$$

where $c = 1/\sqrt{\mu_0 \varepsilon_0}$, the velocity of propagation of an electromagnetic wave in a vacuum and $n = \sqrt{\varepsilon/\varepsilon_0}$, the refractive index of the medium. A similar derivation also leads to the equivalent wave equation in terms of the magnetic field flux density whereby

$$\nabla^2 \mathbf{B} - \frac{n^2}{c^2} \frac{\partial^2 \mathbf{B}}{\partial t^2} = 0 \tag{7.9}$$

7.1.2 Helmholtz equation

A solution to these equations describes a propagating electromagnetic wave. For what follows, it is helpful to consider the temporal and spatial components separately. If the wave is assumed to be monochromatic, as in the case of a laser source, for example, the temporal component is simply an oscillation in time at a fixed frequency and a solution to the wave equation can thus be defined as

$$\mathbf{E}(x, y, z, t) = \mathbf{E}(x, y, z)e^{-j\omega t} \tag{7.10}$$

where ω is the angular frequency of the electromagnetic wave. Substituting this expression into equation 7.8, one arrives at the Helmholtz equation:

$$(\nabla^2 + k^2)\mathbf{E}(x, y, z) = 0 \tag{7.11}$$

where the wavenumber k is defined as

$$k = \frac{2\pi n v}{c} = \frac{2\pi}{\lambda} \tag{7.12}$$

and v is the frequency of light, given by $\omega = 2\pi v$.

7.1.3 Scalar Theory

The differential operator ∇^2 acts independently on each rectilinear component of the electric field, **E**, and the magnetic field, **H,** so it is possible to summarise equation 7.11 as a single, complex, scalar wave equation that represents a generic component at position P.

$$(\nabla^2 + k^2)\mathrm{E}(P) = 0 \tag{7.13}$$

This approximation breaks down when there is coupling between the separate components and occurs when boundary conditions are imposed on a wave, for example when light passes through an aperture. The **E** and **H** fields interact with the material the aperture is made from and the effect extends into the aperture by several wavelengths. However, scalar theory is accurate so long as the diffracting elements are large compared to the wavelength of propagation.

7.1.4 Huygens-Fresnel principle

Due to the mathematical complexity involved when describing the diffraction of electromagnetic waves there are consequently very few rigorous solutions to the spatial component of the wave equation, and those that do exist are subject to limiting boundary conditions. As a result, approximate methods must be used to describe practical light propagation. The Huygens-Fresnel principle is considered the most generally applicable approach and has been shown to match experimental results closely in most practical situations. It states that every point on a propagating wavefront can be considered a secondary source of spherical wavelets, and that these wavelets interfere to form the envelope of the next wavefront as shown in Figure 7.1.

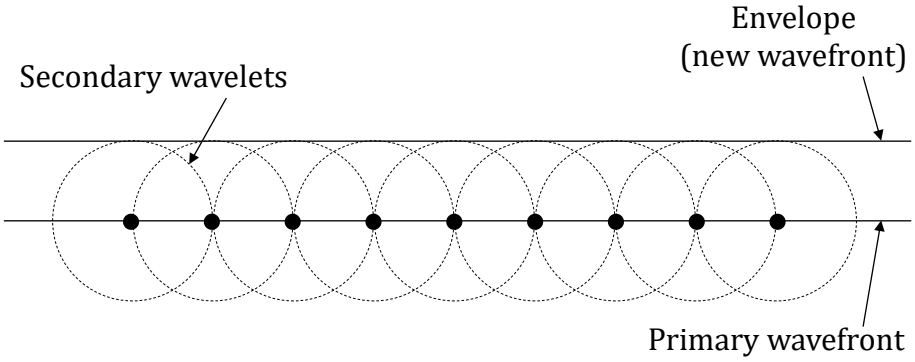

Figure 7.1: Illustration of the Huygens-Fresnel principle.

Using this approach, it is possible to describe mathematically the component of light at an arbitrary point P_1 in the (x_1, y_1) plane that has propagated from such a secondary source in an arbitrary position P_0 in the parallel (x_0, y_0) plane some distance z away (as shown in Figure 7.2). In this case, the electric field can be written as such:

$$\mathrm{E} = \mathrm{E}_0 \left\{ \frac{\exp(jkr_{01})}{r_{01}} \right\} \cos\theta \tag{7.14}$$

where r_{01} is the distance between both points, E_0 is a complex number describing the phase and amplitude of light at P_0 and θ is the angle between the line r_{01} and the line z that describes the perpendicular distance between both planes.

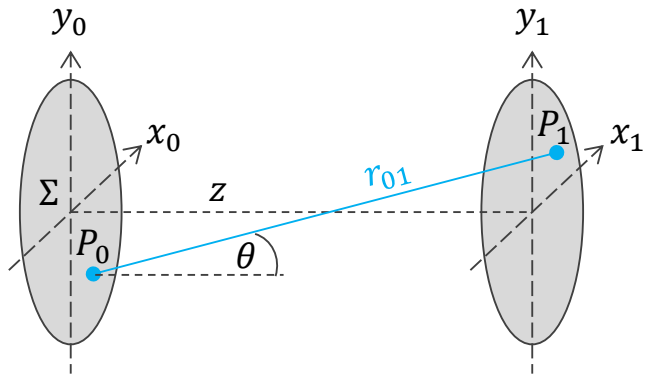

Figure 7.2: Geometry of light propagation from a point P_0 in the plane (x_0, y_0) to a point P_1 in the plane (x_1, y_1) in the z direction.

The total field at the point P_1 can be found by integrating over the input wave area, Σ, assuming prior knowledge of the amplitude and phase of light across this area, $E_0(P)$:

$$\mathrm{E}(\mathrm{P}_1) = \frac{1}{j\lambda} \iint_{\Sigma} E(P_0) \frac{\exp(jkr_{01})}{r_{01}} \cos\theta \, ds \tag{7.15}$$

The $\cos\theta$ term is given exactly by:

$$\cos\theta = \frac{z}{r_{01}} \tag{7.16}$$

which allows equation 7.15 to be rewritten as:

$$\mathrm{E}(\mathrm{P}_1) = \frac{z}{j\lambda} \iint_{\Sigma} E(P_0) \frac{\exp(jkr_{01})}{r_{01}^2} ds \tag{7.17}$$

Also, the r_{01} term can be expressed from geometrical considerations as:

$$r_{01} = \sqrt{z^2 + (x_1 - x_0)^2 + (y_1 - y_0)^2} \tag{7.18}$$

The derivation behind equation 7.15 was initiated by Fresnel who applied calculus to Huygens' wave theory. Kirchhoff later derived a very similar expression by applying Green's theorem to find a solution to the homogenous wave equation. (The $1/j\lambda$ factor in front of the surface integral comes from a combination of the normalisation factor of the volume integral and the derivatives from Green's identity when converting from a volume integral to a surface integral.) His approach required two assumptions about the boundary conditions that were shown to be inconsistent with each other, but his integral solution was shown to closely match experimental results in most cases regardless. These inconsistencies were later removed by Sommerfeld with the use of alternative Green's functions. One further assumption was made when deriving equation 7.15 which is that $r_{01} \gg \lambda$.

7.1.5 Further approximations

To reduce the complexity of the Huygens-Fresnel principle several further approximations can be made. First, the binomial expansion of $\sqrt{1+b}$ is used to find an approximation for r_{01} in equation 7.18. This is effectively the mathematical equivalent of the paraxial approximation often used in optics. First take z outside of the square root:

$$r_{01} = z\sqrt{1 + \left(\frac{x_1 - x_0}{z}\right)^2 + \left(\frac{y_1 - y_0}{z}\right)^2} \tag{7.19}$$

Then taking only the first two terms of the binomial expansion:

$$r_{01} = z\left[1 + \frac{1}{2}\left(\frac{x_1 - x_0}{z}\right)^2 + \frac{1}{2}\left(\frac{y_1 - y_0}{z}\right)^2\right] \tag{7.20}$$

This is substituted into the exponential in equation 7.17 but one only need retain the first term ($r_{01} = z$) in the squared denominator:

$$\mathrm{E}(x_1, y_1) = \frac{e^{jkz}}{j\lambda z} \iint_{-\infty}^{\infty} E(x_0, y_0) \exp\left\{\frac{jk}{2z}[(x_1 - x_0)^2 + (y_1 - y_0)^2]\right\} dx_0 dy_0 \qquad (7.21)$$

where the finite boundary conditions are conserved in the definition of $E(x_0, y_0)$. Equation 7.21 can be expressed as a convolution:

$$\mathrm{E}(x_1, y_1) = \iint_{-\infty}^{\infty} E(x_0, y_0)\, h(x_1 - x_0, y_1 - y_0) dx_0 dy_0 \qquad (7.22)$$

where the convolution kernel is given by

$$h(x_1 - x_0, y_1 - y_0) = \frac{e^{jkz}}{j\lambda z} \exp\left\{\frac{jk}{2z}((x_1 - x_0)^2 + (y_1 - y_0)^2)\right\} \qquad (7.23)$$

7.1.6 One dimension and simplification

The simulation that has been developed in this thesis is limited to a one-dimensional problem, which means that equations 7.22 and 7.23 become

$$\mathrm{E}(x_1) = \int_{-\infty}^{\infty} E(x_0)\, h(x_1 - x_0) dx_0 \qquad (7.24)$$

and

$$h(x_1 - x_0) = \frac{e^{jkz}}{j\lambda z} \exp\left\{\frac{jk}{2z}(x_1 - x_0)^2\right\} \qquad (7.25)$$

respectively. Furthermore, as only the measurement of the speckle contrast is of interest, the absolute magnitude and phase of the laser light can be neglected. This then permits the $\frac{e^{jkz}}{j\lambda z}$ term in equation 7.25 to be ignored, yielding the following forms:

$$\mathrm{E}(x_1) = \int_{-\infty}^{\infty} E(x_0)\, h(x_1 - x_0) dx_0 = E(x_1) \otimes h(x_1) \tag{7.26}$$

$$h(x_1) = \exp\left\{\frac{jk}{2z} x_1^2\right\} \tag{7.27}$$

Therefore, to propagate light from one plane to another, parallel plane separated by a distance z it is necessary to calculate $h(x_1)$ and convolve the input field with this kernel.

The simplified Huygens-Fresnel principle given in equations 7.26 and 7.27 were implemented in MATLAB to simulate the propagation of light through free-space between the LC cell and the microscope objective, and from the objective to the projection screen. The code written to simulate the propagation of light from the LC device to the microscope objective is given by,

```
h.lc_lens = exp(0.5*1i*laser.k*(x.*x)/lens.z.in);
lens.E.in = conv(lc.E.out,h.lc_lens);
lens.E.in = lens.E.in(1+(n/2):17*n/2);
```

Code 7.1: MATLAB implementation of light propagation from LC cell to MS objective.

The array `x` describes the position across the field in meters, with `x=0` defined as the centre of the beam. It extends from -4 mm to 4 mm, which is the width of the objective aperture. The array consists of 65,536 values yielding a `Δx` of 122 nm, which is smaller than the wavelength of light being modelled.

`lc.E.out` is a complex array that represents the electric field of the laser light immediately after the LC cell. `lens.E.in` is a complex array that represents the light electric field immediately before the lens while `laser.k` and `lens.z.in` are constants related to the experimental set-up.

The output of the convolution is larger than the size of the microscope objective aperture so the points outside the central 8 mm are discarded before applying the lens transformation as shown in line 3 of Code 7.1.

The same approach is used to propagate the light electric field immediately after the lens `lens.E.out` to a plane immediately before the screen, where `screen.E.in`. `lens.z.out` is the distance between the lens and the screen. The code written to carry out this propagation is given by,

```
h.lens_screen = exp(0.5*1i*laser.k*(x.*x)/lens.z.out);
screen.E.in = conv(lens.E.out,h.lens_screen);
```

Code 7.2: MATLAB implementation of light propagation from MS objective to screen.

The corresponding planes and the separation of these planes are illustrated in terms of the MATLAB parameters in Figure 7.3.

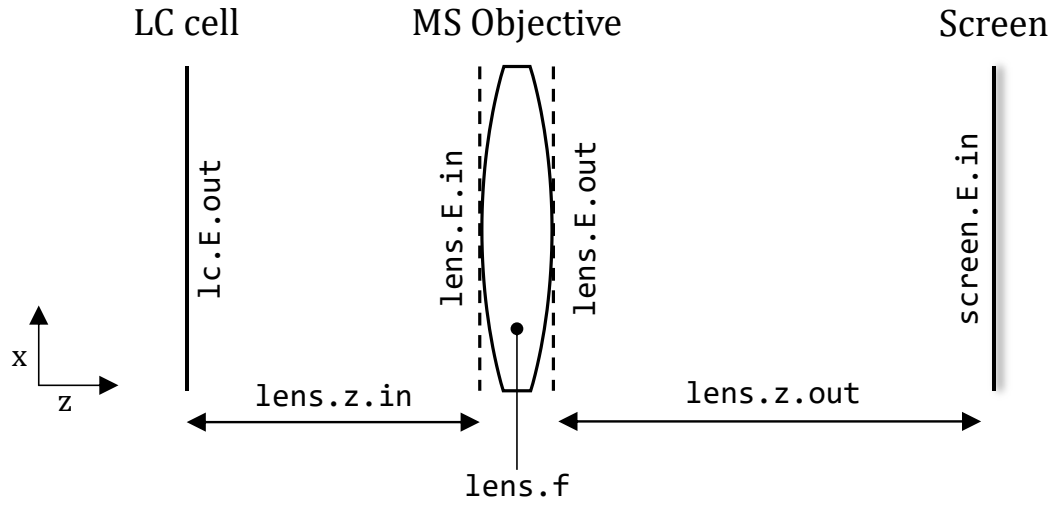

Figure 7.3: Illustration showing the location of the LC cell and the screen in relation to the microscope objective. The relevant distances and the electric field of the light at the respective positions are described in terms of the MATLAB parameters used in the light propagation code. Propagation is from left (LC cell) to right (screen).

7.1.7 Lens model

A plane wave entering a simple lens with minimal aberration will exit the lens as a spherically converging wave. The point of convergence will be a distance f from the lens known as the focal length, which from the lensmakers equation for a thin lens can be described by

$$f = (n-1)\left(\frac{1}{R_1} - \frac{1}{R_2}\right) \tag{7.28}$$

where n is the refractive index of the lens, and R_1 and R_2 are the radii of curvature of each side of the lens as shown in Figure 7.4:

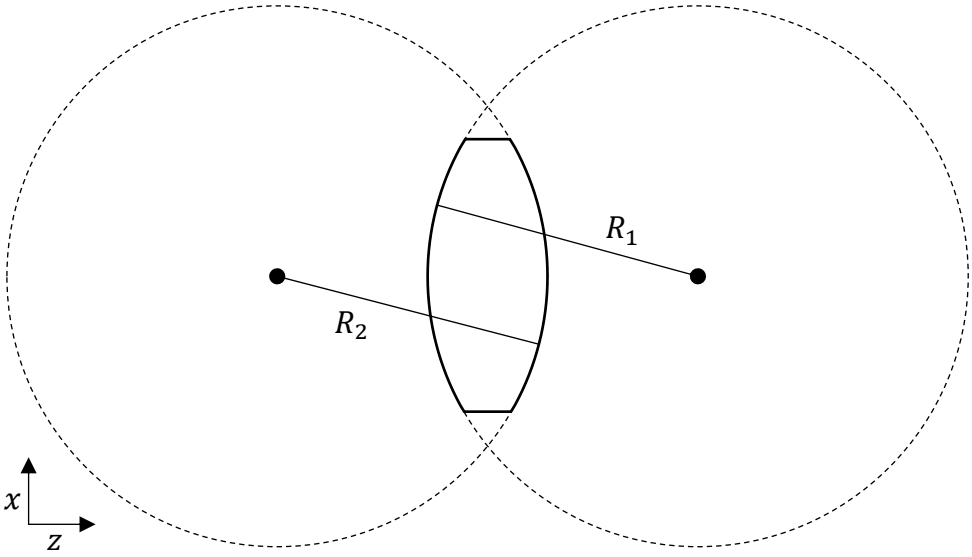

Figure 7.4: Side profile of a simple lens construction. $x = 0$ corresponds to the centre of the lens.

If the focal point is defined as having zero phase, simple geometry can be used to trace back to the lens and find the phase change exerted by the lens on the incident light. The distance between the focus point and a position on the plane at the lens is given by $\sqrt{f^2 + x^2}$. For light with wavenumber k the phase of light at this plane must be:

$$-jk\sqrt{f^2 + x^2} \tag{7.29}$$

This provides a transmission function for the lens of

$$t_l(x) = \exp\left(-jk\sqrt{f^2 + x^2}\right) \tag{7.30}$$

Therefore, the phase change introduced by a lens with any given focal length can be modelled by multiplying equation 7.30 by the incoming electric field. As a result, this permits light propagation to be modelled at any distance from the lens using the convolution method described in Section 7.1.6, which was implemented in MATLAB as shown in Code 7.3:

```
lens.E.out = lens.E.in.*exp(-1i*laser.k*sqrt(lens.f*lens.f + (x.*x)));
```

Code 7.3: MATLAB implementation of light propagation through MS objective.

`lens.E.out` is a complex array that represents the light electric field immediately after the lens. `lens.E.in` and `x` are as described previously. `laser.k` and `lens.f` are constants related to the experimental set-up.

7.1.8 In-focus imaging

In the experiments developed for measuring the speckle contrast in this thesis, the image that is formed on the camera sensor is a focussed image of the pattern that is formed on the screen, which can be calculated by the use of the propagation equation and the lens transfer function shown in Code 7.1 and Code 7.3. However, this operation can be simplified mathematically, following the method of Goodman [111], to a single convolution with the Fourier transform of the pupil function. To obtain this, consider the linearity of monochromatic wave propagation. If the field

at the object plane is represented as $E_o(x_o, y_o)$, at a distance z_2 behind the lens, the field distribution can then be represented by $E_i(x_i, y_i)$ as shown in Figure 7.5.

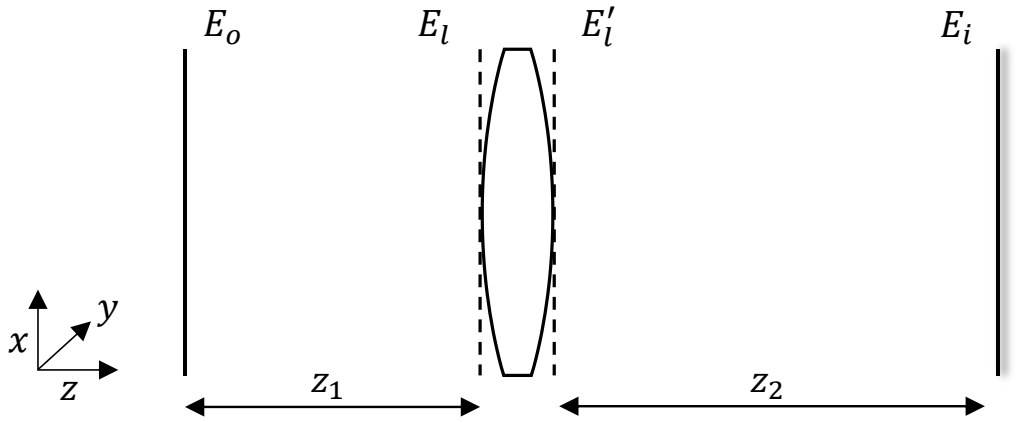

Figure 7.5: The geometry for image formation from E_o in the object plane (x_o, y_o) to E_i in the image plane (x_i, y_i). The lens is in the 'lens plane' (x, y).

A single point source in the object plane will create a field distribution in the image plane and for a given geometry one could calculate a 'transfer function' h to describe this propagation. Due to the principle of linearity, any number of point sources in the object plane would create their respective fields in the image plane also using the same transfer function. Therefore, to find the total optical field one simply uses a superposition integral over the area of the object plane given by

$$E_i(x_i, y_i) = \iint_{-\infty}^{\infty} h(x_i, y_i; x_o, y_o) E_o(x_o, y_o) dx_o dy_o \tag{7.31}$$

Once again, this derivation will start with the two-dimensional problem and simplify later to one-dimension for the MATLAB code. To apply this equation to the problem at hand, it is necessary to work out the transfer function, h. If the optical system produces a high-quality image of the object, h will need to closely represent a Dirac delta function with an appropriate magnification constant M:

$$h(x_i, y_i; x_o, y_o) \approx K\delta(x_i \pm Mx_o, y_i \pm My_o) \tag{7.32}$$

where K is a complex constant and the $\pm$ signs allow for image inversion. The image plane must exist at a distance z_2 where equation 7.32 is most closely approximated.

To find h with minimal difficulty a simple delta function is used as the object field and the propagation equations derived in Sections 7.1.6 and 7.1.7 are applied. The light field at E_l (immediately before the lens) will be a spherical wave diverging from the delta function, written assuming that the paraxial approximation is valid, as

$$E_l(x, y) = \frac{1}{j\lambda z_1} \exp\left\{\frac{jk}{2z_1}[(x - x_o)^2 + (y - y_o)^2]\right\}. \tag{7.33}$$

After passing through the lens of focal length f the optical field becomes E_l' (using a two-dimensional version of equation 7.30

$$E_l'(x, y) = E_l(x, y)P(x, y) \exp\left(-jk\sqrt{f^2 + x^2 + y^2}\right). \tag{7.34}$$

Take the first term from the binomial expansion of $\sqrt{f^2 + x^2 + y^2}$ and simplify this to give equation 7.35. From herein, the coefficient $\frac{1}{j\lambda z_1}$ in equation 7.33 is ignored as it merely contributes to a constant phase offset.

$$E_l'(x, y) = E_l(x, y)P(x, y) \exp\left(-\frac{jk}{2f}(x^2 + y^2)\right) \tag{7.35}$$

$P(x, y)$ is the pupil function of the lens, which according to Kirchhoff's boundary conditions is defined as being 1 within the aperture and 0 everywhere else. Using the Fresnel diffraction formula (equation 7.21) for propagation over the distance z_2, the field at E_i is then given by

$$\mathrm{E_i}(x_i, y_i) = \frac{1}{j\lambda z_2} \iint_{-\infty}^{\infty} E_l'(x, y) \exp\left\{\frac{jk}{2z_2}[(x_i - x)^2 + (y_i - y)^2]\right\} dxdy \tag{7.36}$$

where the constant phase factor e^{jkz} has been removed. Combining equations 7.33, 7.35 and 7.36 one arrives at a somewhat cumbersome equation for h

$$\begin{aligned} h(x_i, y_i; x_o, y_o) \\ &= \frac{1}{\lambda^2 z_1 z_2} \exp\left[\frac{jk}{2z_1}(x_o^2 + y_o^2)\right] \exp\left[\frac{jk}{2z_2}(x_i^2 + y_i^2)\right] \\ &\times \iint_{-\infty}^{\infty} P(x, y) \exp\left\{\frac{jk}{2z_1}\left(\frac{1}{z_1} + \frac{1}{z_2} - \frac{1}{f}\right)(x^2 + y^2)\right\} \\ &\times \exp\left\{-jk\left[\left(\frac{x_o}{z_1} + \frac{x_i}{z_2}\right)x + \left(\frac{y_o}{z_1} + \frac{y_i}{z_2}\right)y\right]\right\} dxdy \end{aligned} \tag{7.37}$$

where like terms have been combined and constant terms taken outside the double integral. Clearly, this is not in a form similar to equation 7.32 so approximations are required to progress.

First, the quadratic phase term in the integral can be eliminated if

$$\left(\frac{1}{z_1} + \frac{1}{z_2} - \frac{1}{f}\right) = 0 \tag{7.38}$$

which is indeed the familiar thin-lens law from geometric optics required for imaging. The quadratic phase term depending on (x_i, y_i) before the double integral can also be ignored because only the intensity distribution at the image plane is of interest and this term only effects the phase distribution.

The third quadratic phase function in terms of (x_o, y_o) cannot be directly cancelled or ignored. However, consider the area on the image plane over which a point source in the object plane contributes with any significance. Assuming the system creates a high-quality image, this area should be very small otherwise the

image would appear very blurry. Within this area the phase can be expected to only vary by a small fraction of a radian, so the quadratic phase factor can be replaced by a single phase that depends solely on the image plane scaled by the magnification ratio $M = -z_2/z_1$:

$$\exp\left[\frac{jk}{2z_1}(x_o^2 + y_o^2)\right] \rightarrow \exp\left[\frac{jk}{2z_1}\left(\frac{x_i^2 + y_i^2}{M^2}\right)\right] \tag{7.39}$$

This term can now be ignored because, as before, only the intensity distribution of the image plane is of interest, not the phase. This approximation was shown to be accurate providing the object size is no greater than about $1/4$ the size of the lens aperture [113], which is reasonable in the case of laser speckle. The expression for h now becomes

$$\begin{aligned} h(x_i, y_i; x_o, y_o) \\ &= \frac{1}{\lambda^2 z_1 z_2} \iint_{-\infty}^{\infty} P(x, y) \\ &\times \exp\left\{-jk\left[\left(\frac{x_o}{z_1} + \frac{x_i}{z_2}\right)x + \left(\frac{y_o}{z_1} + \frac{y_i}{z_2}\right)y\right]\right\} dxdy \end{aligned} \tag{7.40}$$

This can be simplified further by introducing M and including a minus sign to remove the effects of image inversion:

$$\begin{aligned} h(x_i, y_i; x_o, y_o) \\ &\approx \frac{1}{\lambda^2 z_1 z_2} \iint_{-\infty}^{\infty} P(x, y) \\ &\times \exp\left\{-j\frac{2\pi}{\lambda z_2}[(x_i - Mx_o)x + (y_i - My_o)y]\right\} dxdy \end{aligned} \tag{7.41}$$

Now, if normalised object-plane variables are introduced:

$$\widetilde{x_o} = Mx_o \quad \widetilde{y_o} = My_o \tag{7.42}$$

this can be simplified even further

$$\begin{aligned} &h(x_i, y_i; \widetilde{x_o}, \widetilde{y_o}) \\ &\quad = \frac{1}{\lambda^2 z_1 z_2} \iint_{-\infty}^{\infty} P(x, y) \\ &\quad \times \exp\left\{-j\frac{2\pi}{\lambda z_2}[(x_i - \widetilde{x_o})x + (y_i - \widetilde{y_o})y]\right\} dxdy \end{aligned} \tag{7.43}$$

and h now depends only on the differences between coordinates $(x_i - \widetilde{x_o}, y_i - \widetilde{y_o})$. Finally, the coordinates can be normalised,

$$\tilde{x} = \frac{x}{\lambda z_2} \quad \tilde{y} = \frac{y}{\lambda z_2} \quad \tilde{h} = \frac{1}{|M|}h \tag{7.44}$$

which can be substituted into equation 7.31 to give the more concise form of,

$$E_i(x_i, y_i) = \iint_{-\infty}^{\infty} \tilde{h}(x_i - \widetilde{x_o}, y_i - \widetilde{x_o}) \left[\frac{1}{|M|} E_o\left(\frac{\widetilde{x_o}}{M}, \frac{\widetilde{y_o}}{M}\right)\right] d\widetilde{x_o} d\widetilde{y_o}, \tag{7.45}$$

which is equivalent to the following convolution and scaling,

$$E_i(x_i, y_i) = \tilde{h}(x_i, y_i) \otimes E_g(x_i, y_i), \tag{7.46}$$

where E_g is the geometrical-optics prediction of the image

$$E_g(x_i, y_i) = \frac{1}{|M|} E_o\left(\frac{x_i}{M}, \frac{y_i}{M}\right) \tag{7.47}$$

and the coordinate differences have been written into the definition of h to become

$$\tilde{h}(x_i, y_i) = \iint_{-\infty}^{\infty} P(\lambda z_2 \tilde{x}, \lambda z_2 \tilde{y}) \exp[-j2\pi(x_i \tilde{x} + y_i \tilde{y})]\, d\tilde{x} d\tilde{y} \tag{7.48}$$

which is the point-spread function introduced by diffraction. Also, this expression is mathematically equivalent to the Fourier transform of the scaled pupil function P.

To summarise this rather lengthy derivation, in-focus imaging has been reduced to a convolution of a scaled geometrical image of the object (projection screen) with the Fourier transform of the pupil function (camera lens aperture). To implement this in MATLAB, the study is constrained to one dimension and one further simplification is applied for the sake of minimising computation time. The pupil function for the simple one-dimensional lens used in this simulation is simply a top hat function which simplifies equation 7.48 to

$$\tilde{h}(x_i) = \int_{-\mathrm{r_{lens}}}^{r_{lens}} 1 \cdot \exp[-j2\pi x_i \tilde{x}]\, d\tilde{x}, \tag{7.49}$$

where r_{lens} is the radius of the lens pupil, represented by `eye.r` in the MATLAB code. The Fourier transform of a top hat function is well-known to be a sinc function,

$$\tilde{h}(x_i) = \mathrm{sinc}\left\{\frac{2\pi x_i r_{lens}}{\lambda z_2}\right\}, \tag{7.50}$$

which is called `h_psf` in the code. The scaling by M of the geometrical image is accounted for by introducing a scaled vector for position in the x-dimension at the image plane, `retina.x`. `eye.z.in` and `eye.z.out` are z_1 and z_2, respectively. `laser.lambda` is the laser wavelength λ and `x` is as defined previously.

Finally, the electric field of the light at the camera `retina.E.in` is converted into intensity by taking the absolute value of the complex array squared. This is shown in Code 7.4.

```
retina.x = x*(-eye.z.out/eye.z.in);
h_psf = sinc(retina.x*2*pi*eye.r/(eye.z.out*laser.lambda));
retina.E.in = conv(screen.E.out,h_psf);
retina.I = abs(retina.E.in).*abs(retina.E.in);
```

Code 7.4: MATLAB implementation of light propagation from the screen to the camera.

The MATLAB terms for the relevant planes and distances are illustrated in Figure 7.6.

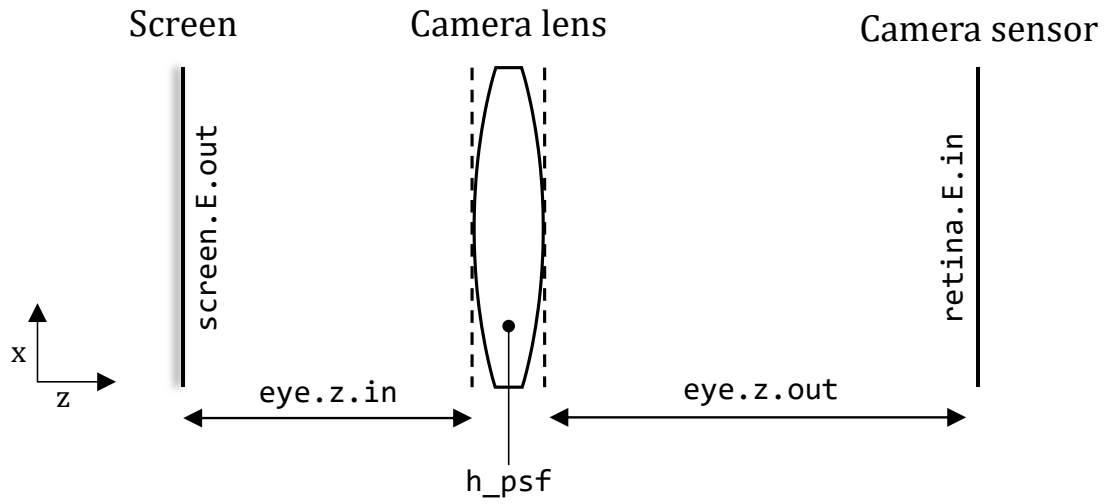

Figure 7.6: Diagram of the MATLAB terms used in the light propagation code. Propagation is from left (screen) to right (camera sensor).

7.2 Modelling the projection screen

When light is incident on a surface it can interact with that surface in a variety of ways depending on the surface properties. Specular reflection occurs when light is incident on polished metals or dielectrics like a mirror or glass, where the surface is free from roughness at a length scale of the order of the wavelength of incident light. Light is reflected directly at the interface between the surrounding medium and the surface at the same angle to the surface normal as the incident ray. This is known as the *Law of Reflection* which can be derived from Fermat's principle of least time.

Diffuse reflection is such that incident light is scattered over a range of angles. For materials such as metals, which light is unable to penetrate, this is a result of surface roughness, for example with sand-blasted metal. In this case, light is completely reflected from the surface over a wide range of angles. In most other materials the light is also scattered beneath the surface by the fibres, cells or crystals that the material is composed of. Incident light can be scattered multiple times beneath the surface and re-emerge from the surface at a different position. Indeed, materials that are observed as being white appear so because light with wavelengths across the visible spectrum are reflected and refracted multiple times under the surface of the material before some of the light is directed back towards the observer. In contrast, light reflected from the rough side of aluminium foil is diffuse reflected purely from the surface, which is why it does not appear white despite the fact that all incident wavelengths are present in the reflected light.

The projection screen used in this thesis was a piece of printing paper. Printing paper is predominantly made from several layers of intertwined soft or hardwood fibres. Fibre thickness is typically of the order of 10 μm and their length is of the order of 1 mm. Coating can be applied to the surface to fill the cavities between fibres and decrease surface roughness and provide a more glossy finish, although this reduces ink absorption. Filler pigments are often added to increase light scattering, making it opaquer. Paper is also naturally somewhat yellow in colour, so fluorophores are added that absorb UV light and emit blue light to make it appear whiter.

Light interacts with paper in three ways: a small amount of specular reflection at the surface, diffuse reflection when interacting with the bulk and fluorescence.

There was no need to model fluorescence in this study as the wavelengths used are limited to the visible spectrum. Likewise, there is very little specular reflection from the matte printing paper used in the experiments described in this thesis.

For diffuse reflection the reflected radiance from a given point in a specific direction can be described by the bidirectional reflectance distribution function, and much work has been done measuring this function for a wide range of materials [114] [115] [116]. An ideal diffuse reflector reflects light with equal luminance in all directions and is known as a Lambertian surface.

When modelling light incident on the paper projection screen that was used in the experiments described in this study, it was necessary to find an approximate model that can scatter incident light to create speckle even in incident plane waves, but that was not so computer-intensive as to slow the code down excessively. A simple model was proposed whereby the incoming light field is multiplied by a complex vector with unity amplitude and a randomly varying phase between 0 and 2π [117]. Several simple phase distributions were considered for use, examples of which can be seen in Figure 7.7. Screen 1 has uniformly distributed random phase elements between 0 and 2π. Screen 2 has uniformly distributed random phase elements every 64 values (7.8 μm), values in-between are linearly interpolated. Screen 3 has uniformly distributed random phase elements every 64 values (7.8 μm), values in-between are repeated. Screen 4 allows each subsequent phase value to vary from the previous by $\pm\pi/2$. Screen 5 allows each subsequent phase value to vary from the previous by $\pm\pi/16$. Finally, Screen 6 has a phase of zero throughout, which essentially acts like a mirror. This is used for comparison with experimental results. A summary of these screen properties is presented in Table

7.1.

Screen	Distance between randomly generated phase values	Phase value generation method	Values in-between
1	0.12 µm	UDRN $0-2\pi$	N.A.
2	7.8 µm	UDRN $0-2\pi$	Linear interp.
3	7.8 µm	UDRN $0-2\pi$	Repeated
4	0.12 µm	UDRN $\pm\pi/2$	N.A.
5	0.12 µm	UDRN $\pm\pi/16$	N.A.
6	N.A.	N.A.	N.A.

Table 7.1: Summary of screen properties used in Figure 7.7. UDRN – uniformly distributed random number

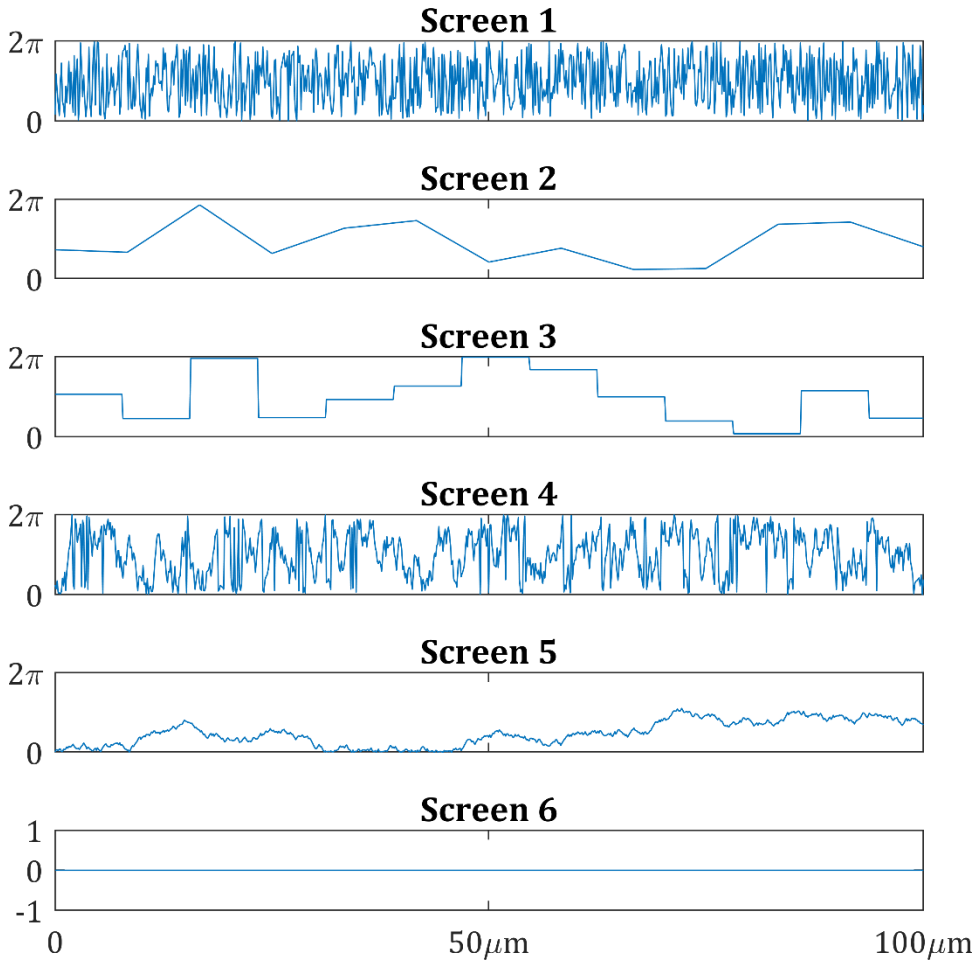

Figure 7.7: Examples of the phase component for the six screens tested for the simulation of the paper projection screen. Only the first 100 μm of each screen is shown for comparison.

To test these screens, incident light with uniform amplitude and uniformly random phase was input to the simulation in the place of an output from the LC device. 100 different simulations were completed for each screen. This simulates the propagation of 100 statistically independent phase distributions of laser light. For each run, the resulting intensity fields observed by the camera for that run and every previous run were summed together to calculate the cumulative speckle contrast. This cumulative speckle contrast is expected to reduce for every additional intensity field that is added and enables the observation of speckle reduction with an effective increase in integration time of the camera. In theory, 100 statistically independent speckle patterns, each with speckle contrast of 1, should combine to a speckle contrast of $\frac{1}{\sqrt{100}} = 0.1$.

Also, for comparison, incident light with uniform amplitude and phase was also input in to the simulation in the place of an output from the LC device, which simulates an unscrambled laser beam with uniform intensity. This should be observed to have a speckle contrast value of 1. The results of these simulations are shown in Figure 7.8.

It is clear from this graph that only Screens 5 and 6 allow the cumulative speckle contrast to reduce to the expected value of 0.1. However, Screen 6 has a speckle contrast larger than 1 for uniform incident light and does not actually scatter the incident light in any way. Screen 5 has a speckle contrast of 0.955 for uniform incident light which is close to the expected value of 1.

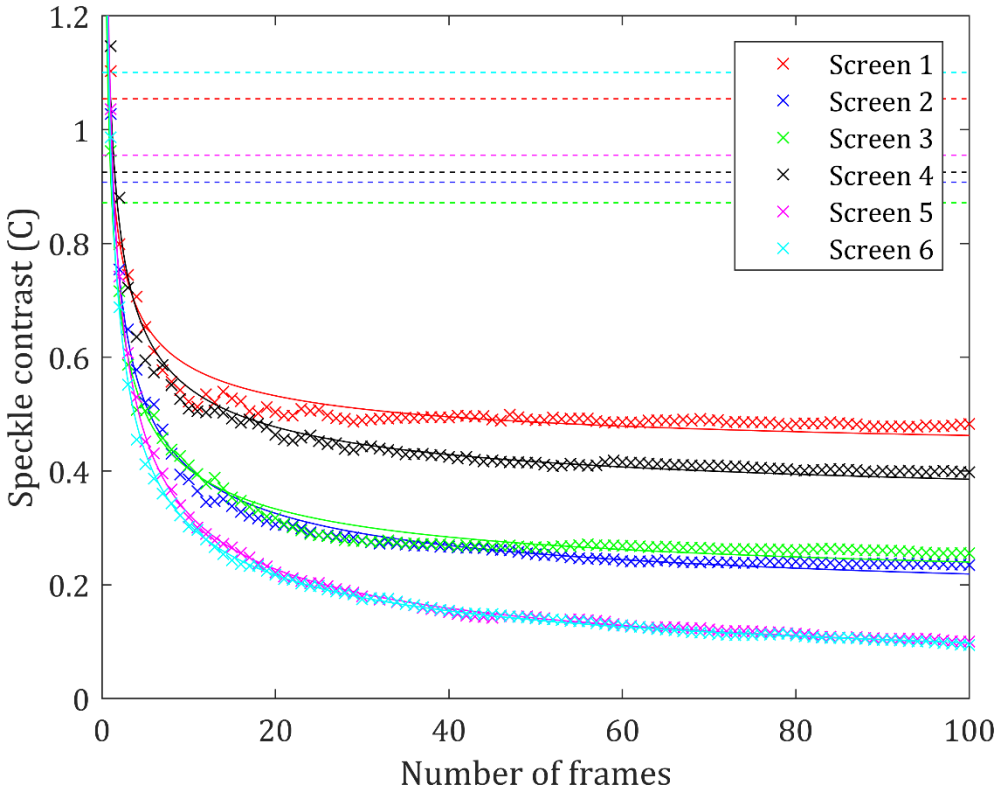

Figure 7.8: Cumulative speckle reduction for the six screen types that were considered to simulate the paper screen used in the experiments. The crosses represent the cumulative speckle reduction for a number of frames summed together. The lines are fits to this data of the form $ax^{-0.5} + b$ which shows that C reduces approximately by $1/\sqrt{N}$ as expected from Goodman [1]. The dotted lines represent the speckle contrast measured for each screen with a uniform light input.

To better understand how light interacts with different surfaces, an experiment was undertaken to measure speckle contrast for a range of camera integration times across a range of surfaces. The surfaces used were diffuse reflectors with 120, 220, 600 and 1500 grit polishes (Thorlabs [52]), printing paper and a mirror. A highly coherent He-Ne laser was passed through a 20 μm-thick planar aligned glass cell containing the nematic host E7 dispersed with 4.7 wt.% chiral dopant BDH1281, operating at optimum speckle reducing conditions of 14 V/µm and 75 Hz. Photographs were taken with a range of integration times (analogous to the cumulative speckle contrast values in Figure 7.8) for each surface. The speckle contrast was also measured without the LC cell in place and the results can be seen in Figure 7.9.

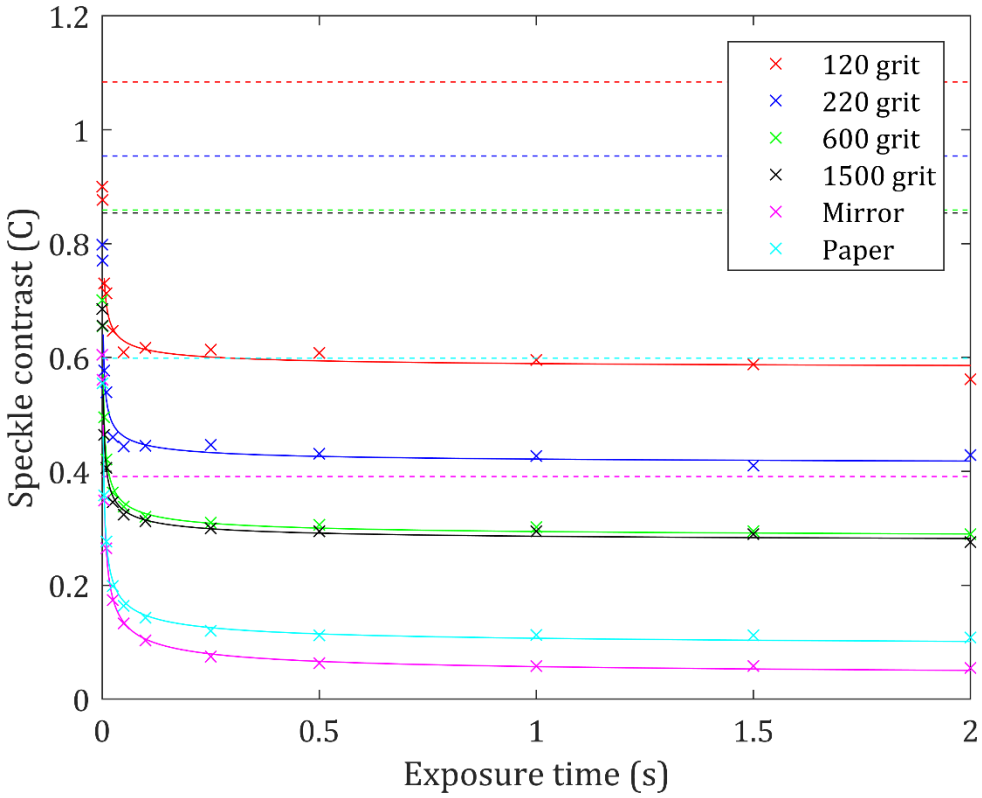

Figure 7.9: Plot of the speckle contrast, C, as a function of exposure time observed for a range of different projection screens. The data points represent speckle contrast of a He-Ne laser after propagating through an LC cell under maximum speckle reduction conditions (E = 14.2 $V/\mu m$, 95 Hz square wave). The LC mixture was E7 + 4.7 wt.% BDH1281, the cell thickness was 20 μm and the temperature at which measurements were carried out was T = 25°C. The solid lines represent a fit to the data of the form $ax^{-0.5} + b$, which shows that C reduces approximately by $1/\sqrt{N}$ in accordance with the work of Goodman [1]. The dotted line represents the speckle contrast of a He-Ne that has not passed through an LC cell.

These results are an interesting comparison to the simulated results in Figure 7.8. The diffuse reflectors that light cannot penetrate are unable to reduce speckle below 0.3: the finer the grit, the lower the speckle contrast. Grits of 120, 220, 600 and 1500 are equivalent to surface roughness of the order of 125 µm, 68 µm, 25.8 μm and 15.3 μm, respectively [118]. Even though the 1500 grit reflector consists of particles with average sizes that are of the same order as the size of the fibres that make up the paper, the speckle contrast is limited to $C = 0.3$. Similarly, for Screen 2 and 3 in Figure 7.8 that have phase randomness that are of the same order of magnitude, these are also limited to a minimum speckle contrast of $C \approx 0.3$.

The paper used as a projection screen does not exhibit surface roughness on a length scale as small as the 122 nm resolution used in screen 5, but by applying a random phase perturbation at such length scales this is considered to be a reasonable approximation to the effect of both surface and volume scattering present in real paper. For these reasons Screen 5 was used for all the simulations carried out in the following chapter.

Beyond the approximations related to scattering and surface roughness, the angle of the camera relative to the screen was ignored for simplicity. Also, polarisation is not modelled at any point in these simulations. For this reason, the speckle reduction of $1/\sqrt{2}$ caused by the depolarising effect of interaction with paper is not modelled. Instead, the objective of this simulation is to observe trends in the speckle reduction that are caused by a change in the properties of the LC device and the inaccuracies caused by the approximations used in this study are not expected to affect the trends that are observed in the data.

7.3 Modelling propagation through LC device

7.3.1 Electric field-induced LC director profile

When the LC cell is undergoing dynamic scattering the director profile is highly complex and rapidly changing. Developing a complete model of this is beyond the scope of this work so instead several simplifying assumptions are made. First, the cell is modelled at an instantaneous point in time with a fixed director profile. Secondly, the LC cell is limited to two dimensions: the width of the laser beam and the thickness of the cell (typically 1 mm × 20 μm throughout this thesis). The molecules are assumed to arrange themselves into helical domains with a fixed

pitch, but with a randomly aligned helical axis, locally over a small area. Furthermore, the cell is assumed to consist of many of these domains randomly positioned throughout the bulk. The size of these helical domains varies randomly between two set limits and this construction allows the cells to respond to changes in pitch, birefringence and cell thickness. The domain size can then be adjusted to find a good match with experimental data. To simulate the effects of turbulence, multiple speckle patterns that have been obtained for different static domain director profiles are summed together. This approach is analogous to changing the exposure time of the camera in the practical experiment.

A script was written in MATLAB to create this director profile. A random location in the cell is chosen and given a random helical axis direction described in spherical coordinates. The domain radius r is then randomly selected from a value between the upper and lower limit set previously. Each grid point within this domain is then attributed a 'tilt' and 'twist' angle, which are the corresponding spherical coordinate angles that represent the local director orientation. These tilt and twist angles are calculated geometrically from the orientation of the helical axis, pitch and position within the domain. Once the domain is filled, a new random position is chosen with a new random helical axis orientation. If a new domain overlaps a previously formed domain then it can be overwritten. This process repeats until the entire array is populated with a quasi-random distribution of randomly aligned helical domains. To improve the efficiency of this process, when the matrix representing the cell is 90% filled, new domains can only be centred around an empty grid point. The array has a spatial resolution of 24.42 nm; sufficiently small as to allow numerous values within a single pitch of even the

shortest-pitched chiral nematic LC materials studied in this thesis.

An array representing tilt and twist of the local director orientation for each position in the cell can then be used as an input for the LC beam propagation code (see Section 7.3.2). Alternatively, this can be converted to the six unique elements of the optical dielectric tensor matrix ε_r:

$$\boldsymbol{D} = \varepsilon_0 \varepsilon_r \boldsymbol{E}$$

$$\begin{pmatrix} D_x \\ D_y \\ D_z \end{pmatrix} = \varepsilon_0 \begin{pmatrix} \varepsilon_{xx} & \varepsilon_{xy} & \varepsilon_{xz} \\ \varepsilon_{xy} & \varepsilon_{yy} & \varepsilon_{yz} \\ \varepsilon_{xz} & \varepsilon_{yz} & \varepsilon_{zz} \end{pmatrix} \begin{pmatrix} E_x \\ E_y \\ E_z \end{pmatrix} \tag{7.51}$$

In this format, it is possible to add scattering particles to the LC cell by randomly selecting locations in the cell and setting

$$\begin{aligned} \varepsilon_{xx} = \varepsilon_{yy} = \varepsilon_{zz} = n_{scat}^2 \\ \varepsilon_{xy} = \varepsilon_{yz} = \varepsilon_{xz} = 0 \end{aligned} \tag{7.52}$$

where n_{scat} is the refractive index of the scattering particle. A MATLAB code was written that can add these scattering particles to any LC director profile, with any chosen size, shape, refractive index and density.

Examples of the refractive indices for visible light travelling along the optical axis (z-axis in Figure 7.3) are shown in Figure 7.10, Figure 7.11 and Figure 7.12 for a chiral nematic LC with pitch values of 300 nm, 600 nm and 500 nm, respectively. The radius of each domain is limited to be 0.5 - 1 μm. The ordinary (n_o) and extraordinary (n_e) refractive indices are set to 1.5 and 1.7, respectively. The arrays shown are limited to dimensions of 20 × 20 μm for illustration purposes only. Figure 7.12 has 1% (by area) of additional square-shaped scattering particulates of size 0.5 μm and refractive index $n = 1.8$.

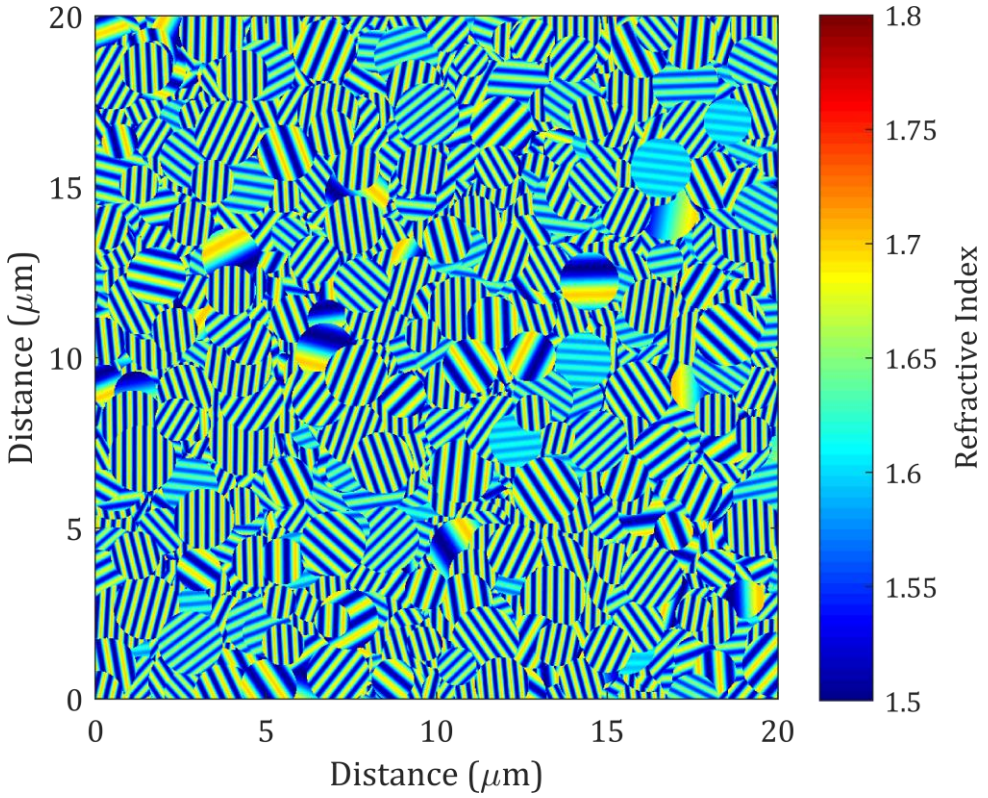

Figure 7.10: Refractive index for light propagating along the x-axis for a chiral nematic LC with a 300 nm pitch.

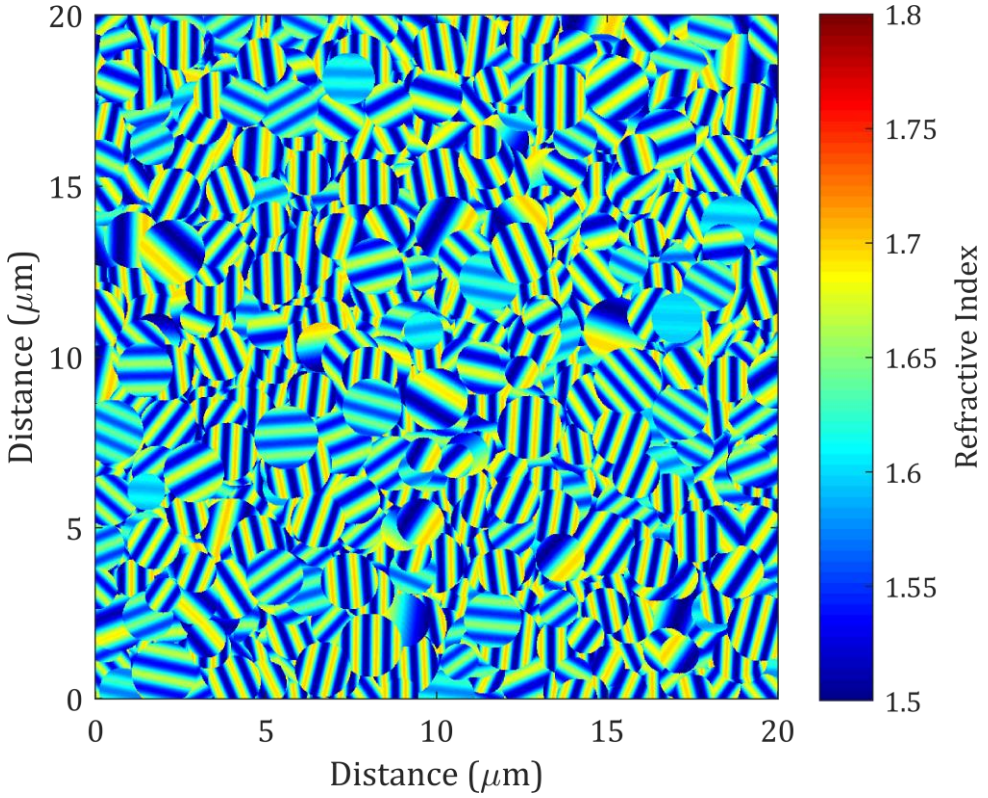

Figure 7.11: Refractive index for light propagating along the x-axis for a chiral nematic LC with a 600 nm pitch.

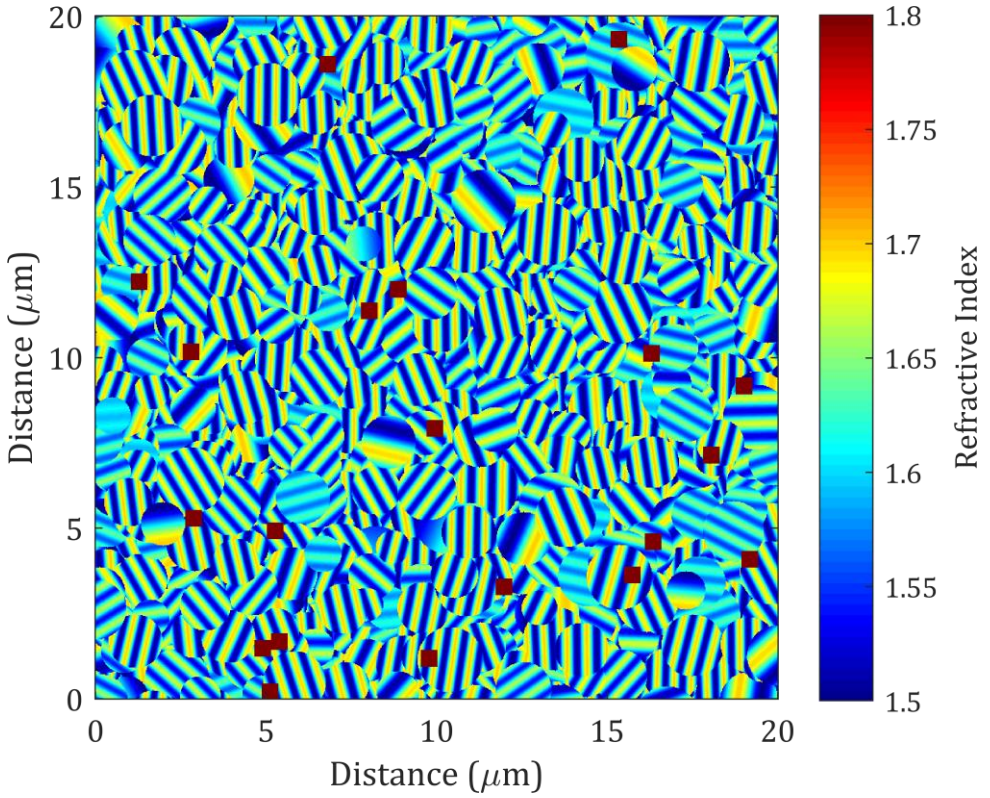

Figure 7.12: Refractive index for light propagating along the x-axis for a chiral nematic LC with a 500 nm pitch, with 1% (by area) of additional square-shaped scattering particulates, size 0.5 µm, refractive index 1.8.

Once the static director profiles have been obtained these can then be used as the input to a MATLAB script that sets up and runs the simulation of the laser beam propagating through the LC device.

7.3.2 LC cell beam propagation

Accurately modelling light propagation through a highly complex LC cell is beyond the scope of the code written in this thesis. As a result, the code that was used was developed previously by Kriezis and Elston [119]. This beam propagation method utilises a Crank-Nicholson scheme to connect the known field values at one plane to the unknown field values in the next plane. It employs a transparent boundary condition [120] that allows light to exit the computational boundaries and avoid being internally reflected in a manner that would be unrealistic in a practical LC

device.

The code is capable of modelling scattering of up to 30-40° from the optical axis although it is unable to model large-angle scattering or back scattering. It is also capable of modelling Mie scattering, but cannot deal with Rayleigh scattering. The code can model material up to 100 μm wide and thick, and model the domain structure down to a spatial resolution of 24.4 nm. The output of the code is the real and imaginary components of the x, y and z components of the electric field. In this case, only the x-components are taken, which is equivalent to a combination of passing the outgoing light through a linear polariser and taking the scalar approximation. This is purely for simplification as the rest of the simulation code does not consider the polarisation of light, and assumes that the x, y and z components of the electric field can be treated independently.

7.3.3 Statistical LC output field

Unfortunately, the code described in Section 7.3.2 is very slow to run on a desktop PC and often 100 or more electric light field outputs are required for each LC parameter set in order to model speckle reduction through superposition of speckle patterns. Also, the code as it stands is currently unable to model LC cells with a lateral width greater than 100 μm. In terms of the actual experimental arrangement, the laser beam is approximately 1 mm wide at the LC device. Consequently, a method of rapidly creating numerous larger electric fields at the output of the LC device was required.

The output light electric fields were analysed in MATLAB and the amplitude was found to have characteristics of gaussian white noise passed through a low-pass cut-off filter (with approximately a gaussian profile in Fourier space) with a strong

zero-order plane-wave component. The phase component was always simply a uniformly random array of values between 0 and 2π. It was also noted that these amplitude characteristics varied for different LC parameters but remained similar within multiple runs for the same LC parameters.

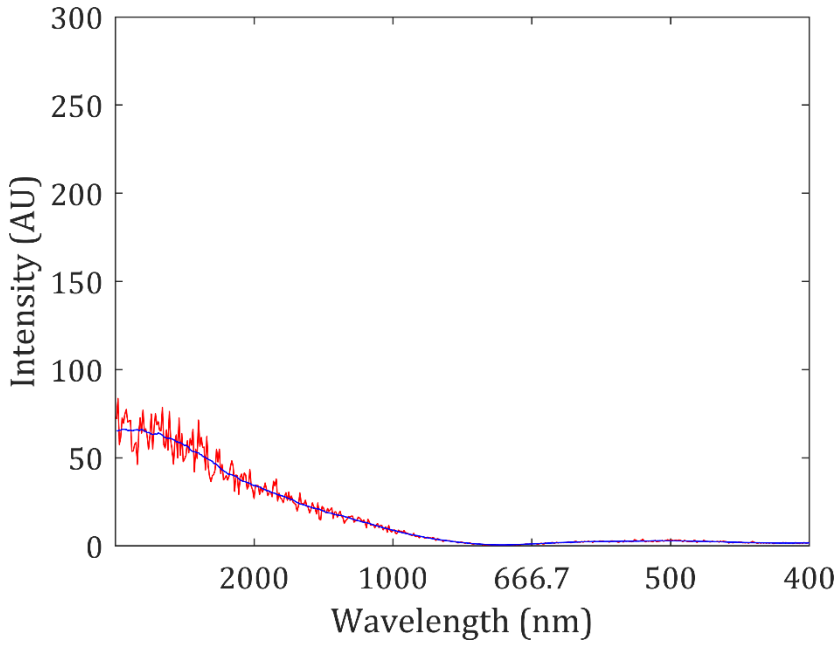

Figure 7.13: (red) Average of the amplitude of the Fourier transform of 10 complex output fields from a cell of pitch $p = 600\ nm$, $n_o = 1.5$, $n_e = 1.7$, domain size range $1p - 2p$, cell thickness 20 μm, cell width 100 μm for a laser, $\lambda = 632.8\ nm$. (blue) Moving mean fit used to extract shape in Fourier domain.

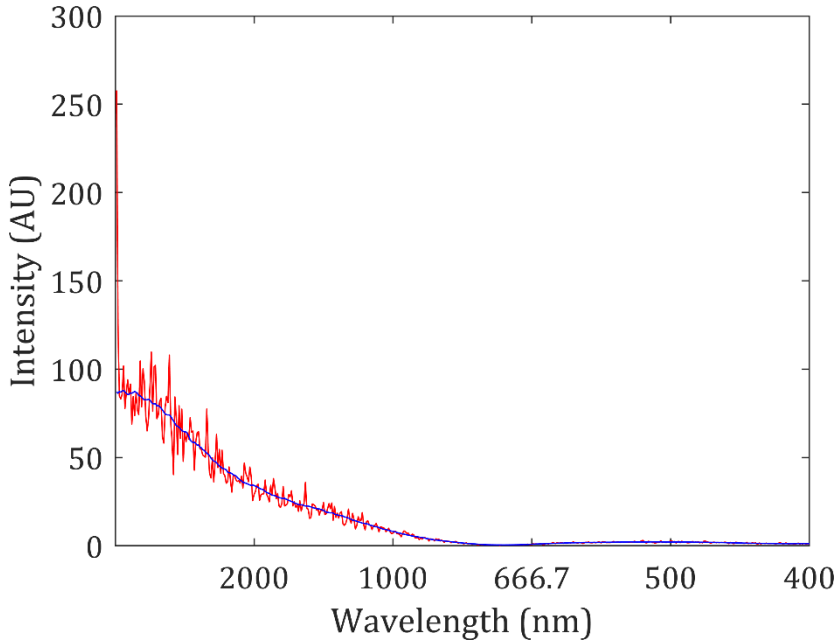

Figure 7.14: (red) Average of the amplitude of the Fourier transform of 10 complex output fields from a cell of pitch $p = 600\ nm$, $n_o = 1.525$, $n_e = 1.675$, domain size range $1p - 2p$, cell thickness 20 μm, cell width 100 μm for a laser, $\lambda = 632.8\ nm$. (blue) Moving mean fit used to extract shape in Fourier domain.

Examples of this are shown in Figure 7.13 and Figure 7.14 for comparison. Here, ten complex output fields from the optical simulator for two different LC cells are Fourier transformed and their amplitude components are taken and averaged together. A clear shape not too dissimilar to a gaussian curve with a second higher-order peak is observed in both, with a strong DC peak clearly visible in the second plot. The cells have identical parameters except that Figure 7.13 has a birefringence of $\Delta n = 0.2$, whereas Figure 7.14 has a birefringence of $\Delta n = 0.15$.

To create electric fields with these statistical properties, but at the full 1 mm width required, the following steps need to be taken:

- For a given set of experimental parameters, generate 10 field outputs using the beam propagation method code with a width of 100 μm.
- Take the Fourier transform of each output and take their amplitudes.
- Take the mean for each point in the spatial Fourier domain across the 10 outputs.
- Take a fit of this mean m using a moving mean.
- Calculate the average noise n around this mean across the Fourier space.
- Create gaussian white noise of width 1 mm and scale its amplitude by n before adding m.
- Scale the field amplitude suitably to represent the full 1 mm width.
- Multiply each element in this field amplitude array by a uniformly random phase between 0 and 2π.
- Perform an Inverse Fourier Transform of the complex array.

In this way, many statistically similar, full-size electric field arrays can be produced rapidly for any set of experimental parameters. These can then be input to the

simulation that models light propagation from the output of the LC cell to the camera.

The electric field output from this code represents `lc.E.out` in Code 7.1 and Figure 7.3 but with a spatial resolution 5 times smaller. The resolution is reduced to match that required for `lc.E.out` by using one in every five values from the high-resolution output and discarding all points in-between. The higher resolution (24 nm) was only necessary to sufficiently model pitch values down to 200 nm and domain sizes of a similar scale. The lower resolution used beyond this point is 122 nm as described in Section 7.1.6.

7.4 Summary

This chapter has described the development of a MATLAB code that simulates the propagation of monochromatic laser light through a liquid crystal diffuser, free-space and a simple converging lens, as well as reflecting from a simple projection screen. Several simplifications were introduced to describe this propagation mathematically, starting with Maxwell's equations. This code was implemented in MATLAB, alongside the use of a third-party code that was used to simulate the propagation through the liquid crystal diffuser. Due to the limitations of this code it was necessary to create larger arrays of data more quickly, which was achieved by analysing the statistics of the optical simulation outputs and creating new arrays with matching statistical properties. The next chapter discusses the results obtained from the simulation code and compares them to the results obtained from the experiments presented in the preceding Chapters.

8 Simulating the Speckle Contrast for an LC device

In the previous chapter, a model that simulates the LC speckle reduction system was developed. In this chapter, the results of these simulations for a range of different LC device parameters are presented and discussed. The effect of domain size, pitch, birefringence, cell thickness, addition of scattering particles, cell temperature and laser wavelength on speckle contrast and transmission are explored. Where possible, the simulated results presented in this chapter are compared with the experimental results of Chapters 4-6 and with findings already published in the literature.

8.1 Calculation of the speckle contrast

The electric field that is output from the simulation described in Chapter 7 is converted to intensity by taking the square of each amplitude value in the complex array. The array is 65,536 elements wide and represents a width of 2.6 mm across the real 6.4 mm-wide detector. The mean and standard deviation of the central half of this intensity array (16,384 – 49,152, representing 1.3 mm) is used to calculate the speckle contrast for each frame. To calculate transmission, the simulated light is propagated through an empty cell and the sum of the intensity values across the central half of the resulting intensity array is recorded. Transmission for a simulated LC device is defined here as follows:

$$\frac{\sum intensity\ values\ through\ LC\ device}{\sum intensity\ values\ through\ empty\ device} \times 100 \tag{8.1}$$

This is analogous to the method of transmission measurement described in Section 4.2.3 of Chapter 4 and used in all experimental results presented in Chapters 4-6.

Examples of the output intensity fields are given in Figure 8.1. Here the intensity field after simulation through one set of LC parameters with an increasing number of consecutive runs combined is presented. In this case a reduction in the speckle contrast from 1.0, to 0.30, to 0.10 is observed, which follows the $1/\sqrt{N}$ dependence [1].

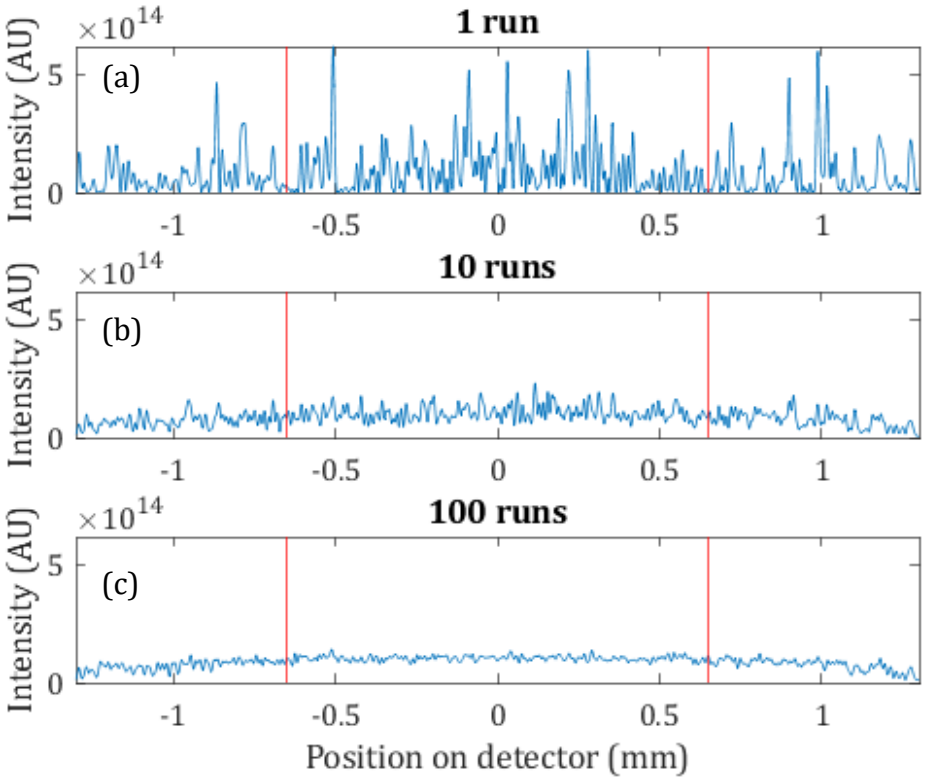

Figure 8.1: Plot of intensity arrays for (a) a single simulated run, (b) 10 combined simulated runs, (c) 100 combined simulated runs through a chiral nematic LC cell of pitch $p = 600\ nm$, $n_o = 1.5$, $n_e = 1.7$, domain size range $1p - 2p$, cell thickness $d = 20\ \mu m$, cell width $1\ mm$ for a laser, $\lambda = 632.8\ nm$, beam width $1\ mm$. Speckle contrast is calculated from the values between the two red lines on each plot.

For each set of parameters this method was applied, and the cumulative speckle

contrast is then plotted for an increasing number of superimposed frames. An example of this plot for the same cell parameters as above is shown in Figure 8.2.

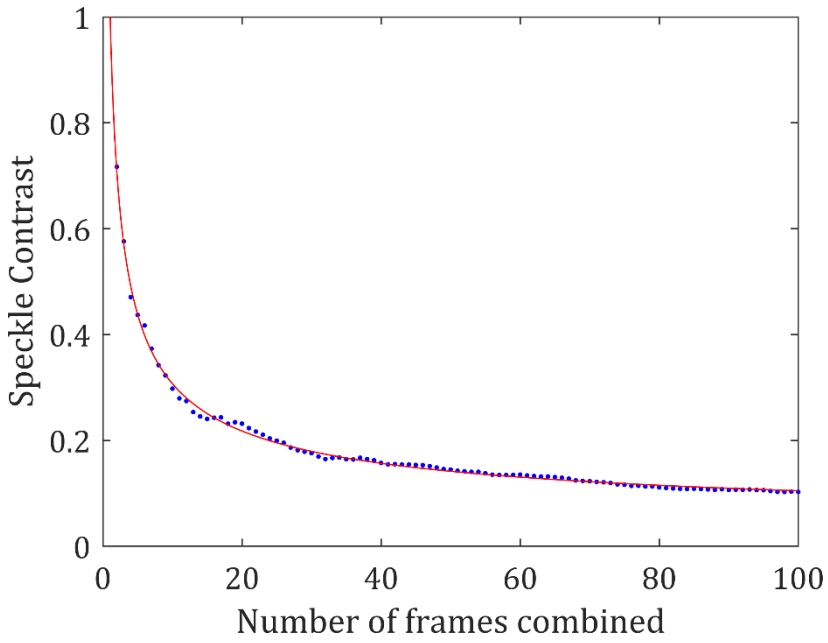

Figure 8.2: Plot of the cumulative speckle contrast for an increasing number of combined intensity fields for simulated light passing through a chiral nematic LC cell of pitch $p = 600\ nm$, $n_o = 1.5$, $n_e = 1.7$, domain size range $1p - 2p$, cell thickness $d = 20\ \mu m$, cell width $1\ mm$ for a laser, $\lambda = 632.8\ nm$, beam width $1\ mm$. The blue dots represent the calculated speckle contrast values. The red line is a fit of the form $ax^{-0.5} + b$ which shows that C reduces approximately by $1/\sqrt{N}$ in accordance with the work of Goodman [1].

When a set of different cell parameters are to be compared, the value plotted will be the speckle contrast for 100 frames superimposed on to each other, representing the speckle reduction of a laser that has passed through 100 distinct LC domain profiles. It is noted that this model assumes that all simulated cells move between 100 distinct domain profiles in the same amount of time. It is unable to model changes in the physical and electro-optical properties, such as viscosity and dielectric permittivity, that effect how quickly an LC sample can move between distinct alignment configurations.

8.2 Domain size and pitch

The range of domain sizes can be controlled in the MATLAB code, but the true shape and size of these domains in a practical LC device are unknown. As a result, the simulation was run with a range of domain sizes over a range of pitch values to observe how the domain size influences the resulting speckle contrast. The domain ranges tested were 244 – 488 nm, 244 – 1465 nm, 488 – 977 nm, 733 – 1465 nm and $p - 2p$ nm, where p is the pitch of that particular LC cell. During the creation of the LC domain, each domain is randomly assigned a diameter between the specified limits. Figure 8.3 is a plot of (a) speckle contrast and (b) transmission as a function of pitch for this range of domain sizes.

In Section 4.2 in Chapter 4 experimental data for speckle contrast as a function of pitch was presented, over a similar range of pitch values. Each mixture showed a clear decrease in speckle contrast as the pitch decreased. This relationship is not seen in its entirety in any of the simulated results, with most data sets showing little variation across the range of pitch values tested here. It is likely that this is a result of the simplifications used when developing the simulation model. For example, short pitch cells require high concentrations of chiral dopant that are likely to change the physical and electro-optical properties of the LC mixture.

However, the $1p - 2p$ model does show a reduction in speckle contrast as the pitch reduces from $3000 - 600$ μm, with the speckle contrast increasing as the pitch is further reduced. This may well be because, as stated in Chapter 7, the beam propagation method used cannot model Rayleigh scattering. Pitch values smaller than the order of an optical wavelength with similar sized domains would be considered to be in the regime of Rayleigh scattering. Also, while the conventional

understanding in the field is that small concentrations of chiral dopant have a very limited effect on the LC material properties, it is also known that a chiral nematic has a higher viscosity than the equivalent achiral nematic host [35]. Furthermore, mixtures with particularly small pitch values require relatively high concentrations of chiral dopant (> 5 wt.% for high twisting power dopants, > 20 wt.% for low twisting power dopants) which are likely to have some effect on the material properties of the LC mixture relevant to speckle reduction. For these reasons, all of the results that were obtained with particularly short pitch values should be examined with caution.

The experimental results showed that the transmission decreased across all mixtures to a minimum value at $500 \leq p \leq 1000$ nm, before increasing as the pitch is further decreased. Once again, this trend was not replicated in its entirety in the results from simulations. However, the adaptive domain size model ($1p - 2p$) does reveal that the transmission decreases with pitch without reaching a minimum value before the minimum pitch value of $p = 250$ nm. All the set domain sizes show quite consistent transmission from $500 \leq p \leq 3000$ nm, with a marked decrease in transmission below $p = 500$ nm.

One possible explanation for the departure from the experimental trends in the transmission at low pitch values could once again be that the simulation cannot model Rayleigh scattering. There is a clear reduction in transmission as the set domain sizes are reduced, with the smallest domain size range ($244 - 488$ nm) never exhibiting more than 7% transmission. Similarly, all data sets have a noticeable reduction in transmission at pitch values of ≤ 400 nm.

While the limitations imposed by simplifications do result in some variation

between simulated and experimental results, the adaptive domain model that sets domain sizes as $1p - 2p$ does follow experimental trends very well for pitches above 400 nm. Consequently, it was selected for use in the majority of simulated results that follow in the remainder of this chapter.

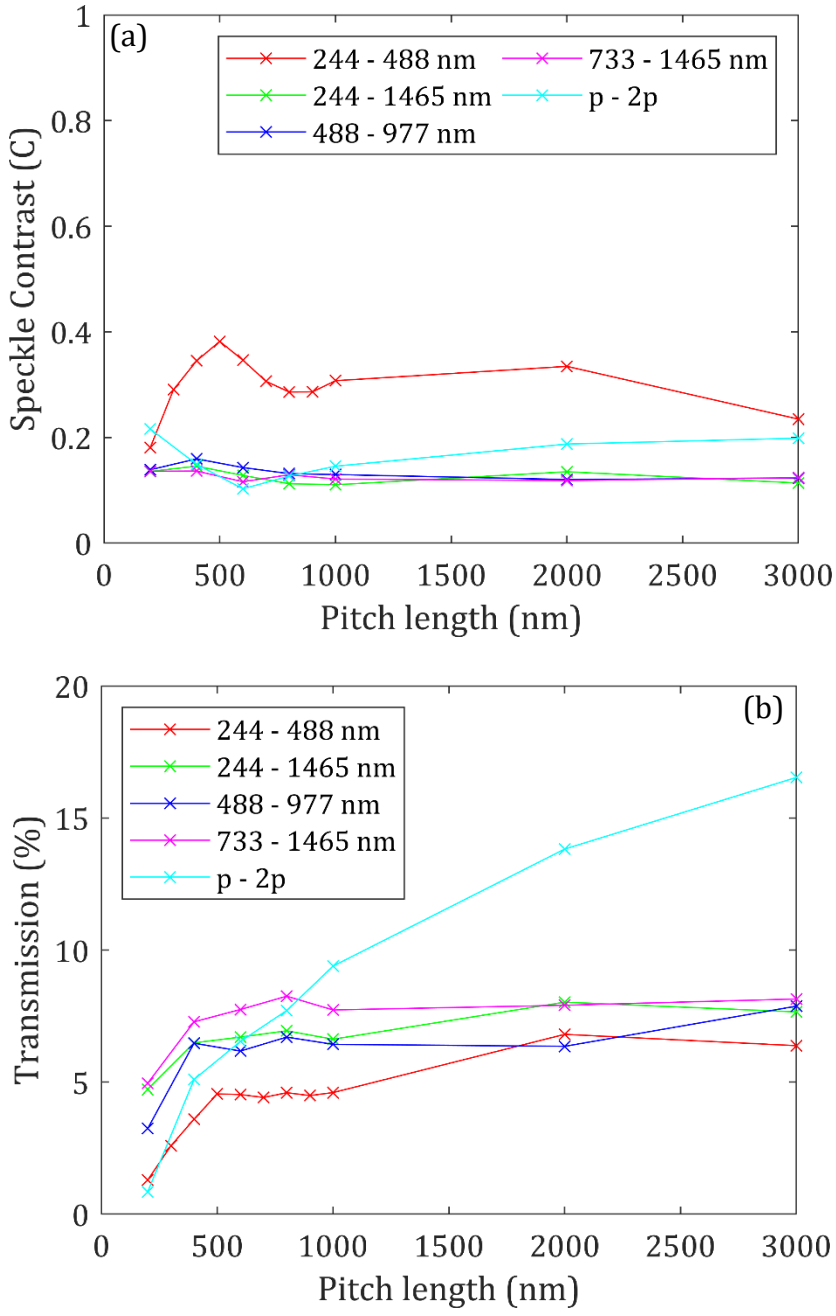

Figure 8.3: Simulations of (a) the speckle contrast and (b) the transmission over a range of domain sizes as a function of the pitch. Simulation results were obtained for light with $\lambda = 632.8\ nm$, a beam diameter of 1 mm, a cell thickness of $d = 20\ \mu m$, and a chiral-nematic LC with $n_o = 1.5$ and $n_e = 1.7$. Data points represent simulated values whereas the lines are a linear interpolation to guide the eye.

8.3 Birefringence

In Section 4.3 of Chapter 4, the effect of a variation in the birefringence on speckle contrast and transmission was reported. It was found that an increase in the birefringence increases light scattering and reduces transmission in all cases. Speckle contrast was found to decrease with an increase in birefringence between $0.091 \leq \Delta n \leq 0.233$, although mixtures made from E7 and BL006, with $\Delta n = 0.212$ and 0.274, respectively, showed little variation across a range of pitch values. It was postulated that this could be because the decrease in speckle contrast per unit increase in birefringence reduces as the birefringence increases.

In this section, LC domains with a range of birefringence values ($0.05 \leq \Delta n \leq 0.25$) are simulated over a range of pitch values ($400 \leq p \leq 1000$ nm*).* The adaptive domain size model was used, and the average refractive index of each LC model is $n_{av} = 1.6$. The cell thickness is set to $d = 20$ µm and the laser wavelength is $\lambda = 632.8$ nm. Figure 8.4 is a plot of (a) the speckle contrast and (b) the transmission as a function of LC birefringence.

It is clear from these plots that a larger birefringence results in an increase in light scattering, manifested by the reduction of both the speckle contrast and transmission. Further, as postulated in Chapter 4, the reduction in the speckle contrast reduces between larger birefringence values, reaching a minimum in the simulations at $0.15 \leq \Delta n \leq 0.20$. These findings are in excellent agreement with the experimental results presented in Section 4.3. To ensure that this trend was not influenced by using the adaptive domain size model, these simulations were repeated with a set domain size model and the same results were obtained. These birefringence simulations show that the optimum LC mixture, in terms of speckle

reduction and transmission, is expected to have a birefringence of approximately $0.15 \leq \Delta n \leq 0.20$. LCs with higher birefringence are expected to offer little more in the way of further reduction in the speckle contrast, at the cost of reduced transmission.

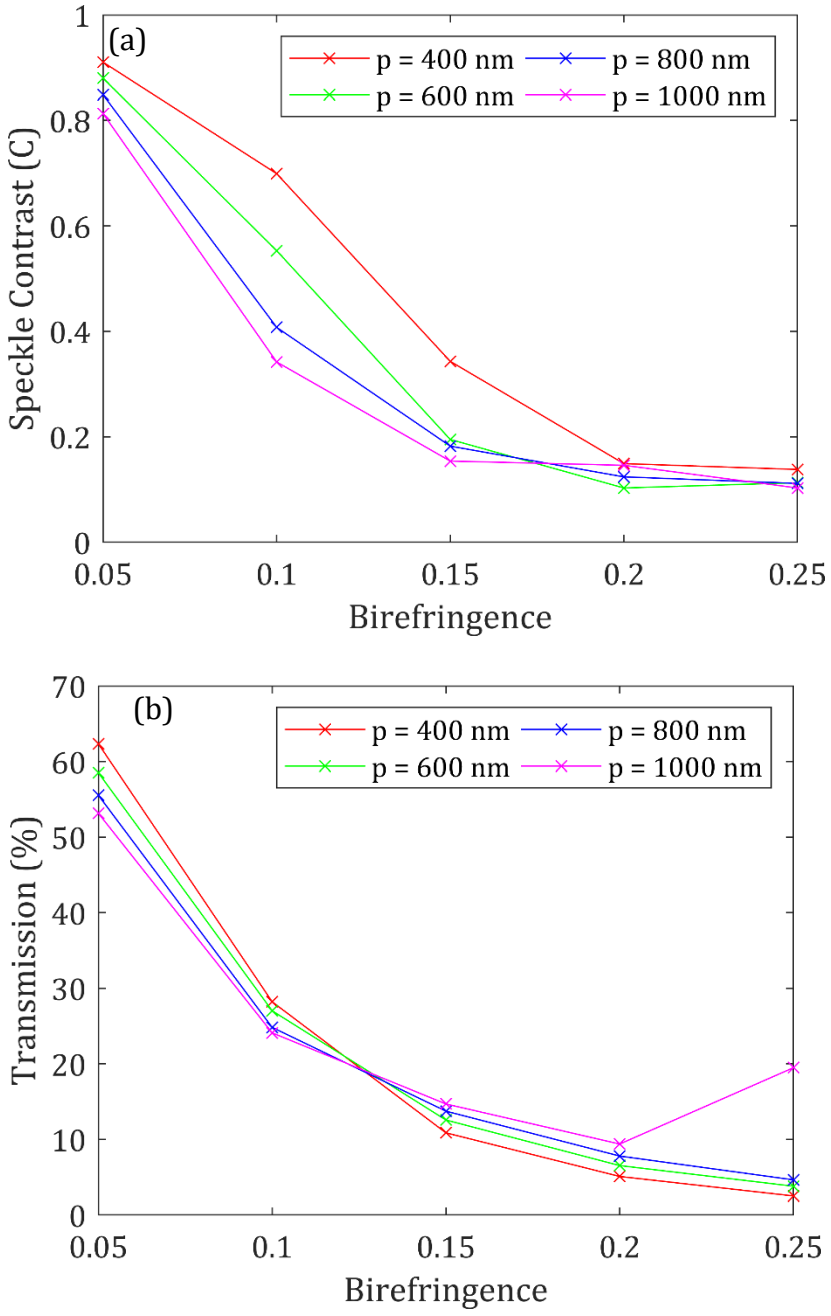

Figure 8.4: Simulations of (a) the speckle contrast and (b) the transmission over a range of pitch values as a function of birefringence. The simulations were carried out for light with $\lambda = 632.8\ nm$, a beam diameter of 1 mm and a cell thickness of $d = 20\ \mu m$. The simulations consisted of a chiral nematic LC with a birefringence ranging from $0.05 \leq \Delta n \leq 0.25$, with $n_{av} = 1.6$, pitch of $400 \leq p \leq 1000\ nm$ and domain size $p - 2p$. Data points represent simulated values whereas the lines represent a linear interpolation to guide the eye.

8.4 Cell thickness

In Section 6.1 of Chapter 6, the relationship between cell thickness and device performance is explored. It was concluded that the experimental results clearly showed that an increase in the cell thickness resulted in an increase in the light scattering which manifested itself as a reduction in both the speckle contrast and the transmission. This was in agreement with published work on light scattering in LC devices [89] [90]. In this section, this is explored further in the form of simulations of laser propagation through a LC device with a varying device thickness ranging from $5 \leq d \leq 50$ μm. The LC parameters used throughout these simulations were $n_o = 1.5, n_e = 1.7, p = 300$ nm or 600 nm . In Figure 8.5 the speckle contrast and transmission are plotted as a function of cell thickness for both pitch values.

Speckle contrast clearly reduces with an increase in cell thickness, as found in the experimental work. Indeed, Figure 6.4 of Chapter 6 shows a very similar relationship between cell thickness and speckle contrast to these simulated results albeit with fewer data points. The speckle contrast reduction per unit increase of cell thickness decreases as the cell thickness increases until a minimum is reached, at which point a further increase in the cell thickness ceases to reduce the speckle contrast further. Specifically, the longer pitch cell with $p = 600$ nm was found to reach a minimum at $d = 20$ μm, whereas the short pitch cell with $p = 300$ nm was found to reach a minimum at $d = 35$ μm. Meanwhile, the transmission reduces in a similar manner with an increase in cell thickness but does not reach a minimum value within the range of cell thicknesses tested in this study. Clearly, the optimum cell thickness for each simulated mixture occurs at the smallest cell thickness at

which speckle contrast has reached its minimum value. Further increases in cell thickness only serve to reduce light transmission. This shows that cell thickness can be used to optimise the performance of a LC-based speckle reducer. Further experimental work should be undertaken with a larger range of cell thicknesses to explore the effect.

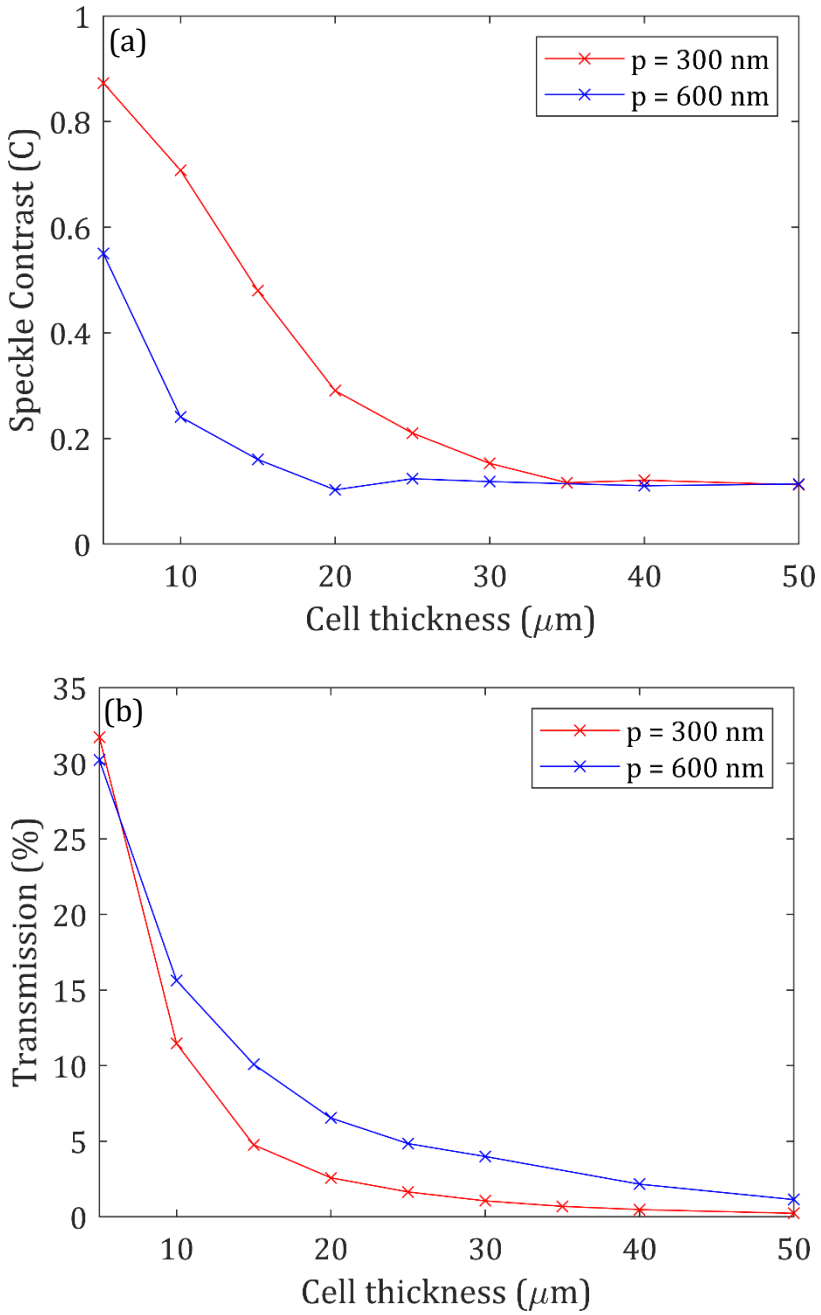

Figure 8.5: Simulations of (a) the speckle contrast and (b) the transmission for two different pitch values as a function of the cell thickness. The simulations were carried out for light with $\lambda = 632.8\,nm$, a beam diameter of $1\,mm$, a cell thickness ranging from $5 \leq d \leq 50\,\mu m$, and a chiral-nematic LC with $n_o = 1.5$ and $n_e = 1.7$ and a pitch of either $p = 300\,nm$ or $600\,nm$. Data points represent simulated values whereas lines are linear interpolations to guide the eye.

8.5 Scattering Particulates

In Section 6.2 of Chapter 6, experimental results were presented for LC cells doped with additional scattering particulates. Cells were prepared using a chiral-nematic LC with a short pitch ($p = 270$ nm or 320 nm) and high birefringence ($\Delta n = 0.212$ or 0.274) doped with either 1 μm-diameter SiO_2 particles of refractive index $n = 1.457$ at $\lambda = 632.8$ nm, or < 25 nm-diameter TiO_2 particles of refractive index $n = 2.584$ at $\lambda = 632.8$ nm. It was found that small weight concentrations of 0.25 wt.% of both types of scattering particles led to an increase in the speckle contrast, but at a larger weight concentration of 5 wt.% the SiO_2 particles did seem to reduce the speckle contrast slightly from $C = 0.46$ to $C = 0.43$.

As previously stated, the simulation developed in this thesis is unable to model scattering at length scales that are below optical wavelengths. Consequently, scattering particle sizes were limited to $500 - 1000$ nm diameters. The TiO_2 particulates cannot be modelled at the size used. In this section, a simulation for a range of weight concentrations (0 – 5 wt.%) of the 1 μm-diameter SiO_2 particles dispersed in a chiral-nematic LC with equivalent refractive indices to that of the nematic LC, E7, is presented. Following this, the effect of varying the refractive index of the scattering particulates that are either dispersed at 1 wt.% or 10 wt.% concentration in the same LC host mixture is explored. Finally, the impact of varying the birefringence of the chiral nematic host while keeping the refractive index of the scattering particulates fixed is considered.

8.5.1 *Varying SiO_2 particle concentration in a chiral nematic E7 LC mixture*

Figure 8.6 is a plot of (a) the speckle contrast and (b) the transmission at a range of pitch values as a function of the weight concentration of the scattering particulates

with refractive index $n = 1.457$ and size 1 μm. The chiral-nematic LC is considered to have refractive indices of E7 at 25°C and $\lambda = 632.8$ nm: $n_o = 1.5189$ and $n_e = 1.7305$.

All mixtures show a decrease in the speckle contrast with an increase in the concentration of the scattering particulates. The simulated mixture with $p = 270$ nm , matching the pitch used in experiments, performed worse for concentrations below 1 wt.% than the base LC mixture without scattering particulates, in agreement with the experimental results presented in Chapter 6. The two longer-pitched mixtures exhibited a lower speckle contrast for all concentrations of particulates than that observed for the respective base mixtures without additional scattering particulates. The short pitch mixture with $p = 270$ nm has a domain size smaller than the particulates and a very short length-scale refractive index variation so the addition of low concentrations of particles might serve to reduce the spatial variation in the refractive index considerably, which could explain the behaviour that is observed. At 0.25 wt.% there are only five scattering particulates present in a cell of thickness $d = 20$ μm and width $w = 100$ μm. Higher concentrations are required to increase light scattering in the E7-based mixture.

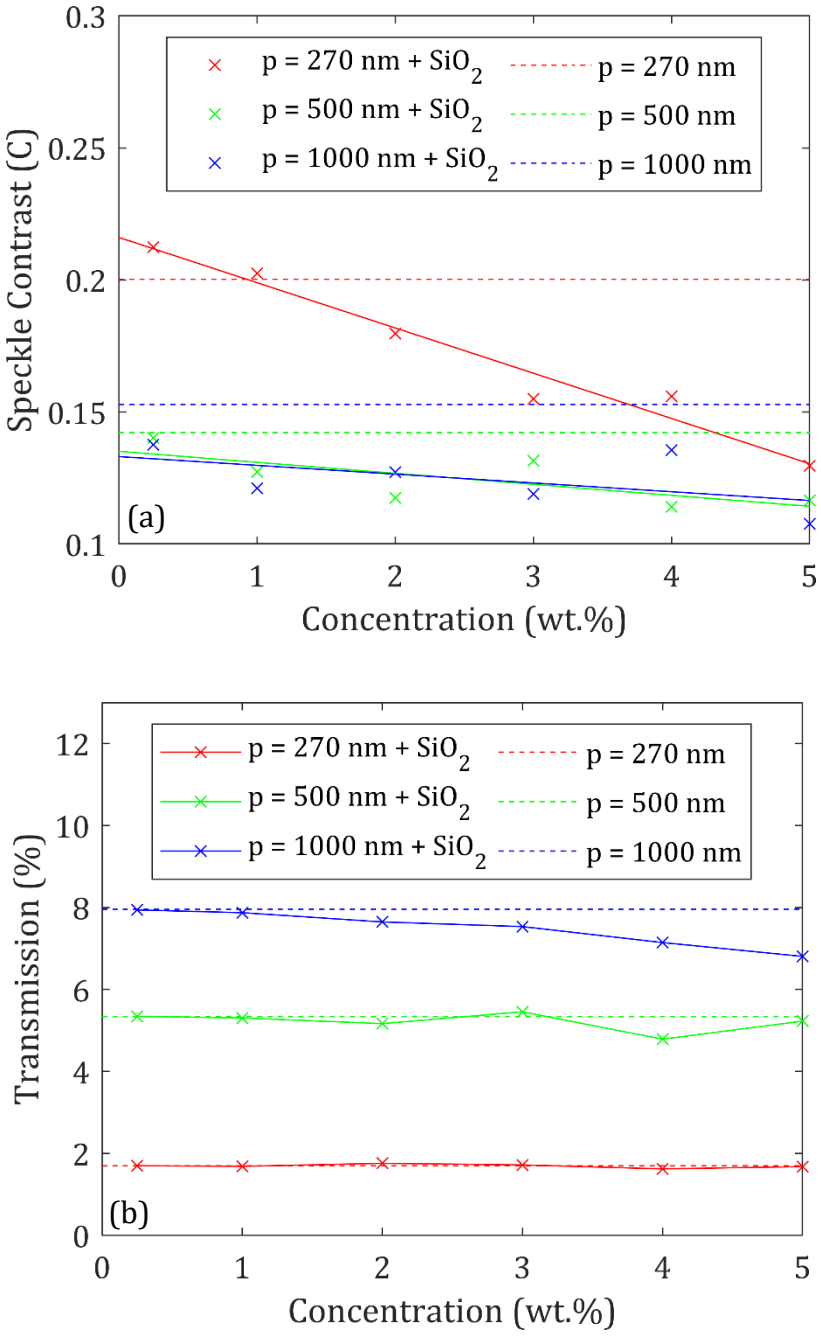

Figure 8.6: Simulations of (a) the speckle contrast and (b) the transmission as a function of particle size. Simulations carried out for light with $\lambda = 633\ nm$, a beam diameter of 1 mm, a cell thickness of $d = 20\ \mu m$ and a chiral nematic LC modelled with refractive indices equivalent to the nematic E7 at 25°C and $\lambda = 633\ nm$: $n_o = 1.5189$ and $n_e = 1.7305$. A pitch of $p = 270\ nm$ was used for the chiral nematic with a domain size of $p - 2p$. Each cell consisted of $0.25 - 5\%$ (by area) of square scattering particulates inserted at random locations with $n_{scat} = 1.457$ and particle size 1 μm, to match the SiO_2 scattering particulates used in Section 6.2 in Chapter 6. Data points represent simulated values whereas the solid line is (a) a line of best fit or (b) a linear interpolation to guide the eye. The dashed line is the (a) speckle contrast or (b) transmission for a LC cell without additional scattering particulates.

8.5.2 *Varying scattering particulate properties in a fixed LC mixture*

The next simulation involves varying the value of the refractive index of the scattering particulates for a range of particle sizes. Specifically, the range of values from $1.8 \leq n \leq 2.5$ and particle sizes ranging from $500 - 1000$ nm are considered. As before, the host LC mixture has refractive indices of $n_o = 1.5$ and $n_e = 1.7$ and a pitch of $p = 500$ nm. Figure 8.7 is a plot of (a) the speckle contrast and (b) the transmission as a function of the particle size at a weight concentration of 1 wt.%. Figure 8.8 are equivalent plots for a weight concentration of 10 wt.%.

These plots show that the transmission reduces as the refractive index of the particulates increases, especially at the higher concentration of 10 wt.%. This is consistent with a decrease in the transmission shown in LC mixtures with a large birefringence. Despite the reduction in transmission, there is no clear relationship between the magnitude of the refractive index of the scattering particulates and the resulting speckle contrast after passing through the LC device. Most simulated cells reduce speckle contrast slightly further with the additional scattering particulates than the same LC mixture without particles, but only from $C = 0.14$ to $C \geq 0.11$. This is likely because the base LC mixture has a birefringence of $\Delta n = 0.2$, which was shown in Figure 8.4 to correspond to the birefringence at which speckle contrast reaches its minimum value when plotted as a function of the birefringence of the LC host. Increasing the refractive index of the scattering particle relative to the base LC mixture appears to have a similar effect to increasing the LC birefringence beyond $\Delta n = 0.2$: a reduction in transmission without a significant change in speckle contrast.

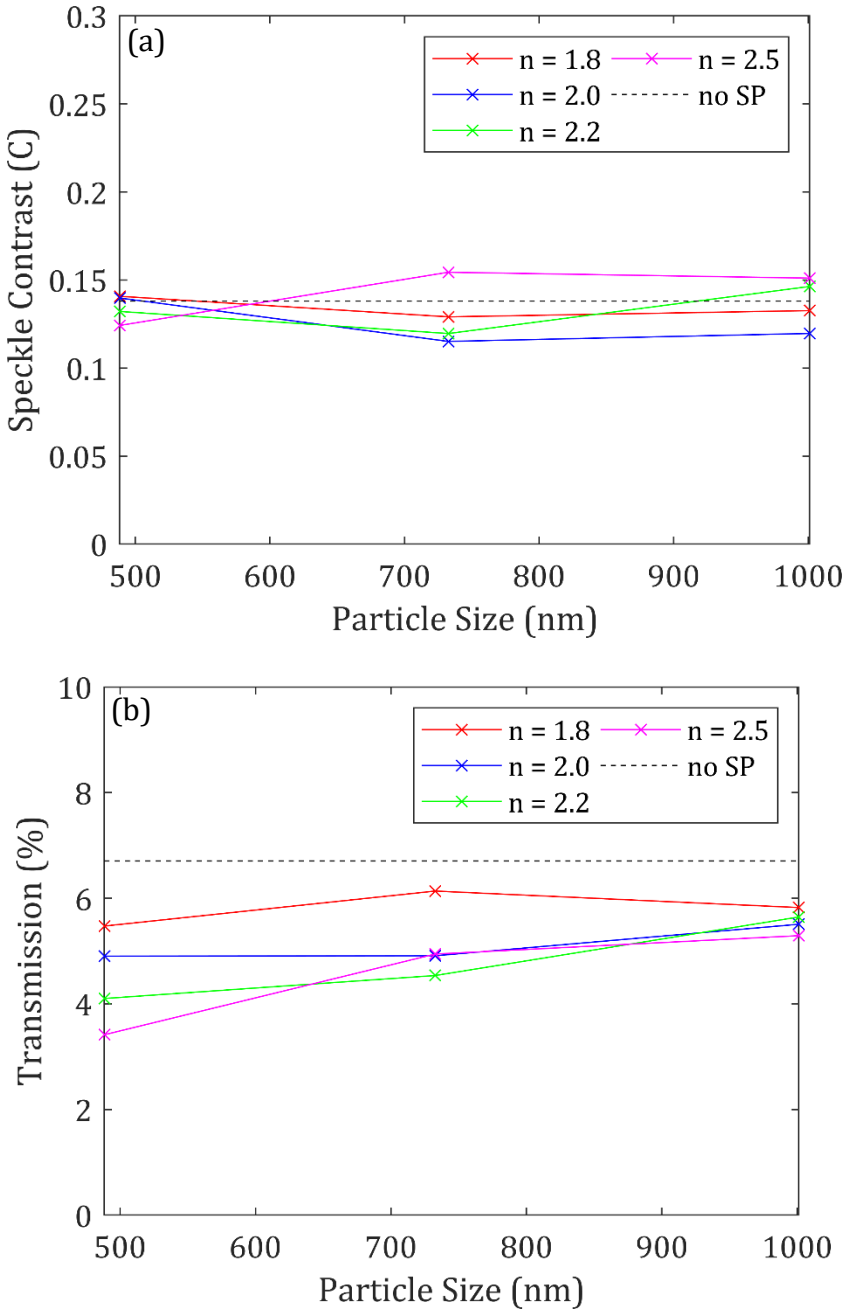

Figure 8.7: Simulations of (a) the speckle contrast and (b) the transmission for scattering particulates with 4 different refractive index values as a function of the particle size. Simulations were carried out for light with $\lambda = 633\ nm$, a beam diameter of 1 mm, a cell thickness of $d = 20\ \mu m$ and the chiral nematic LC was modelled with refractive indices of $n_o = 1.5$ and $n_e = 1.7$. The pitch was $p = 500\ nm$ and the domain size $p - 2p$. Each cell has had 1% (by area) of square scattering particles added at random locations in the cell with $n_{scat} = 1.8 - 2.5$ and particle size $0.5 - 1\ \mu m$. Data points represent simulated values whereas lines are linear interpolations to guide the eye. The dashed line represents either (a) the speckle contrast or (b) the transmission for an identical LC cell but without the additional scattering particulates.

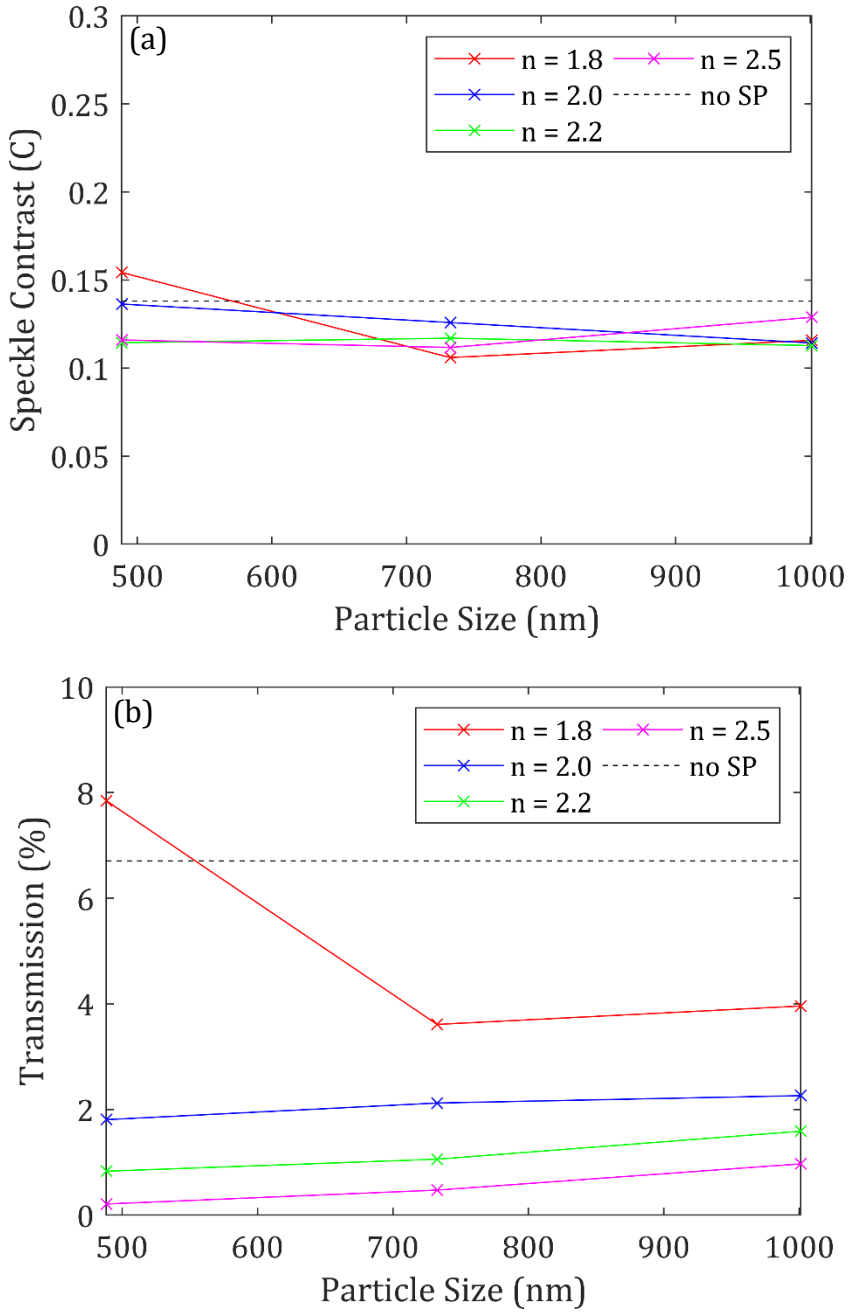

Figure 8.8: Simulations of (a) the speckle contrast and (b) the transmission for scattering particulates with four different refractive index values as a function of the particle size. Simulations were carried out for light with $\lambda = 633\ nm$, beam diameter 1 mm, cell thickness of $d = 20\ \mu m$ and the LC was modelled using refractive indices of $n_o = 1.5$ and $n_e = 1.7$. The pitch was $200 \leq p \leq 1000\ nm$ and the domain size $p - 2p$. Each cell has had 10% (by area) of square scattering particulates added at random locations in the cell with $n_{scat} = 1.8 - 2.5$ and particle size $0.5 - 1\ \mu m$. Data points represent simulated values whereas lines are linear interpolations to guide the eye. The dashed lines represent either (a) the speckle contrast or (b) the transmission for an identical LC cell without additional particulates.

The same reasoning could be applied to the experiments presented in Section 6.2.1 of Chapter 6. TiO_2 particles ($n = 2.584$ at 633 nm) have a much greater

difference in refractive index to the nematic LC host, E7 ($n_o = 1.5189$ and $n_e = 1.7305$ at 633 nm and 25°C), than the SiO_2 ($n = 1.457$ at 633 nm) particles, but they both failed to improve speckle reduction, and the transmission through the device was smallest for the TiO_2-doped sample. However, care must be taken when comparing these results as the simulations cannot model molecular interactions or changes to the physical or electro-optical properties as a result of particle-doping. Further, the variation in particle sizes used (25 nm for TiO_2 and 1 μm for SiO_2) is expected to have significant effect on the light scattering behaviour.

8.5.3 *Varying birefringence of LC mixture with fixed SP properties*

It has been shown that a LC device with a large birefringence is not significantly improved with the addition of scattering particulates regardless of their refractive index. In this experiment the influence of the addition of one type of SP on the device performance is explored for LC mixtures with a range of birefringence values. Specifically, 1 wt.% of particles with $n = 1.8$ and size 1 μm are dispersed into LC mixtures with $0.05 \leq \Delta n \leq 0.25$. Figure 8.9 is a plot of (a) the speckle contrast and (b) the transmission as a function of birefringence for mixtures both with and without additional scattering particulates.

From this data it is clear that the speckle contrast can be greatly reduced with the addition of scattering particulates if the base LC mixture has a low birefringence to begin with. The speckle contrast and transmission for devices with scattering particles are approximately independent of the mixture birefringence, with both remaining almost constant for all the simulations run in this study. Meanwhile, the mixture without scattering particles tends towards the same values of the speckle contrast and transmission observed for the mixtures with scattering particles as

birefringence increases, with a trend that is commensurate to the results reported in Section 8.3.

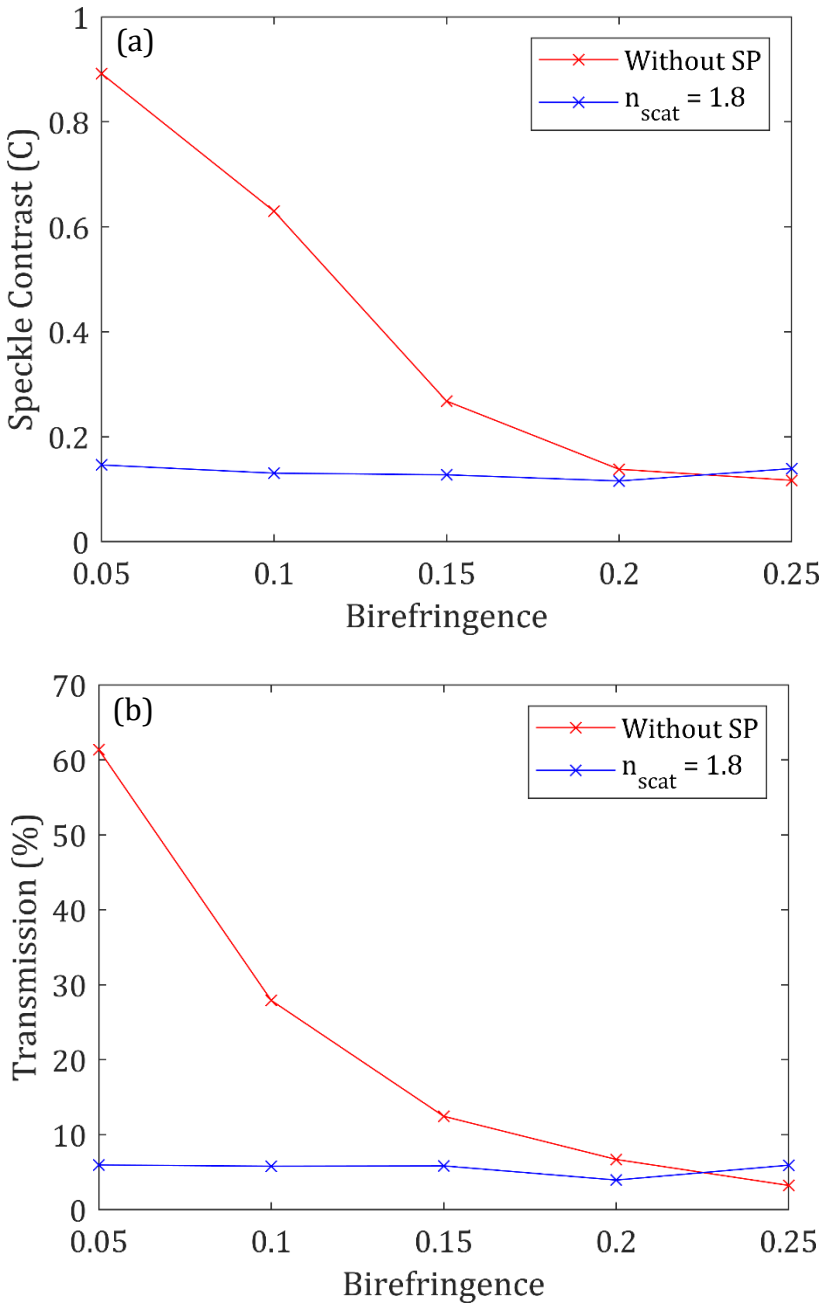

Figure 8.9: Simulations of (a) the speckle contrast and (b) the transmission both with and without scattering particulates as a function of the birefringence of the LC host. Simulations were carried out for light with $\lambda = 633\ nm$, a beam diameter 1 mm, cell thickness of $d = 20\ \mu m$ and an LC that was modelled with a birefringence ranging from $0.05 \leq \Delta n \leq 0.25$, with $n_{av} = 1.6$, pitch of $p = 500\ nm$ and domain size $p - 2p$. Each cell had 1% (by area) of square scattering particulates added at random locations in the cell with $n_{scat} = 1.8$ and a particle size of $1\ \mu m$. Data points represent simulated values whereas lines represent linear interpolations to guide the eye.

The results presented here potentially provide some explanation why scattering

particles added both experimentally, in Section 6.2 of Chapter 6, and in simulation, in Section 8.5.3, to high birefringence LCs (with $\Delta n \geq 0.2$) has very little effect on speckle contrast and transmission. These results suggest that the use of scattering particles could allow the base LC mixture to be chosen purely for its physical, conductive and dielectric properties, which could be chosen to reduce the field amplitude required for maximum speckle reduction, ignoring the birefringence value. It also shows that there is no significant benefit to adding scattering particles to LCs with birefringence values of $\Delta n \geq 0.2$. Further experimental work combining low birefringence LCs with scattering particles is needed to confirm this hypothesis.

8.5.4 *Summary*

It is worth noting that these simulations cannot model the molecular interaction between the chiral nematic LC and the scattering particulates. For example, the cyano groups in the nematic LC mixture, E7, are known to form hydrogen bonds with SiO_2 particles. It is likely that doping with particles such as these, especially at higher concentrations, would also serve to change other physical and electro-optical properties such as the viscosity and dielectric permittivity. However, this study does show that increasing the concentration of particles reduces the speckle contrast without significantly reducing the transmission even in LC devices with a high birefringence host. Also, an increase of the variation in the refractive index of the scattering particles relative to the LC refractive indices serves to reduce transmission without significantly reducing the speckle contrast in a LC device with a large birefringence ($\Delta n = 0.2$). Finally, it was shown that additional scattering particulates are most beneficial in LC mixtures with a small birefringence. Furthermore, the speckle contrast and transmission appear to be independent of

the birefringence of the LC host when only 1 wt.% of scattering particles are added to the mixture.

8.6 Temperature

In Section 6.3 of Chapter 6 an increase in cell temperature was shown to decrease speckle contrast and increase transmission. Speckle reduction was considered to be due, at least in part, to the reduction in viscosity at increased temperatures that permits the molecules to move more freely thus increasing the number of observed independent speckle patterns per unit time. Meanwhile, an increase in transmission was attributed to the decrease in birefringence that the LCs exhibit at increased temperatures. This is in agreement with both experimental and simulated experiments presented in Section 4.3 of Chapter 4 and Section 8.3 of this chapter.

In this section, the effect of cell temperature is modelled using measured refractive indices and rotational viscosity values of the nematic LC, E7, over a temperature range of $T = 25°\text{C} - 55°\text{C}$. These values are presented in Table 8.1. The refractive indices are used directly as the LC mixture parameters and the viscosity is modelled by relating it to the number of frames that are superimposed in the simulation. This is directly related to the exposure time of the camera, and it was shown in Section 6.3.7 of Chapter 6 that a decrease in viscosity is analogous to an increase in exposure time. Specifically, it was postulated that the relationship between viscosity γ and exposure time t was

$$\gamma \propto t^{-0.5} \tag{8.2}$$

For each experiment, the number of speckle patterns N integrated by the camera is

directly proportional to the exposure time. Consequently, the relationship between viscosity and N can be written as

$$N = k\gamma^{-2} \tag{8.3}$$

where k is a constant of proportionality. In this case a value of k was chosen such that N at 55°C was 100, and at lower temperatures $N < 100$. For this simulation, $k = 0.0784$. The speckle contrast for N superimposed frames was calculated from the $ax^{-0.5} + b$ fit of cumulative speckle contrast against N, as shown in Figure 8.2. Transmission was calculated using 100 superimposed frames as in all other simulations because the average transmission should be independent of N.

Temp (°C)	n_o	n_e	Δn	γ	N
25	1.5189	1.7305	0.2116	0.2078	1.8
35	1.5191	1.7142	0.1951	0.1045	7.2
45	1.5221	1.6919	0.1698	0.0531	27.8
55	1.5377	1.6440	0.1063	0.0280	100

Table 8.1: Refractive indices (n_o and n_e), rotational viscosity (γ Pa s) and number of frames (N) used to model the 'viscosity' of the chiral nematic LC device based upon the mixture E7 at $\lambda = 633\ nm$ and at temperatures of $T = 25$, 35, 45 and 55°C [70]

Figure 8.10 is a plot of (a) speckle contrast and (b) transmission for a range of pitch values as a function of cell temperature. The trends seen in both plots are found to compare very favourably with the experimental results presented in Sections 6.3.3 and 6.3.4 of Chapter 6. As the temperature increases, the speckle contrast reduces, with a slight increase in the speckle contrast occurring just below the clearing temperature. Meanwhile, an increase in temperature serves to increase

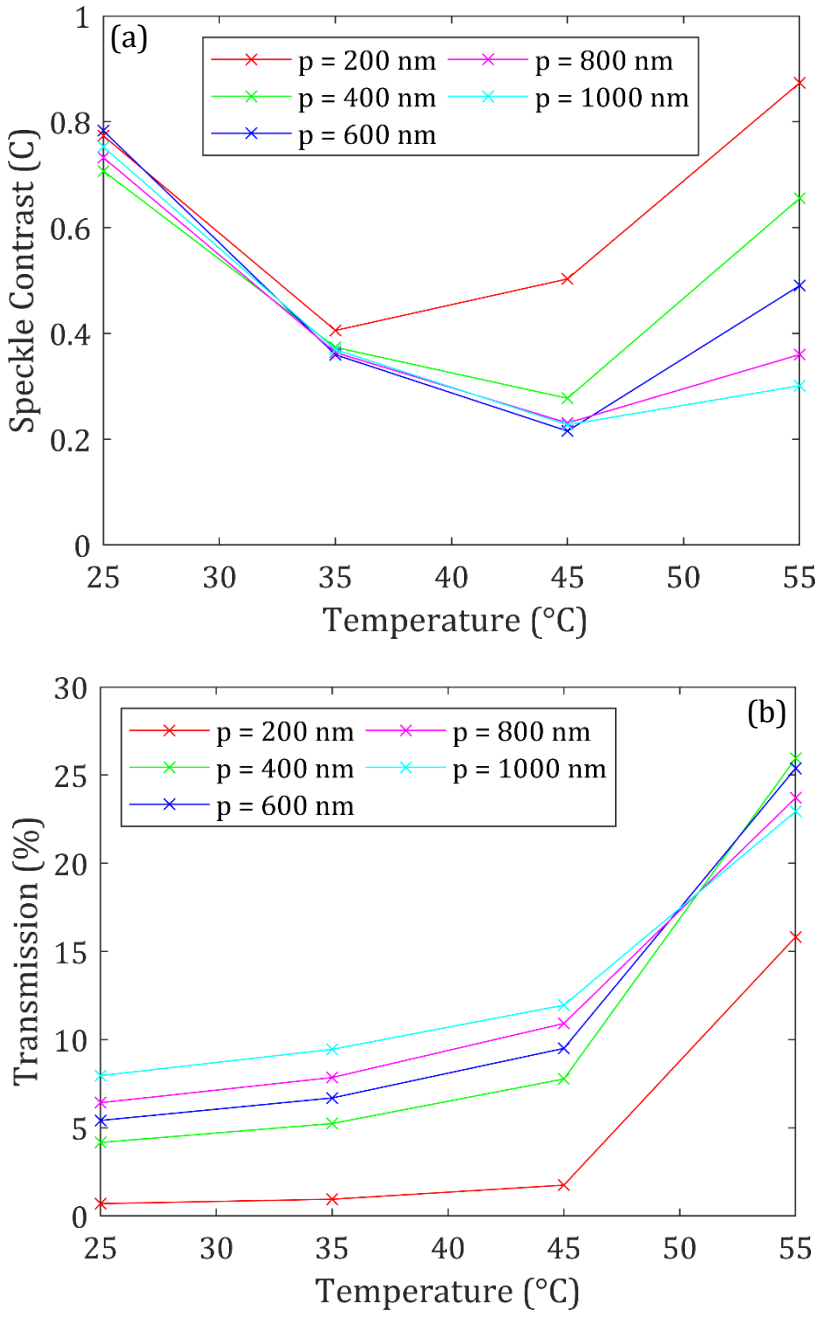

Figure 8.10: Simulations of (a) the speckle contrast and (b) the transmission for five different pitch values as a function of temperature. The simulations were carried out for light with $\lambda = 633\ nm$, a beam diameter of 1 mm and a cell thickness of $d = 20\ \mu m$. The LC was modelled with refractive indices that were equivalent to those of the nematic E7 at the respective temperature and laser wavelength, and the viscosity was accounted for by varying the number of frames that are superimposed within a timeframe relative to the E7 viscosity values, as shown in Table 8.1. The pitch of the helix ranged from $200 \leq p \leq 1000\ nm$ and the domain size was $p - 2p$. Data points represent simulated values whereas the lines are linear interpolations to guide the eye.

transmission, especially near the clearing temperature. The speckle contrast values themselves are considerably higher than that found experimentally, but this is predominantly due to the arbitrary choice of the constant of proportionality, k,

chosen to avoid extrapolation beyond $N = 100$. The experiment was repeated with a range of values for k and the same trends were seen between speckle contrast and temperature but with less variation between speckle contrast values, as shown in Figure 8.11.

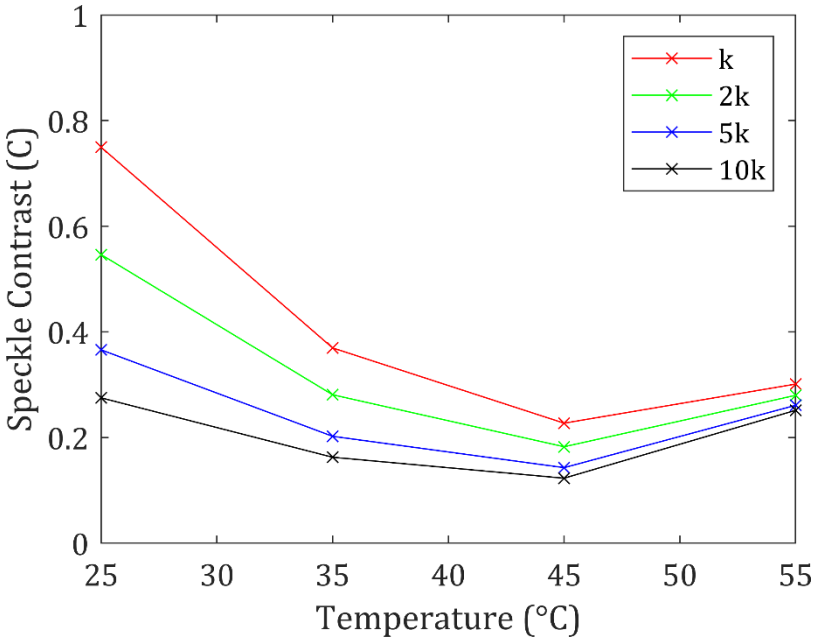

Figure 8.11: Speckle contrast for four different k-values as a function of temperature. The pitch of the chiral nematic LC was fixed at $p = 1000\ nm$. All other parameters match those used in Figure 8.10. Data points represent simulated values whereas lines are linear interpolations to guide the eye.

In conclusion, the results presented in this section show that for each LC mixture there is an optimum temperature for speckle reduction. It is postulated that an increase in the temperature results in more speckle patterns per unit time, but at the cost of reduced birefringence. Just below the clearing temperature, the birefringence becomes so low that the reduction in viscosity no longer outweighs the effect of reduced birefringence. This leads to the conclusion that high birefringence is perhaps less important for speckle reduction than low viscosity, and limiting birefringence allows for greater transmission. Further, it would be of interest to test cells doped with scattering particulates at high temperatures as their

refractive index would be unaffected by the temperature. This would allow a test of a cell with reduced viscosity that retains a wide range of refractive indices.

8.7 Laser wavelength

The final simulation presented in this chapter considers the effect that the laser wavelength λ has on the resulting speckle contrast and transmission. In this experiment three different wavelengths are considered: $\lambda = 465, 520, 633$ nm. The LC refractive indices are taken from published material for E7 at 25°C and at the relevant wavelength. Figure 8.12 is a plot of (a) speckle contrast and (b) transmission as a function of pitch for each wavelength. There is little variation in speckle contrast between the wavelengths, but at all pitch values there is a decrease in both speckle contrast and transmission with a decrease in wavelength. This is likely to be predominantly due to the increase in birefringence at shorter wavelengths in E7 and is in agreement with the simulated results presented in Section 8.3 and previously published results for scattering phenomena in LCs [121].

The same simulation was also undertaken, but this time using the refractive indices for either BL006 or 5CB and the same trend was seen. However, the variation in speckle contrast and transmission values at different wavelengths was smaller for BL006 and larger for 5CB. This is consistent with the birefringence simulations from Section 8.3 also, because $\Delta n_{5CB} < \Delta n_{E7} < \Delta n_{BL006}$. Small variations in the birefringence were shown to have a decreasing effect on the speckle contrast and the transmission as the birefringence increases, especially for $\Delta n > 0.2$.

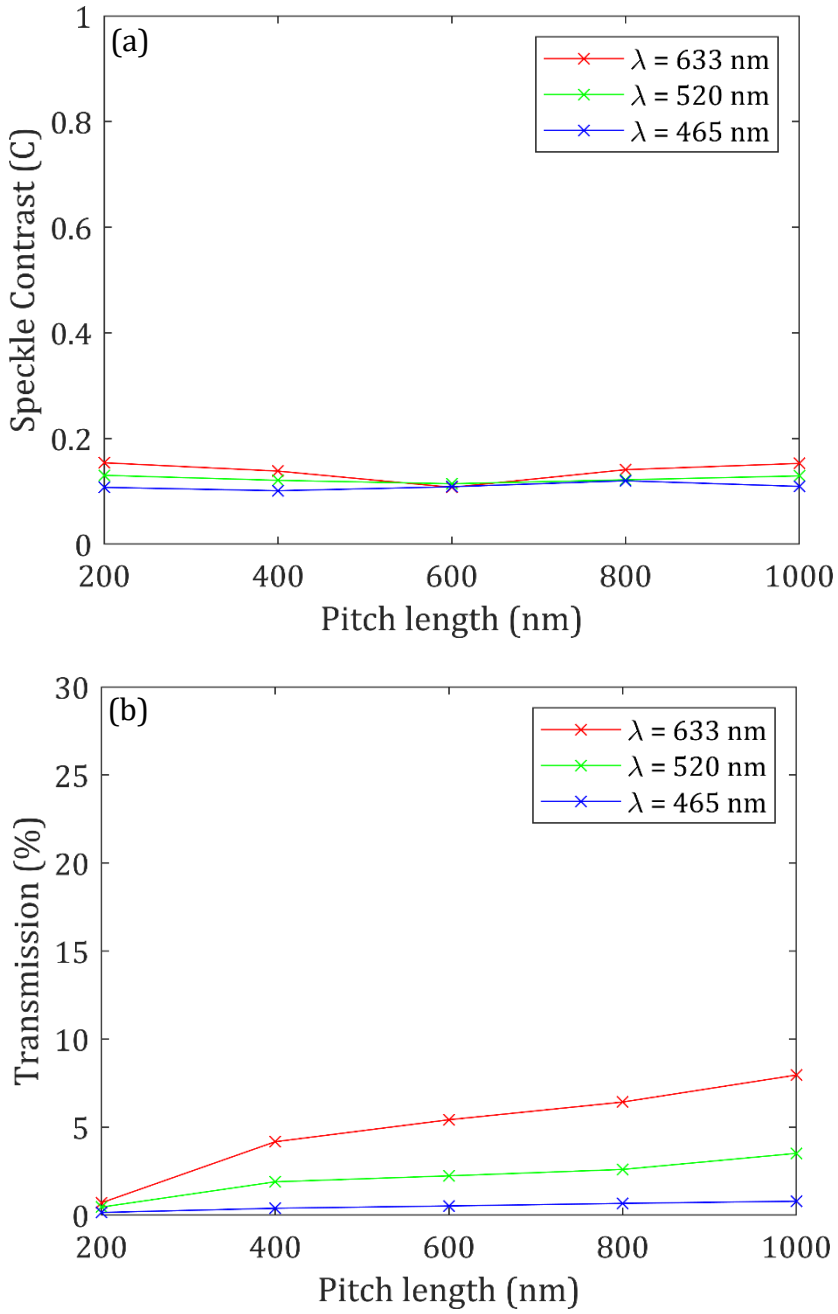

Figure 8.12: Simulations of (a) the speckle contrast and (b) the transmission over a range of laser wavelengths as a function of the pitch of the chiral nematic LC. Laser with $\lambda = 633, 520, 465\ nm$, a beam diameter of 1 mm, a cell thickness of $d = 20\ \mu m$ and an LC modelled with refractive indices that are equivalent E7 at 25°C and the respective laser wavelength, as shown in Table 4.2. The pitch of the chiral nematic LC ranges from $200 \leq p \leq 3000\ nm$ and the domain size is $p - 2p$. The data points represent simulated values whereas the lines are linear interpolations to guide the eye.

	λ (nm)		
	450	**546**	**633**
n_o	1.5425	1.5268	1.5189
n_e	1.8005	1.7512	1.7305
Δn	0.2580	0.2244	0.2116

Table 8.2: Refractive indices (n_o and n_e) of E7 at $\lambda = 450, 546, 633\ nm$ and 25°C [70].

The experiments were repeated once more for an LC mixture with $n_o = 1.5$ and $n_e = 1.7$ for each wavelength. Once again, a decrease in the speckle contrast and transmission was observed with a reduction in the laser wavelength. This is consistent with well-known theory that the Rayleigh scattering of light increases with λ^{-4} [112].

8.8 Concluding Remarks

The simulation results presented in this chapter provide a valuable insight into the optics of light scattering in chiral-nematic LC speckle reducing devices. Although the results presented in this chapter are limited by the assumptions required to create mathematical models of light propagation and do not directly model molecular movement as a result of an applied electric field, they have made it possible to isolate and test parameters such as birefringence that cannot be easily varied in real LC mixtures without changes to other important material parameters. Furthermore, the results have shown an excellent correlation to experimental data presented in Chapters 4-6 of this thesis.

Section 8.3 showed that increased birefringence reduces speckle contrast and transmission up to $0.15 \leq \Delta n \leq 0.20$, and that a further increase serves only to

reduce transmission. This not only matches the significant decrease in speckle contrast and transmission shown in an experimental test of LCs with birefringence values ranging from 0.091 – 0.233 (Section 4.3.1, Chapter 4) , but it also explains why very little variation in speckle contrast and transmission was seen when chiral nematic LC devices consisting of either E7 or BL006 were compared, both with birefringence values of $\Delta n > 0.2$ (Section 4.3.2, Chapter 4).

Section 8.4 showed that an increase in the cell thickness decreases the speckle contrast and transmission through increased light scattering. Specifically, speckle contrast reduced by 60-80% and transmission reduced by 80-90% with an increase in cell thickness of $t = 5$ μm to $t = 20$ μm. This trend is consistent with the experimental data presented in Section 6.1 of Chapter 6, as well as previous work on light scattering in LCs [89] [90].

It was shown in Section 8.5 that the addition of scattering particulates to the chiral nematic LC mixture only lead to significant reduction in speckle contrast and transmission when used in combination with LC mixtures that consist of a low birefringence host. This would explain why doping with particulates in E7 and BL006 showed no significant reduction experimentally in Sections 6.2.1 and 6.2.2 of Chapter 6. Further, it was shown that an increase in the concentration of scattering particulates (from 0.25 – 5 wt.%) does decrease the speckle contrast and transmission even in LCs with a large birefringence, which was also shown in Section 6.2 of Chapter 6.

Viscosity at high temperatures was modelled indirectly in Section 8.6 by relating the reported values of the rotational viscosity of the nematic LC, E7, with the number of speckle patterns superimposed within a timeframe in the simulation.

The subsequent results were found to be in good qualitative agreement with the experimental results for chiral nematic LC mixtures based on E7, BL006 and 5CB presented in Section 6.3 of Chapter 6, with the speckle contrast reducing while the transmission and temperature increased up until just below the transition temperature. The arbitrarily chosen proportionality constant was shown to have no effect on the trends seen when it was varied.

Finally, the simulation results presented in Section 8.7 matched published results for scattering in LCs very well, with decreased speckle contrast and transmission found with reduced wavelength. This was tested for the refractive indices of E7, BL006 and 5CB at $T = 25°C$, as well as for a hypothetical LC with refractive indices independent of wavelength.

Overall, the presented simulation results match very well with experimental results presented in this thesis and in the published literature. It has been shown that there is an optimum birefringence for any LC material, above which the speckle contrast is not significantly reduced, and that scattering particulates are most beneficial in mixtures with a low birefringence host. Viscosity has been shown to be extremely important, with reduced viscosity at high temperatures outweighing the effect of reduced birefringence. In summary, the ideal LC mixture should combine minimal viscosity with birefringence as low as possible to allow for sufficient speckle reduction while retaining good transmission. Further, scattering particulates could be combined with low birefringence LCs that exhibit low viscosity to improve performance. Cell thickness of $20 \leq t \leq 35$ μm is preferred for maximum speckle reduction.

9 Conclusions and Future Work

The work in this thesis has one collective aim: to design and optimise a speckle reducing device based on a chiral-nematic liquid crystal device. The application of a low-frequency electric field causes the director to fluctuate in a chaotic manner as a result of electrohydrodynamic instabilities caused by competing dielectric and conductive forces. This in turn applies a time-varying and spatially-random phase perturbation to incident laser light, disrupting the coherent wave front and reducing the appearance of speckle. An overview of speckle statistics, speckle reduction and liquid crystal properties was provided in Chapter 2.

A novel and automated method of speckle measurement is implemented throughout the work, designed to match human speckle observation, and a summary of this measurement system can be found in Chapter 3. A proof of concept device is demonstrated at the beginning of Chapter 4 and is shown to reduce the speckle contrast of a He-Ne laser to $C = 0.157$. This is found to be consistent over a period of 1 hour, with little hysteresis shown when the electric field amplitude and frequency are varied repeatedly.

Chapters 4 – 6 present experimental results that investigate the effect a variation in device properties have on device performance in terms of speckle reduction, transmission and required field parameters. In Chapter 7, an optical model is developed that is used to further study these parameters, and the results

of these simulations are presented and discussed in Chapter 8. This chapter presents concluding remarks on each device property tested in this thesis.

9.1 Pitch

In Chapter 4 the relationship between pitch, p, and device performance was investigated for a range of mixtures covering a wide range of pitch values: $224 \leq p \leq 2050$ nm. It was found that for all mixtures the speckle contrast reduces significantly, and approximately linearly, with pitch over the range $500 \leq p \leq 2000$ nm, with the speckle contrast reducing by at least 50% for the optimum pitch value. Mixtures with a pitch shorter than 500 nm show little further reduction in speckle contrast. The transmission appeared to decrease somewhat linearly with pitch, reaching a mixture-specific minimum of $10 - 30\%$ at $500 < p < 1000$ nm. As the pitch was further reduced the transmission was shown to increase in all mixtures by up to a factor of 2. It is postulated that the reduction in speckle contrast and transmission with pitch is due to an increase in the spatial frequency of the refractive index variation. It is not clear why the transmission reaches a minimum before increasing with further reduction in pitch, but it is beneficial to device performance.

The electric field amplitude for peak speckle reduction was shown to be inversely proportional to pitch and independent of mixture composition. Peak speckle reduction was seen at electric fields of $E < 5$ V/μm for a pitch of $p > 1000$ nm, and short pitch mixtures of $p \approx 250\,nm$ required an electric field amplitude of $E \approx 20$ V/μm. This trend is in good agreement with the relationship between pitch and threshold electric field amplitude for the field-induced chiral

nematic-nematic transition in chiral nematics and it is noted that peak speckle reduction occurs at field amplitudes just below this critical threshold. The square-wave frequency for peak speckle reduction was shown to be approximately inversely proportional to pitch also, although there appeared to be a slight variation between mixtures in terms of the constant of proportionality. This follows the known relationship between Hurault relaxation frequency and pitch (equation 4.2), and a variation in mixture viscosity and elastic constants would account for the slight variation between different mixtures.

It was concluded that short pitch mixtures are preferred for a speckle reducing device with maximum speckle reduction and transmission. The best performing cell in this experiment was a mixture of the nematic E7 with chiral dopant BDH1281 to provide a pitch of $p = 273\,\text{nm}$. This was found to reduce speckle contrast to $C = 0.142$ with a transmission of 21.9%: a speckle reduction of 77% or approximately $1/\sqrt{20}$. Further work could be carried out to explore the performance of mixtures with a shorter pitch by using high twisting power chiral dopants such as R5011, as well as equipment capable of delivering field amplitudes above 20 V/μm. If the trends seen in this work are extrapolated, it is expected that this would result in a mixture capable of comparable speckle reduction but with transmission significantly above 20%.

9.2 Birefringence

Chapter 4 continued with a study of birefringence and speckle reduction. Three mixtures with $p = 425 \pm 5\,\text{nm}$ were prepared using three different nematic hosts with birefringence of $\Delta n = 0.091, 0.180$ and 0.233. It was shown that increased

birefringence over this range resulted in a reduction in speckle contrast from $C = 0.566$ to $C = 0.161$, and transmission from 47% to 11%. A further experiment was carried out comparing the performance of two mixtures with larger birefringence: E7 ($\Delta n = 0.212$) and BL006 ($\Delta n = 0.274$) across a range of pitch values. It was shown that there was little variation in speckle reduction but that generally the BL006 mixtures exhibited reduced transmission when compared to the E7 mixtures with similar pitch.

In Chapter 8, the importance of the birefringence was explored through simulations for a range of pitch values. In each simulation the number of superimposed speckle images was kept constant. This was considered equivalent to keeping the material properties such as viscosity, dielectric anisotropy and conductivity constant. In all cases, the speckle contrast and transmission decreased with increasing birefringence, with approximately an inverse relationship between birefringence and speckle contrast or transmission. The results showed that the speckle contrast reaches a minimum for $0.15 < \Delta n < 0.2$, but that the transmission continues to reduce up to $\Delta n = 0.25$, which was the largest birefringence that was tested. This is in good agreement with the experimental results and explains why there is little difference in speckle reduction between E7 and BL006 cells of similar pitch despite a reduction in transmission.

The birefringence studies have shown that the optimum mixture for maximum speckle reduction while retaining optimum transmission is $0.15 < \Delta n < 0.20$. Speckle contrast is reduced when independent speckle patterns are superimposed so it can be surmised that a small birefringence does not result in sufficient phase variation of the incident laser light so as to produce many

independent speckle patterns. The same amount of director fluctuations per unit time in a larger birefringent material will increase the range of phase perturbations until the birefringence becomes sufficiently high as to impose phase perturbation between 0 and 2π. Further increases in birefringence will cause more light to be scattered out of the numerical aperture of the collection lens but will not reduce speckle contrast further due to the cyclic nature of phase. Transmission will continue to reduce while speckle contrast does not.

Further work could be carried out using LC mixtures with moderate birefringence so as to find the optimum value for maximising speckle contrast without compromising transmission. A more comprehensive experimental review of LCs with birefringence in the range tested here could be used to find a quantitative relationship between birefringence and speckle reduction, as was achieved through simulation.

9.3 Ionic dopants

In Chapter 5 the ionic dopant CTAB was added to a range of chiral nematic LC mixtures with the aim of increasing the conductivity anisotropy. This was expected to reduce the threshold electric field for dynamic scattering and possibly increase speckle reduction as a result of an increase in the number of ions and their mobility. In all cases, the addition of 0.1 wt.% - 1.0 wt.% of CTAB was shown to increase the range of field conditions over which dynamic scattering was observed to reduce speckle contrast, but in general this was not accompanied by a reduction in peak speckle reduction, or the field amplitude required to achieve it. Furthermore, it was shown that the addition of CTAB caused the cell to deteriorate when exposed to high

amplitude electric fields of $E > 12\ \mathrm{V/\mu m}$. This behaviour is in agreement with previous reports on the use of CTAB with low frequency, high-amplitude electric fields and is expected to be the result of an irreversible electro-chemical reaction that occurs at the electrodes.

It is postulated that the CTAB may be oxidised to form bromine gas which is consistent with the yellowing of the mixture that is observed. In order to avoid an irreversible deterioration, the work in this thesis suggests that the concentration by weight of CTAB should be limited to < 0.2 wt.% and the electric field amplitude should not exceed 12 V/μm. Within the limitations of the devices that include CTAB, it was found that they behave consistently for periods of at least one hour and exhibit hysteresis of less than 1%, but the short pitch cells that are preferred for maximum speckle reduction require electric fields above this limit for peak performance.

Consequently, it was concluded that CTAB is not a sensible choice of ionic dopant, and instead it was suggested that redox dopants should be considered as these undergo reversible reactions at the electrodes, avoiding the cell deterioration seen here. In this way they have been shown to increase lifetime and scattering over the use of ionic dopants in LC scattering devices and have also been reported to increase conductivity anisotropy in the LC mixture more than ionic dopants [82] [83]. However, it is suggested that the experimental procedure be extended to measure current density in these cells as low power consumption is a beneficial property of these devices and may be expected to increase with the addition of ionic species.

Alternatively, device deterioration might be limited with the use of passivating

layers that isolate the electrode surface from the LC mixture. This has been shown previously to avoid electrolytic decomposition of an ionic dopant using a layer of silica or polyimide [74]. Finally, an alternative choice of ionic dopant with a more stable anion has also been shown to prevent cell deterioration [74].

9.4 Cell thickness

Chapter 6 begins with an experimental study of cell thickness. It is shown that an increase in the cell thickness from 5 μm to 20 μm results in a decrease in the speckle contrast of 40-60% and a decrease in transmission of approximately 50%. This is due to increased volume scattering and is in good agreement with the published literature on light scattering in LC cells. The electric field amplitude for peak performance appears to be independent of cell thickness. This is in agreement with the independence shown between cell thickness and the critical electric field amplitude required for the chiral nematic-nematic transition in the literature. The voltage threshold for dynamic scattering was found to follow a linear dependence on cell thickness, in agreement with reports on scattering in nematic and smectic mixtures.

Simulations carried out in Chapter 8 were able to model a greater variation in the cell thickness from 5 μm to 50 μm. Over this range it is clear that speckle contrast and transmission decrease with increased cell thickness, as shown experimentally, and that the relationship is approximately inverse. Speckle contrast reaches a minimum at $t = 20$ μm for a cell with $p = 600$ nm and at $t = 35$ μm for a cell with $p = 300$ nm. Meanwhile, transmission in both mixtures continually decreased across the range of cell thicknesses tested, tending towards 0% in both cases. Similar reasoning can be applied to this result as to the birefringence test:

there appears to be a cell thickness that corresponds to a phase perturbation of $0 - 2\pi$ being applied to the light, and a further increase in the cell thickness serves to scatter light over a wider range of angles which reduces transmission but does not further decrease speckle contrast. Devices with a smaller thickness impose a smaller range of phase perturbations on the transmitted light.

It was also shown experimentally that 9 μm -thick devices suffer from lifetime and hysteresis issues that the 5 μm and 20 μm cells did not. At present, it is not clear why this is the case. However, it is concluded that a cell thickness of 20 μm is preferred for speckle reduction. It would be of interest to test thicker cells experimentally, but the voltage required to apply the necessary electric field amplitude for peak speckle reduction in short-pitch LC mixtures was larger than that accessible with the equipment that was available during the study presented in this thesis. Alternatively, a chiral nematic mixture with a longer pitch could be tested in a thicker cell as the field amplitude required for peak performance will be lower. A wedge cell could be used to test a continuous range of cell thicknesses and the results of such an experiment could be used to find a quantitative relationship between cell thickness and speckle contrast as was achieved through simulation. Furthermore, it would be of interest to test cells with different alignment layers, or without alignment layers altogether.

9.5 Scattering particles

Section 6.2 of Chapter 6 presented experimental results for mixtures that had been doped with additional scattering particulates. Scattering particles have been used to increase scattering in LCs previously, as well as to manipulate the electro-optical properties. In this thesis, two different particulates are added to chiral nematic LC

mixtures, SiO_2 particles of diameter 1 μm and refractive index $n = 1.457$ and TiO_2 particles of diameter 25 nm and refractive index $n = 2.584$. At a weight concentration of 0.25 wt.%, both particulates reduced the field amplitude and frequency required for peak performance slightly, but both caused an increase in the speckle contrast. It was suggested this might be due to hydrogen bonds formed between the cyano groups in the E7 host and the particulates, causing an increase in viscosity. Furthermore, the optical simulations presented in Section 8.5.1 show that concentrations of < 2 wt.% of SiO_2 particles are expected to increase speckle contrast in short-pitched mixtures, most likely due to a decrease in the spatial frequency of the refractive index. A higher concentration of 5 wt.% of SiO_2 particulates was also tested and a 7% reduction in speckle contrast was observed compared to the undoped mixture.

Simulations were also carried out to consider the effect of adding a weight concentration of 1% scattering particulates with $n = 1.8$ into a chiral nematic mixture for different values of the birefringence. It was shown that the speckle reduction and transmission was independent of the base mixture birefringence. Furthermore, the device performance for LC mixtures with high birefringence ($\Delta n > 0.2$) were not found to be any better with the addition of scattering particulates than devices filled with the base chiral nematic mixture. This is in agreement with the experimental results that were obtained for devices with relatively high birefringent nematic LC hosts, E7 and BL006, doped with additional scattering particulates. Increasing the refractive index of the scattering particulates was also shown to have no obvious effect on speckle reduction, while reducing transmission.

In conclusion, scattering particles appear to be a viable route towards increasing the scattering in mixtures with low birefringence. In this way, a low-birefringence LC mixture could be chosen with a low viscosity and advantageous electric properties and the poor optical properties can be compensated for with the addition of scattering particulates. Furthermore, it would be of interest to test mixtures with added scattering particulates at elevated temperatures. Under these conditions the mixture would exhibit significantly reduced viscosity and the reduced birefringence in the chiral nematic mixture is expected to be compensated for with the presence of scattering particulates. Finally, nano-particles such as TiO_2 could be used to modify the electrical properties of a mixture [97] [98] [99] and therefore merit further investigation in this regard.

9.6 Temperature

Section 6.3 of chapter 6 presents the relationship between cell temperature and device performance for three mixtures based on the nematic hosts, 5CB, E7 and BL006. Each cell was tested at 5°C intervals from room temperature up to their respective clearing temperatures. In all cases, increased temperature was shown to reduce speckle contrast, increase transmission, reduce the electric field amplitude required for peak performance and increase the driving frequency. It is proposed that this is due to a significant reduction in viscosity with increased temperature that allows the director to fluctuate more rapidly under the influence of an electric field. Also, birefringence is known to reduce with increasing temperature and this would account for the increase in transmission.

It was shown that an increase in temperature is analogous to an increase in camera exposure time, thus confirming that a greater number of ‘independent’

speckle patterns are created per unit time. In fact, it was postulated that this is predominantly a result of a reduction in viscosity and have suggested that rotational viscosity shows an inverse relationship with $\sqrt{N}$, where N is the number of independent speckle patterns that a mixture can produce. This hypothesis was used to simulate the viscosity changes with increased temperature alongside the known changes in the birefringence of E7 at increased temperatures. The simulated results were in close agreement with experimental results, showing a reduction in speckle contrast and an increase in transmission with increased temperature.

When comparing performance at temperatures just below the clearing point with those obtained at room temperature, the speckle contrast was found to be reduced by up to 50% and the transmission increased by up to a factor of 2. From these findings, it is clear that viscosity has a very large impact on device performance, and future work should be undertaken to investigate the use of low-viscosity LCs and viscosity reducing agents. Furthermore, mixtures could be chosen that have a clearing temperature just above the desired operating temperature of the device for optimum performance.

9.7 Laser wavelength

In Section 8.7 of Chapter 8 it was shown through simulations that there is a slight reduction in speckle contrast and transmission with a decrease in the laser wavelength. This was the case both when the wavelength-dependent refractive indices were used for a simulated mixture based on the nematic host E7, and for a simulated mixture with refractive indices that were independent of wavelength. This is in good agreement with well-known theory that Rayleigh scattering of light

is proportional to λ^{-4}. Consequently, it is expected that the device developed in this work will show improved speckle reduction when used with lasers of shorter wavelength. Furthermore, for applications such as laser projection, multiple laser wavelengths are expected to be used simultaneously. A basic RGB (red, green, blue) configuration would be expected to provide a further reduction in speckle contrast of $1/\sqrt{3}$ as a result of spectral decorrelation of speckle patterns.

9.8 Concluding remarks

Through optimisation of material and device properties it has been shown that a device based on a chiral-nematic LC mixture is capable of reducing speckle to an almost imperceivably low level of $C = 0.07$ while retaining a high transmission of 50%. The device is very compact, vibration free and exhibits excellent lifetime and minimal hysteresis. With the understanding developed in this thesis it is expected that the design can be further optimised through the selection of optimised LC mixture parameters and device architecture. Encouragingly, the cells developed in this work already outperform all of the LC-based devices introduced in Section 2.5, as well as the commercially available Optotune speckle reducer [122]. This electroactive polymer-based moving diffuser was tested in the experimental set-up used throughout this thesis and was shown to reduce speckle to only $C = 0.18$ with a transmission, as defined in Section 4.2.3, of 60%.

Reduced viscosity was shown to be the dominant method of improving speckle reduction, allowing the electric field to operate at higher frequencies and thus causing the director to fluctuate more rapidly in time. Speckle reduction was also shown to improve to a lesser extent with increased birefringence, but at the

expense of transmission. This was shown most clearly with the temperature experiments in Section 6.3. Increasing the temperature caused significant reduction in both viscosity and birefringence, but the devices showed an increase in speckle reduction and transmission. Furthermore, decreasing the pitch below the wavelength of the laser source causes scattering centres to become smaller than the wavelengths corresponding to visible light. Consequently, the birefringence experienced by visible light reduces and both speckle reduction and transmission are shown to increase.

It is therefore concluded that the optimal mixture in terms of low speckle contrast and high transmission comprises a LC with short pitch ($p < 300$ nm), low viscosity and moderate birefringence ($\Delta n \approx 0.15$). Low pitch and viscosity are the most important properties, and birefringence could be increased if required with the use of specially selected scattering particles. (Further work is required to explore their use in low Δn LCs and over a wider range of particle sizes.) These properties would be expected to produce a device capable of speckle reduction to $C < 0.04$ and a transmission of over 80%, thus matching or exceeding the optical performance of all other speckle reduction techniques found in the literature by the author.

The electric field amplitude for peak speckle reduction was found to be closely related to that required for the field-induced chiral nematic-nematic transition. This is known to be proportional to the square root of $K_{22}/\Delta\varepsilon$, and inversely proportional to the pitch. Consequently, while a short pitch is preferred for optimal optical performance, the electric field amplitude could be minimised by reducing the ratio of K_{22} to $\Delta\varepsilon$. The addition of the ionic dopant CTAB did not

improve the optical performance or reduce the field amplitude for peak speckle reduction but it did widen the electric field parameter space over which speckle reduction was observed, while limiting the lifetime and maximum electric field amplitude. However, the use of redox dopants could be explored in future work.

References

[1] J. W. Goodman, Speckle phenomena in optics: theory and applications, Roberts & Company, 2006.

[2] M. Francon, Laser Speckle and Applications in Optics, Academic Press, 1979.

[3] R. A. B. J. H. J. Rabal, Dynamic Laser Speckle and Applications, CRC, 2008.

[4] M. N. Akram and X. Chen, "Speckle reduction methods in laser-based picture projectors," *Optical Review,* vol. 23, no. 1, pp. 108-120, 2016.

[5] D. Huang, E. a. Swanson, C. P. Lin, J. S. Schuman, W. G. Stinson, W. Chang, M. R. Hee, T. Flotire, K. Gregory, C. a. Puliafito and J. G. Fujimoto, "Optical Coherence Tomography," *Science,* vol. 254, pp. 1178-1181, 1991.

[6] D. Léger, E. Mathieu and J. C. Perrin, "Optical surface roughness determination using speckle correlation technique.," *Applied optics,* vol. 14, no. 4, pp. 872-877, 1975.

[7] J. A. Leendertz, "Interferometric displacement measurement on scattering surfaces utilizing speckle effect," *Journal of Physics E: Scientific Instruments,* vol. 3, no. 3, pp. 214-218, 1970.

[8] J. W. Goodman, "Some Effects of Target-Induced Scintillation on Optical Radar Performance," *Proceedings of the IEEE,* vol. 53, no. 11, pp. 1688-1700, 1965.

[9] M. S. Pierce, R. G. Moore, L. B. Sorensen, S. D. Kevan, O. Hellwig, E. E. Fullerton and J. B. Kortright, "Quasistatic X-Ray Speckle Metrology of Microscopic Magnetic Return-Point Memory," *Physical Review Letters,* vol. 90, no. 17, p. 4, 2003.

[10] C. B. Burckhardt, "Speckle in Ultrasound B -Mode Scans," *IEEE Transactions on Sonics and Ultrasonics,* Vols. SU-25, no. 1, pp. 1-6, 1978.

[11] S. Roelandt, Y. Meuret, G. Craggs, G. Verschaffelt, P. Janssens and H. Thienpont, "Standardized speckle measurement method matched to human speckle perception in laser projection systems," *Optics Express,* vol. 20, no. 8, pp. 8770-8783, 2012.

[12] G. Zheng, B. Wang, T. Fang, H. Cheng, Y. Qi, Y. W. Wang, B. X. Yan, Y. Bi, Y. Wang, S. W. Chu, T. J. Wu, J. K. Xu, H. T. Min, S. P. Yan, C. W. Ye and Z. D. Jia, "Laser digital cinema projector," *IEEE/OSA Journal of Display Technology,* 2008.

[13] N. E. Yu, J. W. Choi, H. Kang, D.-K. Ko, S.-H. Fu, J.-W. Liou, A. H. Kung, H. J. Choi, B. J. Kim, M. Cha and L.-H. Peng, "Speckle noise reduction on a laser projection display via a broadband green light source," *Optics Express,* 2014.

[14] B. Redding, M. A. Choma and H. Cao, "Speckle-free laser imaging using random laser illumination," *Nature Photonics,* 2012.

[15] "Sony MP-CL1A," [Online]. Available: https://www.sony.com/electronics/projector/mp-cl1a.

[16] J. Li, "Design of optical engine for LCOS laser display with rotated diffuser plate," *Microwave and Optical Technology Letters,* vol. 55, no. 1, pp. 138-141, 2013.

[17] S. C. Shin, S. S. Yoo, S. Y. Lee, C. Y. Park, S. Y. Park, J. W. Kwon and S. G. Lee, "Removal of hot spot speckle on laser projection screen using both the running screen and the rotating diffuser," *Displays,* vol. 27, no. 3, pp. 91-96, 2006.

[18] M. Sun and Z. Lu, "Speckle suppression with a rotating light pipe," *Optical Engineering,* vol. 49, no. 2, p. 024202, 1 2 2010.

[19] P. H. Yao and C. H. Chen, "Low speckle laser illuminated projection system with a vibrating diffractive beam shaper," *Optics Express,* vol. 20, no. 15, pp. 16552-16566, 2012.

[20] T. K. T. Tran, S. Subramaniam, C. P. Le, S. Kaur, S. Kalicinski, M. Ekwinska, E. Halvorsen and M. N. Akram, "Design, Modeling, and characterization of a microelectromechanical diffuser device for laser speckle reduction," *Journal of Microelectromechanical Systems,* 2014.

[21] M. N. Akram, Z. Tong, G. Ouyang, X. Chen and V. Kartashov, "Laser speckle reduction due to spatial and angular diversity introduced by fast scanning micromirror.," *Applied Optics,* vol. 49, no. 17, pp. 3297-3304, 2010.

[22] D.-K. Yang and S.-T. Wu, Fundamentals of Liquid Crystal Devices, Chichester, UK: John Wiley

& Sons, Ltd, 2014.

[23] P. S. Salter, "Flexoelectricity and Chirality in Complex Liquid Crystal Systems," DPhil Thesis, *University of Oxford*, 2010.

[24] W. H. De Jeu, E. P. Raynes, A. H. Price and M. G. Clark, "Liquid Crystalline Materials: Physical Properties and Intermolecular Interactions," *Philosophical Transactions of the Royal Society of London. Series A, Mathematical and Physical Sciences,* vol. 309, pp. 217-229, 1983.

[25] F. C. Frank, "On the theory of liquid crystals," *Discussions of the Faraday Society,* pp. 19-28, 1958.

[26] S. M. Morris and H. J. Coles, "Chiral Nematic Liquid Crystals and Electric, Magnetic, and Mechanical Fields," in *Handbook of Liquid Crystals: 8*, Second Edi ed., T. K. J. W. Goodby, P. J. Collings and a. P. R. C. Tschierske, H. F. Gleeson, P. Raynes Eds., Wiley-VCH Verlag GmbH & Co, 2014.

[27] L. M. Blinov, Electro-optical and magneto-optical properties of liquid crystals, Wiley, 1983, p. 341.

[28] K. Sueda, K. Tsubakimoto, N. Miyanaga and M. Nakatsuka, "Speckle suppression of laser light using liquid crystals aligned by photoisomerization of dye molecules," *Applied Physics Letters,* 2002.

[29] A. A. Andreev, T. B. Andreeva, I. N. Kompanets, M. V. Minchenko and E. P. Pozhidaev, "Speckle-noise suppression due to a single ferroelectric liquid-crystal cell," *Journal of the Society for Information Display,* vol. 17, no. 10, pp. 801-807, 2009.

[30] I. N. Kompanets, A. L. Andreev, T. B. Andreeva and M. V. Minchenko, "Speckle Suppression by Means of Ferroelectric LC Cell," *SID Symposium Digest of Technical Papers,* pp. 1065-1068, 2010.

[31] A. L. Andreev, T. B. Andreeva and I. N. Kompanets, "Speckle Reduction Due to using the Electro-optical Cell with Helix-free FLC," *SID 2014 Digest,* vol. 31, no. 1, pp. 411-414, 2014.

[32] H. Furue, A. Terashima, M. Shirao, Y. Koizumi and M. Ono, "Control of laser speckle noise using liquid crystals," *Japanese Journal of Applied Physics,* vol. 50, no. 9 PART 3, p. 09NE14, 2011.

[33] H. Furue, Y. Sugimoto, K. Iwami, W. Weng and M. Ono, "Control of Laser Speckle Noise by Using Polymer-Dispersed LC," *Molecular Crystals and Liquid Crystals,* vol. 612, no. 1, pp. 245-250, 2015.

[34] J. I. Trisnadi, "Hadamard speckle contrast reduction," *Optics Letters,* vol. 29, no. 1, pp. 11-13, 2004.

[35] P. J. Collings and M. Hird, Introduction to liquid crystals chemistry and physics, Taylor & Francis, 1997, p. 298.

[36] G. Heilmeier, L. Zanoni and L. Barton, "Dynamic scattering: A new electrooptic effect in certain classes of nematic liquid crystals," *Proceedings of the IEEE,* vol. 56, no. 7, pp. 1162-1171, 1968.

[37] N. Éber, P. Salamon and Á. Buka, "Electrically induced patterns in nematics and how to avoid them," *Liquid Crystals Reviews,* vol. 4, no. 2, pp. 101-134, 2 7 2016.

[38] G. H. Heilmeier, L. A. Zanoni and L. A. Barton, "Dynamic scattering in nematic liquid crystals," *Applied Physics Letters,* vol. 13, no. 1, pp. 46-47, 17 7 1968.

[39] W. Helfrich, "Electrohydrodynamic and Dielectric Instabilities of Cholesteric Liquid Crystals," *The Journal of Chemical Physics,* vol. 55, no. 2, pp. 839-842, 1971.

[40] D. Coates, W. A. Crossland, J. H. Morrisy and B. Needham, "Electrically induced scattering textures in smectic a phases and their electrical reversal," *Journal of Physics D: Applied Physics,* vol. 11, no. 14, pp. 2025-2034, 1 10 1978.

[41] W. Haas, J. Adams and G. Dir, "Optical storage effects in liquid crystals," *Chemical Physics Letters,* vol. 14, no. 1, 1972.

[42] D.-K. Yang, M. Yu and H. Yang, "Stabilized Electrically Induced Helfrich Deformation and Enhanced Color Tuning in Cholesteric Liquid Crystals," *Soft Matter,* 2017.

[43] Mettler-Toledo Ltd, 64 Boston Road, Beaumont Leys, Leicester, LE4 1AW: www.uk.mt.com.

[44] INSTEC, 5589 Arapahoe Avenue #208, Boulder, Colorado 80303, USA: www.instec.com.

[45] Agilent Technologies, 5301 Stevens Creek Blvd, Santa Clara, CA 95051, United States: www.agilent.com.

[46] Olympus, KeyMed House, Stock Road, Southend-on-Sea, SS2 5QH, UK: www.olympus.co.uk.

[47] QImaging, 19535 56th Avenue, Suite 101, Surrey, BC, Canada, V3S 6K3: www.qimaging.com.

[48] Ocean Optics, 8060 Bryan Dairy Rd, Largo, FL 33777, USA: https://oceanoptics.com.

[49] Tektronix Inc, 14150 SW Karl Braun Drive, P.O. Box 500, Beaverton, OR 97077, United States: www.tek.com.

[50] FLC Electronics AB, Sippedalsvagen 8, S-433 31 Partille, Sweden: www.flcelectronics.com.

[51] Lumentum Operations LLC (formally JDS Uniphase), 400 North McCarthy Blvd, Milpitas, California 95035, United States: www.lumentum.com.

[52] Thorlabs Inc, 56 Sparta Avenue, Newton, New Jersey 07860, United States: www.thorlabs.com.

[53] J. W. Goodman, "Some fundamental properties of speckle," *J. Opt. Soc. Am.,* vol. 66, no. 11, pp. 1145-1150, 1976.

[54] D. C. Initiatives, "Recommended Practice," July 2015. [Online]. Available: http://www.dcimovies.com/Recommended_Practice/#4projection3d.

[55] S. V. Pokorny J., "How much light reaches the retina?," in *Documenta Ophthalmologica Proceedings Series*, 1997, pp. 491-512.

[56] W. J. Smith, Modern Optical Engineering, New York: McGraw-Hill International Book Co, 1966.

[57] C. A. Curcio, K. R. Sloan, R. E. Kalina and A. E. Hendrickson, "Human photoreceptor topography," *Journal of Comparative Neurology,* vol. 292, pp. 497-523, 1990.

[58] S. Hecht and S. Shlaer, "Intermittent stimulation by light: V. The relation between intensity and critcal frequency for different parts of the spectrum.," *The Journal of general physiology,* vol. 19, no. 6, pp. 965-977, 1936.

[59] J. Krauskopf and J. D. Mollon, "The independence of the temporal integration properties of individual chromatic mechanisms in the human eye.," *The Journal of physiology,* vol. 219, no. 3, pp. 611-23, 12 1971.

[60] Y. S. Kwon, "Transverse Electric Field Effect in a Cholestric Liquid Crystal," *Molecular Crystals and Liquid Crystals,* vol. 65, no. 3-4, pp. 227-240, 20 3 1981.

[61] G. H. Heilmeier and J. E. Goldmacher, "A new electric-field-controlled reflective optical storage effect in mixed-liquid crystal systems," *Applied Physics Letters,* vol. 13, no. 4, pp. 132-133, 1968.

[62] L. Melamed and D. Rubin, "Electric field hysteresis effects in cholesteric liquid crystals," *Applied Physics Letters,* vol. 16, no. 12, 1970.

[63] F. Rondelez, H. Arnould and C. J. Gerritsma, "Electrohydrodynamic effects in cholesteric liquid crystals under ac electric fields," *Physical Review Letters,* vol. 28, no. 12, pp. 735-737, 1972.

[64] M. De Zwart and T. W. Lathouwers, "Electric field-induced pitch contraction in the planar cholesteric texture of a liquid crystal with a large negative dielectric anisotropy," *Physics Letters A,* vol. 55, no. 1, pp. 41-42, 3 11 1975.

[65] H. Arnould-Netillard and F. Rondelez, "Electrohydrodynamic Instabilities in Cholesteric Liquid Crystals with Negative Dielectric Anisotropy," *Molecular Crystals and Liquid Crystals,* vol. 26, no. 1-2, pp. 11-31, 1974.

[66] M. L. Sartirana, B. Valenti and R. Bartolino, "Elastic Deformations and Electrohydrodynamic Instabilities in Large Pitch Cholesteric Liquid Crystals under an Electric Field," *Molecular Crystals and Liquid Crystals,* vol. 98, no. 1, pp. 321-347, 17 9 1983.

[67] J. P. Hurault, "Static distortions of a cholesteric planar structure induced by magnetic or ac electric fields," *The Journal of Chemical Physics,* vol. 59, no. 4, pp. 2068-2075, 15 8 1973.

[68] P. S. Salter, G. Carbone, E. J. Botcherby, T. Wilson, S. J. Elston and E. P. Raynes, "Liquid crystal director dynamics imaged using two-Photon fluorescence microscopy with remote focusing," *Physical Review Letters,* vol. 103, no. 25, 2009.

[69] P. S. Salter, C. Kischka, S. J. Elston and E. P. Raynes, "The influence of chirality on the

difference in flexoelectric coefficients investigated in uniform lying helix, grandjean and twisted nematic structures," *Liquid Crystals,* vol. 36, no. 12, pp. 1355-1364, 2009.

[70] J. Li, "Refractive Indices Of Liquid Crystals And Their Applications In Display And Photonic Devices," Doctoral Dissertation, *University of Central Florida*, 2005.

[71] J.-S. Kim, M. Jamil, J. E. Jung, J. E. Jang, J. W. Lee, F. Ahmad, M.-K. Woo, J. Y. Kwak and Y. J. Jeon, "Rotational viscosity calculation method for liquid crystal mixture using molecular dynamics," *Journal of Information Display,* vol. 12, no. 3, pp. 135-139, 2011.

[72] C. Kischka, "Flexoelectricity in Nematic Liquid Crystals," DPhil Thesis, *University of Oxford*, 2011.

[73] S.-Y. Lu and L.-C. Chien, "Carbon nanotube doped liquid crystal OCB cells: physical and electro-optical properties.," *Optics express,* vol. 16, no. 17, pp. 12777-12785, 2008.

[74] M. V. Mitrokhin, L. Johnsen, R. Fagerberg, C. Kristiansen, F. J. Farrand, K. H. Holm, R. Palm, K. Netland and V. L. Aristov, "Prevention of smectic-A LC mixtures electrolytic degradation," *Molecular Crystals and Liquid Crystals,* vol. 411, 2004.

[75] M. V. Mitrokhin, L. Johnsen, R. Fagerberg, B. Holter and V. L. Arisov, "Adsorption processes during the filling of a display with a smectic A LC mixture," *Liquid Crystals,* vol. 31, no. 3, pp. 317-324, 2004.

[76] D. F. Aliev and G. M. Bayramov, "On the Electrophysical Properties of Polycomponent Mixtures Exhibiting the Smectic A Phase," *Mol. Cryst. Liq. Cryst.,* vol. 213, no. 1, pp. 137-143, 1992.

[77] D. J. Gardiner and H. J. Coles, "Organosiloxane liquid crystals for fast-switching bistable scattering devices," *Journal of Physics D: Applied Physics,* vol. 39, no. 23, pp. 4948-4955, 7 12 2006.

[78] E. A. Konshina and D. P. Shcherbinin, "Study of dynamic light scattering in nematic liquid crystal and its optical, electrical and switching characteristics," *Liquid Crystals,* vol. 45, no. 2, pp. 292-302, 26 1 2018.

[79] D. J. Gardiner and H. J. Coles, "Enhancing lifetime in a bistable smectic A liquid crystal device," *Journal of Physics D: Applied Physics,* vol. 40, no. 4, pp. 977-981, 21 2 2007.

[80] D. J. Gardiner and H. J. Coles, "Highly anisotropic conductivity in organosiloxane liquid crystals," *Journal of Applied Physics,* vol. 100, no. 12, p. 124903, 15 12 2006.

[81] D. J. Gardiner, "Electro-optic studies of bistable smectic A organosiloxane liquid crystals," PhD Thesis, *University of Cambridge*, 2006.

[82] A. A. Khan, S. M. Morris, D. J. Gardiner, M. M. Qasim, T. D. Wilkinson and H. J. Coles, "Improving the stability of organosiloxane smectic A liquid crystal random lasers using redox dopants," *Optical Materials,* vol. 42, pp. 441-448, 2015.

[83] H. S. Lim and J. D. Margerum, "Improved dc dynamic scattering with redox dopants in ester liquid crystals," *Applied Physics Letters,* vol. 28, no. 9, pp. 478-480, 28 5 1976.

[84] G. Brière, R. Herino and F. Mondon, "Correlation between Chemical and Electrochemical Reactivity and dc Conduction in the Isotropic Phase of a Liquid Crystalline p - Methoxybenzylidene- p-n -butylaniline," *Molecular Crystals and Liquid Crystals,* vol. 19, no. 2, pp. 157-177, 28 12 1972.

[85] S. Matsumoto, K. Mizunoya, M. Kawamoto, Y. Wada and H. Tomii, "Effect of Liquid Crystal Classes on the Improvement of Dynamic Scattering by Electron Donor-Acceptor Dopants," *Molecular Crystals and Liquid Crystals,* vol. 71, no. 3-4, pp. 259-268, 20 8 1981.

[86] A. I. Baise, I. Teucher and M. M. Labes, "Effect of charge-transfer acceptors on dynamic scattering in a nematic liquid crystal," *Applied Physics Letters,* vol. 21, no. 4, pp. 142-143, 1972.

[87] B. Gosse and J. P. Gosse, "Degradation of liquid crystal devices under d.c. excitation and their electrochemistry," *Journal of Applied Electrochemistry,* vol. 6, no. 6, pp. 515-519, 11 1976.

[88] H. S. Lim, J. D. Margerum and A. Graube, "Electrochemical Properties of Dopants and the D-C Dynamic Scattering of a Nematic Liquid Crystal," *Solid state science and technology,* no. iii, pp. 1389-1394, 1977.

[89] A. Andreev, T. Andreeva, I. Kompanets, N. Zalyapin, H. Xu, M. Pivnenko and D. Chu, "Fast bistable intensive light scattering in helix-free ferroelectric liquid crystals," *Appl. Opt.,* vol.

55, no. 13, pp. 3483-3492, 2016.

[90] S. Hurley, D.-K. Yang and C. Mullin, "20.4: The Scattering Profile of Polymer Stabilized Cholesteric Texture Displays," *SID Symposium Digest of Technical Papers,* vol. 41, no. 1, p. 293, 1 5 2010.

[91] S. Hirata, I. Matsuzaki, A. Yanagita and T. Tako, "Successive Transitions in Cholesteric Liquid Crystals," *Journal of the Physical Society of Japan,* vol. 50, no. 12, pp. 3862-3868, 15 12 1981.

[92] R. Eidenschink and W. H. De Jeu, "Static scattering in filled nematic: new liquid crystal display technique," *Electronics Letters,* vol. 27, no. 13, p. 1195, 1991.

[93] A. Glushchenko, H. Kresse, V. Reshetnyak, Y. Reznikov and O. Yaroshchuk, "Memory effect in filled nematic liquid crystals," *Liquid Crystals,* vol. 23, no. 2, pp. 241-246, 1997.

[94] M. Kreuzer, T. Tschudi and R. Eidenschink, "Erasable Optical Storage in Bistable Liquid Crystal Cells," *Molecular Crystals and Liquid Crystals Science and Technology. Section A. Molecular Crystals and Liquid Crystals,* vol. 223, no. 1, pp. 219-227, 1992.

[95] F. Haraguchi, K. I. Inoue, N. Toshima, S. Kobayashi and K. Takatoh, "Reduction of the threshold voltages of nematic liquid crystal electrooptical devices by doping inorganic nanoparticles," *Japanese Journal of Applied Physics, Part 2: Letters,* vol. 46, no. 33-35, pp. 8-10, 2007.

[96] T. Hegmann, H. Qi and V. M. Marx, "Nanoparticles in liquid crystals: Synthesis, self-assembly, defect formation and potential applications," *Journal of Inorganic and Organometallic Polymers and Materials,* vol. 17, no. 3, pp. 483-508, 2007.

[97] C.-Y. Tang, S.-M. Huang and W. Lee, "Electrical properties of nematic liquid crystals doped with anatase TiO2 nanoparticles," *Journal of Physics D: Applied Physics,* vol. 44, no. 35, p. 355102, 2011.

[98] T.-r. Chou, J. Hsieh, W.-t. Chen and C.-y. Chao, "Influence of particle size on the ion effect of TiO2 nanoparticle doped nematic liquid crystal cell," *Japanese Journal of Applied Physics,* vol. 53, p. 071701, 2014.

[99] G. Pathak, S. Pandey, R. Katiyar, A. Srivastava, R. Dabrowski, K. Garbat and R. Manohar, "Analysis of photoluminescence, UV absorbance, optical band gap and threshold voltage of TiO2nanoparticles dispersed in high birefringence nematic liquid crystal towards its application in display and photovoltaic devices," *Journal of Luminescence,* vol. 192, no. February, pp. 33-39, 2017.

[100] Z. Tong, W. Cheng, S. Jia and X. Chen, "Weak-scattering static diffuser by fast pumping dispersed-nanoparticles in a long distance using microfluidic flows for efficient laser speckle reduction," *Optics Express,* vol. 26, no. 16, p. 20270, 6 8 2018.

[101] R. Katiyar, G. Pathak, A. Srivastava, J. Herman and R. Manohar, "Analysis of electro-optical and dielectric parameters of TiO2nanoparticles dispersed nematic liquid crystal," *Soft Materials,* vol. 16, no. 2, pp. 126-133, 2018.

[102] S. P. Yadav, R. Manohar and S. Singh, "Effect of TiO2 nanoparticles dispersion on ionic behaviour in nematic liquid crystal," *Liquid Crystals,* vol. 42, no. 8, pp. 1095-1101, 2015.

[103] M. C. W. Van Boxtel, R. H. C. Janssen, C. W. M. Bastiaansen and D. J. Broer, "Viscoelastic liquid crystal colloids for the continuous processing of twisted nematic electro-optical cells," *Citation: Journal of Applied Physics,* vol. 89, p. 838, 2001.

[104] G. Vertogen and W. H. de Jeu, Thermotropic Liquid Crystals, Fundamentals, Springer-Verlag Berlin Heidelberg, 1998.

[105] S. T. Wu and C. S. Wu, "Experimental confirmation of the Osipov-Terentjev theory on the viscosity of nematic liquid crystals," *Physical Review A,* vol. 42, no. 4, pp. 2219-2227, 1990.

[106] B. R. Ratna and R. Shashidhar, "Dielectric properties of 4′-n-alkyl-4-cyanobiphenyls in their nematic phases," *Pramana,* vol. 6, no. 5, pp. 278-283, 5 1976.

[107] J. Li, G. Baird, Y.-H. H. Lin, H. W. Ren and S.-T. T. Wu, "Refractive-index matching between liquid crystals and photopolymers," *Journal of the Society for Information Display,* vol. 13, no. 12, p. 1017, 2005.

[108] M. W. Geis, T. M. Lyszczarz, R. M. Osgood, B. R. Kimball, R. K. Reich, D. D. Rathman, D. J. Young, A. H. Loomis, R. A. Murphy, M. Rose, R. Berger, B. M. Tyrrell, S. A. Watson, M. D. Ulibarri, T. Perry, F. Weber, H. Robey, L. Laboratory, H. Takanashi, J. E. Maclennan, N. A.

Clark, H.-y. Wu, C.-y. Wang, C.-j. Lin, R.-p. Pan, S.-s. Lin, C.-d. Lee and C.-s. Kou, "Sub 100 Nanosecond Pretilted Planar-to-Homeotropic Reorientation of Nematic Liquid Crystals under High Electric Field," *J. Appl. Phys,* vol. 37, no. 5, pp. 2587-2589, 1998.

[109] M. Simões, D. S. Simeão, S. M. Domiciano and A. de Campos, "Nematic universality," *Physics Letters, Section A: General, Atomic and Solid State Physics,* vol. 372, no. 32, pp. 5346-5351, 2008.

[110] S. Dixit, R. Manohar and A. K. Arora, "Modification in nematic liquid crystal made by gamma irradiation: Biasing voltage and electro-optical study," *Radiation Effects and Defects in Solids,* vol. 168, no. 4, pp. 297-307, 2013.

[111] J. W. Goodman, Introduction to Fourier Optics, McGraw-Hill, 1996.

[112] M. Born and E. Wolf, Principles of Optics, Cambridge University Press, 1999.

[113] D. A. Tichenor and J. W. Goodman, "Coherent Transfer Function," *Journal of the Optical Society of America,* vol. 62, no. 2, p. 293, 1972.

[114] K. J. Dana, B. van Ginneken, S. K. Nayar and J. J. Koenderink, "Reflectance and texture of real-world surfaces," *ACM Transactions on Graphics,* vol. 18, no. 1, pp. 1-34, 1999.

[115] S. R. Marschner, S. H. Westin, E. P. F. Lafortune and K. E. Torrance, "Image-based bidirectional reflectance distribution function measurement," *Applied optics,* vol. 39, no. 16, pp. 2592-2600, 2000.

[116] G. J. Ward, "Measuring and Modeling Anisotropic Reflection," *Computer Graphics,* vol. 26, no. 2, pp. 265-272, 1992.

[117] D. D. Duncan and S. J. Kirkpatrick, "Algorithms for simulation of speckle (laser and otherwise)," *Proc. SPIE 6855, Complex Dynamics and Fluctuations in Biomedical Photonics V*, 685505, 2008.

[118] "https://www.fine-tools.com/G10019.html," [Online].

[119] E. Kriezis and S. Elston, "A wide angle beam propagation method for the analysis of tilted nematic liquid crystal structures," *Journal of Modern Optics,* vol. 46, no. 8, pp. 1201-1212, 1999.

[120] G. R. Hadley, "Transparent boundary condition for the beam propagation method," *IEEE Journal of Quantum Electronics,* vol. 28, no. 1, pp. 363-370, 1992.

[121] S.-T. Wu and K.-C. Lim, "Absorption and scattering measurements of nematic liquid crystals," *Applied Optics*, vol. 26, issue 9, pp. 1722-1727 (1987).

[122] https://www.optotune.com/products/laser-speckle-reducers